Smart Building and Construction Materials

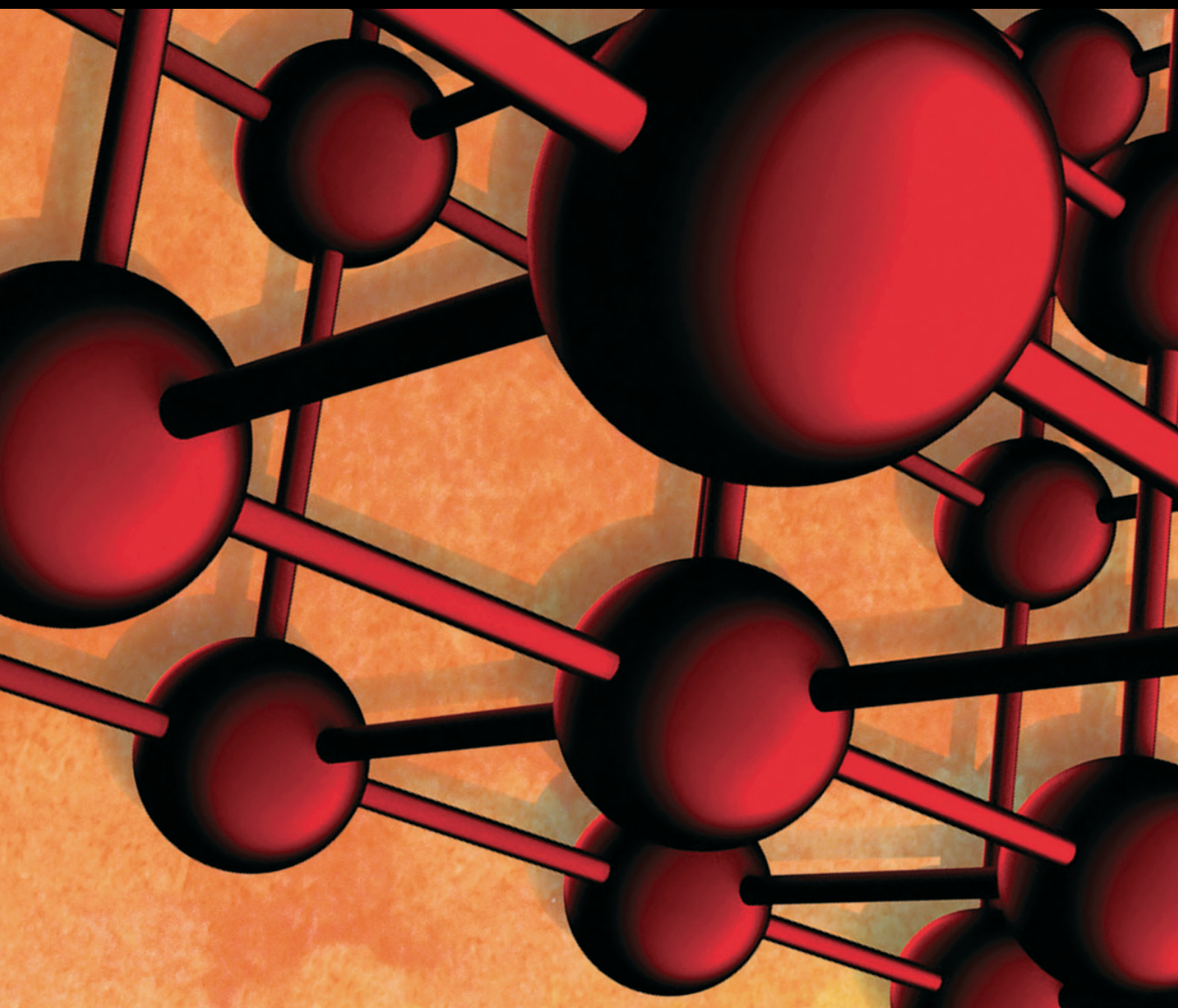Lead Guest Editor: Donglu Shi
Guest Editors: Julian Wang and Wen Deng

Smart Buildings and Construction Materials

Smart Buildings and Construction Materials

Lead Guest Editor: Donglu Shi
Guest Editors: Julian Wang and Wen Deng

Editorial Board

Contents

Editorial
Smart Building and Construction Materials

Donglu Shi ⓘ,[1] Julian Wang ⓘ,[2,3] and Wen Deng ⓘ[4]

[1]*The Materials Science and Engineering Program, Department of Mechanical and Materials Engineering,
College of Engineering and Applied Science, University of Cincinnati, Cincinnati 45221-0072, USA*
[2]*Department of Civil and Architectural Engineering and Construction Management, University of Cincinnati, Cincinnati,
OH 45221, USA*
[3]*School of Architecture and Interior Design, University of Cincinnati, Cincinnati, OH 45221, USA*
[4]*Department of Civil, Architectural and Environmental Engineering, Missouri University of Science and Technology, Rolla,
MO 65409, USA*

Correspondence should be addressed to Donglu Shi; shid@ucmail.uc.edu

Advances and innovations in materials science and engineering have always played a substantial role in civil engineering, building structural design, and construction. In recent years, extensive effort has been devoted to the applications of stimuli-responsive smart materials and nanostructures in buildings. These smart materials used in the built environment can be defined as those offering specific functional and adaptable properties in response to thermal, optical, structural, and environmental stimuli. Not only do these materials enhance the overall performance of new building construction but also promise safer structures, longer durability of building elements, efficient building energy savings, greater environmental sustainability, and even higher indoor user comfort. Given the increasing imperatives for the above, we have organized this themed special issue that focuses on smart buildings and construction materials. The main aim of this special issue is to encapsulate the current interest and state of research related to the smart materials in building and construction applications, underpinning current and future challenges in building energy, environmental sustainability, and structural safety and durability.

In this special issue, after rigorous peer-review processes, the original research papers and review papers accepted cover a wide range of topics that address the critical issues in the development and implementation of smart materials for building design and construction. A total of ten papers in this special issue are listed as follows.

In the article titled, "Applications of Shape Memory Polymers in Kinetic Buildings," J. Li et al. investigated the structures and systems and focused on the mechanisms and behaviors of two-way shape memory effects. Special emphasis was on the potential use of the reversible shape-changing abilities of dynamic envelope structures for building energy efficiency.

S. Hao et al. proposed a heat recovery wall system composed of high thermal mass materials and air cavities which can efficiently recover gas heat from heating stoves and reduce users' exposure to indoor air pollution. They conducted on-site experimental tests to investigate the surface temperature distribution and thermal performance of this specific wall system design.

J. Li et al. examined modular prefabricated buildings with steel structural systems and integrated building envelopes using computational simulations and experimental tests. Their results highlighted the environmental performance of each construction detail and possibilities of optimizing the design of integrated envelopes for environmental sustainability.

S. Antony et al. carried out numerical analysis to study the correlation of delamination onset and investigated the methods to enhance delamination strength of unidirectional pultruded smart composite platforms.

C. Kang et al. evaluated the self-healing performance of concrete containing fly ash and fiber for improving healing performance, by comparing the flexural load and the flexural stiffness before and after crack, using the notched specimen.

S. P. Dunuweera and R. M. G. Rajapakse reviewed the manufacturing processes, mechanical properties, typical uses, and associated environmental emissions of different

types of cement products used in civil and building environment.

R. Zhong et al. developed an optical-fiber-based thermal integrity profiling (TIP) method to provide a comprehensive and accurate evaluation of the defects inside of concrete. The proposed method was compared to the current thermal infrared probe or embedded thermal sensor-based TIP and showed better determination of deflect location and size.

N. Shaheen et al. presented data on use of limestone powder as a carrier medium to immobilize *Bacillus subtilis* and its contribution to self-healing efficiency of cementitious materials in terms of recovery of compressive strength.

I. -H. Yang et al. performed experimental tests to study the flexural responses of high-strength fiber-reinforced concrete beams and high-strength concrete beams. Crack and failure patterns, load capacity, deflection, crack stiffness, ductility, and flexural toughness were compared and investigated.

Y. J. O. Moraes et al. presented results on a passive vibration control system with superelastic shape memory alloy coil springs configuration and evaluated the performance of the proposed system through analytical, numerical, and experimental methods.

This special issue not only is providing the most up-to-date information on focused areas of smart building materials, utilizing advanced materials science, but also intended to serve as an informative tutorial for nontechnical specialists from fields of architectural engineering, civil engineering, materials science, chemistry, computer simulation, and environmental engineering. It will shed new light on the various new strategies adopted for building design, structural engineering, and construction. Both undergraduate and graduate students will find this special issue a valuable reference for their special research projects and thesis works. We hope these articles will provide timely and useful information for the progress of advanced materials applications in smart buildings.

Conflicts of Interest

We, the Guest Editorial team of this special issue, declare that there are no conflicts of interest or private agreements with companies regarding our work for this special issue. We have no financial relationships through employment, consultancies, and either stock ownership or honoraria, with the industry.

Acknowledgments

We are grateful to all authors for their excellent contributions to this special issue.

Donglu Shi
Julian Wang
Wen Deng

Review Article
Applications of Shape Memory Polymers in Kinetic Buildings

Jing Li,[1] Qiuhua Duan,[2] Enhe Zhang,[3] and Julian Wang ⓘ[2,3]

[1]Department of Architecture, North China University of Technology, Beijing 100041, China
[2]Department of Civil and Architectural Engineering and Construction Management, University of Cincinnati, Cincinnati, OH 45221, USA
[3]School of Architecture and Interior Design, University of Cincinnati, Cincinnati, OH 45221, USA

Correspondence should be addressed to Julian Wang; wang4ja@ucmail.uc.edu

Shape memory polymers (SMPs) have attracted significant attention from both industrial and academic researchers, due to their useful and fascinating functionality. One of the most common and studied external stimuli for SMPs is temperature; other stimuli include electric fields, light, magnetic fields, water, and irradiation. Solutions for SMPs have also been extensively studied in the past decade. In this research, we review, consolidate, and report the major efforts and findings documented in the SMP literature, according to different external stimuli. The corresponding mechanisms, constitutive models, and properties (i.e., mechanical, electrical, optical, shape, etc.) of the SMPs in response to different stimulus methods are then reviewed. Next, this research presents and categorizes up-to-date studies on the application of SMPs in dynamic building structures and components. Following this, we discuss the need for studying SMPs in terms of kinetic building applications, especially about building energy saving purposes, and review recent two-way SMPs and their potential for use in such applications. This review covers a number of current advances in SMPs, with a view towards applications in kinetic building engineering.

1. Introduction

Shape memory polymers (SMPs) are an emerging class of intelligent polymers that can change their shapes in predefined ways, in response to appropriate stimulation [1]. Vernon et al. fortuitously discovered "shape memory" in polymers in 1941 [2]. In the 1960s, the utilization of covalently crosslinked polyethylenes (PEs) in heat-shrinkable tubing and film became another important milestone in the development of SMPs [3–6]. Significant efforts began in the 1980s to find additional applications, and this trend has continued in recent years (particularly in Japan and the US) [5, 6]. Compared with shape memory alloys (SMAs), SMPs possess the advantages of high elastic deformation, low cost, low density, and potential biocompatibility and biodegradability [6]. They also have a wide range of tailorable application temperatures and tunable stiffnesses and are easily processed [5].

SMPs typically consist of crosslinked segments that determine the permanent shape and switching segments at transition temperatures that fix the temporary shape [7]. Figure 1 shows the three-dimensional structure of an SMP. In Figure 1, a network-like architecture can be seen resulting from crosslinked net points (the black dots); the switch segment (the grey cube) connects them entropically to form a given macroscopic shape [8]. The permanent shape of the SMP is determined either by physical or chemical crosslinks. Therefore, based on the nature of the crosslinks, conventional SMPs relying on thermal phase changes can be categorized into two types, those that are either chemically or physically crosslinked. According to the nature of the switching segments, SMPs can also be divided into those with either amorphous or crystalline switching segments [7–9].

Upon the reversibility of shape memory effect (SME), SMPs can also be classified into either one-way or two-way SMPs. "One-way" implies that the shape recovery is irreversible. That is, shape shifting during recovery can only proceed from a temporary to a permanent shape and not the reverse (Figure 2). "Two-way" means that the shape change is reversible; the initial and temporary shapes can be

reversed with the appearance and termination of the stimulus. Thus, these two-way SMPs can achieve dual or even triple shape changes (Figures 2 and 3). Two-way SMPs have received considerable attention in recent years because of their ability to change shapes in response to the external stimuli to which they are exposed. Many researchers have proposed potential applications in areas such as artificial muscles, textiles, and actuators [10–12]. In Section 4, we will discuss two-way SMPs and their potentials in detail.

Based on the number of shapes involved in each shape memory cycle, SMPs can be classified as dual, triple, or multi-SMP [13]. A typical SMP is dual (i.e., one temporary shape transformed into a permanent shape). In contrast, triple-SMPs feature two temporary shapes (A and B in Figure 3) in addition to their permanent one (C in Figure 3). First, the temporary shape B must be programmed, followed by the temporary shape A. The appropriate stimulus transforms the second temporary shape into the first (A→B). Subsequently, a second trigger initiates the regeneration of the permanent shape C. A multi-SMP (shown in Figure 3) is able to memorize more than two temporary shapes and subsequently recover in a highly controllable manner [14–16].

One of the most common external stimuli for SMPs is temperature. Many athermal stimulation methods (including electric fields, light, magnetic fields, water, irradiation, and solutions) for SMPs have been studied in the past decade. Based on such methods, SMPs can be classified into temperature-responsive, electric-responsive, magnetic-responsive, photo-responsive, or solution-responsive triple- or multi-SMPs. The corresponding mechanisms and properties (such as mechanical, electrical, optical, shape, constitutive model) of different stimulation methods will be discussed in Section 2.

SMPs are widely used in areas such as biomedical devices, aerospace engineering, textiles, energy, bionics engineering, electrical engineering, the development of household products, and civil and architectural engineering. Many extensive reviews have been conducted and published by various groups. These reviews have covered general aspects of SMPs [15, 16], multifunctional SMPs [17], SMP composites [18, 19], SMP foam [15–19], SMP fibers [20–23], and SMP characterization. However, from the perspective of possible applications, much of the discussion in these review studies has revolved around applications in the biomedical [17, 24, 25] and aerospace engineering [18, 26–28] fields. Given the trend in recent studies of investigating applications in civil and architectural engineering, it is worth reviewing the major efforts and developments there.

SMPs have been fabricated and used for critical civil infrastructure. Li et al. proposed that SMPs be employed as sealants such as SMP-based sealants [29], asphalt-based liquid sealants, two-way shape-changing polymer sealants, rutting resistance asphalt concrete materials, and self-healing materials for damaged structures [30–32]. Two types of SMP-based smart sealants have been successfully applied in compression-sealed joints in concrete pavement [32]. Carbon fiber reinforced SMP composites have been analyzed with the potential for application as lightweight
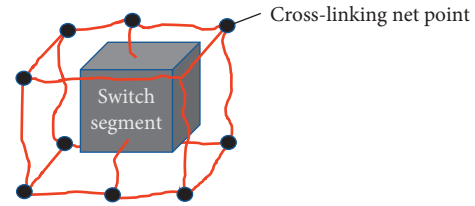
Figure 1: Modular architecture of an SMP.
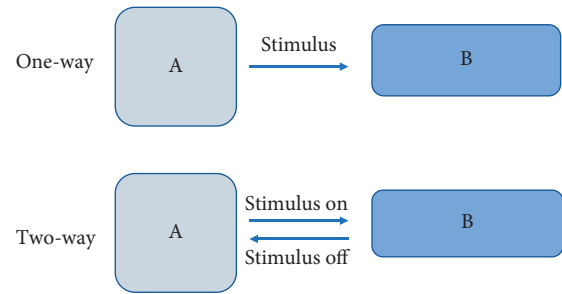
Figure 2: One-way and two-way SMPs.
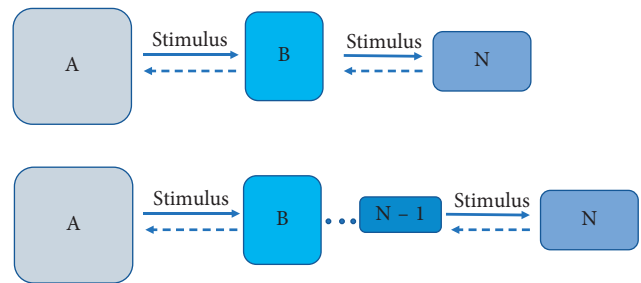
Figure 3: Triple- and multi-SMPs.

compactible structures [22]. SMPs have also been investigated with regards to their use in repairing fatigue-sensitive steel elements [20] and as structural components (beams, rods, plates etc.) for vibration control and remote sensing actuators [33, 34]. Section 3 of this paper provides a brief overview of these applications in built environments.

Nevertheless, two-way SMPs are more intelligent; they can sense environmental changes and respond to them in an optimal manner [35]. Applying two-way SMPs in built environments could offer real benefits, though there are still many difficulties with their proper engineering. Section 4 of this research concisely describes the mechanism of two-way SMPs, reviews certain popular areas of research, and lists particular challenges and opportunities related to their use in building and architecture applications.

2. Mechanisms of Different Stimulus-Responsive SMPs and Their Constitutive Models

2.1. Mechanisms of SMPs

2.1.1. Thermally Responsive SMPs. Most SMPs use heat as their stimulus [1]. These thermally responsive SMPs can be

regarded as thermoplastic elastomers, in which there is a hard phase with a high glass transition temperature (T_g) and a second, switching phase, with an intermediate or melting temperature (T_m) that enables the thermally responsive behavior [36]. The temperature surpassing T_g (or T_m) is symbolized as T_{high} and the temperature being lower than T_g (or T_m) is symbolized as T_{low}. First, the SMPs can be processed into any shape desired as the permanent shape. Then, when the temperature is higher than T_g (or T_m) and reaching T_{high}, a temporary shape can be induced that can be then "frozen" by cooling the deformed state at the low temperature condition, T_{low}. Consequently, when heated above T_g (or T_m), the SMPs transform back to their permanent shape [13, 37]. The schematic drawing in Figure 4 shows this thermally responsive process.

Molecular switches and net points are two major molecular-level components of thermally responsive SMPs. Molecular switches are segments with a thermal transition at T_m that fixes the temporary shape by forming physical crosslinks. Net points that link these switching segments and determine the permanent shape of the polymer network can either be physical crosslinks through physical intermolecular interactions or chemical crosslinks through covalent bonds [36].

2.1.2. Photoresponsive SMPs.

Photoresponsive SMPs can respond to light stimuli by undergoing reversible changes in their properties [37]. There are two main mechanisms that operate in light-induced SMPs: photochemical reactions leading to deformation and the employment of particles that convert light to heat [38, 39]. In photochemical reactions, intrinsically photoresponsive SMPs are produced by incorporating reversible photoreactive molecular switches when a special wavelength of light strikes them; this alters the structure of their crosslinked polymer networks. For example, Lendlein et al. showed that SMPs containing cinnamic groups can be deformed and fixed into predetermined shapes when exposed to alternating wavelengths ($\lambda > 260$ nm or $\lambda < 260$ nm) (Figure 5). The accumulation of structural alterations leads to an evolution of the polymer network and even subsequent macroscopic deformation. Consequently, photochemical SMEs are produced [38–41]. This stimulation is considered unrelated to any temperature changes. Therefore, it should be differentiated from the indirect actuation of thermally responsive SMPs [7]. Another photosensitive function is that molecular switches convert light to heat and then actuate thermally responsive SMPs [39]. Therefore, illumination with the radiant thermal energy of infrared light possessing a wide range of spectra ($500 \sim 4000$ cm^{-1}) can serve as a heat source for photoresponsive SMPs; these can then be applied with noncontact nonmediums [7, 39].

2.1.3. Electrically Responsive SMPs.

Electrically responsive SMPs are also intrinsically of the thermally responsive type [18]. Thermally active SMPs are usually filled with electrically conductive ingredients that reach a certain level of electrical conductivity; this means that electricity, as

a stimulus, enables their resistive actuation [7, 19]. Most SMPs have high levels of electrical and thermal resistance when the actuation is remotely controlled. They are heated via an electric current that passes through the conductive ingredient network within [18]. If the internal temperature is above the transition temperature, T_g, resulting in the permanent shape, then the SMP can be deformed into any shape. If the temperature is between T_g and T_m, a temporary shape can be induced and fixed by cooling the SMP to below T_m. Consequently, heating above the melting temperature, T_m, may trigger deformation recovery (Figure 4) [39]. Compared to the direct external heating method, the internal resistive joule heating method by electricity presents certain advantages, such as convenience, uniform heating, and remote controllability [18].

2.1.4. Magnetically Responsive SMPs.

Similar to electrically responsive SMPs, thermally active SMPs embedded with magnetic particles are magnetically responsive. An alternating magnetic field (AMF) produces inductive heating, which triggers the recovery process. The temperature can be increased rapidly since the heat is normally generated inside the polymer itself [42, 43]. N e' el relaxation (eddy current losses), Brownian motion relaxation (rotational losses), and hysteresis losses are the three main heating mechanisms that operate AMFs. In the N e' el relaxation mechanism, in response to an externally applied AMF, a particle's magnetic dipole changes its orientation within the particle. The particle's magnetic moment of resisting this orientation produces heat, which is also counted in the particle's magnetism [43, 44]. In Brownian motion relaxation, in response to an externally applied AMF, a particle physically rotates to align with the magnetic field; the friction between the rotating particles (responding to the externally applied AMF) and the carrier fluid (due to the viscosity effect of resisting the particle rotation) results in heat [42–44]. In addition to relaxation losses in larger particles with a particle size > 20 nm, thermal energy can be stemmed from magnetic hysteresis losses [44]. Hysteresis describes a path that depends on the magnetic response of magnetic materials to an applied magnetic field. Hysteresis losses mainly occur in domain wall motion, such as when multidomain ferro- or ferrimagnetic particles are exposed to an AMF. The generated heat is proportional to the area of the hysteresis loop and frequency of the AMF [44]. Basically, the heating power associated with relaxation loss lower than that of the hysteresis losses [44].

2.1.5. Solution-Responsive SMPs.

Solution-responsive SMPs present a significant decrease in the modulus during phase transition [45]. Water-driven actuation of SMPs was first discussed in 2005 by Huang [46]. In general, water or solvent molecules are able to infiltrate SMPs. Due to the plasticizing effect of water and solvent on SMPs and the increase in flexibility of macromolecules, the glass transition temperature, T_g, can be decreased after the addition of a small amount of water. When the glass transition temperature, T_g, approaches the ambient temperature, the recovery process of
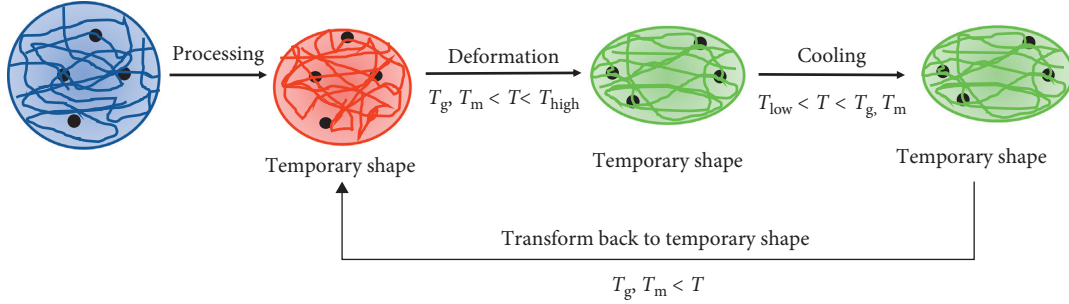
FIGURE 4: Thermomechanical cycle of thermally responsive shape memory polymers.

the water-induced SMP is triggered [18]. The interaction between macro- and micropolymeric molecule of the solution is the main mechanism behind this phenomenon. Three major reasons causing it are as follows: (1) the flexibility of the polymeric chains is magnified by the hydrogen bonding; (2) based on the continuum theories of rubber elasticity, the Mooney–Rivlin equation, and volume change refinement theory, the polymer modulus is destroyed due to the volume change in the polymer caused by the interaction; (3) the solution makes the polymer tender until T_g decreases to the temperature of the solution while T_g of the polymer is higher than the temperature of the solution or the ambient temperature. Consequently, the solution continues affecting the polymer's other aspects. T_g can decrease significantly and reach to the temperature of the solution because the micromolecular of the solution can weaken the elasticity modulus of the SMP. Therefore, the solution can trigger off the actuation of SMPs by means of reducing T_g of the material itself through immersing the SMPs into solution [45].

2.1.6. pH-Responsive SMPs.

The pH-responsive SMPs have great potentials in medical applications. The physiological pH values vary in different sites of the body, which generally appears as a sharp gradient across biological systems on both the cellular and systemic levels in pathological states [47]. A pH-responsive SMP reported by Han et al. can be processed into a temporary shape at pH 11.5 and recover to its initial shape at pH 7 [48]. A pH-responsive SMP based on polyurethane and the pH-stimulated DNA hydrogels have been also proposed [47]. The mechanism of pH-responsive SMP is mainly based on the polymer swelling at different pH values of the environment. The pH value of the environment can act as a switch to control the shape memory without temperature variations. If the pH-responsive SMP prepared with some chemical materials, the key for realizing the SME is the hydrogen bond interaction. For example, the pH-responsive SMP prepared with functionalized cellulose nanocrystals (CNCs), the hydrogen bond interaction between the modified CNCs percolation network, and matrix materials decides the SME [49]; for the pH-responsive SMP synthesized by introducing pyridine rings into the backbone of polyurethane, the hydrogen bond interactions between the N atom of the pyridine ring and H–N of urethane in neutral or
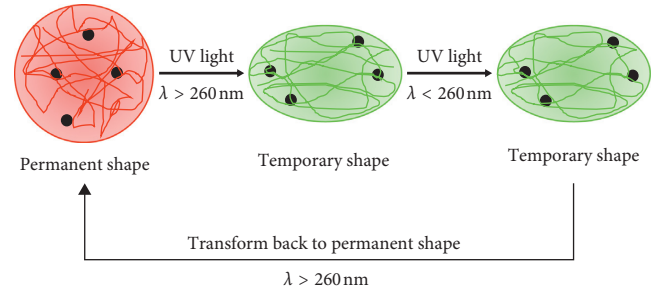
FIGURE 5: Schematic diagram of the molecular mechanism of photoresponsive SMPs.

alkaline environments are the main contributory cause of the SME [47].

2.2. Properties of SMPs

2.2.1. Constitutive Model of SMPs.

The constitutive model describes the relationship between stress and strain. The most important component is the viscoelastic constitutive model. Tobushi et al. developed a linear viscoelastic constitutive model of SMPs, and further established a one-dimensional nonlinear constitutive model [47, 48]. Liu et al. advanced a three-dimensional linear constitutive model in two phases: the active phase at high temperatures and frozen phase at low temperatures [50]. Many researchers have developed different constitutive models of SMPs, based on Tobushi and Liu's research. The overall small-strain constitutive equations are shown as follows [50]:

$$\sigma = \frac{\varepsilon - \varepsilon_s - \int_{T_h}^{T} \alpha \, dT}{(\phi_f/E_i) + ((1 - \phi_f)/E_e)} = E\left(\varepsilon - \varepsilon_s - \int_{T_h}^{T} \alpha \, dT\right), \quad (1)$$

where ε_s is the storable inelastic strain; ϕ_f is the frozen fraction; T_h is the temperature of the thermomechanical cycle starting; E is Young's modulus, $E = 1/((\phi_f/E_i) + ((1 - \phi_f)/E_e))$; E_i is the modulus of the internal energetic deformation, usually E_i = constant; E_e is the modulus of the entropic deformation, usually $E_e = 3NkT$; N is the crosslink density; k is Boltzmann's constant ($k = 1.38 \times 10^{-23}$ Nm/K); α is the coefficient of thermal expansion, $\alpha = d\varepsilon_T/dT$; and ε_T is the thermal strain.

2.2.2. Shape Memory Effect. In order to explain the shape memory effect of SMPs, the shape fixity rate, R_f, and shape recovery rate, R_r, are normally used as characteristic factors. Shape fixing, or fixity, refers to the ability of an SMP to retain a temporary state, and thus store strain energy, by cooling below a transformation temperature. Shape fixing can be quantified by use of the measure:

$$R_f(N) = \frac{\varepsilon_u(N)}{\varepsilon_m(N)} \times 100\%. \tag{2}$$

The shape recovery rate can then be calculated as follows:

$$R_r(N) = \frac{\varepsilon_u(N) - \varepsilon_p(N)}{\varepsilon_u(N) - \varepsilon_p(N-1)}, \tag{3}$$

where $\varepsilon_u(N)$ represents the strain of cycle N after unloading, $\varepsilon_m(N)$ is the temporal strain of cycle N that is achieved after deformation, and R_f may depend on the shape memory cycle number, N. Also, $\varepsilon_p(N)$ and $\varepsilon_p(N-1)$ are the extensions in the tension-free states while expanding the sample in two subsequent cycles, N and $N-1$. At the molecular level, fixing can be designed in an SMP by organizing the constituent chains to crystallize or vitrify at a targeted temperature or by otherwise immobilizing the chains.

3. A Brief Survey of Applications of SMPs in Civil and Architectural Engineering

This section presents a brief review of recent trends in the field of SMPs, with a particular focus on their applications in civil and architectural engineering. Compared with previous reviews of the field [5, 9, 18, 19, 51], this review summarizes information on civil and architectural engineering applications. In general, SMPs are mainly used as sealants and self-healing materials, vibration control systems, and actuators or sensors for structural health monitors. In addition, potential applications as smart materials for built environments are outlined in Figure 6.

3.1. Sealants and Self-Healing Materials. Li et al. presented an SMP-based smart sealant for compression-sealed joints in concrete pavement systems [32]. They also developed an SMP-based syntactic foam that is cored with sandwich structures for the purpose of repeatedly self-healing the impact image [30]. Additionally, they investigated the effects of various design parameters on the closing efficiencies of both pure SMPs and SMP-based syntactic foam [31]. This SMP-based self-healing syntactic foam was successfully tested as a sealant for expansion joint bridges and concrete pavement systems [29, 31, 50, 52, 53]. It was noted that SMP-based foams possessing self-healing properties can also be used in the civil and architectural fields [54]. Therefore, using SMPs as sealants (such as SMP-based, asphalt-based liquid, and two-way shape-changing polymer sealants) has become an important application direction in civil engineering. In addition to sealant applications, the self-healing abilities of SMPs have been also used to form SMP-based composite structures, another important application in civil engineering [55].
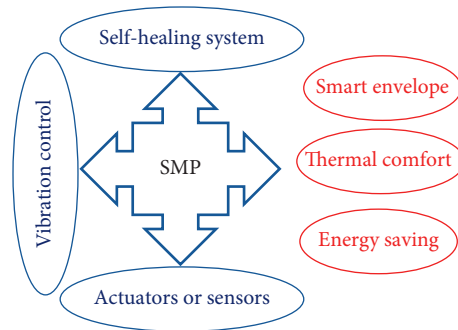
FIGURE 6: Applications of SMPs in civil and architectural engineering.

3.2. Vibration Control Applications. SMP-based structural components (beams, rods, plates, composites, etc.) allow for the tuning of a range of frequency bandwidths and damping properties for vibration control applications [54–56]. Brown et al. described the fabrication process and dynamic vibration testing of an electrically activated SMP [57]. They demonstrated how SMP beams could achieve variable stiffnesses and damping with a reasonable thermal gradient triggered by electricity. The results showed an approximately 7% shift in the natural frequency and 100% change in the damping ratio of a rectangular SMP beam, which could enhance vibrational performance and expand the operational envelope of structures in the built environment. Another example related to applications of structural vibration control is the tunable hybrid SMP vibration absorbers proposed by Lee et al. [33]. The mechanical and damping properties of SMPs show that SMPs can be used as damping materials, opening the door to vibration control applications in earthquake engineering [58].

3.3. Sensors and Actuators. SMPs have been proposed as a candidate for use in sensors and actuators [57–60]. In particular, SMPs with reversible temperature-sensing capabilities have the potential for structural health-sensing technology applications [61]. DiOrio et al. developed such SMPs, which not only can serve in temperature-sensing applications but also provide a viable route for precisely controlling the shape recovery profile [62]. The experiments conducted by Santo showed promising results for different sized actuator applications in structures where SMAs cannot be used for excesses in the actuation rate or low displacement rates [54]. Yao et al. proposed a feasible method for fabricating SMP composites that could be used as flexible actuators [63]. Catastrophic failure could be prevented by detecting deterioration and potential damage at the early stages, which has long been the main goal of structural health monitoring. SMP composites that could sense the stresses, loads, and other factors imposed upon them would enable the use of embedded sensor and actuator technologies in composite structures, providing structural health monitoring and control during service conditions.

3.4. Requirements and Expectations. From the above survey, it should be noted that the application of SMPs in civil and architectural engineering is still at the early stage, and most existing attempts are in the field of structural engineering. The application of SMPs in architecture requires a wide temperature range, desirable and controllable shape-recovery temperatures, and a large extension rate to fulfill the demands of different environments [35, 59, 61]. The high shape recovery temperatures, relatively low recovery stress, slow recovery rate, and one-way shape memory of most existing SMPs, however, present important and exciting challenges for the application of SMPs in built environments [64]. Table 1 summarizes some SMPs with potential application in built environments. Due to a limited number of contributions to this field, only a few practical examples of potential applications have been given. Also, in Table 1, only a small number of applications have been studied at the experimental stage with in-depth testing and measurements [12, 62]. Conversely, others have so far only briefly been described or proposed in the discussion or conclusion sections of the literature, without actual experiments and measurements [12, 64–71, 75–81].

Possible applications using two-way SMPs have been proposed frequently in recent years. Compared to one-way SMPs, two-way SMPs offer the advantage of being reversible within a particular temperature range. Generally speaking, two-way SMPs have received considerable attention because of their ability to change shapes according to the external stimuli to which they are exposed, and the possibility that they could increase the extension rate via different additions, both of which offer possibilities in built environment applications. We discuss this potential in the following section.

4. Potential of SMPs for Building Energy Saving Purposes

4.1. Kinetic Building Envelopes for Building Energy Efficiency. Highly conditioned buildings via mechanical devices may make such buildings insensitive to the environment and uncouple the building envelope from its role as an environmental moderator. However, this ignores the nature of sustainable buildings and their ability to acclimate (or climatically respond) to the environment, taking full advantage of the positive influences found in nature. In the field of building "acclimation," we found many studies from around the world that addressed building envelopes and their impacts on building energy usage and indoor environment issues. Building envelopes are one of the most important design parameters determining the indoor physical environment, thermal and visual comfort, and even occupant work efficiency; thus, the effect on energy usage is substantial. In particular, the thermophysical and optical properties of building envelopes are factors that should be defined by the materials and geometry of building envelope components. Interest is increasing in net-zero energy buildings, but even current high-performance envelopes can rarely achieve that goal. Most available envelope designs function either as heating or cooling in the dominant climate, but not both. In short, such envelope designs provide

less-than-optimal building performance during certain times of year. One way to improve building energy efficiency is to develop kinetic building envelope systems that can alter their thermal and optical properties according to seasonal/daily climatic variations [82]. As more research works related to kinetic buildings have emerged, kinetic building envelope systems have become increasingly likely as a means of defining the optimal climatic responses and heightening indoor comfort. For instance, the developed envelopes with kinetic thermal insulation properties may achieve ~42.6–47.2% cooling and heating energy use savings, relative to the conventional envelopes with static insulation properties in compliance with ASHRAE 90.1-2013 Energy Standard [83].

Importantly, incorporating the shape memory effect into a building envelope component may substantially change its optical and thermal behavior from the point of view of building energy savings. According to the building energy savings mechanism, the behaviors of envelope assemblies including windows, window attachments (i.e., blinds, overhangs, coatings, etc.), wall surfaces, wall insulations, and roof structures are considered an important strategy for responding to external stimuli such as different sun positions, solar radiation levels, wind speeds, temperatures, humidity levels, etc. In order to ensure the significance of such behaviors in a specific envelope component, the stimulus (e.g., temperature, magnetic field, etc.) and application of the SMP must both be considered.

For instance, when it comes to movable window blinds that respond to a variety of solar angles in different seasons (i.e., winter and summer) to potentially utilize or mitigate solar heat gain, a type of thermally responsive SMP can potentially be used in the hinges of the blind structures. The different external air temperatures in winter and summer would then actuate the shape change in the SMP and adjust the angles of the blind slats, as seen in the schematic in Figure 7. Similarly, different SMP layers in a single unit with different T_g values could form various shapes in response to external air temperature changes, which in turn might act as a daylighting control system for potential lighting energy savings, as seen in the schematic in Figure 8. Ideally, these envelope components' changes would be reversible as external stimuli (i.e., temperature, humidity, wind, etc.) are normally periodical. To that end, two-way SMPs show great promise for applications in the fields of dynamic building facades and energy savings. Next, we discuss the mechanisms, properties, and associated possibilities/challenges with two-way SMPs.

4.2. Mechanisms and Properties of Two-Way SMPs

4.2.1. Mechanisms of Two-Way SMPs. According to whether there is a need for an external load for the SMP to operate, two-way shape memory polymers can be classified into two categories: quasi two-way and two-way (see Figure 9) [84].

Not only nematic liquid crystalline elastomers but also single crosslinked (physical or chemical) semicrystalline polymers and their composites can present as two-way SMPs

TABLE 1: Potential applications of shape memory polymers in built environments.

Potential application	Principle	Reference
Active building facades with self-regulating sun protectors	A broad melting temperature range of temperature-memory polymers based on crosslinked copolymer networks	[12]
Self-shading articulated surfaces	Two-part SMP filaments with different T_g values, forming variable stiffness tiles that respond to different incident solar heat levels	[65]
Smart building envelopes	Integrated conventional one-way shape memory (SM), two-way reversible SM, and one-way reversible SM in semicrystalline SMPs	[66]
Adaptive building envelopes	Significant reversible elongation resulting from crystallization of crosslinked poly(cyclooctene) films under tensile loads and induced cooling or heating	[67]
Functional smart architecture	Under various constant stresses, phase-segregated poly ester urethanes (PEUs) with two-way shape changes between $-20°C \sim 60°C$	[68]
Convertible roofs	Using a layering technique to combine the SMP and elastic polymer, which forms novel polymer laminates with a two-way shape-memory effect (two-way SME)	[69]
Interactive kinetic walls	Reversible actuation of ultrathin semicrystalline polymer films (e.g., thin polycaprolactone-gelatin bilayer films that can be unfolded at room temperature, folded at a temperature above the polycaprolactone melting point, and unfolded again at room temperature)	[70]
Ecological architecture	Bidirectional shape memory polymers that can become repetitively actuated two-way SMPs under stress-free conditions	[71]
Changeable architecture	The design and fabrication of polymer particles with two-way SMP abilities between $0°C \sim 43°C$ under stress-free conditions	[72]
Thermally comfortable buildings	Copolymer networks from oligo (ε-caprolactone) an n-butyl acrylate that enable a reversible bidirectional SME at human body temperature	[73]
Decorative architecture	Larger prestretching of two-way SMPs that can achieve longer actuator lengths without a constant external load	[74]
Intelligent buildings	SMPs with various macromolecular architectures including linear, three-, and four-arm star poly (ε-caprolactone) that are functionalized with methacrylate end-groups and two-way SMPs; the amount of recovered strain and the time required are decided by the combination of melting, deformation, and recovery temperatures	[75, 76]
Hybrid solar-thermal facades	Optimization of the load and phase morphology, especially the separation/decoupling of blend phases of SMPs, which increases the crosslink density and crystallinity of polymer networks, further enhancing the SME of the SMPs	[77]
Ecological building systems	Fabrication of two-way SMPs with "switch-spring" composition by interpenetration of the polymer network	[78]
Self-regulating shading systems	Higher gel fractions (above 75%) of semicrystalline elastomeric networks in SMPs achieving a two-way SME at low room temperatures	[79]
Architecture-based energy savings	Carbon black nanoparticles have the ability to lower the response temperature range of polyethylene-based SMPs and maximize the actuation ratio selection via optimal loading	[80]
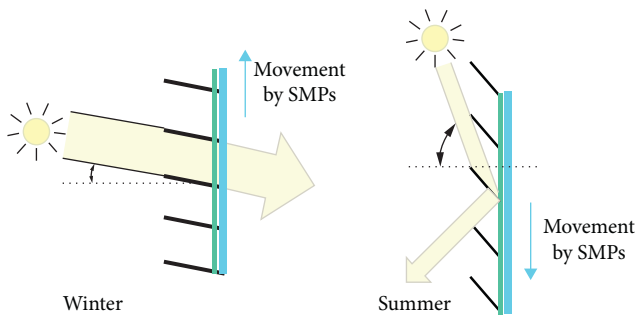
FIGURE 7: Schematic diagram of thermally responsive SMPs in heat controls of window blinds.
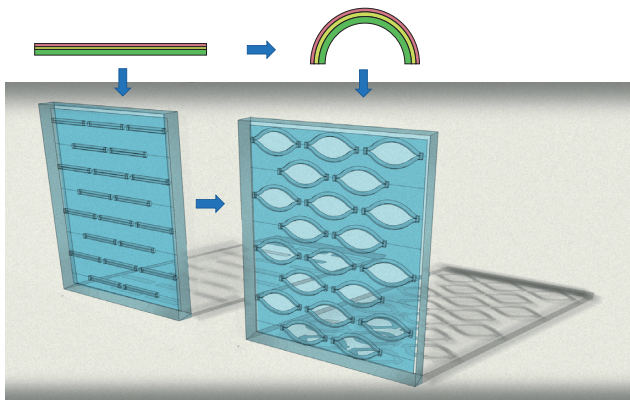
FIGURE 8: Schematic diagram of composite SMPs in shading controls.

under constant external loads [85]. The mechanism for the nematic liquid crystalline elastomers is that the ordering of mesogenic moieties and elastic properties of liquid crystalline elastomers enable a two-way SME in the liquid crystal elastomer. Heating a nematic liquid crystalline elastomer through the nematic-isotropic transition results in the constituent prolate network chain characteristic of the nematic state, contracting it to the spherical configuration of the isotropic phase. A large macroscopic contraction of more than 100% occurs simultaneously. This contraction is reversed upon cooling back to the nematic phase [18].

However, it is necessary for a polydomain nematic liquid crystalline elastomer leading to a two-way SME to apply a finite (∼50 kPa) stress [85]. Thermal-responsive semicrystalline polymers must be subjected to a constant stress to yield a two-way SME. Similarly, the mechanism behind this for thermally responsive SMPs is the transition between the amorphous and crystalline phases. While cooling elongates the crystallization of a semicrystalline polymer under a tensile load, the crosslinked entropy elastic modulus of the amorphous phase decreases, as does the capability of the bearing force of the semicrystalline (amorphous + crystalline phase) polymer, which results in elongation. The shape recovery will be achieved by heating to melt the network subsequently [18, 74, 82].

Nonetheless, the external load greatly limits wider application of two-way SMPs. Some polymer laminates, two-way SMPs, and their composites can achieve driving force

due to an internal force or the anisotropic network. Therefore, they do not need an external force while in operation [84]. A two-way SMP can produce a two-way SME without an external load when it combines chemical and physical crosslinked networks during the synthesizing process, and this is called a dual network. The chemical crosslinks secure the memory of the original shape while heating, and the physical crosslinks restore the temporary shape during cooling [66]. Polymer laminates completely combine ordinary polymers, elastomers, or SMP composites into a thin film, layer by layer. Different properties of composite materials such as the elastic modulus may cause different recovery stresses, resulting in a driving force bending the shape of recovery [69]. Similarly, two-way shape memory polymer composites (SMPCs) synthesize SMPs together so that they form a long molecular chain polymer. The mechanism is the ordering of the crystalline segment and elastomeric network, which enables the two-way SME of SMPCs. The preprogramed crystalline segment melts into the amorphous phase through a glass-rubbery transition. The movement of the crystalline segment is balanced with the crosslinked network to present a simultaneous shrinkage. During the crystallization, the balance is broken by the stored energy in the elastomeric network, providing the driving force for shape recovery [78].

4.2.2. Properties of Two-Way SMPs. Many properties (including thermal, mechanical, and shape memory) of two-way SMPs have been studied [70, 83–85]. Properties are important factors impacting the performance of two-way SMPs in different fields. This review focused on thermally responsive SMPs in built environment applications. Therefore, the temperature range was our first concern, because that built environment temperature decides the feasibility of a two-way SMP. The extension rate was another important consideration, due to the maximizing flexibility of applications for two-way SMPs.

Temperature range is an important thermal property of two-way SMPs. Different materials involved with SMPs present different temperature ranges. Figure 10 lists thermally responsive two-way SMPs, temperature ranges for their reversible shapes, and their transition temperatures. The SMPs listed in Figure 10 include six-arm polyethylene glycol-polycaprolactone (6A PEG-PCL), polyethylene-co-vinyl acetate (cEVA), semicrystalline poly ε-caprolactone (cPCL), crosslinked polyethylene (cPE), 1,6-hexamethylene diisocyanate (HMDI) + PCL + 1,4-butanediol (BD) (HPL), oligo ε-caprolactone (OCL), polycaprolactone (PCL)-gelatin, PCL-poly tetra-methylene ether glycol (PCL-PTMEG), poly cyclooctene-dicumyl peroxide (PCO-DCP), polydopamine-poly ε-caprolactone (PDA-PCL), poly ester urethane (PEU), poly octylene adipate (POA), poly pentadecalactone-poly ε-caprolactone (PPD-PCL), and preelongated shape memory polyurethane with unelongated elastic polyurethane (SMPU-PU). All SMPs shown in Figure 10 had a temperature range minimum to maximum from −20 to 100°C. Among the thermal properties of each material, transition points T_g or T_m were the critical features
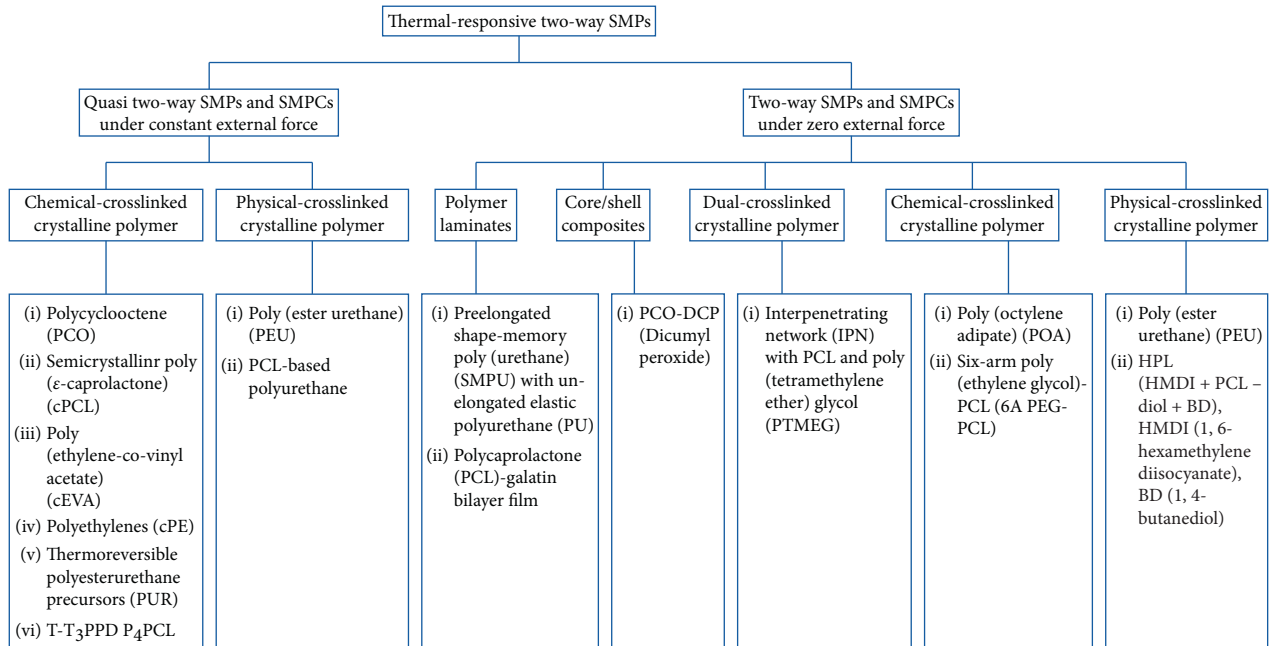
FIGURE 9: Thermally responsive two-way SMPs.

influencing this temperature range. Figure 10 clearly indicates that the temperature range of the poly ester urethane (PEU) was widest among all of the considered materials. PEUs can detect a two-way SME between +60 and −20°C while under a tensile load [65]. Meanwhile, a trained PEU specimen can display a two-way SME cycle between +60 and −10°C under zero external load [86]. Therefore, the temperature range of a PEU covers the built environment temperature. Zhou et al. presented a semicrystalline elastomers—poly octylene adipate (POA) with a temperature between 5 and 38°C, which was close to the built environment temperature [66]. The temperature range of a POA is narrower than that of a PEU, so that a POA may not be usable in some complicated environments. Thus, PEUs are regarded as the best candidate polymer type for the application of two-way SMPs in built environments, because they have a wide temperature range and are stress-free.

In addition to the temperature features, the extension rates of two-way SMPs and SMPCs are another important feature that indicates the shape-changing possibilities. Bothe found the extension rate of a PEU to be $\sigma = 1.5$ MPa (external load) up to 37% [68]. The researcher also explained that the maximum extension rate of a trained PEU with zero external load could reach 36% [87]. Ma et al. found that pure crosslinked polyethylene (cPE) has a 21.3% extension rate [80]. SMPCs and polymer laminates usually have smaller extension rates. For example, poly ε-caprolactone- (PCL-) based materials can achieve elongation (extension) up to 25% [75]. Stoganov et al. described a PCL-gelatin polymer laminate with a ~10% extension rate [70]. It was determined that the extension rates of two-way SMPs and SMPCs can range from ~10% to 37% [65, 75, 80, 86]. PEUs under external loads have the largest extension rates of all, which makes it possible that PEUs as two-way SMPs could be flexibly applied in built environments.

4.3. Challenges to Using Two-Way SMPs in Dynamic Building Envelopes.
Two-way SMPs have excellent properties such as lightweight and reversible shape changing abilities, but there are also challenges to their application in built environments, among which the following three aspects are worth mentioning for future research [66, 77].

4.3.1. Tradeoff between Extension Rate and Transparency.
A 100% extension rate with a high level of transparency is desirable so that two-way SMPs can be applied to dynamic building envelopes. However, it is extremely difficult to achieve this goal. Bothe found that an external load affected the elongation of a PEU; the largest was 37% under a certain tensile load, but the researcher did not develop a numerical model to simulate the relationship between the external load and extension rate [68]. Ma et al. concluded that the addition of carbon black (CB) would greatly decrease elongation. Adding 20% vol. CB to pure cPE, the extension rate decreased from 21.3% to 15.7% [80]. Kolesov et al. studied crosslinked polyethylene (PE)/PCL, and concluded that an increased crosslink density and crystallinity in the polymer network could enhance a two-way SME, as well as the selection of optimal loads [77]. Nevertheless, several studies have examined the relationship between the extension rate and transparency of two-way SMPs, and the impact factors (such as external load, additions, crosslink density, and crystallinity) most affecting them. Better transparency provides improved natural lighting. However, additions to two-way SMPs to increase the extension rate may cause a lower level of transparency. Balancing addition and transparency means a tradeoff. Thus, understanding the relationship between external load and extension rate in two-way SMPs, as well as the key impact factors, are challenges to the broader application of two-way SMPs in built environments.
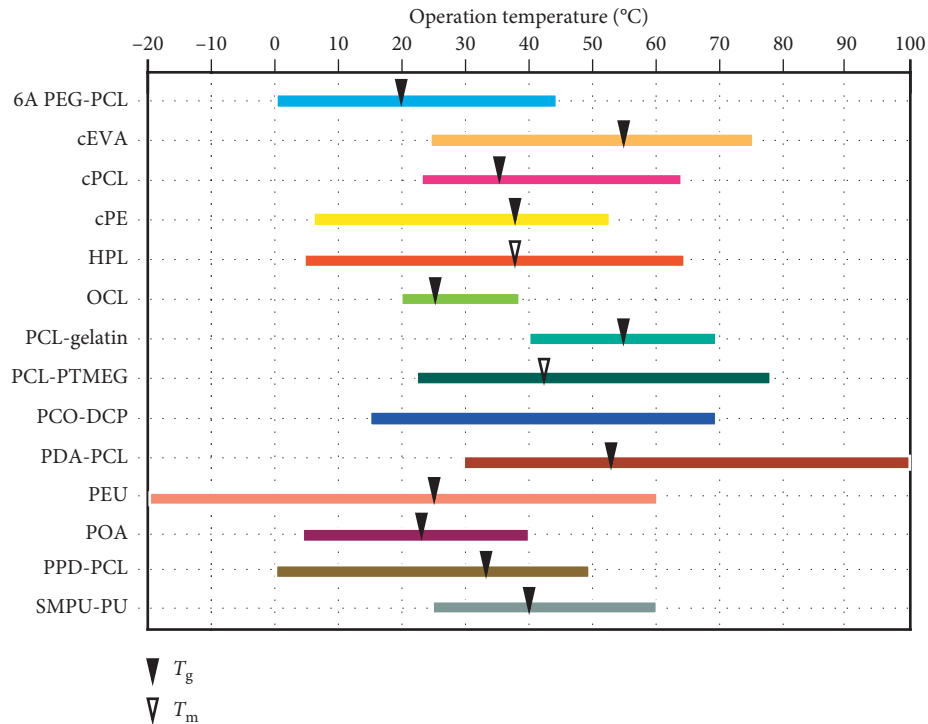
FIGURE 10: Temperature ranges of thermally responsive two-way SMPs.

4.3.2. Methods and Designs for Ideal Temperature Ranges.

It is appropriate in the application of two-way SMPs and SMPCs in built environments for the accurate temperature to range from −15 to 40°C. Two-way SMPs will not respond below the lower temperature range, T_L, and they become irreversible at a temperature point just a little bit higher than the upper temperature range, T_H [66]. Some researchers have studied different methods of changing the temperature ranges of two-way SMPs. Tunable actuation temperatures with two-way SMPs via a photo-crosslinking (UV) method have served to increase the T_H by about 25°C because of the addition of photo-crosslinks [88, 89]. Adding CB to two-way SMPs is also an available approach to affect the operation temperature [80]. Another approach is using polymer laminates such as shape memory polyurethane (SMPU)/PU and PCL-gelatin to change the temperature range [66, 75]. However, none of this research has provided a numerical model to illustrate the impact factors (such as UV, CB, and the composite layer) on the temperature range of reversible cycles. Even though it was determined that the temperature range of a PEU covers the built environment temperature, it is still a challenge to find a PEU with a precise temperature range from −15 to 40°C.

4.3.3. Fabrication Methods for Microstructure Design.

A two-way SMP with a reasonable microstructure, such as composing different SMPs into one device, could possibly change their original properties, thus applying in dynamic building envelopes. However, fabricating appropriate two-way SMPs can be difficult. A novel polymer fabrication process using 3D printing has recently emerged [77, 87, 90–92]. 3D printing is capable of producing advantageous complex structures. With the help of SMPs, 3D printed materials are able to respond to and change shape with a stimulus and this is called 4D printing (self-enveloping/self-folding) [77, 87, 90, 91]. This 4D printing technique was first presented in a water solution but was nonreversible [93]. Ge et al. introduced their design for 4D printing laminates producing a one-way SME in air [94]. Naficy et al. investigated polyether-based polyurethane with hydrogel structure using 3D printing, resulting in a two-way SME in water [82]. Therefore, this novel 3D/4D technique makes possible the fabrication of desirable two-way SMPs with multiple layers or specific microstructures. Nonetheless, it is still a challenge to determine the fabrication process for two-way SMPs in built environments because 3D printed two-way SMPs have thus far only been used in water environments.

5. Conclusions

Smart materials have been applied in building structures and envelopes for various purposes that require specific combinations of optical, thermal, and mechanical properties. In the current work, the general principles of SMPs were described, and previous research with selected application examples in built environments were categorized and reviewed. Special emphasis was given to the potential use of two-way SMPs as adjustable structures for building energy efficiency. Two-way SMPs used in buildings must meet weather and/or room temperature ranges. In addition, properties such as extension rate, transparency, design characteristics, and compatibility with envelope assemblies

also need to be considered. From both experiments and simulations, it is clear that incorporating SMPs into building structures offers the potential to improve building envelope structures and environmental performance. However further investigations are needed into the development of particular two-way SMPs by material scientists and engineers working collaboratively with architectural and structural researchers. Once that work is completed, building designers and engineers can focus on methods for incorporating SMPs, embedding them into existing building structures and envelope assemblies, long-term stability, and any other problems affecting the safety, reliability, and practicability of the thermal energy storage used in buildings.

Conflicts of Interest

The authors declare that there are no conflicts of interest regarding the publication of this paper.

Authors' Contributions

Jing Li, Qiuhua Duan, and Enhe Zhang have equally contributed to this paper.

Acknowledgments

References

[1] M. Behl and A. Lendlein, "Shape-memory polymers," *Materials Today*, vol. 10, no. 4, pp. 20–28, 2007.

[2] L. B. Vernon and H. M. Vernon, "Process of manufacturing articles of thermoplastic synthetic resins," *Google Patents*, vol. 18, no. 7, p. 348, 1941.

[3] J. J. Hitov, W. C. Rainer, E. M. Redding, A. W. Sloan, and W. D. Stewart, "Polyethylene product and process," Google Patents, 1964.

[4] R. J. Perrone, "Silicone-rubber, polyethylene composition; heat shrinkable articles made therefrom and process therefor," Google Patents, 1967.

[5] C. Liu, H. Qin, and P. T. Mather, "Review of progress in shape-memory polymers," *Journal of Materials Chemistry*, vol. 17, no. 16, p. 1543, 2007.

[6] M. D. Hager, S. Bode, C. Weber, and U. S. Schubert, "Shape memory polymer: Past, present and future.pdf," *Progress in Polymer Science*, vol. 49-50, pp. 3–33, 2015.

[7] J. Leng, X. Lan, Y. Liu, and S. Du, "Shape-memory polymers and their composites: Stimulus methods and applications," *Progress in Materials Science*, vol. 56, no. 7, pp. 1077–1135, 2011.

[8] H.-Y. Jiang and A. M. Schmidt, "The structural variety of shape-memory polymers," in *Shape-Memory Polymers and Multifunctional Composites*, J. S. Leng and S. Y. Du, Eds., pp. 21–63, CRC Press, Baco Raton, FL, USA, May 2010.

[9] D. Ratna and J. Karger-Kocsis, "Recent advances in shape memory polymers and composites: a review," *Journal of Materials Science*, vol. 43, no. 1, pp. 254–269, 2008.

[10] D. L. Thomsen, P. Keller, J. Naciri et al., "Liquid crystal elastomers with mechanical properties of a muscle," *Macromolecules*, vol. 34, no. 17, pp. 5868–5875, 2001.

[11] J. Hu and S. Chen, "A review of actively moving polymers in textile applications," *Journal of Materials Chemistry*, vol. 20, no. 17, p. 3346, 2010.

[12] M. Behl, K. Kratz, U. Noechel, T. Sauter, and A. Lendlein, "Temperature-memory polymer actuators," *Proceedings of the National Academy of Sciences*, vol. 110, no. 31, pp. 12555–12559, 2013.

[13] T. Xie, "Recent advances in polymer shape memory," *Polymer*, vol. 52, no. 22, pp. 4985–5000, 2011.

[14] M. Behl and A. Lendlein, "Triple-shape polymers," *Journal of Materials Chemistry*, vol. 20, pp. 3335–3345, 2010.

[15] Q. Zhao, H. J. Qi, and T. Xie, "Recent progress in shape memory polymer: New behavior, enabling materials, and mechanistic understanding," *Progress in Polymer Science*, vol. 49-50, pp. 79–120, 2015.

[16] J. Hu, Y. Zhu, H. Huang, and J. Lu, "Recent advances in shape-memory polymers: Structure, mechanism, functionality, modeling and applications," *Progress in Polymer Science*, vol. 37, no. 12, pp. 1720–1763, 2012.

[17] M. Behl, M. Y. Razzaq, and A. Lendlein, "Multifunctional shape-memory polymers," *Advanced Materials*, vol. 22, no. 31, pp. 3388–3410, 2010.

[18] H. Meng and G. Li, "A review of stimuli-responsive shape memory polymer composites," *Polymer*, vol. 54, no. 9, pp. 2199–2221, 2013.

[19] Q. Meng and J. Hu, "A review of shape memory polymer composites and blends," *Composites Part A: Applied Science and Manufacturing*, vol. 40, no. 11, pp. 1661–1672, 2009.

[20] M. Zheng and B. Dawood, "Fatigue strengthening of metallic structures with a thermally-activated shape memory alloy (SMA) fiber-reinforced polymer (FRP) patch," *Journal of Composites for Construction*, no. 4, pp. 1–11. In press, 2016.

[21] J. Hu, J. Lu, and Y. Zhu, "New developments in elastic fibers," *Polymer Reviews*, vol. 48, no. 2, pp. 275–301, 2008.

[22] K. Gall, M. Mikulas, N. A. Munshi, F. Beavers, and M. Tupper, "Carbon fiber reinforced shape memory polymer composites," *Journal of Intelligent Material Systems and Structures*, vol. 11, no. 11, pp. 877–886, 2000.

[23] R. Kotek, "Recent advances in polymer fibers," *Polymer Reviews*, vol. 48, no. 2, pp. 221–229, 2008.

[24] Y. Mao, K. Yu, M. S. Isakov, J. Wu, M. L. Dunn, and H. Jerry Qi, "Sequential self-folding structures by 3D printed digital shape memory polymers," *Scientific Reports*, vol. 5, no. 1, p. 13616, 2015.

[25] J. Leng, D. Zhang, Y. Liu, K. Yu, and X. Lan, "Study on the activation of styrene-based shape memory polymer by medium-infrared laser light," *Applied Physics Letters*, vol. 96, no. 11, pp. 2008–2011, 2010.

[26] J. Leng, H. Lu, Y. Liu, W. M. Huang, and S. Du, ""Shape-memory polymers—a class of novel smart materials," *MRS Bulletin*, vol. 34, no. 11, pp. 848–855, 2009.

[27] S. A. Madbouly and A. Lendlein, "Shape-memory polymer composites," *Advance Polymer Science*, vol. 226, pp. 41–95, 2010.

[28] G. L. Jiang and K. Peters, "Intelligent FRP retrofits for critical civil infrastructures," in *Proceedings of SPIE Smart Structures and Materials + Nondestructive Evaluation and Health Monitoring 2007*, vol. 6530, San Diego, CA, USA, March 2007.

[29] G. Li and T. Xu, "A shape memory polymer based self-healing syntactic foam sealant for expansion joint," *Structures Congress*, vol. 137, no. 11, pp. 805–814, 2011.

[30] G. Li and M. John, "A self-healing smart syntactic foam under multiple impacts," *Composites Science and Technology*, vol. 68, no. 15-16, pp. 3337–3343, 2008.

[31] G. Li, A. King, T. Xu, and X. Huang, "Behavior of thermoset shape memory polymer based syntactic foam sealant trained by hybrid two-stage programming," *Journal of Materials in Civil Engineering*, vol. 25, p. 479, 2012.

[32] G. Li, M. Asce, G. Ji, and H. Meng, "Shape memory polymer-based sealant for a compression sealed joint," *Journal of Materials in Civil Engineering*, vol. 27, no. 6, article 04014196, 2013.

[33] C.-Y. Lee, C.-C. Chen, T.-H. Yang, and C.-J. Lin, "Structural vibration control using a tunable hybrid shape memory material vibration absorber," *Journal of Intelligent Material Systems and Structures*, vol. 23, no. 15, pp. 1725–1734, 2012.

[34] K.-T. Lau, "Structural health monitoring for smart composites using embedded FBG sensor technology," *Materials Science and Technology*, vol. 30, no. 13, pp. 1642–1654, 2014.

[35] B. Konarzewska, "Smart materials in architecture: useful tools with practical applications or fascinating inventions for experimental design?," *IOP Conference Series: Materials Science and Engineering*, vol. 245, no. 5, article 052098, 2017.

[36] A. Lendlein and S. Kelch, "Shape-memory effect from permanent shape," *Angewandte Chemie International Edition*, vol. 41, no. 12, pp. 2034–2057, 2002.

[37] M. R. Aguilar and J. San Román, "Introduction to smart polymers and their applications," in *Smart Polymers and their Applications*, pp. 1–11, Elsevier, New York, NY, USA, 2014.

[38] K. N. Long, T. F. Scott, H. Jerry Qi, C. N. Bowman, and M. L. Dunn, "Photomechanics of light-activated polymers," *Journal of the Mechanics and Physics of Solids*, vol. 57, no. 7, pp. 1103–1121, 2009.

[39] T. Liu, T. Zhou, Y. Yao et al., "Stimulus methods of multi-functional shape memory polymer nanocomposites: a review," *Composites Part A: Applied Science and Manufacturing*, vol. 100, pp. 20–30, 2017.

[40] Y. Yu, M. Nakano, and T. Ikeda, "Directed bending of a polymer film by light," *Nature*, vol. 425, no. 6954, p. 145, 2003.

[41] A. Lendlein, H. Jiang, O. Jünger, and R. Langer, "Light-induced shape-memory polymers," *Nature*, vol. 434, no. 7035, pp. 879–882, 2005.

[42] R. Mohr, K. Kratz, T. Weigel, M. Lucka-Gabor, M. Moneke, and A. Lendlein, "Initiation of shape-memory effect by inductive heating of magnetic nanoparticles in thermoplastic polymers," *Proceedings of the National Academy of Sciences*, vol. 103, no. 10, pp. 3540–3545, 2006.

[43] M. Heuchel, M. Y. Razzaq, K. Kratz, M. Behl, and A. Lendlein, "Modeling the heat transfer in magneto-sensitive shape-memory polymer nanocomposites with dynamically changing surface area to volume ratios," *Polymer*, vol. 65, pp. 215–222, 2015.

[44] M. Y. Razzaq, M. Behl, and A. Lendlein, "Memory-effects of magnetic nanocomposites," *Nanoscale*, vol. 4, no. 20, p. 6181, 2012.

[45] H. B. Lv, Y. J. Liu, D. X. Zhang, J. S. Leng, and S. Y. Du, "Solution-responsive shape-memory polymer driven by forming hydrogen bonding," *Advanced Materials Research*, vol. 47–50, pp. 258–261, 2008.

[46] W. M. Huang, B. Yang, L. An, C. Li, and Y. S. Chan, "Water-driven programmable polyurethane shape memory polymer: demonstration and mechanism," *Applied Physics Letters*, vol. 86, no. 11, pp. 1–3, 2005.

[47] H. Chen, Y. Li, Y. Liu, T. Gong, L. Wang, and S. Zhou, "Highly pH-sensitive polyurethane exhibiting shape memory and drug release," *Polymer Chemistry*, vol. 5, no. 17, pp. 5168–5174, 2014.

[48] X. J. Han, Z. Q. Dong, M. M. Fan et al., "PH-induced shape-memory polymers," *Macromolecular Rapid Communications*, vol. 33, no. 12, pp. 1055–1060, 2012.

[49] Y. Li, H. Chen, D. Liu, W. Wang, Y. Liu, and S. Zhou, "PH-responsive shape memory poly(ethylene glycol)-poly(ε-caprolactone)-based polyurethane/cellulose nanocrystals nanocomposite," *ACS Applied Materials and Interfaces*, vol. 7, no. 23, pp. 12988–12999, 2015.

[50] Y. Liu, K. Gall, M. L. Dunn, A. R. Greenberg, and J. Diani, "Thermomechanics of shape memory polymers: uniaxial experiments and constitutive modeling," *International Journal of Plasticity*, vol. 22, no. 2, pp. 279–313, 2006.

[51] F. Liu and M. W. Urban, "Recent advances and challenges in designing stimuli-responsive polymers," *Progress in Polymer Science*, vol. 35, no. 1-2, pp. 3–23, 2010.

[52] H. Tobushi, K. Okumura, S. Hayashi, and N. Ito, "Thermomechanical constitutive model of shape memory polymer," *Mechanics of Materials*, vol. 33, no. 10, pp. 545–554, 2001.

[53] H. Tobushi and T. Hashimoto, "Thermomechanical constitutive modeling in shape memory polymer of polyurethane series," *Journal of Intelligent Material Systems and Structures*, vol. 8, no. 8, pp. 711–718, 1997.

[54] M. Irie, "Shape memory polymer," in *Shape Memory Materials*, K. Otsuka and C. M. Wayman, Eds., Cambridge University Press, Cambridge, UK, October 1999.

[55] Y. Liu, A. Rajadas, and A. Chattopadhyay, *Self-Healing Nanocomposite Using Shape Memory Polymer and Carbon Nanotubes*, Vol. 8692, SPIE, Bellingham, WA, USA, 2013.

[56] G. Li and W. Xu, "Thermomechanical behavior of thermoset shape memory polymer programmed by cold-compression: testing and constitutive modeling," *Journal of the Mechanics and Physics of Solids*, vol. 59, no. 6, pp. 1231–1250, 2011.

[57] R. Brown, K. Singh, and F. Khan, "Fabrication and vibration characterization of electrically triggered shape memory polymer beams," *Polymer Testing*, vol. 61, pp. 74–82, 2017.

[58] C. Meiorin, M. I. Aranguren, and M. A. Mosiewicki, "Vegetable oil/styrene thermoset copolymers with shape memory behavior and damping capacity," *Polymer International*, vol. 61, no. 5, pp. 735–742, 2012.

[59] G. Li and D. Nettles, "Thermomechanical characterization of a shape memory polymer based self-repairing syntactic foam," *Polymer*, vol. 51, no. 3, pp. 755–762, 2010.

[60] S. J. Dyke, B. F. Spencer Jr., M. K. Sain, and J. D. Carlson, "An experimental study of MR dampers for seismic protection," *Smart Materials and Structures*, vol. 7, no. 5, pp. 693–703, 1998.

[61] J. Kunzelman, T. Chung, P. T. Mather, and C. Weder, "Shape memory polymers with built-in threshold temperature sensors," *Journal of Materials Chemistry*, vol. 18, no. 10, p. 1082, 2008.

[62] A. M. DiOrio, X. Luo, K. M. Lee, and P. T. Mather, "A functionally graded shape memory polymer," *Soft Matter*, vol. 7, no. 1, pp. 68–74, 2011.

[63] Y. Yao, T. Zhou, J. Wang et al., "'Two way' shape memory composites based on electroactive polymer and thermoplastic membrane," *Composites Part A: Applied Science and Manufacturing*, vol. 90, pp. 502–509, 2016.

[64] J. Xu and J. Song, "Thermal responsive shape memory polymers for biomedical applications," *Biomedical*

Engineering—Frontiers and Challenges, pp. 125–142, InTech, Rijeka, Croatia, 2011.

[65] D. T. Clifford, R. J. Zupan, J. C. Brigham, R. V. Beblow, M. Whittock, and N. Davis, "Application of the dynamic characteristics of shape-memory polymers to climate adaptive building facades," in *Proceedings of 12th Conference of Advanced Building Skins*, pp. 171–178, Bern, Switzerland, October 2017.

[66] J. Zhou, S. A. Turner, S. M. Brosnan et al., "Reversible shape memory in semicrystalline elastomers," *Macromolecules*, vol. 47, no. 5, pp. 1768–1776, 2014.

[67] T. Chung, A. Romo-Uribe, and P. T. Mather, "Two-way reversible shape memory in a semicrystalline network," *Macromolecules*, vol. 41, no. 1, pp. 184–192, 2008.

[68] M. Bothe and T. Pretsch, "Two-way shape changes of a shape-memory poly(ester urethane)," *Macromolecular Chemistry and Physics*, vol. 213, no. 22, pp. 2378–2385, 2012.

[69] S. Chen, J. Hu, H. Zhuo, and Y. Zhu, "Two-way shape memory effect in polymer laminates," *Materials Letters*, vol. 62, no. 25, pp. 4088–4090, 2008.

[70] V. Stroganov, M. Al-Hussein, J. U. Sommer, A. Janke, S. Zakharchenko, and L. Ionov, "Reversible thermosensitive biodegradable polymeric actuators based on confined crystallization," *Nano Letters*, vol. 15, no. 3, pp. 1786–1790, 2015.

[71] M. Behl, K. Kratz, J. Zotzmann, U. Nöchel, and A. Lendlein, "Reversible bidirectional shape-memory polymers," *Advanced Materials*, vol. 25, no. 32, pp. 4466–4469, 2013.

[72] T. Gong, K. Zhao, W. Wang, H. Chen, L. Wang, and S. Zhou, "Thermally activated reversible shape switch of polymer particles," *Journal of Materials Chemistry B*, vol. 2, no. 39, pp. 6855–6866, 2014.

[73] M. Saatchi, M. Behl, U. Nöchel, and A. Lendlein, "Copolymer networks from oligo (ε -caprolactone) and n -butyl acrylate enable a reversible bidirectional shape-memory effect at human body temperature," *Macromolecular Rapid Communications*, vol. 36, no. 10, pp. 880–884, 2015.

[74] K. K. Westbrook, P. T. Mather, V. Parakh et al., "Two-way reversible shape memory effects in a free-standing polymer composite," *Smart Materials and Structures*, vol. 20, no. 6, 2011.

[75] S. Pandini, S. Passera, M. Messori et al., "Two-way reversible shape memory behaviour of crosslinked poly (ε-caprolactone)," *Polymer*, vol. 53, no. 9, pp. 1915–1924, 2012.

[76] M. Messori, M. Degli Esposti, K. Paderni et al., "Chemical and thermomechanical tailoring of the shape memory effect in poly(ε-caprolactone)-based systems," *Journal of Materials Science*, vol. 48, no. 1, pp. 424–440, 2013.

[77] I. Kolesov, O. Dolynchuk, S. Borreck, and H. J. Radusch, "Morphology-controlled multiple one- and two-way shape-memory behavior of cross-linked polyethylene/poly (ε-caprolactone) blends," *Polymers for Advanced Technologies*, vol. 25, no. 11, pp. 1315–1322, 2014.

[78] Y. Wu, J. Hu, J. Han et al., "Two-way shape memory polymer with 'switch–spring' composition by interpenetrating polymer network," *Journal of Materials Chemistry A*, vol. 2, no. 44, pp. 18816–18822, 2014.

[79] J. Li, W. R. Rodgers, and T. Xie, "Semi-crystalline two-way shape memory elastomer," *Polymer*, vol. 52, no. 23, pp. 5320–5325, 2011.

[80] L. Ma, J. Zhao, X. Wang et al., "Effects of carbon black nanoparticles on two-way reversible shape memory in crosslinked polyethylene," *Polymer (United Kingdom)*, vol. 56, pp. 490–497, 2015.

[81] R. Bogue, "Smart materials: a review of recent developments," *Assembly Automation*, vol. 32, no. 1, pp. 3–7, 2012.

[82] S. Naficy, R. Gately, R. Gorkin, H. Xin, and G. M. Spinks, "4D Printing of Reversible Shape Morphing Hydrogel Structures," *Macromolecular Materials and Engineering*, vol. 302, no. 1, 2017.

[83] J. Wang and L. Beltran, "A method of energy simulation for dynamic building envelopes," in *Proceedings of ASHRAE and IBPSA-USA SimBuild 2016, Building Performance Modeling Conference*, pp. 298–303, Salt Lake City, UT, USA, August 2016.

[84] M. ming Huang, X. Dong, W. Liu, X. Gao, and D. Wang, "Recent progress in two-way shape memory crystalline polymer and its composites," *Acta Polymerica Sinica*, vol. 4, pp. 563–579, 2017.

[85] H. Qin and P. T. Mather, "Combined one-way and two-way shape memory in a glass-forming nematic network," *Macromolecules*, vol. 42, no. 1, pp. 273–280, 2009.

[86] G. Barot and I. J. Rao, "Constitutive modeling of the mechanics associated with crystallizable shape memory polymers," *Zeitschrift fur Angewandte Mathematik und Physik*, vol. 57, no. 4, pp. 652–681, 2006.

[87] M. Bothe and T. Pretsch, "Bidirectional actuation of a thermoplastic polyurethane elastomer," *Journal of Materials Chemistry A*, vol. 1, no. 46, pp. 14491–14497, 2013.

[88] V. Srivastava, S. A. Chester, and L. Anand, "Thermally actuated shape-memory polymers: experiments, theory, and numerical simulations," *Journal of the Mechanics and Physics of Solids*, vol. 58, no. 8, pp. 1100–1124, 2010.

[89] Z. Wang, J. Liu, J. Guo, X. Sun, and L. Xu, "The study of thermal, mechanical and shape memory properties of chopped carbon fiber-reinforced TPI shape memory polymer composites," *Polymers*, vol. 9, no. 11, p. 594, 2017.

[90] M. Danvenport and C. Risleyis, "Information visualization the state of the art for maritime domain awareness," Conract Report, Defence R&D, Atlantic, QC, Canada, August 2006.

[91] H. Xie, C. Y. Cheng, X. Y. Deng et al., "Creating poly (tetramethylene oxide) glycol-based networks with tunable two-way shape memory effects via temperature-switched netpoints," *Macromolecules*, vol. 50, no. 13, pp. 5155–5164, 2017.

[92] K. Wang, Y. G. Jia, and X. X. Zhu, "Two-way reversible shape memory polymers made of cross-linked cocrystallizable random copolymers with tunable actuation temperatures," *Macromolecules*, vol. 50, no. 21, pp. 8570–8579, 2017.

[93] S. Tibbits, "4D printing: multi-material shape change," *Architectural Design*, vol. 84, no. 1, pp. 116–121, 2014.

[94] Q. Ge, H. J. Qi, and M. L. Dunn, "Active materials by four-dimension printing," *Applied Physics Letters*, vol. 103, no. 13, article 131901, 2013.

Research Article

Experimental Investigation of the Surface Temperature Distribution and Thermal Performance of an Intermittent Combustion Chinese Heated Wall

Shimeng Hao [iD],[1,2] **Yuejia Xu** [iD],[3] **Changming Yu** [iD],[4] **Yehao Song,**[3] and **Zhenghao Lin** [iD][3]

[1]*School of Architecture and Urban Planning, Beijing University of Civil Engineering and Architecture, No. 1, Zhanlanguan Rd. Xicheng District, Beijing 100044, China*
[2]*Beijing Advanced Innovation Center for Future Urban Design, Beijing University of Civil Engineering and Architecture, No. 1, Zhanlanguan Rd. Xicheng District, Beijing 100044, China*
[3]*School of Architecture, Tsinghua University, No. 1, Tsinghua Yuan, Haidian District, Beijing 100084, China*
[4]*School of Landscape Architecture, Beijing Forestry University, No. 35, Tsinghua East Road, Haidian District, Beijing 100083, China*

Correspondence should be addressed to Yuejia Xu; xu-yj12@mails.tsinghua.edu.cn

Chinese heated walls represent a traditional space heating technique that is still widely used in vernacular houses in northern China. Such walls efficiently recover gas heat from heating stoves and reduce users' exposures to indoor air pollution. This experimental study proposed a heat recovery system composed of a heated wall and fireplace. Test rooms were set up to evaluate the surface temperature distribution and thermal performance of the heated wall in response to several combustion patterns. The results show that an intermittent combustion heated wall heated only by a stove used for cooking can produce a relatively more comfortable indoor environment without extra energy consumption. In this research, indoor air temperature was increased by 3.3 to 4.0°C over the control room. The temperature distribution of the heated wall's surface was nonuniform, with a temperature range of 116.03°C. It was also found that the combustion pattern had a major impact on the initial and peak temperatures of the wall body's surface during combustion.

1. Introduction

In developing countries, exposure to high concentrations of indoor air pollution primarily comes from the combustion of traditional biomass fuels [1, 2]. Over half of the world's population is exposed on a daily basis to harmful emissions that have adverse effects on the respiratory, cardiovascular, immune, and nervous systems [3–5]. In China, it is estimated that nearly 80% of all household fuel consumed is in the form of solid biomass or coal, while burning typically takes place in low-efficiency, traditional stoves [1, 3, 6]. Apart from the indoor air pollution, these traditional stoves or braziers produce additional problems including a low level of efficiency and poor performance with regard to space heating [6–8].

In the past, several traditional heat recovery systems have been developed, such as the Roman hypocaust [9, 10], Korean ondol [11–14], Chinese kang [15–20], and others. Some of these have been renovated and are still in use today. The Chinese heated wall is one such traditional heating system that is still in use in northern China (as shown in Figure 1). A typical heated wall is a hollowed brick wall connected to a coal stove. The wall body stores the heat from the hot gas and slowly releases it into the adjacent room. In central China, especially in areas with subhumid continental monsoon climates, people are less equipped to deal with cold winters. Beginning in 2011, we conducted long-term field measurements and investigations in the rural area of Chongqing Province in central China [21]. Existing rural houses frequently fail to achieve thermal comfort, especially

Figure 1: Traditional Chinese heated walls commonly used in northern China (photograph: left: http://www.huitu.com/photo/show/20121107/154758101200.html; right: http://news.163.com/14/1014/10/A8GSPI7D00014AED_mobile.html).

during wintertime. According to the field measurements performed in February of 2012, the average indoor air temperature was 2.45°C, far below the thermal comfort zone. The heating season can stretch up to six months, from October to the following March.

We analyzed the impacts of cooking activities on indoor environmental quality and estimated the potential for heat recovery from cooking stoves that could be used for space heating. Fire pits and traditional cooking stoves are widely used in this area, directly discharging toxic gases indoors; they feature no heat recovery devices of any kind (as shown in Figure 2). The peak concentration value of PM2.5 while cooking in a traditional house was 48.055 mg/m^3, and the peak value of CO concentration was 28.3 ppm. During the heating season, the average energy consumptions for wood and charcoal were 536 kg and 126 kg per household, respectively. We conducted in-depth observations of occupants' behavior, including their cooking patterns and other activities. In this paper, a heat recovery system composed of a heated wall and fireplace was proposed for potential use in this rural area of central China, on the basis of precedent studies. The heated wall was connected to a stove used only for cooking which, unlike those used in northern China, recovered heat intermittently from cooking activities.

Several relevant precedent studies have been conducted that evaluated the thermal performance of heated walls [22, 23] and fireplaces [24]. Wang et al. established a dynamic heat transfer model for heated walls based on a theoretical analysis and lab testing [22]. These researchers determined that the heated wall's body released 45% of the total heat generated by fuel combustion into the surrounding room. The heat released by the indoor chimney provided an additional 25%, and approximately 30% of the heat was released to the outdoors. The influence of the heated wall on indoor temperature was also simulated and measured. Zhang et al. applied PCM to the inner surface of a heated wall and simulated its thermal performance [23]. It was found that the indoor temperature fluctuation could be reduced by applying PCM. Shan et al. set up a test room and studied the influence of a fireplace on the indoor thermal environment [24]. The experiment results showed that a fireplace could reduce indoor air pollution and significantly improve the indoor thermal comfort. A PM level of 10 could be reduced by 72.9%, compared to using a brazier.

Moreover, after 4 hours of burning, the indoor air temperature was 10°C higher than the temperature outdoors.

Though the influence of fireplaces on indoor environment quality is well understood, there are few studies related to the influence of different combustion patterns on the thermal performance of heated walls, especially in terms of intermittent combustion. Therefore, in this research, a heated wall was constructed to test its impact on indoor thermal comfort after intermittent combustion. Key parameters including the wall body's surface temperature distribution, indoor air temperature, and indoor relative humidity were measured under different combustion scenarios.

2. Design of the Heat Recovery System

A heat recovery system based on the traditional heated wall was designed for potential use in rural areas of central China. The system was comprised of two parts (as shown in Figure 3): a heated wall connected to a cooking stove (which could be replaced in the future with an innovative, highly energy efficient biomass stove) and a fireplace. Both were connected at different heights to a chimney. All inlets and outlets could be shut by iron plates. The heat recovery system could be transformed from one mode to another, simply by controlling these iron plates (Figure 4).

During winter days, the heated wall's inlets and outlets could be left open when users were cooking. The hot flue gas would then heat the wall body (built with bricks, rammed earth, or adobe, and thus with a relatively high thermal mass) when it flowed through the cavity. The inlets and outlets could then be shut to trap the gas in the flue. The wall body would then release its heat to the adjacent rooms via convection and radiation. In the evening, the heated wall's outlets could be shut and the fireplace outlet opened. This would allow the fireplace to directly heat the room as well as the adjacent wall, releasing heat into the adjacent room even after the fire burned out. In summer, the heated wall's inlet could be shut to let the flue gas discharge directly from the chimney and thus reduce its influence on indoor air temperature.

The positive effect of the heat recovery system could be optimized with a proper building layout (Figure 5). In this research, four rooms were arranged around the heat recovery system; these included a kitchen, bedroom, dining

FIGURE 2: Traditional heating and cooking methods commonly used in central and southern China.
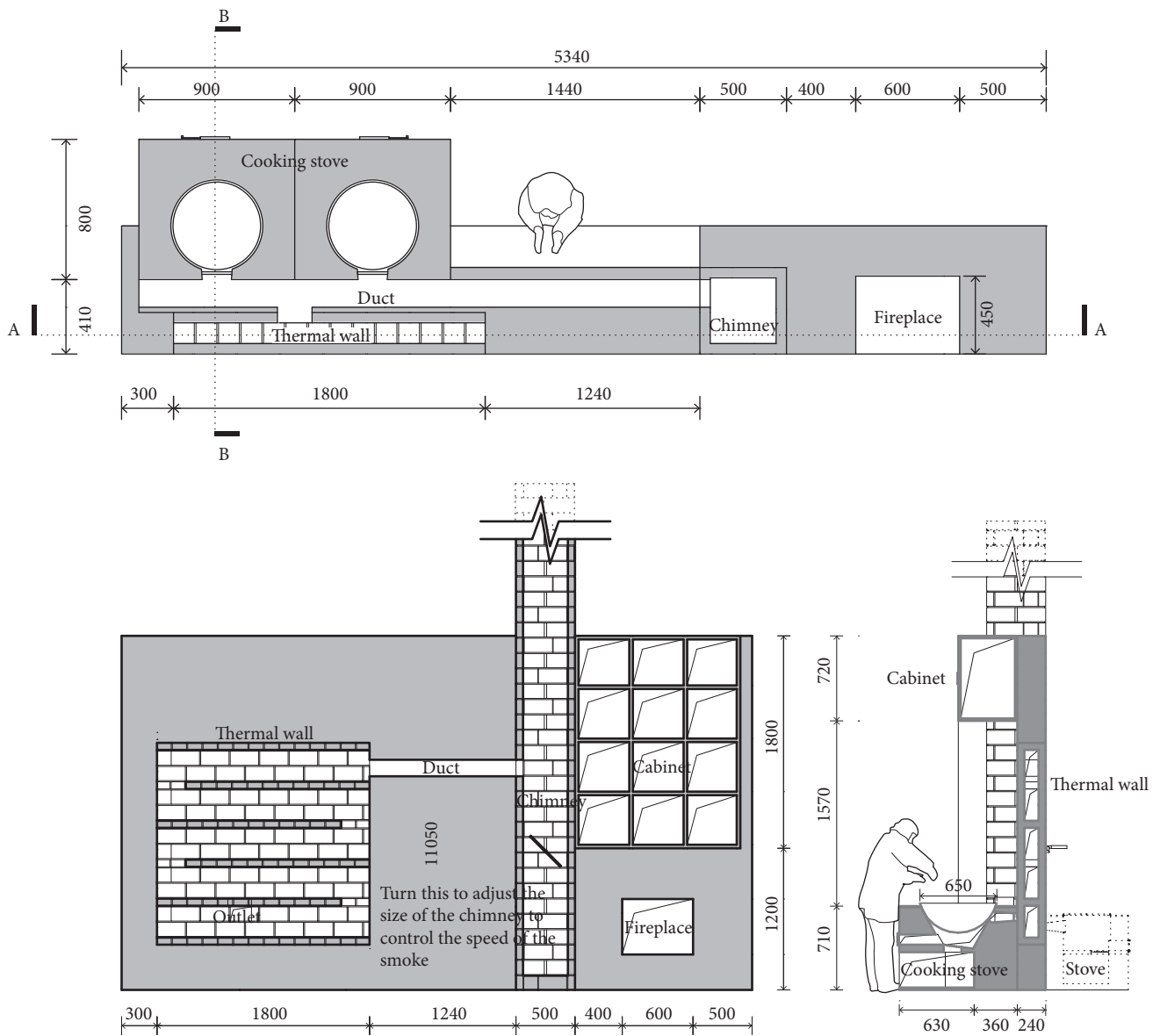
FIGURE 3: The proposed heat recovery system for potential use in rural areas of central China.

room, and living room. Taking the winter mode as an example, the waste heat generated by the cooking stove was recovered and released into the dining room by the heated wall. In the evening, the fireplace heated the living room; meanwhile, the wall between the bedroom and living room was also heated, providing an acceptable air temperature in
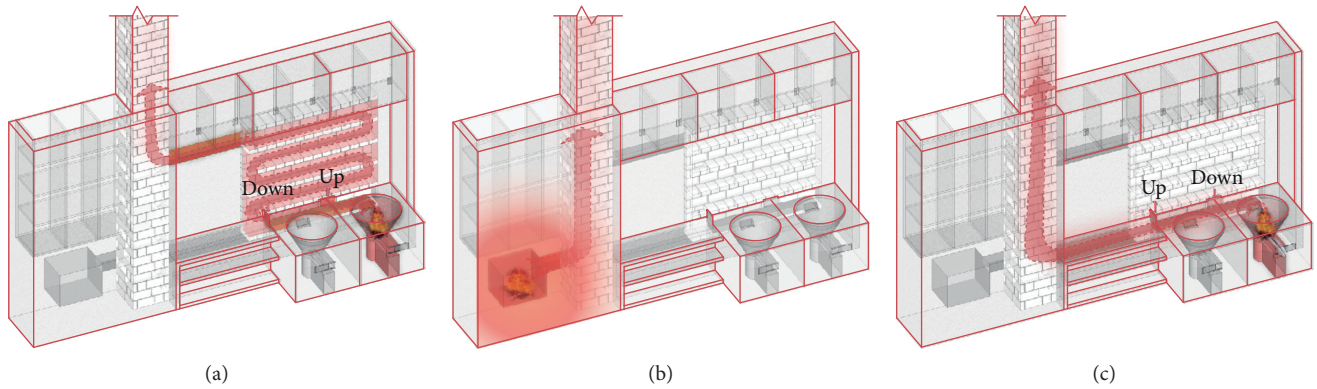
FIGURE 4: Operation modes for the heat recovery system, applied in different seasons. (a) Winter mode, heating with heated wall; (b) winter mode, heating with fireplace; and (c) winter mode, cooking without enabling the heated wall.
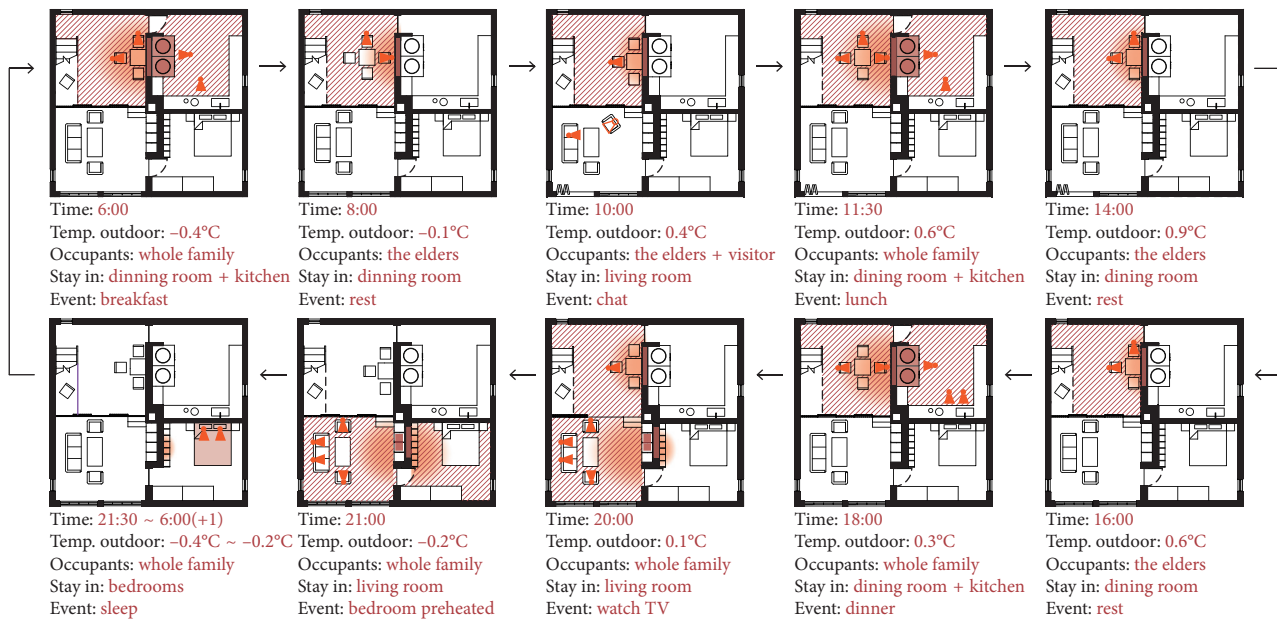
FIGURE 5: Prototype layout for applying the heat recovery system (winter mode).

the bedroom for sleeping. In this way, indoor thermal comfort was, to a certain extent, improved but without increasing energy consumption.

3. Experiment Setup

In order to verify the influences of the heated wall on indoor thermal comfort and temperature distribution across the wall's surface, two identical test rooms were set up in Beijing, China. A heated wall was constructed in one of the test rooms to establish a comparative study. The physical dimensions and building materials of both rooms were identical. The eastern and western walls were 3.2 m, and the northern and southern walls were 4.5 m. The storey height was 2.5 m. The flat roof was equipped with a simple suspended ceiling. The doors and windows were installed on the southern side. The window size was 1 m × 1 m, and the door opening was 0.9 m × 1.9 m. The walls were comprised of 240 mm-thick bricks without a thermal insulation layer. The doors and windows were composed of aluminum alloy door frames and single-pane glass. The wood combustion stove and chimney were located on the southern, outdoor side of the test room. The heated wall was adjacent to the western wall. The heated wall's inlet and outlet were set up to the south. The heated wall was constructed using bricks 1.3 m in height, 2.1 m in width, 240 mm in thickness, 60 mm for the two-sided wall surface, and 120 mm for the cavity. The cavity was divided into two zones by a smoke baffle plate. The heated wall was of a single-side heat dissipation type (Figure 6). To avoid the influence of direct solar radiation on indoor temperature, the room with the heated wall (referred to hereafter as the experiment room) and the room without the heated wall (referred to hereafter as the comparison room) were positioned close to the north side of a three-floor structure. During the testing period, the building's envelope received no direct solar radiation from any direction.

(a)

(b)

(c)

(d)
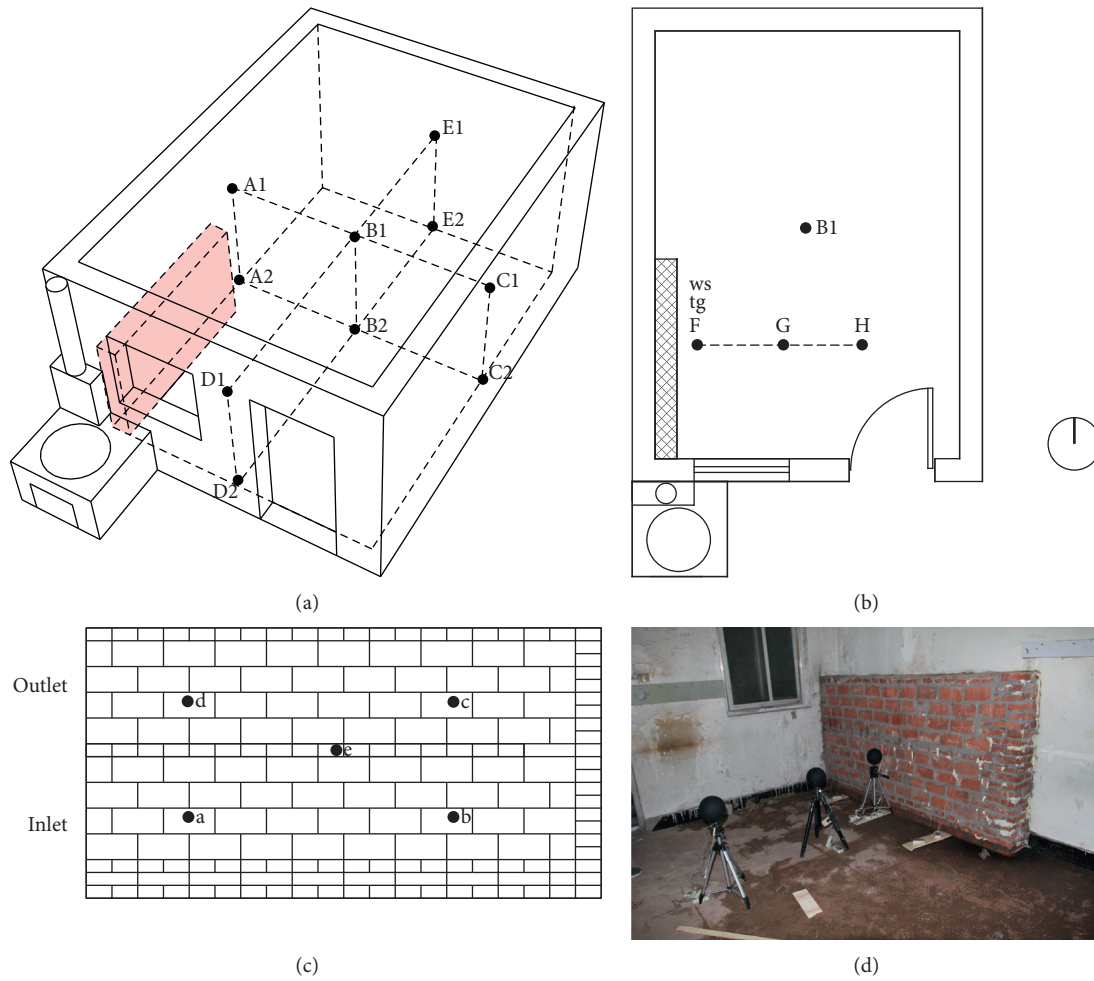
FIGURE 6: Layout of the test room and testing point arrangement: (a) axonometric view, (b) plan view, and (c, d) heated wall.

Cooking patterns were studied to support the experiment setup. Table 1 shows the seasonal variation in the number of daily meals. In summer, 22.8% of respondents have two meals per day, while in winter that number has risen to 43.9%. That is, 26.3% of respondents change their eating schedule according to the seasons. As for the average time spending on cooking (Figure 7), the cooking time in summer is 40.8 min on average, while it increases to 60.9 min in winter. According to field survey, firewood and liquefied petroleum gas (LPG) are the main energy sources for cooking. The average amount of firewood consumption for each meal is 7.1 kg for summer and 9.4 kg for winter.

Three testing scenarios were established, as follows: Tests 1 and 2 simulated actual cooking patterns, including two or three intermittent combustions per day. Test 1 continued for 24 hours, with two meals per day. Test 2 was similar but extended for two days; the first day involved two meals and the second day involved three. The cooking time and duration were based on previous field studies [21]. Test 3 involved a one-time combustion in order to determine the heated wall's surface temperature distribution and influence on the indoor thermal environment in a single heat transfer process (Table 2). Tests were conducted intermittently from

TABLE 1: Seasonal variation in the number of daily meals.

Number of daily meals	Summer		Winter	
	Frequency	Valid percent (%)	Frequency	Valid percent
2 times/day	9	15.8	23	40.4%
3 times/day	48	84.2	34	59.6%

November of 2014 to April of 2015. During the testing period, the doors and windows were kept closed.

All the testing instruments are listed in Table 3. There were seven measurement points set on the surface of the heated wall (i.e., points F-L in Figure 6). Air temperature and humidity data loggers were also installed in both of the two test rooms, as well as outdoors (i.e., points A-E). The data sampling interval was 5 min. Infrared thermographs of the heated wall's surface were taken during Test 1 at 10 to 120 min intervals. The outdoor weather conditions during the testing period were as follows. Tests 1 and 2 were conducted in November. The mean outdoor air temperatures were 6.06°C and 3.11°C, respectively. The mean relative humidity levels were 74.59% and 51.32%, respectively. Test 3 was conducted at the end of March. The mean outdoor air

(a)

(b)
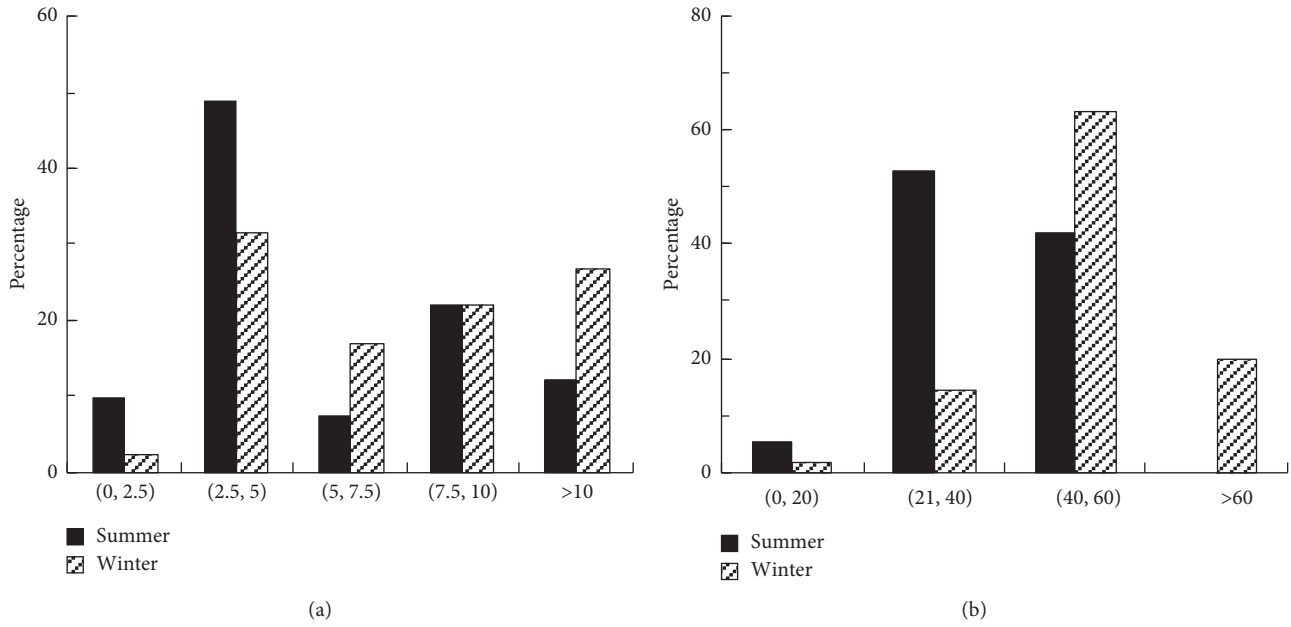
FIGURE 7: (a) The average time spending on cooking and (b) the average amount of firewood consumption for each meal.

TABLE 2: Testing scenarios (Tests 1–3).

Test	Date	Combustion(s)	Amount of wood for one combustion (kg)	Number	Ignition	Time stopped adding wood	Time outlet was shut
Test 1	2014-11-23 8:40~22:00	Two times per day	7.5	1a	9:00	9:40	10:10
				1b	16:00	16:40	17:05
Test 2	2014-11-29, 8:30~2014-12-1 7:20	Two times for day 1, three times for day 2	7.5	2a	9:00	9:40	10:10
				2b	16:00	16:40	17:05
				2c	8:00	8:40	9:10
				2d	12:00	12:30	12:50
				2e	19:00	19:35	19:55
Test 3	2015-3-25 19:30~21:35	Single combustion	7.5	3a	19:45	20:30	21:00

TABLE 3: Testing instruments used in the experiment.

Parameter	Instrument	Measurement range	Resolution
Thermography	VarioCAM HR inspect	−40~2000°C	0.05°C
Surface temperature	WZY-1 thermocouple	−40~100°C	0.1°C
Air temperature	WSZY-1 auto-logger	−40~100°C	0.1°C
Relative humidity		0~100% RH	0.1% RH

temperature was 10.9°C, while the relative humidity was 35.36%.

4. Observations and Results

4.1. Heated Wall Surface Temperature Distribution. Infrared thermographs were taken to analyze the temperature distribution of the heated wall's surface (Figure 8).

Before the first combustion began (8:00–9:00), the wall's surface temperature distribution was relatively even. The mean temperature was 11.18°C, and the temperature range was 8.61°C (SD = 1.06). Soon after ignition (9:00–10:00), the wall surface temperature began to rise at a gradually increasing speed. Soon after the flame was extinguished, the mean temperature of the wall reached its peak at 36.44°C, at which point the largest temperature difference on the heated wall's surface was created. The temperature range was as much as 116.03°C (SD = 16.17). During combustion, the mean speed of the temperature's rise on the heated wall was 0.37°C/min, while the maximum was 0.68°C/min. The surface near the inlet had the maximum rising speed, with a mean value of 1.75°C/min and maximum of 2.74°C/min. After the flame was extinguished for 15 to 20 min, the surface temperature began to decrease. The mean speed of the temperature decrease was −0.04°C/min. The process for the temperature decrease was much slower than the increase process. The wall temperature near the inlet began to decrease rapidly for one hour after extinguishing,
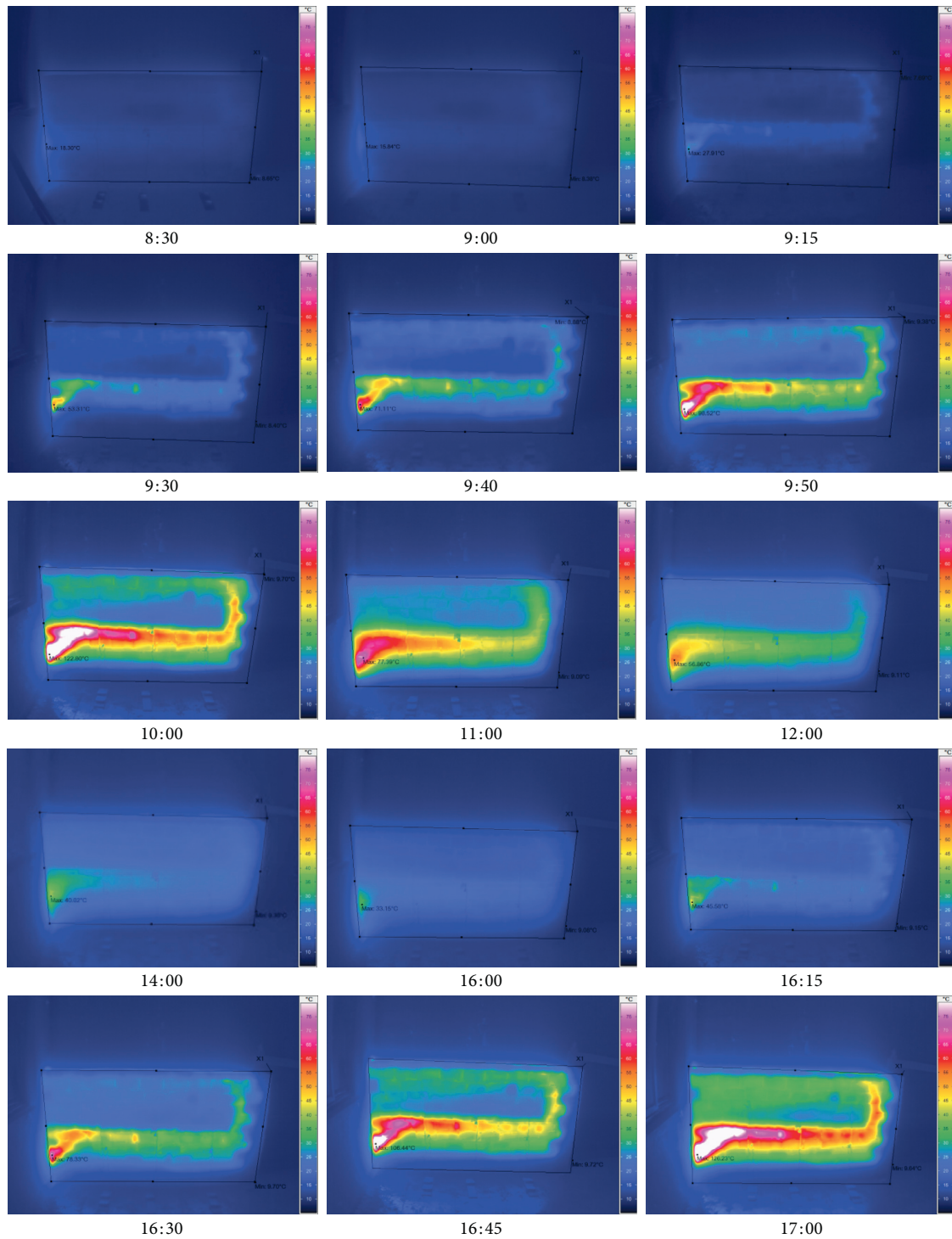
FIGURE 8: Infrared thermographs of a heated wall's surface (Test 1).

reaching $-0.76°C/min$. Then, it gradually decreased until the next combustion began. A single combustion increased the mean temperature of the heated wall's surface by 18.99 to 22.11°C. The mean temperature of the heated wall's surface was still above 20°C four hours after extinguishing. It is clear from the infrared thermographs that the heat exchange process between the high-temperature smoke and wall body mainly took place in the lower zone of the flue (Zone 1). The smoke in Zone 1 had a higher temperature and thus more efficient heat exchange with the wall body. The wall temperature significantly increased and the smoke temperature rapidly reduced. The smoke temperature in the upper flue (Zone 2) was lower, and the surface temperature variation of the wall body was relatively small.

4.2. Influence of Different Combustion Patterns on the Initial Surface Temperature. As previously described, Tests 1, 2, and 3 adopted different combustion patterns. Test 1 included two intermittent combustions at a time interval of 6 h. Test 2 was comprised of five intermittent combustions at intervals of 6 h, 15 h (overnight), 3 h, and 6 h. In Figure 9, we used Δt_1 to represent the amplitude of the temperature variation during a single combustion. The values of Δt_1 at the same measuring points were similar when there was a set amount of fuel. Taking measuring point F as an example, the values of Δt_{1-F} ranged from 32.0°C to 35.4°C. That is, Δt_1 was mainly determined by the efficiency and energy density of the combustion. The outdoor weather conditions comprised one of the main factors affecting combustion efficiency. When there were higher levels of outdoor air velocity, the value of Δt_1 rose correspondingly.

Though the combustion pattern had little influence on the value of Δt_1, it did have a major impact on the initial and peak temperatures of each combustion. Values for Δt_2 and Δt_3 were used to represent the temperature differences in peak and initial values for the two adjacent combustions, respectively. The combustion patterns included several intermittent combustions (i.e., Tests 1 and 2) and significantly increased the initial and peak temperatures of the heated wall's exterior surface.

In Test 1, the peak temperature of the second combustion was improved by 4.7°C. The initial temperature was improved by 6.5°C, on average. In Test 2, the Δt_2 values ranged from 2.6°C to 9.6°C, on average. There was a 20.7°C increase of the peak surface temperature and a 14.6°C increase in the initial surface temperature under the cumulative effect of five intermittent combustions (Table 4).

4.3. Critical Time Nodes for the Heated Wall's Dynamic Temperature Process. Three critical time nodes (t_i, t_s, and t_f) were identified to describe the combustion process. Specifically, the times of ignition, feeding fuel stopped, and fire burning out were represented by t_i, t_s, and t_f, respectively (Figure 10). To describe the dynamic thermal process of the heated wall surface's temperature over time, the temperature change rate a_i(°C/min) was calculated by the following equation (Equation (1) and Figure 10):

$$a_i = \frac{T_{i+1} - T_i}{t}. \tag{1}$$

Five time nodes (t_1–t_5) were extracted from the temperature change rate curve (Figure 10(b)), where at the turning point, t_1, the exterior surface temperature began to rise. The temperature change rate reached its peak value at t_2 and fell back to 0°C/min at t_3. This meant that the surface temperature of the heated wall's body began to decrease. The rate of descent increased until it reached t_4. Then, the temperature descent slowed to a relatively steady state after t_5.

After igniting the fuelwood (t_i) for 10 to 20 min, the heated wall's temperature began to increase (t_1). Then, the temperature increase sped up. After ceasing to add firewood to stove (t_s) for 5 to 20 min, the rate of the temperature increase reached its peak value (t_2). After the fire burning out and closing the flue (t_f) for 10 to 25 min, the heated wall's temperature reached its maximum value (t_3). At this time, the temperature difference between the measurement points also reached its maximum. Then, the wall temperature began to decline. After 5 to 30 min, the speed of the temperature reduction reached its maximum (t_4). After the combustion was finished for 3 h to 4 h, the wall temperature stabilized (t_5) until the next combustion was initiated.

4.4. Influences of the Heated Wall on the Indoor Thermal Environment. During the entire testing period, the air temperature in the experiment room was higher than that in outdoors or in the comparison room (Figure 11). Test 1 yielded a mean outdoor air temperature of 6.9°C, while the mean air temperatures in the experiment and comparison rooms were 10.9°C and 7.6°C, respectively. Test 2 had a mean outdoor air temperature of 4.9°C. The mean air temperature in the experiment room was 9.9°C, while the mean air temperature in the comparison room was only 5.9°C.

There was an approximate 0.5 h time lag between the rising indoor air temperature and initiation of combustion. After closing the inlet and outlet of the flue, the indoor temperature began to rapidly increase. It reached its peak about 1h after the fire burned out, indicating that high-efficiency heat exchange was enhanced by this process.

It was also determined that, with the same quantity of fuel and burn time, the temperature's rising amplitude during each combustion process remained relatively stable, between 2.1°C and 3.0°C. Furthermore, the tests showed that the heated wall operated under an intermittent combustion pattern, which simulated the cooking pattern commonly adopted by rural Chinese. This had a significant effect on improving the indoor thermal comfort. In Test 1, the indoor air temperature was 8.7°C before the first combustion started. The indoor air temperature was increased by 1.5°C before the second combustion started, while the air temperature in the comparison room only improved by 0.6°C during the same period. In Test 2, after five combustions (represented by five cooking activities), the indoor temperature increased from 6.1°C to 13.3°C. During the same period, the indoor temperature of the comparison room decreased to 5.7°C from 6.2°C. It was affected by the outdoor air's temperature reduction.

The relative air humidity in the experiment room was relatively higher than that in the comparison room, which can be explained by the increase in absolute humidity due to the combustion activity (Figures 12 and 13). During each combustion, the absolute indoor humidity of the experiment room increased by 0.4 to 1.4 g/m³. As compared to the room without a heated wall, the indoor absolute humidity was 0.3–2.7 g/m³ higher in the experiment room. One factor affecting this phenomenon was the relatively high water content of the firewood and building materials used to build the heated wall.
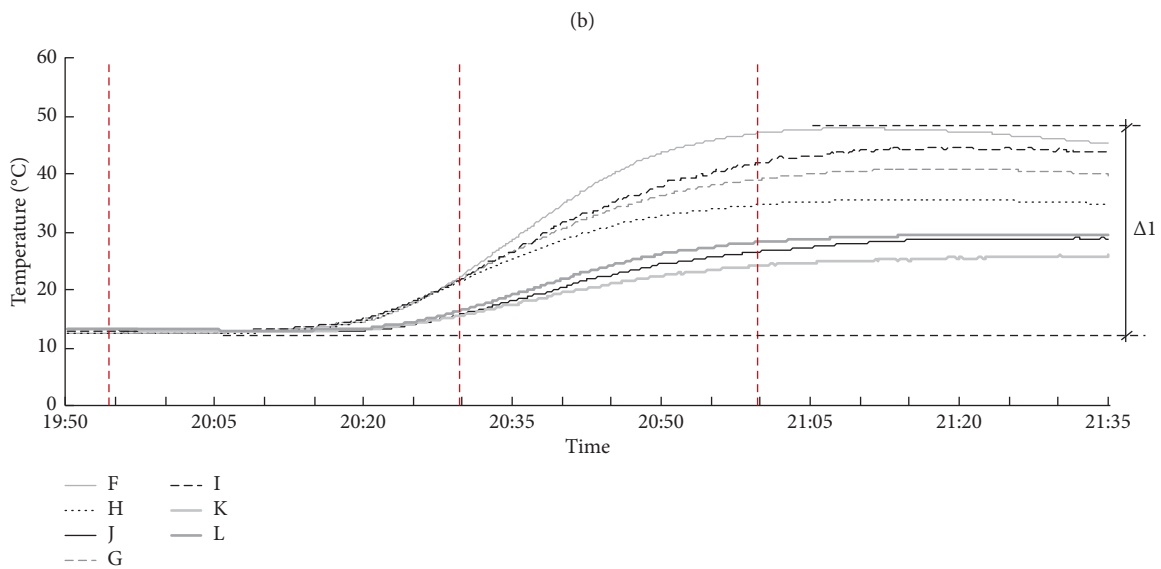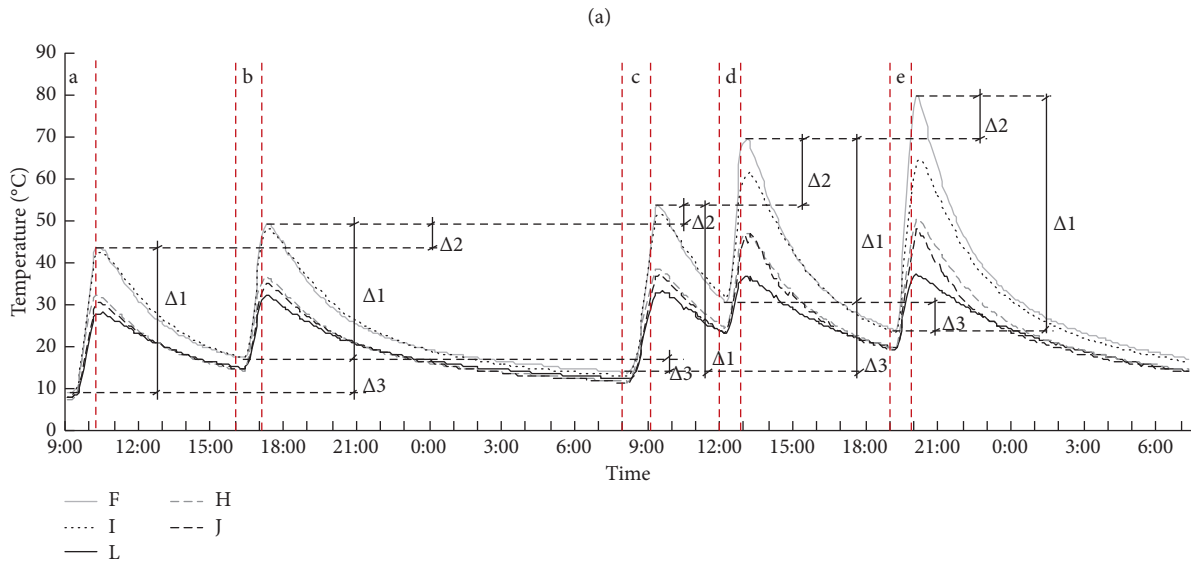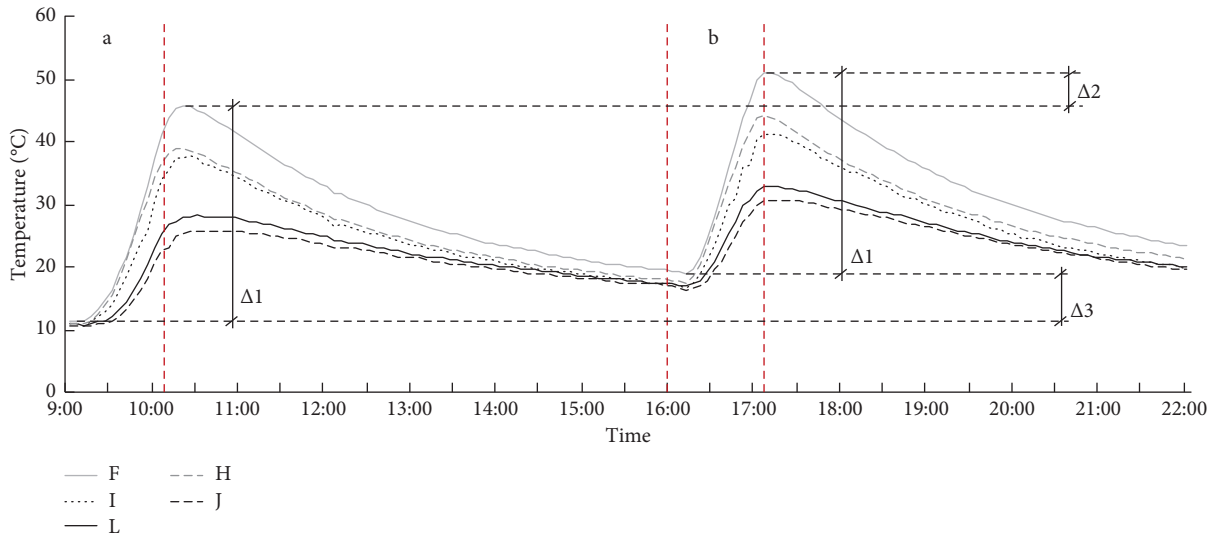
FIGURE 9: Heated wall temperature distributions: (a) Test 1, (b) Test 2, and (c) Test 3.

TABLE 4: Peak (Δt_2) and initial temperature differences (Δt_3) of the heated wall surface.

Measuring point		Test 1			Test 2		
		1b-1a (°C)	2b-2a (°C)	2c-2b (°C)	2d-2c (°C)	2e-2d (°C)	Cumulative total (°C)
F	Δt_2	5.4	5.5	4.8	15.9	10	36.2
	Δt_3	7.6	8.4	−3.5	16.9	−6.7	15.1
H	Δt_2	5.1	4.4	1.9	8.8	3.2	18.3
	Δt_3	6.7	7.3	−2.8	13	−5	12.5
I	Δt_2	3.6	5.6	3.2	10	3.3	22.1
	Δt_3	6.1	9.4	−4.4	18.7	−8.3	15.4
J	Δt_2	5	4.4	2.2	9.8	1.1	17.5
	Δt_3	6	13.9	−3.2	11.9	−4.3	18.3
L	Δt_2	4.6	4.3	1.1	3.4	0.5	9.3
	Δt_3	6.3	7.1	−2.7	10.9	−3.5	11.8

(a)

(b)

FIGURE 10: (a) Test 1 temperature change rate at point F on the heated wall; (b) time node diagram of the temperature change rate of the heated wall (measuring point F).

5. Conclusions

In this research, the proposed heat recovery system design evolved from the Chinese traditional heated wall. Two test rooms were set up and key variables measured to evaluate the thermal performance of the improved heated wall. The following conclusions were drawn based on the study results:

(1) The improved heated wall system consists of a hollow wall, biomass stove, and a fireplace. With a proper building layout, this system can support a more comfortable and healthier indoor environment without extra energy consumption. Main living spaces should be arranged around the heated wall system in coordination with the local life pattern.

(2) As can be observed from the infrared thermographs, the heat exchange process between the high-temperature smoke and wall body mainly took place in the lower zone of the flue. The temperature distribution of the heated wall's exterior surface was highly nonuniform. The temperature range was as much as 116.03°C.

(3) The temperature rises in the heated wall's surface during each combustion were relatively the same when there was a set amount of fuel. The amplitude of the temperature rise was mainly determined by the efficiency and energy density of the combustion. The combustion pattern (including combustion times, intervals, and fuel quantity) had a major impact on the initial and peak values of the wall body's surface temperature during each combustion.

(4) Five critical 4ime nodes (t_1–t_5) were extracted from the temperature change rate curve to describe the dynamic changes in the heated wall's surface temperature. The process was divided into the following stages: t_1-t_2 represent the acceleration of surface temperature increments, t_2-t_3 were the deceleration of surface temperature increments, t_3-t_4 were the acceleration of surface temperature decrements, t_4-t_5 were the deceleration of surface temperature decrements, and t_5 was a relatively stable state.

(5) Indoor temperature can be increased by 3.3–4.0°C (as compared to the control room) with the installation of a heated wall. However, the relative and

(a)

(b)
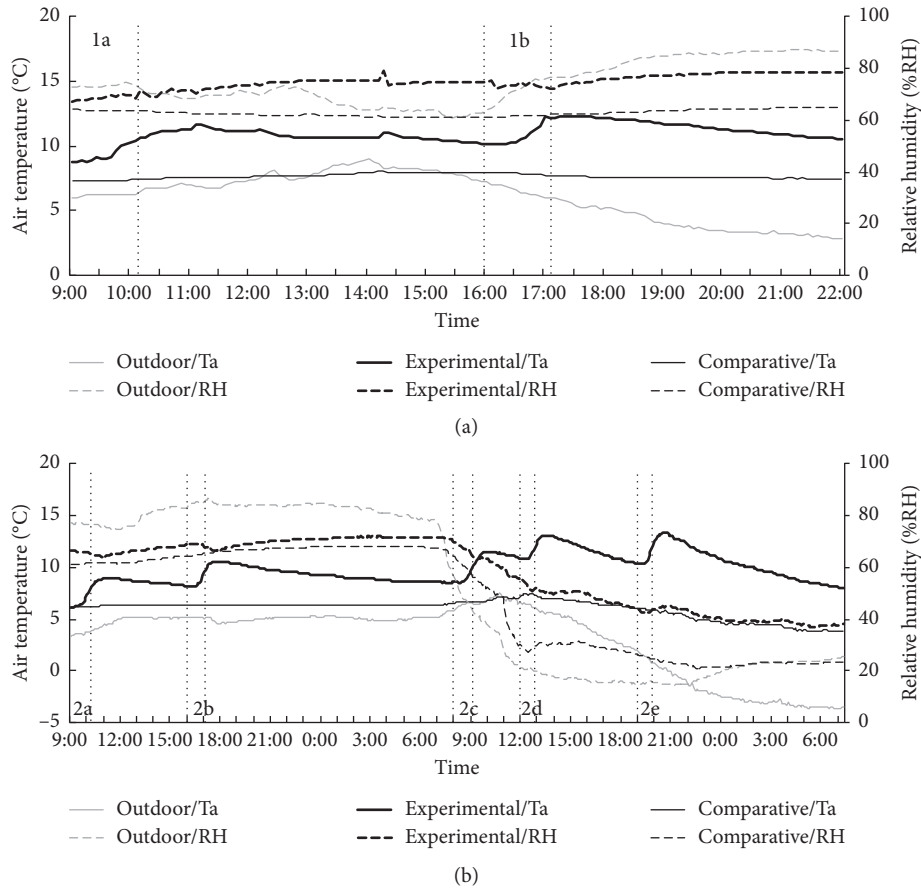
FIGURE 11: Air temperature and humidity variations: (a) Test 1 and (b) Test 2.

(a)

(b)
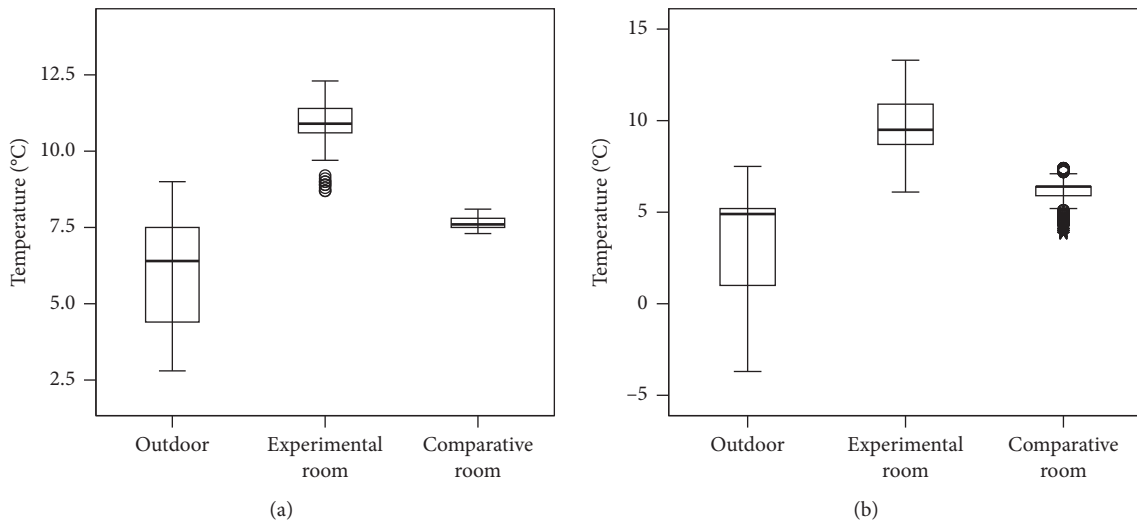
FIGURE 12: Continued.

(c)

(d)
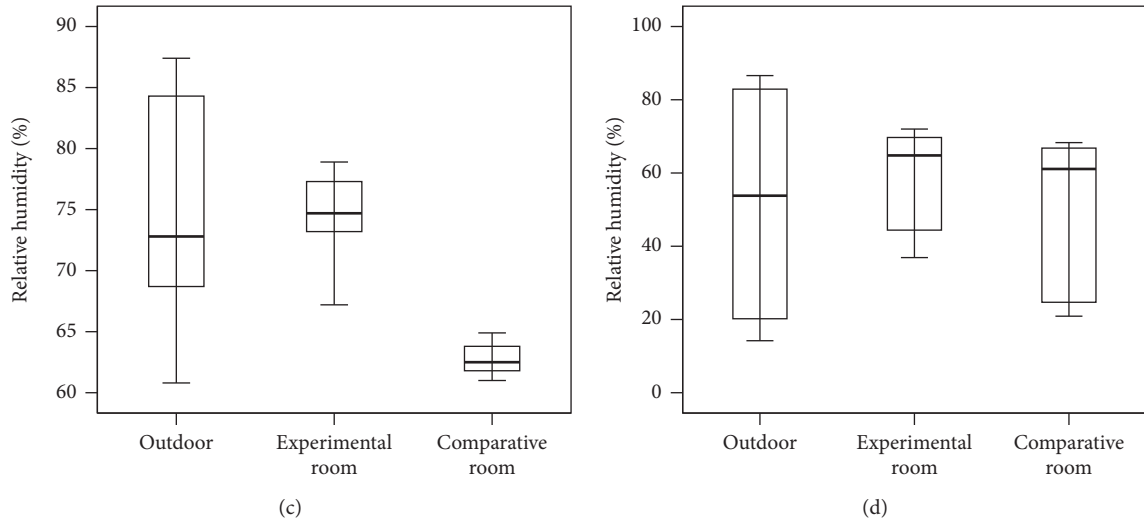
FIGURE 12: Outdoor and indoor temperatures and humidity variations: (a, c) Test 1; (b, d) Test 2.

(a)

(b)
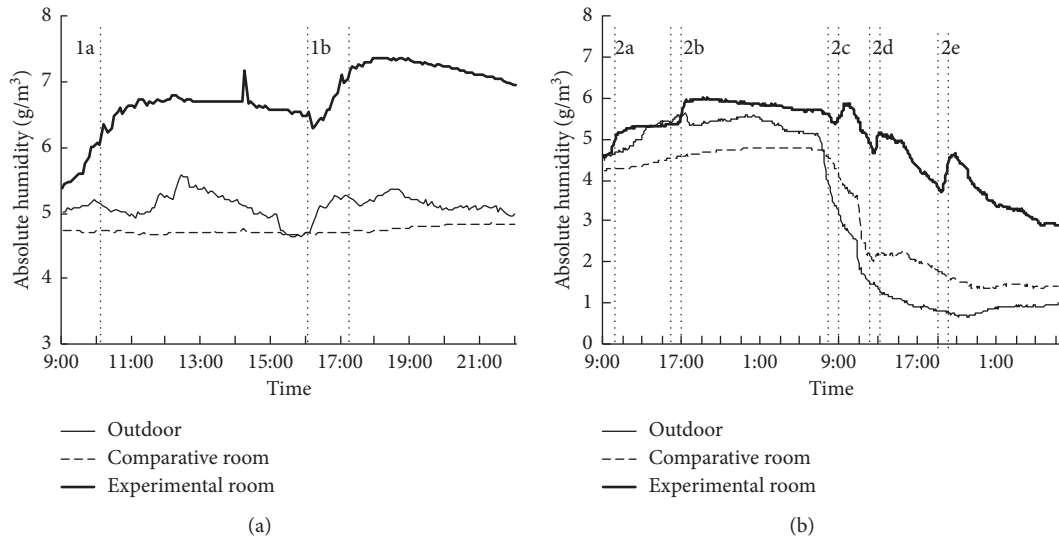
FIGURE 13: Absolute humidity variations: (a) Test 1 and (b) Test 2.

absolute humidity values in the experiment room were relatively higher than those in the comparison room, which can be explained by the high water content of the firewood and building materials used to build the heated wall.

Nomenclature

Δt_1: Amplitude of temperature variation during one combustion °C
Δt_2: Temperature difference in peak value between two adjacent combustions °C
Δt_3: Temperature difference in initial value between two adjacent combustions °C
T_i: Ignition of the fuelwood
T_s: Firewood no longer added
T_f: Open fire stopped and flue closed
t_1: Beginning of the temperature rise in the wall

t_2: Peak speed of the temperature increase reached
t_3: Beginning of wall temperature reduction and peak wall temperature reached
t_4: Peak temperature reduction reached
t_5: Tendency towards stable wall temperature
a_i: Temperature change rate at time i °C/min
T_i: Surface temperature of the heated wall's exterior surface at time i °C
Δt: Data sampling interval in min.

Data Availability

The datasets generated during and/or analyzed during the current study are available from the corresponding author on reasonable request.

Conflicts of Interest

The authors declare that they have no conflicts of interest.

Acknowledgments

References

[1] Z. Chowdhury, L. Campanella, C. Gray et al., "Measurement and modeling of indoor air pollution in rural households with multiple stove interventions in Yunnan, China," *Atmospheric Environment*, vol. 67, pp. 161–169, 2013.

[2] E. T. Gall, E. M. Carter, C. M. Earnest, and B. Stephens, "Indoor air pollution in developing countries: research and implementation needs for improvements in global public health," *American Journal of Public Health*, vol. 103, no. 4, pp. e67–72, 2013.

[3] C. L'Orange, J. Volckens, and M. DeFoort, "Influence of stove type and cooking pot temperature on particulate matter emissions from biomass cook stoves," *Energy for Sustainable Development*, vol. 16, pp. 448–455, 2012.

[4] I. S. Riddervold, J. H. Bønløkke, A.-C. Olin et al., "Effects of wood smoke particles from wood-burning stoves on the respiratory health of atopic humans," *Particle and Fibre Toxicology*, vol. 9, no. 1, p. 12, 2012.

[5] E. Nielsen, "Health effects assessment of exposure to particles from wood smoke," *Toxicology Letters*, vol. 172, p. S120, 2007.

[6] A. Oikonomou and F. Bougiatioti, "Architectural structure and environmental performance of the traditional buildings in Florina, NW Greece," *Building and Environment*, vol. 46, no. 3, pp. 669–689, 2011.

[7] B. A. Begum, S. K. Paul, M. Dildar Hossain, S. K. Biswas, and P. K. Hopke, "Indoor air pollution from particulate matter emissions in different households in rural areas of Bangladesh," *Building and Environment*, vol. 44, no. 5, pp. 898–903, 2008.

[8] J. Zhang and K. R. Smith, "Household air pollution from coal and biomass fuels in China: measurements, health impacts, and interventions," *Environmental Health Perspectives*, vol. 115, no. 6, pp. 848–855, 2007.

[9] N. K. Bansal and India, "Characteristic parameters of a hypocaust construction," *Building and Environment*, vol. 34, no. 3, pp. 305–318, 1998.

[10] T. Rook, "The development and operation of Roman hypocausted baths," *Journal of Archaeological Science*, vol. 5, no. 3, pp. 269–282, 1978.

[11] D.-K. Kim, "The natural environment control system of Korean traditional architecture: comparison with Korean contemporary architecture," *Building and Environment*, vol. 41, no. 12, pp. 1905–1912, 2006.

[12] M.-S. Yeo, I.-H. Yang, and K.-W. Kim, "Historical changes and recent energy saving potential of residential heating in Korea," *Energy and Buildings*, vol. 35, no. 7, pp. 715–727, 2003.

[13] K.-H. Lee, D.-W. Han, and H.-J. Lim, "Passive design principles and techniques for folk houses in Cheju Island and Ullūng Island of Korea," *Energy and Buildings*, vol. 23, no. 3, pp. 207–216, 1996.

[14] C. Bae and C. Chun, "Research on seasonal indoor thermal environment and residents' control behavior of cooling and heating systems in Korea," *Building and Environment*, vol. 44, no. 11, pp. 2300–2307, 2009.

[15] G. Cao, J. Jokisalo, G. Feng, L. Duanmu, M. Vuolle, and J. Kurnitski, "Simulation of the heating performance of the Kang system in one Chinese detached house using biomass," *Energy and Buildings*, vol. 43, no. 1, pp. 189–199, 2011.

[16] Z. Zhuang, Y. Li, B. Chen, and J. Guo, "Chinese Kang as a domestic heating system in rural northern China—a review," *Energy and Buildings*, vol. 41, no. 1, pp. 111–119, 2009.

[17] W. He, Q.Y. Jiang, J. Ji, and W. Wei, "A study on thermal performance, thermal comfort in sleeping environment and solar energy contribution of solar Chinese Kang," *Energy and Buildings*, vol. 58, pp. 66–75, 2013.

[18] M. Yang, X. Yang, P. Wang, M. Shan, and J. Deng, "A new Chinese solar kang and its dynamic heat transfer model," *Energy and Buildings*, vol. 62, pp. 539–549, 2013.

[19] M. Yang, X. Yang, Z. Wang, and P. Wang, "Thermal analysis of a new solar kang system," *Energy and Buildings*, vol. 75, pp. 531–537, 2014.

[20] P. Wang, M. Shan, D. Xiong, and X. Yang, "A new Chinese kang with forced convection: system design and thermal performance measurements," *Energy and Buildings*, vol. 85, pp. 410–415, 2014.

[21] S. Hao, Y. Song, G. Zhang et al., "Design strategies on heat recovery of cooking stove in rural houses of China," in *Proceedings of 31st International PLEA (Passive and Low Energy Architecture) Conference*, Ahmedabad, India, December 2014.

[22] P. Wang, M. Yang, X. Yang, and M. Shan, "Thermal performance of a traditional Chinese heated wall with the in-series flow pass: experiment and modeling," *Energy and Buildings*, vol. 84, pp. 46–54, 2014.

[23] X. Zhang, G. Feng, and G. Feng, "Comparative analysis of heating wall with inner PCM and traditional heating wall in rural area of north China," *Building Energy Environment*, vol. 4, pp. 27–30, 2010, in Chinese.

[24] M. Shan, D. Li, and X. Yang, "Study on influences of combustion of fire place on indoor environment and thermal comfort in rural residences," *Building Science*, vol. 27, pp. 10–14, 2011, in Chinese.

Research Article

Optical-Fiber-Based Smart Concrete Thermal Integrity Profiling: An Example of Concrete Shaft

Ruoyu Zhong, Ruichang Guo, and Wen Deng [ID]

Missouri University of Science and Technology, Rolla, MO, USA

Correspondence should be addressed to Wen Deng; wendeng@mst.edu

Concrete is currently the most widely used construction material in the world. The integrity of concrete during the pouring process could greatly affect its engineering performance. Taking advantage of heat production during the concrete curing process, we propose an optical-fiber-based thermal integrity profiling (TIP) method which can provide a comprehensive and accurate evaluation of the integrity of concrete immediately after its pouring. In this paper, we use concrete shaft as an example to conduct TIP by using the optical fiber as a temperature sensor which can obtain high spatial resolution temperature data. Our method is compared with current thermal infrared probe or embedded thermal sensor-based TIP for the concrete shaft. This innovation makes it possible to detect defects inside of the concrete shaft with thorough details, including size and location. First, we establish a 3D shaft model to simulate temperature distribution of concrete shaft. Then, we extract temperature distribution data at the location where the optical fiber would be installed. Based on the temperature distribution data, we reconstruct a 3D model of the concrete shaft. Evaluation of the concrete integrity and the existence of the potential defect are shown in the paper. Overall, the optical-fiber-based TIP method shows a better determination of defect location and size.

1. Introduction

Concrete is currently the most widely used construction material all over the world. Concrete consists of both fine and coarse aggregates that are bonded by cement paste. Hydration reaction occurs when cement is blended with water. This hydration is an exothermal reaction, which means it generate heat and results in temperature rise during concrete curing. At the beginning, tricalcium aluminate (C_3A) reacts with water and generates a large amount of heat, but the reaction would not last long. It is followed with a short period that release less heat called the dormant phase. After a short period of dormancy, the alite and belite start to react and continuously generate heat. The maximum heat generation would last 10 to 20 hours after pouring. Since cementitious material can generate a large amount of heat, defects of concrete would lead to temperature divergence in the concrete structure. By taking advantage of such a feature of concrete, we propose an innovative method of optical fiber-based thermal integrity profiling (TIP) to inspect the concrete integrity and use the concrete shaft as an example to demonstrate the method.

Since the concrete shaft serves as the deep foundation, the quality of the concrete shaft is critical for the safety of superstructures. Defects within the concrete shaft would degrade the shaft performance (Figure 1). The existence of defects within the concrete shaft is mainly due to some problems of construction and design deficiencies [1]. Among 5,000 to 10,000 shafts tested, 15% of shafts showed the deviation from ideal signal and 5% of tested shafts showed indisputable defect indication [2, 3]. Since both excavation and concreting are blind processes when building drilled shafts, it is impossible to completely prevent defects from happening during construction. Determination of whether defects exist in the concrete shaft and how severe the defects are, are crucial to evaluate whether the concrete shaft would satisfy its design purpose. Among the existing methods, nondestructive testing is a widely accepted method for shaft integrity testing.

Currently, major nondestructive testing methods include low strain integrity test and cross-hole sonic logging (CSL). The low strain integrity test, also known as sonic pulse echo method, uses light hammer impacts and evaluates the

(a)   (b)   (c)   (d)
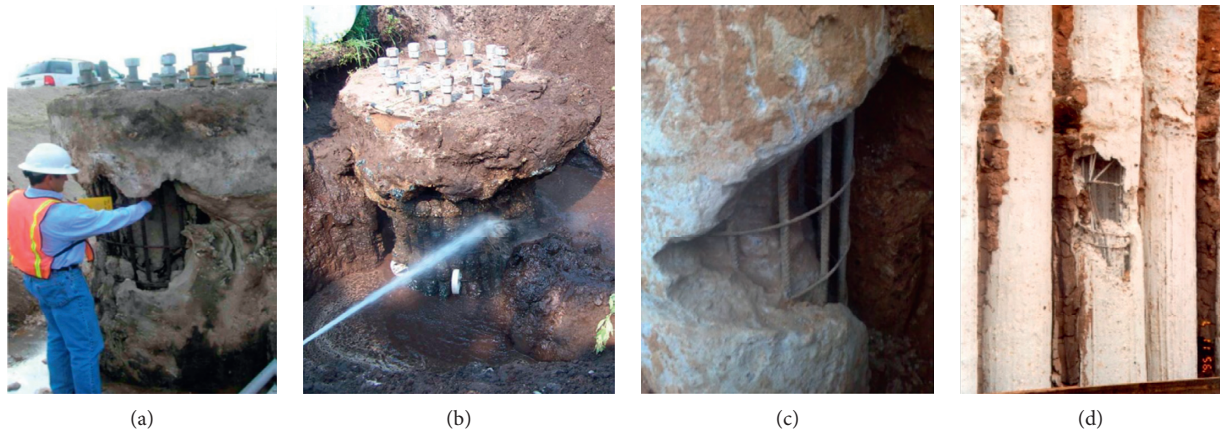
FIGURE 1: Different kinds of defects (images are from an online source).

collected force and velocity recordings to evaluate shaft integrity [4–6]. The low strain integrity test is cost-efficient and effective. However, this method has limitations including operator's familiarity and experience, and length/width ratio of the concrete shaft. CSL is a widely used nondestructive integrity test method. For CSL, 3–8 access tubes must be installed within a shaft cross section [7]. Then, a signal generator coupled with receiver is lowered, maintaining a consistent elevation, to test the integrity of concrete shaft. This method has higher accuracy, but is limited within the reinforcement cage. The CSL method only tests the integrity of concrete shaft between the access tubes, while outside of that zone is left untested. However, the bending capacity of the concrete shaft is mainly dependent on the outer part. The core of the concrete shaft has little contribution to bending capacity [8, 9]. The integrity of the outer part of concrete shaft should be evaluated as well.

TIP, which is a new nondestructive testing method, makes use of the hydration heat generated during concrete curing to determine whether defects exist and estimates their size and location according to the temperature distribution along the concrete shaft [10–12]. Temperature distribution is measured by lowering a thermal probe with infrared thermocouples into access tubes or by an embedded thermal sensor during the curing process. Inverse modeling of temperature distribution would provide information on whether the reinforcement cage has been misplaced or improper formation has happened. In addition, the location and type of defect would be indicated from the data. A relatively cool region indicates a shortage of concrete at that particular location, whereas a relatively warm region indicates extra concrete. Compared with previous methods, TIP covers a larger area and provides a more comprehensive result. However, due to the limited amount of access tubes, temperature data for inverse modeling could be insufficient to accurately predict temperature distribution of the concrete shaft which could limit further development of this method [11, 13].

Referring to advancements in optical fiber studies, Rayleigh scattering caused by local refractive index fluctuations along the glass fiber can be used to measure strains and temperature. Every point on the optical fiber can send a different Rayleigh scattering signal when subjected to temperature change, and therefore, every point along the fiber acts as a temperature sensor [14–18]. This feature of optical fibers makes it an ideal temperature sensor to measure high spatial resolution temperature distribution. Currently, this technology has been applied to measuring and recording temperature data, for example, in car engines, microwave ovens, or large furnaces for the steel industry. Advances in the research on Rayleigh scattering-based optical fiber make its application on TIP possible. By applying this optical fiber to TIP as a temperature sensor, more comprehensive and consistent temperature data can be provided. The conventional method sets an access tube every 300 mm diameter, and a measurement point within access tubes with vertical intervals less than 500 mm. In this optical-fiber based method, the optical fiber would be wrapped around the reinforcement cage spirally and densely with negligible cost of the fiber itself. Even if the vertical interval is the same as the conventional method when wrapping the optical fiber, the horizontal interval would still be significantly smaller. Temperature data measured by optical-fiber-based TIP would have high spatial resolution. The measured temperature data interval can be as small as 4 mm. Thus, the inverse modeling of temperature distribution can produce a more reliable integrity report [19–22].

The objective of this paper is to address the advantages of our proposed optical-fiber-based TIP method regarding its inverse modeling of temperature distribution of defected concrete shaft by having high resolution spatial temperature data. We used finite element method (FEM) to simulate temperature distribution of a defective concrete shaft. Temperature data were extracted in two different ways based on the concepts of our new method and conventional infrared thermal probe method. Based on the temperature distribution data, we reconstructed the 3D geometry of concrete shaft based on two methods. The impact of the size and location of the defect on temperature distribution is discussed in this paper.

2. Methodology

2.1. Governing Equation.

The principle of TIP is to take advantage of the correlation between the shape of the concrete shaft and temperature distribution. The temperature distribution is simulated using FEM. The governing equation of temperature (T) distribution in concrete shaft is as follows:

$$\frac{\rho C_{\mathrm{p}} \partial T}{\partial t} = \left[\frac{\partial}{\partial x}\left(k\frac{\partial T}{\partial x}\right) + \frac{\partial}{\partial y}\left(k\frac{\partial T}{\partial y}\right) + \frac{\partial}{\partial z}\left(k\frac{\partial T}{\partial z}\right)\right] + Q,$$

(1)

where C_{p} represents the heat capacity of the material, k is the thermal conductivity of the material, and Q is the heat source of the material.

2.2. Heat Generation.

The total amount of heat production and the rate of heat production are two important factors of temperature distribution. These two factors determine the temperature of the concrete shaft and the timing for TIP to be performed. The amount of heat and heat production rate are related to the ingredients of the concrete. Concrete with different proportions would generate different amounts of heat. The total heat production can be determined by using the following equations [23]:

$$\begin{aligned}
Q_0 &= Q_{\mathrm{cem}}p_{\mathrm{cem}} + 461p_{\mathrm{slag}} + Q_{\mathrm{FA}}p_{\mathrm{FA}}, \\
Q_{\mathrm{cem}} &= 500p_{\mathrm{C_3S}} + 260p_{\mathrm{C_2S}} + 866P_{\mathrm{C_3A}} + 420p_{\mathrm{c_4AF}} \\
&\quad + 624p_{\mathrm{SO_3}} + 1186p_{\mathrm{FreeCaO}} + 850p_{\mathrm{MgO}}, \\
Q_{\mathrm{FA}} &= 1800p_{\mathrm{FACaO}}.
\end{aligned}$$

(2)

The degree of hydration can be determined by the following equations [10, 23]:

$$\begin{aligned}
\alpha(t) &= \alpha_{\mathrm{u}}\exp\left(-\left[\frac{\tau}{t_e}\right]^{\beta}\right), \\
\alpha_u &= \frac{(1.031w/\mathrm{cm})}{(0.194 + w/\mathrm{cm})} + 0.5p_{\mathrm{FA}} + 0.3p_{\mathrm{SLAG}} < 1, \\
\beta &= p_{\mathrm{C_3S}}^{0.227} \cdot 181.4 \cdot p_{\mathrm{C_3A}}^{0.146} \cdot \mathrm{Blaine}^{-0.535} \cdot p_{\mathrm{SO_3}}^{0.558} \\
&\quad \cdot \exp\left(-0.647p_{\mathrm{SLAG}}\right), \\
\tau &= p_{\mathrm{C_3S}}^{-0.401} \cdot 66.78 \cdot p_{\mathrm{C_3A}}^{-0.154} \cdot \mathrm{Blaine}^{-0.804} \cdot p_{\mathrm{SO_3}}^{-0.758} \\
&\quad \cdot \exp\left(2.187 \cdot p_{\mathrm{SLAG}} + 9.5 \cdot p_{\mathrm{FA}} \cdot p_{\mathrm{FACaO}}\right),
\end{aligned}$$

(3)

where $\alpha(t)$ represents the degree of hydration of cement at time t, w/cm is the water-cement ratio, and β and τ are determined by the cementitious constituent fractions. According to ASTM D7949-14, the recommended timing to perform TIP would be 12 hours after concrete placement until the number of days is equivalent to the foundation diameter in meters divided by 0.3 m.

2.3. Heat Transport.

Heat transport is another important factor for temperature evolution within the concrete shaft. Heat is dissipated into the surrounding soil simultaneously after heat is generated due to hydration. Heat transport includes three mechanisms: conduction, convection, and radiation. In this situation, heat conduction is the predominant mechanism in heat transport. Heat conduction in the material is represented by thermal conductivity k.

Soil consists of solids, air, and water. The specific value of thermal conductivity of soil is determined by the constitution of soil and the thermal conductivity of each phase. The thermal conductivity can be determined by using the following equation [24–26]:

$$k_1 = k_{\mathrm{s}} - n[k_{\mathrm{s}} - S_{\mathrm{w}}k_{\mathrm{w}} - (1 - S_{\mathrm{w}})k_a],$$

(4)

where n denotes porosity and S_{w} represents the degree of saturation.

However, this model does not consider the effect caused by the shape of the void inside of soil. Thus, they introduce a shape factor $\chi = \sqrt{S_{\mathrm{w}}}$ into the equation to represent the effect caused by the shape of the void. Then, the equation becomes

$$k = \sqrt{S_{\mathrm{w}}}\{k_{\mathrm{s}} - n[k_{\mathrm{s}} - S_{\mathrm{w}}k_{\mathrm{w}} - (1 - S_{\mathrm{w}})k_a]\} + (1 - \sqrt{S_{\mathrm{w}}})k_a.$$

(5)

2.4. Heat Capacity.

We assume that the temperature of the soil is the same among the three phases and that the heat capacity of the soil is also related to the three phases. The heat required to raise the temperature of soil one degree can be calculated by $C_s m_{\mathrm{s}} + C_w m_{\mathrm{w}} + C_g m_{\mathrm{g}}$. The total weight of the soil is $m_{\mathrm{s}} + m_{\mathrm{w}} + m_{\mathrm{g}}$. Therefore, the value of soil heat capacity can be determined as follows:

$$C_{\mathrm{p}} = \frac{C_s m_{\mathrm{s}} + C_w m_{\mathrm{w}} + C_g m_{\mathrm{g}}}{m_{\mathrm{s}} + m_{\mathrm{w}} + m_{\mathrm{g}}}.$$

(6)

Considering that the mass of air is negligible, the equation can be simplified as

$$C_{\mathrm{p}} = \frac{C_s + C_w w}{1 + w},$$

(7)

where w is water content.

2.5. Simulation Parameters.

A common concrete shaft consists of two parts: concrete and reinforcement cage. To get the data of temperature distribution, the sensor must be deployed inside of concrete shaft. As mentioned above, the optical fiber would be wrapped around the reinforcement cage spirally so that temperature along the fiber would be obtained. When it comes to conventional TIP, temperature can only be measure through access tubes or at the points where embedded sensors are set.

In order to simulate the temperature evolution and distribution within the shaft, a 3D model is established as shown in Figure 2. The model consists of four parts: concrete inside reinforcement cage, concrete outside reinforcement cage, soil surrounding shaft, and soil below shaft. In this
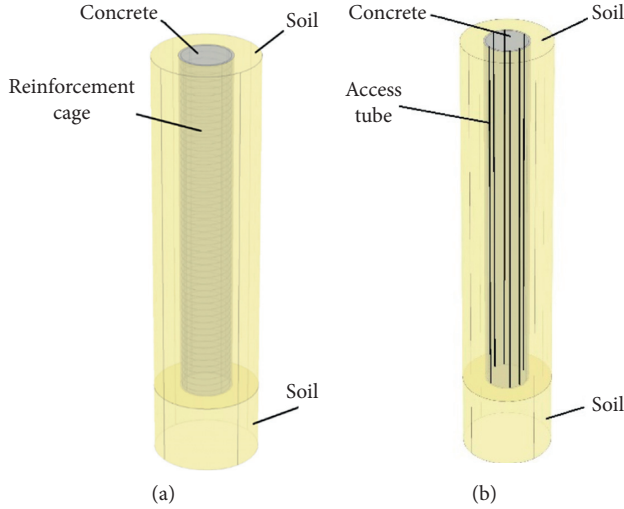
Figure 2: Shaft-soil model.

Table 1: Soil properties.

Properties	Unit	Value
Density	kg/m^3	1800
Soil solid thermal conductivity	W/m·K	5
Water thermal conductivity	W/m·K	0.5
Air thermal conductivity	W/m·K	0.05
Soil solid heat capacity	J/(kg·K)	850
Water heat capacity	J/(kg·K)	4190
Porosity	%	51.1
Water content	%	39.8
Saturation	%	97

Figure 3: Flow chart.

case, heat transfer into the reinforcement cage has been neglected since the reinforcement cage has a low heat capacity, high thermal conductivity, and relatively small volume. However, simulation of the reinforcement cage surface is still necessary because the reinforcement cage is where the optical sensor and access tubes are deployed. The location of the reinforcement cage surface would be the interface between the core concrete cylinder and the concrete cover. To get as much data as possible for high spatial resolution temperature distribution data, optical fiber is chosen to be deployed spirally. The pitch of optical fiber is 300 mm. To simulate access tubes in the conventional TIP method, we use vertical lines to represent the access tubes. According to ASTM D7949-14, one access duct should be placed every 300 mm in diameter. Therefore, there would be 6 vertical lines on the reinforcement cage in our setting.

The thickness of soil outside the concrete shaft is chosen based on the distance between two concrete shafts. In this case, the thickness is equal to the diameter of the concrete shaft. The properties of soil are listed in Table 1.

This simulation was conducted using FEM. The mesh type is free tetrahedral, with the minimum element size of 0.21 m. Several defects would be set on the shaft. Size and location are important factors we will inspect when evaluating the quality of the concrete shaft. The flow chart of the simulation can be found in Figure 3. In the simulation, the ability of the optical-fiber-based TIP and the conventional TIP to detect defect size and location will be compared and discussed.

3. Result and Discussion

In this section, we discuss the result of simulations using two different ways to extract data based on the concept of different TIP methods. Location and size of the defects are considered. First, we compare the results from two methods regarding how defect location will affect the result. Then, we investigate how defect size will affect the result.

3.1. Location Prediction. When performing TIP, we consider the location of the peak value as the location of the defect. To compare the accuracy of both methods, numerical simulation of a 6-foot diameter concrete shaft with a 12-inch sized cubic defect at selected locations is conducted. The location and size of defects are listed in Table 2. The location selected would be: defect is exactly at the measurement point of access tube method, defect is shifted from measurement point of access tube method, and defect is between measurement points of access tubes, separately (Figure 4). The result is shown in Figure 5; the concave region indicates the region that has negative value of temperature divergence. The region with dark blue color is the determination of defect by each method. The area of dark blue region indicates the size of the defect, whereas the location of that region indicates the location of the defect.

When the defect is located at the position where the infrared thermal probe measures temperature, both methods provide accurate determination of location. Furthermore, the temperature distribution can roughly indicate the shape of the defect. When the defect is shifted from the position where the infrared thermal probe measures temperature, although both methods can detect the defect, the result from conventional TIP method deviates from the actual location of the defect. At the same time, the optical-fiber-based TIP method can still have an accurate prediction of defect location. When the defect happened to be located between two measurement points of the conventional TIP method, although both methods can detect the defect, the result from

5
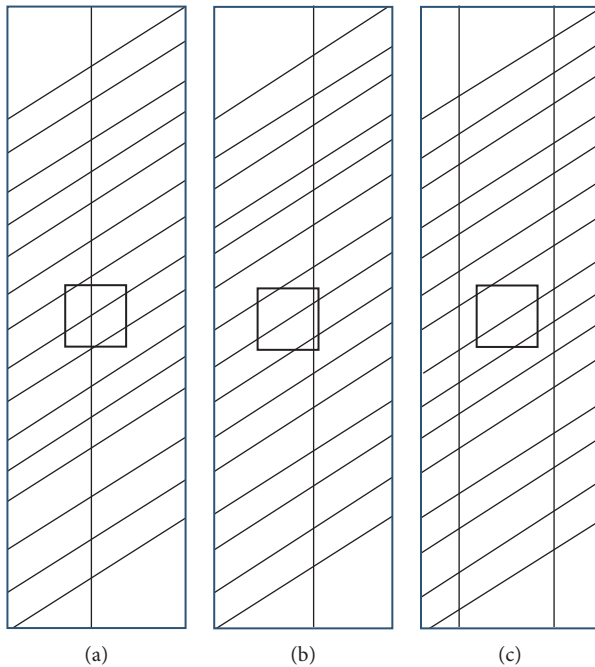
FIGURE 4: Schematic of defect location. (a) Defect located on access tube, (b) defect shifted from access tube, and (c) defect located between access tubes.

the conventional TIP method can hardly predict the location of the defect. The temperature distribution between access tubes does not show a significant peak value. The location of the defect can be anywhere within the low temperature region. Optical-fiber-sensor-based TIP, on the other hand, can still have an accurate determination of the defect.

According to the result presented above, in all three situations, the optical-fiber-based TIP method has great outcome despite the location of the defect. The even distribution of measurement points and relatively small interval not only increase the possibility of the defect being located at the measurement point, but also diminish the effect when the peak value is not located at the measurement point, which contributes to more accurate reconstructed temperature distribution.

Considering that in most situations, the defect is not located exactly at the measurement point, we could draw a conclusion that the optical-fiber-based TIP method would always have the same or better determination of defect location.

3.2. Size Sensitivity. The size of the defect is also a significant factor that needs to be considered for shaft integrity test. The size of defect is related to the magnitude of temperature divergence. The peak value of temperature distribution is crucial to determine the size of the defect. To compare the accuracy of both methods, numerical simulation of a 6-foot concrete shaft is conducted with different defects of different sizes located between access tubes (Table 3). The size of the defects is 18 inches, 15 inches, and 10 inches (Figure 6). An anomaly that has 12% of area reduction is an anomaly

needed for further evaluation. Both methods should have the ability to detect defects at this size.

The result is shown in Figure 7; the concave region indicates that the region that has a negative value of temperature divergence. The region with dark blue color is the determined defect by each method. The area of dark blue region indicates the size of the defect, whereas the location of that region indicates the location of the defect.

When the defect is a 15-inch cube at the lateral surface of the concrete shaft, both methods can detect the existence of the defect. However, the optical fiber method has a larger temperature divergence, closer to the actual temperature distribution in that region. When the defect is a 10-inch cube at the lateral surface of concrete shaft, the infrared thermocouple probe or embedded sensor-based TIP cannot detect the defect between access tubes. The temperature divergence caused by the defect would only be maintained within a certain zone. Once the effect zone is located totally between access tubes, conventional TIP may miss the existing defect which may have a negative effect on the performance of the concrete shaft. The optical-fiber-based TIP method can still detect defects. The area of defect is smaller compared with the result shown in Figure 7, indicating that the size of the defect is smaller than the result shown in Figure 7. This demonstrates that the TIP method has the ability to measure size based on the temperature distribution result.

Since the size of defect is related to the magnitude of temperature divergence, accurate temperature distribution is crucial to defect size evaluation. The value of peak temperature divergence decreases from the center of defect outward. As distance from center of defect increase, the temperature distribution would be closer to the intact part. The closer the measurement point is to the center of the defect, the higher the accuracy of temperature distribution measurement would be. The conventional TIP has no measurement point between access tubes, which limits the minimum size of defect that can be detected. Optical-fiber-based TIP, on the other hand, has the ability to detect smaller defects due to high spatial resolution. However, if the size of the defect is too small, even optical-fiber-based TIP will not be able to detect it.

4. Conclusion

In this paper we proposed an optical-fiber-based TIP method. This method can be an improvement of infrared thermocouple probes and embedded sensors which are applied to conventional TIP by having high spatial resolution temperature data. The method also changes the way to deploy sensors from vertically deployed to spirally deployed around the reinforcement cage. These two changes enable TIP to measure a high resolution and consistent temperature distribution within the concrete shaft, leading to more accurate determination of integrity of the concrete shaft.

To verify the advantages of optical-fiber-based TIP, we investigate two factors of defects: location and size. In the location section, we set three situations: defect on access tube, shift from access tube, and between access tubes. When

(a)   (b)   (c)

(d)   (e)   (f)

(g)   (h)   (i)
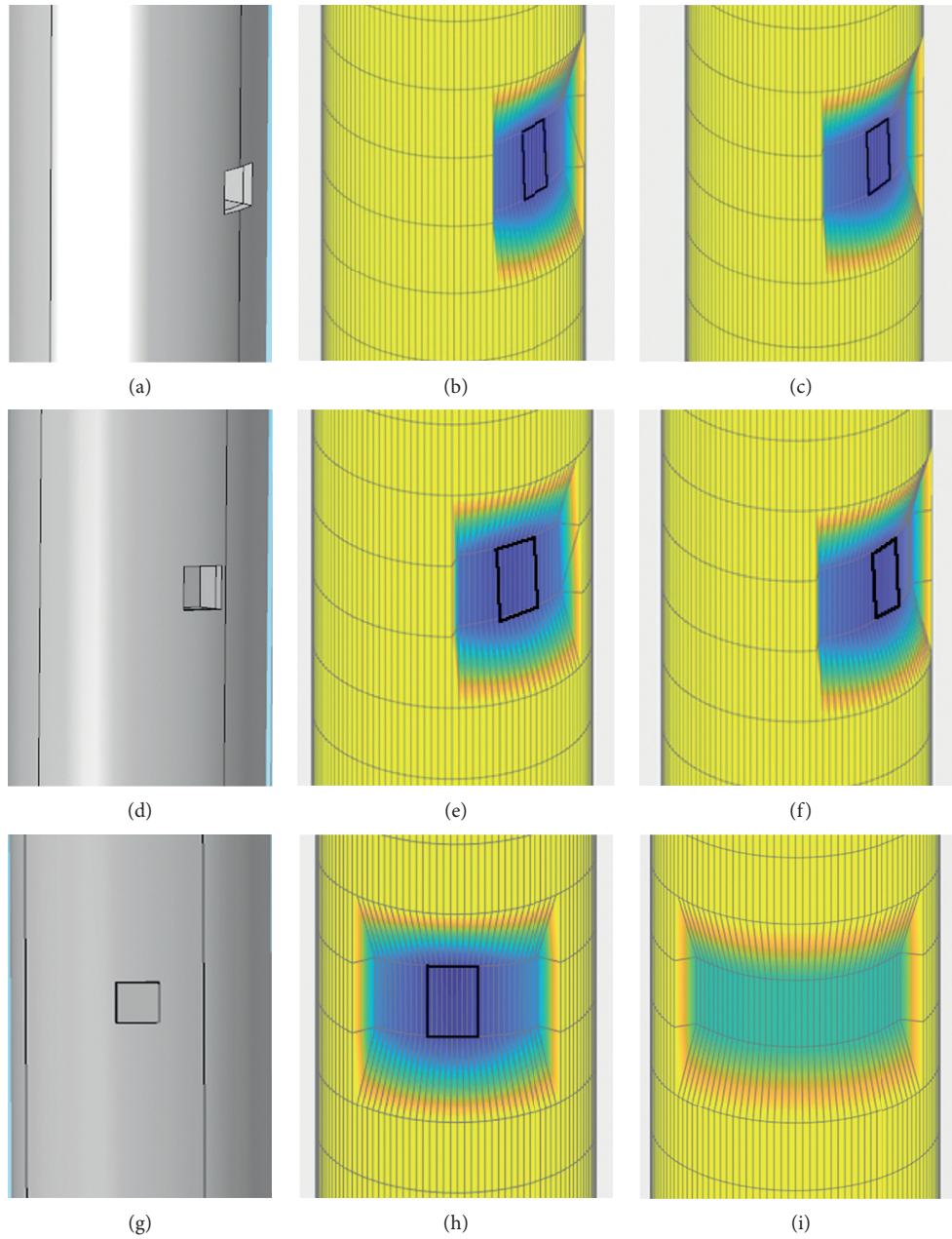
FIGURE 5: Result of simulation with different locations. (a, d, g) Actual location of defect, (b, e, h) location determination by the optical fiber method, and (c, f, i) location determination by the conventional method.

TABLE 2: Location determination by different methods.

Situation	Actual location			Optical fiber method			Conventional method		
	Depth	θ	r	Depth	θ	r	Depth	θ	r
On tube	7.5 m	180	0.6096	7.58 m	179.7	0.6148	7.58 m	181	0.6148
Around tube	7.5 m	171	0.6096	7.575 m	169	0.6175	7.575 m	179.7	0.619
Between tubes	7.5 m	150	0.6096	7.576 m	149.1	0.6096	N/A	N/A	0.774

the defect is located exactly on the access tube, both methods have an accurate determination of the location. However, when the defect is located between access tubes where conventional TIP does not have a measurement point, optical-fiber-based TIP shows higher accuracy on location determination. We also simulate three situations with different size defects located between access tubes. Since optical-fiber-based TIP has measurement points evenly
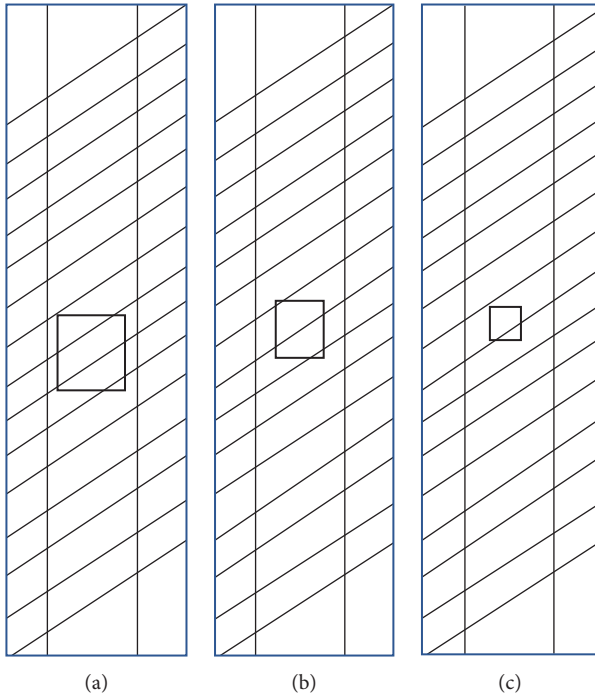
FIGURE 6: Schematic of defect location. (a) 18-inch cube, (b) 15-inch cube, and (c) 10-inch cube.
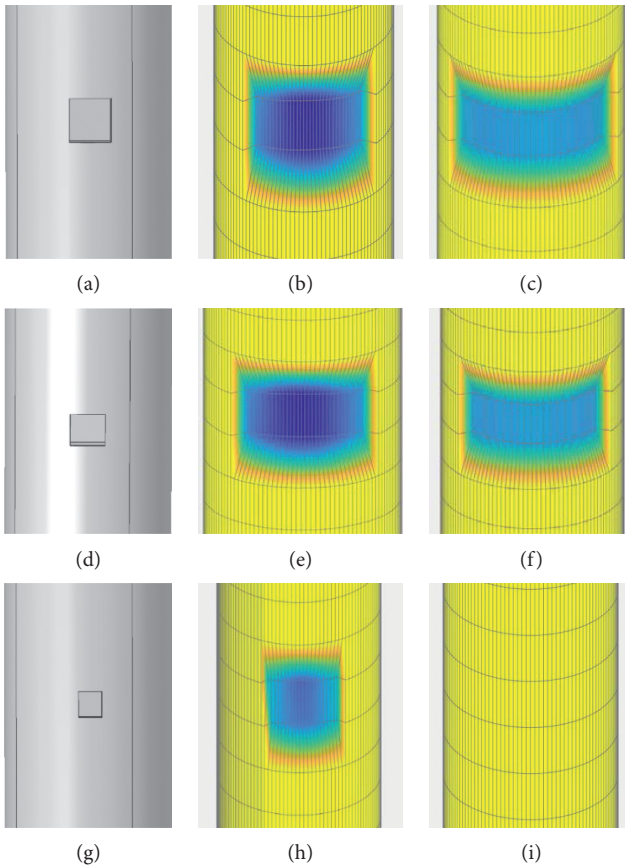
FIGURE 7: Result of simulation with different sizes. (a, d, g) Actual size of defect, (b, e, h) size determination by the optical fiber method, and (c, f, i) size determination by the conventional method.

TABLE 3: Size determination.

Actual size	Optical fiber method	Conventional method
18-inch cube	17.60 inches	13.34 inches
15-inch cube	14.68 inches	10.90 inches
10-inch cube	9.84 inches	5.45 inches

distributed at the surface, the sensitivity of optical-fiber-based TIP to the size of the defect is significantly higher. In the simulation regarding the shape of the defect, since measurement points of optical-fiber-based TIP distribute evenly within the defect, a more precise outline of the defect is depicted by optical-fiber-based TIP. Overall, optical-fiber-based TIP shows higher accuracy in prediction of shaft defects.

Data Availability

The data used to support the findings of this study are available from the corresponding author upon request.

Conflicts of Interest

The authors declare that they have no conflicts of interest.

Acknowledgments

References

[1] M. O'Neill, *Integrity Testing of Foundations*, Transportation Research Board, Washington, DC, USA, 1991.

[2] O. Klingmuller and F. Kirsch, *Current Practices and Future Trends in Deep Foundations*, American Society of Civil Engineers, Reston, VA, USA, 2004.

[3] D. Brown and A. Schindler, "High performance concrete and drilled shaft construction," in *Proceedings of GSP 158 Contemporary Issues in Deep Foundations*, Denver, CO, USA, February 2007.

[4] N. Massoudi and W. Teffera, "Non-destructive testing of piles using the low strain integrity method," in *Proceedings of 5th International Conference on Case Histories in Geotechnical Engineering*, pp. 13–17, Missouri University of Science and Technology, New York, NY, USA, April 2004.

[5] J. C. Ashlock and M. K. Fotouhi, "Thermal integrity profiling and crosshole sonic logging of drilled shafts with artificial defects," in *Proceedings of Geo-Congress 2014 Technical Papers, GSP 234 © ASCE*, Atlanta, Georgia, February 2014.

[6] S.-J. Hsieh, R. Crane, and S. Sathish, "Understanding and predicting electronic vibration stress using ultrasound excitation, thermal profiling, and neural network modeling," *Nondestructive Testing and Evaluation*, vol. 20, no. 2, pp. 89–102, 2005.

[7] D. Li, L. Zhang, and W. Tang, "Closure to "reliability evaluation of cross-hole sonic logging for bored pile integrity" by

D. Q. Li, L. M. Zhang, and W. H. Tang," *Journal of Geotechnical and Geoenvironmental Engineering*, vol. 133, no. 3, pp. 343-344, 2007.

[8] K. Johnson, G. Mullins, and D. Winters, "Concrete temperature control via voiding drilled shafts," in *Proceedings of Contemporary Issues in Deep Foundations, ASCE Geo Institute, GSP 158*, no. 1, pp. 1–121, Denver, CO, USA, October 2007.

[9] K. R. Johnson, "Temperature prediction modeling and thermal integrity profiling of drilled shafts," in *Proceedings of Geo-Congress 2014 Technical Papers, GSP 234 © ASCE*, Atlanta, Georgia, February 2014.

[10] G. Mullins, "Thermal integrity profiling of drilled shafts," *DFI Journal-The Journal of the Deep Foundations Institute*, vol. 4, no. 2, pp. 54–64, 2010.

[11] G. Mullins, "Advancements in drilled shaft construction, design, and quality assurance: the value of research," *International Journal of Pavement Research and Technology*, vol. 6, no. 2, pp. 993–999, 2013.

[12] K. R. Johnson, "Analyzing thermal integrity profiling data for drilled shaft evaluation," *DFI Journal-The Journal of the Deep Foundations Institute*, vol. 10, no. 1, pp. 25–33, 2016.

[13] A. G. Davis, "Assessing reliability of drilled shaft integrity testing," *Transportation Research Record*, vol. 1633, pp. 108–116, 1998.

[14] D. Samiec, *Distributed Fiber Optic Temperature and Strain Measurement with Extremely High Spatial Resolution*, Polytech GmbH, Waldbronn, Germany, 2011.

[15] W. Pei, W. Yua, S. Li, and J. Zhou, "A new method to model the thermal conductivity of soil–rock media in cold regions: an example from permafrost regions tunnel," *Cold Regions Science and Technology*, vol. 95, pp. 11–18, 2013.

[16] T. J. Moore, M. R. Jones, D. R. Tree, and D. D. Allred, "An inexpensive high-temperature optical fiber thermometer," *Journal of Quantitative Spectroscopy and Radiative Transfer*, vol. 187, pp. 358–363, 2017.

[17] H. Su, H. Jiang, and M. Yang, "Dam seepage monitoring based on distributed optical fiber temperature system," *IEEE Sensors Journal*, vol. 15, no. 1, pp. 9–13, 2015.

[18] R. K. Palmer, K. M. McCary, and T. E. Blue, "An analytical model for the time constants of optical fiber temperature sensing," *IEEE Sensors Journal*, vol. 17, no. 17, pp. 5492–5511, 2017.

[19] A. Leal-Junior, A. Frizera-Neto, C. Marques, and M. Pontes, "A polymer optical fiber temperature sensor based on material features," *Sensors*, vol. 18, no. 2, p. 301, 2018.

[20] Y. Rui, C. Kechavarzi, O'. L. Frank, C. Barker, D. Nicholson, and K. Soga, "Integrity testing of pile cover using distributed fibre optic sensing," *Sensors*, vol. 17, no. 12, p. 2949, 2017.

[21] Y. Cardona-Maya and J. F. Botero-Cadavid, "Refractive index desensitized optical fiber temperature sensor," *Revista Facultad de Ingeniería*, no. 85, pp. 86–90, 2017.

[22] J. Huang, X. Lan, M. Luo, and H. Xiao, "Spatially continuous distributed fiber optic sensing using optical carrier based microwave interferometry," *Optics Express*, vol. 22, no. 15, pp. 18757–18769, 2014.

[23] A. Schindler and K. Folliard, "Heat of hydration models for cementitious materials," *ACI Materials Journal*, vol. 102, no. 1, pp. 24–33, 2005.

[24] W. Liu, P. He, and Z. Zhang, "A calculation method of thermal conductivity of soils," *Journal of Glaciology and Geocryology*, vol. 24, no. 6, pp. 770–773, 2002.

[25] C. S. Blázquez, A. F. Martín, I. M. Nieto, and D. Gonzalez-Aguilera, "Measuring of thermal conductivities of soils and rocks to be used in the calculation of a geothermal installation," *Energies*, vol. 10, no. 795, pp. 1–19, 2017.

[26] D. Barry-Macaulay, A. Bouazza, R. M. Singh, B. Wang, and P. G. Ranjith, "Thermal conductivity of soils and rocks from the Melbourne (Australia) region," *Engineering Geology*, vol. 164, pp. 131–138, 2013.

Research Article

A Comparative Experimental Study on the Flexural Behavior of High-Strength Fiber-Reinforced Concrete and High-Strength Concrete Beams

In-Hwan Yang [ID],[1] **Changbin Joh** [ID],[2] **and Kyoung-Chul Kim**[3]

[1]*Professor, Kunsan National University, Department of Civil Engineering, Kunsan, Jeonbuk 54150, Republic of Korea*
[2]*Research Fellow, Korea Institute of Civil Engineering and Building Technology, Structural Engineering Research Institute, Goyang, Gyeonggi 10223, Republic of Korea*
[3]*Senior Engineer, DM Engineering, Department of Structural Engineering, Seoul 05288, Republic of Korea*

Correspondence should be addressed to In-Hwan Yang; ihyang@kunsan.ac.kr

Received 19 March 2018; Revised 28 June 2018; Accepted 30 July 2018; Published 4 September 2018

Academic Editor: Wen Deng

The flexural responses of high-strength fiber-reinforced concrete (HSFRC) beams and high-strength concrete (HSC) beams are compared in this study. A series of HSFRC and HSC beams were tested under pure flexural loading. The effects of the type of concrete, compressive strength of the concrete, and tensile rebar ratio on the flexural behavior of the concrete beams were investigated. The flexural behavior of the HSFRC and HSC beams including the induced crack and failure patterns, load and deflection capacity, crack stiffness, ductility index, and flexural toughness was compared. The crack stiffness of the HSC and HSFRC beams increased with the rebar ratio. For the same rebar ratios, the crack stiffness of the HSFRC beams was much greater than that of the HSC beams. The ductility index of the HSC beams decreased sharply with an increase in the rebar ratio, but the ductility index of the HSFRC beams did not show a clear decrease with increasing rebar ratio. The flexural toughness of the HSFRC beams was greater than that of the HSC beams at higher rebar ratios of 1.47% and 1.97%, indicating that the energy absorption of the HSFRC beams was greater than that of the HSC beams. Test results also indicated that HSFRC developed better and more consistent ductility with higher rebar ratio. In addition, the tested bending strength and sectional analysis results were compared.

1. Introduction

Compared to conventional concrete, high-strength concrete (HSC) develops higher compressive strength along with improved durability, ductility, and high elastic modulus that have recently promoted its extended application to many structures [1–3]. For example, Min et al. [4] investigated the shrinkage characteristics of high-strength concrete for large underground space structures to explore what ingredient in the mixture affected these characteristics. Ho et al. [5] evaluated analytically the effectiveness of adding confinement for ductility improvement of HSC columns. They concluded that the use of HSC could reduce the size of columns at the cost of some reduction in the flexural ductility of the columns.

Many tests have been performed to evaluate the flexural behavior of HSC beam specimens [6–9]. The results of Ashour [8] showed that the flexural rigidity increased with greater compressive strength of the concrete. The test results of Mohammadhassani et al. [10] showed that an increase in tensile rebar ratio improved the ultimate load capacity but decreased the deflection ductility index. The ductility index is thus significantly influenced by the rebar ratio. Compared with normal-strength concrete, the increased compressive strength of HSC makes it more brittle and less resistive to crack opening and propagation. Therefore, the tensile reinforcement of HSC beams is important for controlling the deflection of the beams and the crack formation within the beams.

The addition of steel fibers can increase the ductility, fracture toughness, and loading capacity of concrete members [11, 12]. High-strength fiber-reinforced concrete (HSFRC) is an advanced cement composite material reinforced with steel fiber and has a limited porosity for

a concrete matrix. In HSFRC, steel fiber is an important factor affecting both the mechanical properties and structural capacity of concrete members [13–16]. Several studies on the flexural behavior of HSFRC beams have been conducted [17–20]. Chunxiang and Patnaikuni [18] investigated the effects of different steel fibers on the flexural behavior of beams. They concluded that the addition of steel fibers significantly improved the flexural performance, including the bending strength and deflection capacity. To examine the influence of steel fiber on the flexural behavior of HSFRC members, Su et al. [19], Guan et al. [20], and Mertol et al. [21] conducted studies with different volume dosages of steel fiber. They reported that the bearing capacity of HSFRC increased with the steel fiber volume dosage. In addition, a flexural analysis of ultra-high-performance concrete beams, which can be regarded as a kind of HSFRC, was suggested by Chen and Graybeal [22], Bae et al. [23], and Ning et al. [24].

However, most experimental studies on the flexural behavior of HSC and HSFRC were performed on either HSC beams or HSFRC beams. There are few direct comparison studies on experimental results of HSFRC beams and HSC beams, which have almost the same concrete compressive strength. To enhance the understanding of the difference between the flexural behavior of HSFRC beams and that of HSC beams, an experimental investigation is needed.

Therefore, this study intends to compare the characteristics of the flexural behavior of HSC and HSFRC beams that have nearly identical concrete compressive strengths. The test parameters include the compressive strength of the concrete and tensile rebar ratio of the concrete beams. The compressive strengths of 100 MPa and 120 MPa are considered, and the tensile rebar ratios of 0.98%, 1.47%, and 19.7% are used in this study. The comparison of the flexural behavior of the HSFRC beams and HSC beams is done in terms of the crack and failure patterns, crack stiffness, bending capacity, and ductility. Finally, a comparison of the sectional analysis and experimental results of the bending strength is performed.

2. Experimental Program

2.1. Mixture Proportions of the HSC and HSFRC.
In this study, three mixing proportions, H100, H120, and HF120, were used to fabricate test beams, as shown in Table 1. The three-digit numbers in each mixture name represented the target compressive strength of the concrete. The H100 and H120 mixtures were used to fabricate the HSC beams, while the HF120 mixture was used to fabricate the HSFRC beams.

The H100 and H120 mixtures had low water-binder ratios of 0.2 and 0.15 to attain the high compressive strength of concrete. The cement used in these two mixtures was ordinary Portland cement (OPC). Blast furnace slag (BFS) and silica fume (SF) were also used as binders in the H100 and H120 mixtures. Coarse aggregates with a maximum size of 20 mm and a density of 2.6 g/cm^3 were included in the H100 and H120 mixtures, and sand was used as fine aggregate.

The HF120 mixture did not include coarse aggregates but did include zirconium and 1% steel fibers by volume of concrete. Richard and Cheyrezy [11] suggested that limiting the coarse aggregates in the mixture could create a homogenous and dense cementitious matrix. In addition, coarse aggregates were excluded in the HF120 mixture to limit microcrack formation in the interface zone between the coarse aggregate and cementitious matrix. Crushed quartz with an average diameter of 10 μm and a density of 2,600 kg/m^3 was used as a filler material in the HF120 mixture. The steel fibers used in this study were straight and had a diameter of 0.2 mm and length of 19.5 mm, as shown in Figure 1. The density of the steel fiber was 7,500 kg/m^3, and its yield strength was 2,500 MPa.

Conventional concrete usually includes only OPC as binder. However, additionally to OPC, HSFRC in this study also included blast furnace slag, silica fume, and zirconium as binders, as well as filler and steel fiber. Therefore, the HSFRC was about five times more expensive than the conventional concrete.

Compared with laboratory specimens, the structural members actually used onsite have larger length and sectional dimensions, and it also takes more time to complete the placing of HSFRC. It may thus be more difficult to control the workability and flow of HSFRC onsite than in laboratory condition. The placing method and workability of the HSFRC mixture influence sensitively the orientation and distribution of steel fibers and consequently affect the mechanical properties of HSFRC. Therefore, the difficulty in achieving workability and flow should be considered for structural applications because the large dimension and placing time delay of HSFRC may cause significant variation in the mechanical properties of concrete.

2.2. Material Properties.
The compressive strengths of the HSFRC and HSC were obtained through compressive testing on cylindrical specimens. Three concrete mixtures with different compressive strengths were used in this study. The mean compressive strengths of the H100, H120, and HF120 cylindrical specimens were 96.9, 118.3, and 135.5 MPa, respectively, as shown in Table 2. The measured compressive strengths of the H100 and H120 specimens almost reached the target compressive strengths of 100 and 120 MPa. However, the measured compressive strength of the HF120 specimen was greater than its target compressive strength of 120 MPa. After the compressive strength test, the relationship between the stress and strain of each specimen was obtained to compute the compressive strength and elastic modulus, as shown in Figure 2. The mean elastic moduli of the H100, H120, and HF120 specimens were 37511, 38623, and 39192 MPa, respectively, as shown in Table 2.

Five $100 \times 100 \times 400$ mm prenotched prismatic specimens were fabricated from each batch to determine the tensile strength of the HSFRC. A three-point bending test on a prenotched prism was used to obtain the tensile strength of the HSFRC [25]. A notch was cut into the tensile zone, and a clip gauge was attached at the notch to measure the crack mouth opening displacement (CMOD). The load-CMOD

TABLE 1: Mixing proportions.

Mixture	W/B	W (kg/m^3)	OPC (kg/m^3)	BFS (kg/m^3)	SF (kg/m^3)	Zr (kg/m^3)	S (kg/m^3)	F (kg/m^3)	G (kg/m^3)	Steel fiber (V_f) (%)
H100	0.2	165.0	557.5	165.0	82.5	—	571.1	—	792.4	—
H120	0.15	150.0	700.0	150.0	150.0	—	467.5	—	765.1	—
HF120	0.22	209.0	770.0	135.0	—	58.0	847.0	231.0	—	1.0

Note. W: water; B: binders; OPC: ordinary Portland cement; BFS: blast furnace slag; SF: silica fume; Zr: zirconium; S: sand; F: filler; G: coarse aggregate.

FIGURE 1: Steel fiber used for the HSFRC mixture (HF120).

curves of notched specimens are shown in Figure 3. Based on the measured load-CMOD relationship curve, an inverse analysis was performed to estimate the tensile strength of the HSFRC. The inverse analysis procedure followed that of Yang et al. [17], using the measured load-CMOD relationship. The mean tensile strength of the HF120 mixture prismatic specimens was 7.8 MPa, as shown in Table 2.

In this study, a high-strength reinforcement bar (rebar) with a nominal diameter of 16 mm (D16) was used to reinforce the HSFRC and HSC beam specimens. The mean yield strengths of the rebar used in the H100, H120, and HF120 series beams were 607.9, 595.8, and 670.0 MPa, respectively, as shown in Table 2.

2.3. Details of the Structural Test Specimen and Instrumentation. To understand the flexural behavior of HSFRC and HSC beams, a total of 9 beam specimens were fabricated and tested. The cross section of the beams was rectangular with a beam width of 200 mm and a beam height of 250 mm, and the overall length of the beams was 3,300 mm. The dimensions and reinforcement details of the beams are shown in Figure 4. To avoid shear failure, all the specimens were reinforced by stirrups with a diameter of 10 mm at a spacing of 150 mm. The stirrups were used only in the shear spans, but they were not included in the 600 mm long constant moment region. The main parameters in the test program were the type of concrete (HSC and HSFRC), compressive strength of the concrete, and rebar ratio, as shown in Table 2. Two types of concrete beams, namely, HSC and HSFRC beams, were cast with different rebar ratios, which ranged between 0.98 and 1.97%. Two target concrete compressive strengths of 100 and 120 MPa were considered.

All the specimens were tested by using the four-point loading method. The load was applied using a hydraulically operated actuator and transferred from the actuator to the beam through a spread beam. The beams were set on a pair of steel supports with a clear span of 3,000 mm. The distance from the load to the middle of the constant moment zone was 300 mm. Each beam test was conducted under displacement control at a constant speed of 1.5 mm/min.

To measure the deflection that occurred during the loading, three LVDTs were placed under the constant moment region of the beam. The beam specimens were supported by roller supports as usually done the four-point loading test of beams. Therefore, horizontal LVDT was not included to measure potential support movement in the instrumentation plan. The strain of both the concrete and steel rebar was measured by electrical resistance strain gauges. Four strain gauges were attached to the steel rebar, and five strain gauges were mounted on the side of the beam at midspan, as shown in Figure 5.

3. Experimental Results

3.1. Crack and Failure Patterns. The crack and failure patterns of the HSFRC and HSC beams are shown in Figure 6. The initial cracking of the HSC and HSFRC beams occurred in the constant moment region. However, the cracks propagated more deeply into the compressive zone in the HSC beam than in the HSFRC beam. This result shows that the steel fibers in the HSFRC beams arrested the crack propagation. After an initial crack occurred, new cracks formed, and the widths of the existing cracks continued to enlarge with the load in both the HSFRC and HSC beams. At yield load and maximum load, more cracks formed in the HSFRC beams than in the HSC beams. Here, the yield load, that is the load at rebar yielding, was monitored by strain gauges attached to the rebar, and the maximum load was identified on the load-deflection curve of test beam.

In addition, the crack width in the HSC beams was larger than that in the HSFRC beams. These results indicate that the addition of steel fibers affected the width of the cracks in the HSFRC beams. Steel fibers played a role in bridging the cracks and redistributing the stress in the HSFRC beams, allowing more cracks to form in the HSFRC beams compared to the HSC beams.

The typical failure of the HSC members occurred by a sudden crushing of the concrete in the compressive zone, while the typical failure of the HSFRC beams resulted from the steel fiber pulling out of the HSFRC matrix. The measurement of the load and crack width relationship is shown in Figure 7. The crack widths in the HSFRC beams were smaller than those in the HSC beams at the same load level, up to the yielding of the rebar. For example, at the yield load of the H100-R1 beam (78 kN), the crack width of the HF120-R1 beam was 0.15 mm while the values of the H100-R1 and

TABLE 2: Details of the beam specimens.

Beam specimens	Concrete type	Beam section		Concrete			Rebar				
		Width (mm)	Height (mm)	Compressive strength f_c' (MPa)	Elastic modulus E_c (MPa)	Tensile strength f_t (MPa)	Nominal diameter (mm)	Number of rebars	Yielding strength f_y (MPa)	Area of rebar A_s (mm²)	Rebar ratio (ρ) (%)
H100-R1	HSC	200	250				16	2	607.9	397.2	0.98
H100-R2	HSC	200	250	96.9	37,511	—	16	3	607.9	595.8	1.47
H100-R3	HSC	200	250				16	4	607.9	794.4	1.97
H120-R1	HSC	200	250				16	2	595.8	397.2	0.98
H120-R2	HSC	200	250	118.3	38,623	—	16	3	595.8	595.8	1.47
H120-R3	HSC	200	250				16	4	595.8	794.4	1.97
HF120-R1	HSFRC	200	250				16	2	670.0	397.2	0.98
HF120-R2	HSFRC	200	250	135.5	39,192	7.8	16	3	670.0	595.8	1.47
HF120-R3	HSFRC	200	250				16	4	670.0	794.4	1.97
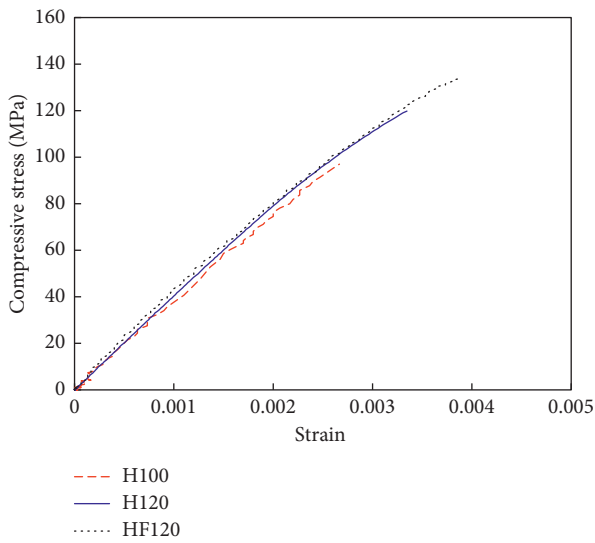
FIGURE 2: Compressive stress-strain curves.
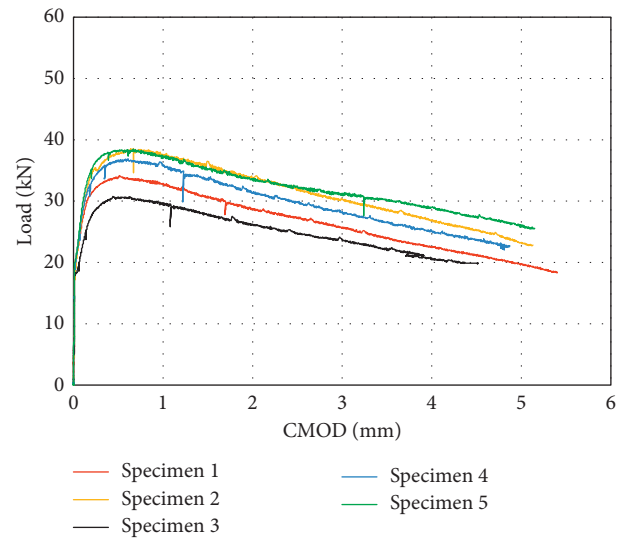
FIGURE 3: Load-CMOD relationship curves.

H120-R1 beams were 1.2 and 0.4 mm, respectively. For the rebar ratio of 1.47% (R2), at the yield load of the H100-R2 beam (129 kN), the H100-R2 and H120-R2 exhibited the crack widths of 0.8 and 1.73 mm, respectively, while the HF120-R2 had hairline cracks with the width of 0.2 mm. Similarly, at the yield load of the H100-R3 beam (129 kN), the H100-R3 and H120-R3 beams exhibited crack widths larger by 3.6 and 4.3 times, respectively, compared with the HF120-R3 beam. This result indicates that the steel fibers in the HSFRC beams affected the crack behavior.

In the HSFRC beams, after the load reached the peak load, the width of one crack increased suddenly and developed into a major crack. The major crack of the HSFRC beam occurred at the bottom of the beam and propagated upward to the compressive zone. Because the steel fibers resisted the opening of the crack, the major crack widened with the increase in the load until the fibers were pulled out of the matrix. Thus, the width of the major crack in the HSFRC members was clearly wider than the widths of the other cracks.

3.2. Load-Deflection Relationship. The load-deflection curves of the HSC and HSFRC beams with various rebar

ratios are shown in Figure 8. The test results show that the bending strength of both the HSC beams and HSFRC beams increased with the rebar ratio. For the H120 series beams, the maximum loads of the H120-R2 and H120-R3 beams increased, respectively, by 32.4% and 71.2% compared with that of the H120-R1 beam. For the HF120 series beams, the maximum loads of the HF120-R2 and HF120-R3 beams increased, respectively, by 23.9% and 58.6% compared with that of the HF120-R1 beam. These results show that the maximum load of the HSC beams underwent greater increase rate with higher rebar ratio than that of the HSFRC beams.

The test results also show that the deflection of the HSC beams at the maximum load decreased with the increase in the rebar ratio. For the H100 series beams, at the maximum load, the deflection of the H100-R1 beam was greater than that of the H100-R2 and H100-R3 beams. For the H120 series beams, at the maximum load, the deflection of the H120-R1 beam was also greater than that of the H120-R2 and H120-R3 beams. However, in contrast, the deflection of the HSFRC beams at the maximum load increased with the rebar ratio. At the maximum load, the deflection of the
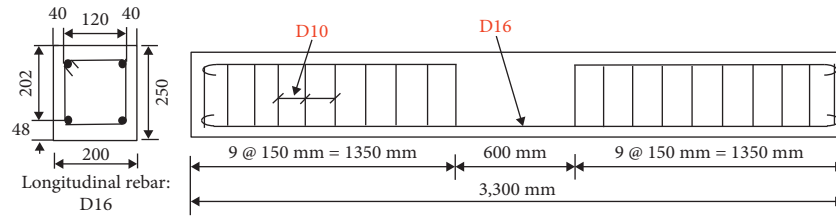
FIGURE 4: Dimensions of the beams.
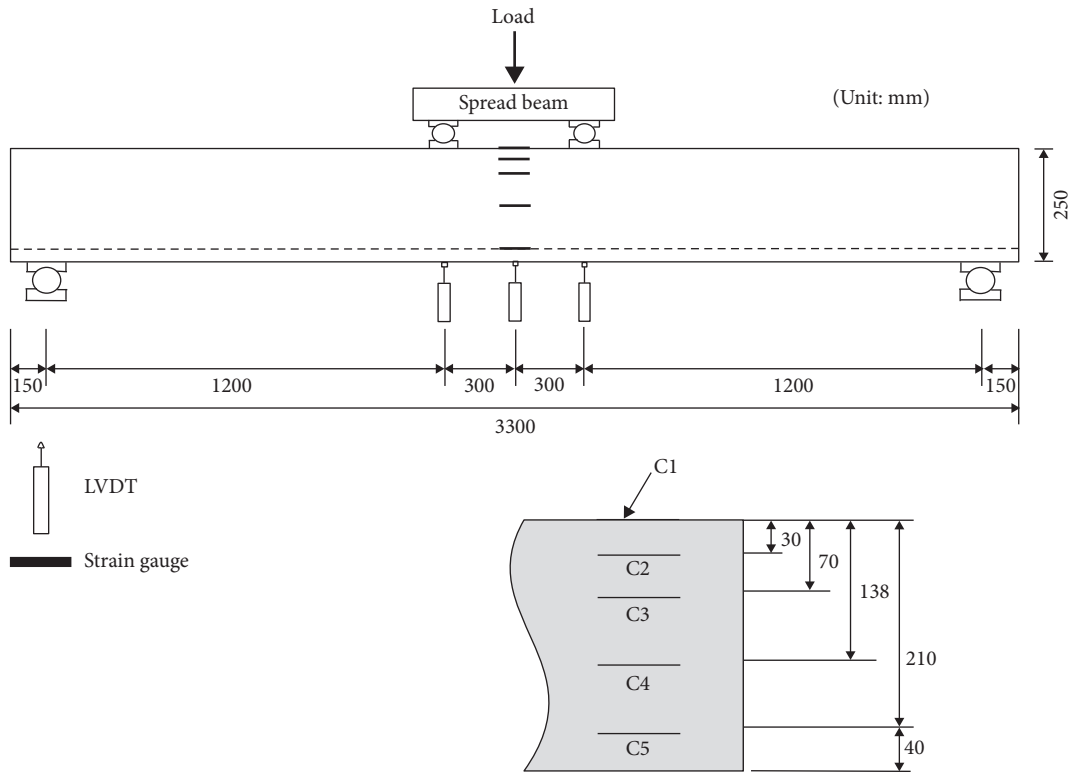
FIGURE 5: Instrumentation used for the flexural tests of the beams.

H120-R2 beam

HF120-R2 beam

(a)

H120-R2 beam

HF120-R2 beam

(b)

FIGURE 6: Continued.

H120-R2 beam   HF120-R2 beam

(c)
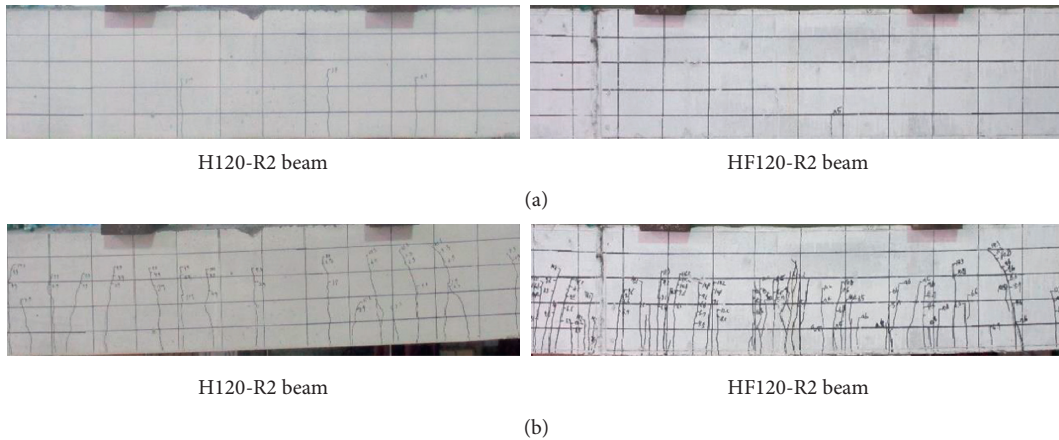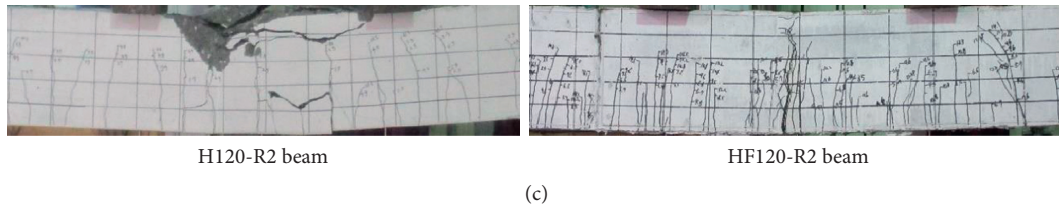
FIGURE 6: Crack and failure patterns of the HSC and HSFRC beams. (a) Initial cracking state. (b) Yielding state. (c) Ultimate state.

(a)

(b)

(c)
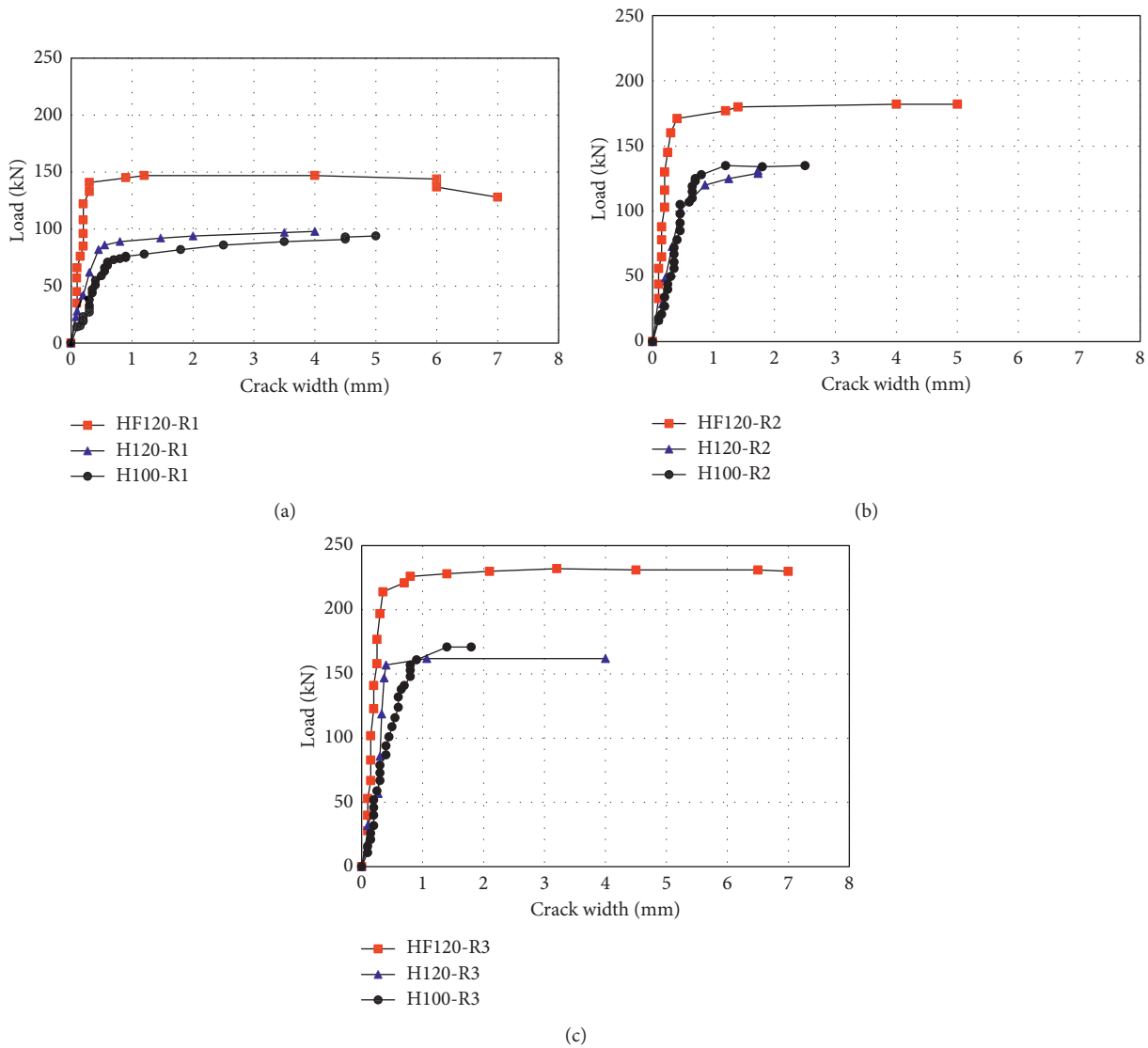
FIGURE 7: Load and crack width relationship. (a) Rebar ratio of 0.98%. (b) Rebar ratio of 1.47%. (c) Rebar ratio of 1.97%.

HF120-R3 beam was greater than those of the HF120-R1 and HF120-R2 beams.

The load-deflection curves of the test beams with different types of concrete are shown in Figure 9. The maximum load of the H100 series beams and that of the H120 series beams did not show a significant difference at the same rebar ratio. These results indicate that the compressive strength had little influence on the flexural behavior of the test beams. However, the maximum loads of the HSFRC beams were much greater

than those of the HSC beams due to the contribution of the steel fiber to the bending strength of the HSFRC beams. Additionally, use of HSFRC improved the bending strength of the beams remarkably.

The test results also show that the deflection capacity of the HSFRC beam at the failure of the beam increased with the increase in rebar ratio. For the rebar ratio of 0.98% (R1), the deflection at the failure of the HF120-R1 beam was less than that of the two other beam types, as shown in
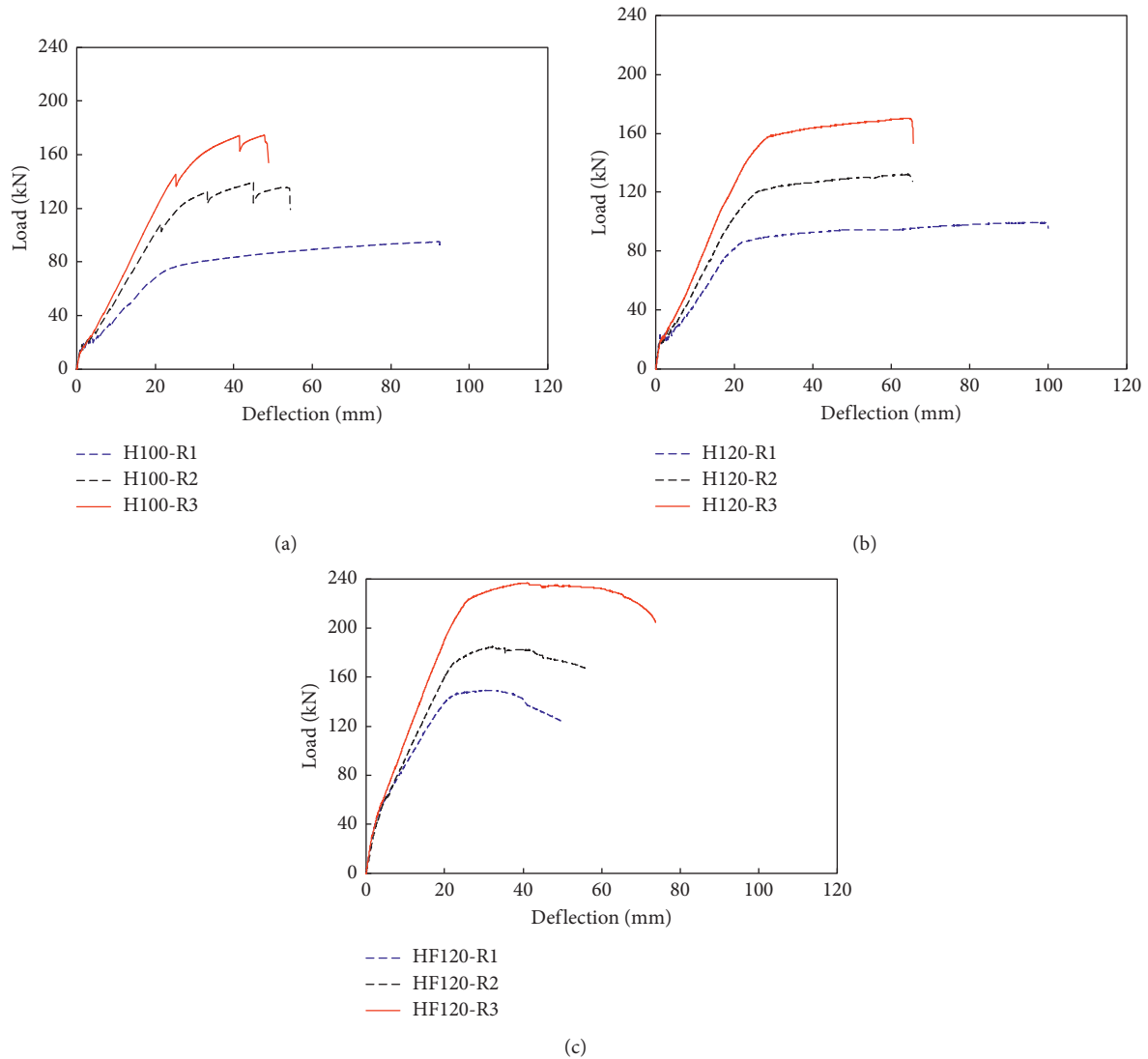
Figure 8: Load-deflection curves at different rebar ratios. (a) H100 series beams. (b) H120 series beams. (c) HF120 series beams.

Figure 9(a). For the rebar ratio of 1.47% (R2), the deflection at the failure of the HF120-R2 beam was similar to that of the two comparison beams, as shown in Figure 9(b). However, for the rebar ratio of 1.97% (R3), the deflection at the failure of the HF120-R3 beam was greater than that of the two comparison beams, as shown in Figure 9(c).

3.3. Crack Stiffness. The stiffness of a concrete beam drops after the initiation of the first crack because the contribution of the concrete to the stiffness of the beam is reduced in the cracked section. Thus, the crack stiffness of the beams was investigated in this study. The crack stiffness is calculated by the following equation [26].

$$K_{cr} = \frac{P_y - P_{cr}}{\Delta_y - \Delta_{cr}}, \qquad (1)$$

where K_{cr} is the crack stiffness, P_y is the yield load, P_{cr} is the cracking load, Δ_y is the deflection corresponding to the yield

load, and Δ_{cr} is the deflection corresponding to the cracking load.

The crack stiffness of each series of concrete beams is shown in Table 3 and Figure 10. For each type of concrete, the crack stiffness of the concrete beam increased with the rebar ratio. The crack stiffnesses of the H100-R1, H100-R2, and H100-R3 beams were 2.35, 3.82, and 4.71 kN/mm, respectively. The crack stiffnesses of the H120 beams were slightly higher, and their corresponding indices were 3.00, 4.11, and 5.09 kN/mm, respectively.

However, under the condition of the same rebar ratio, the crack stiffness of the HF120 series beams was much greater than those of the H100 and H120 series beams. The crack stiffness of the HF120-R1, HF120-R2, and HF120-R3 beams was 5.09, 6.23, and 7.59 kN/mm, respectively. In particular, the crack stiffness of the HF120-R1 beam was 2.2 and 1.7 times greater than those of the H100-R1 and H120-R1 beams, respectively. The crack stiffness of the HF120-R2 beam was also greater by 1.63 and 1.52 times than those of

(a)

(b)

(c)
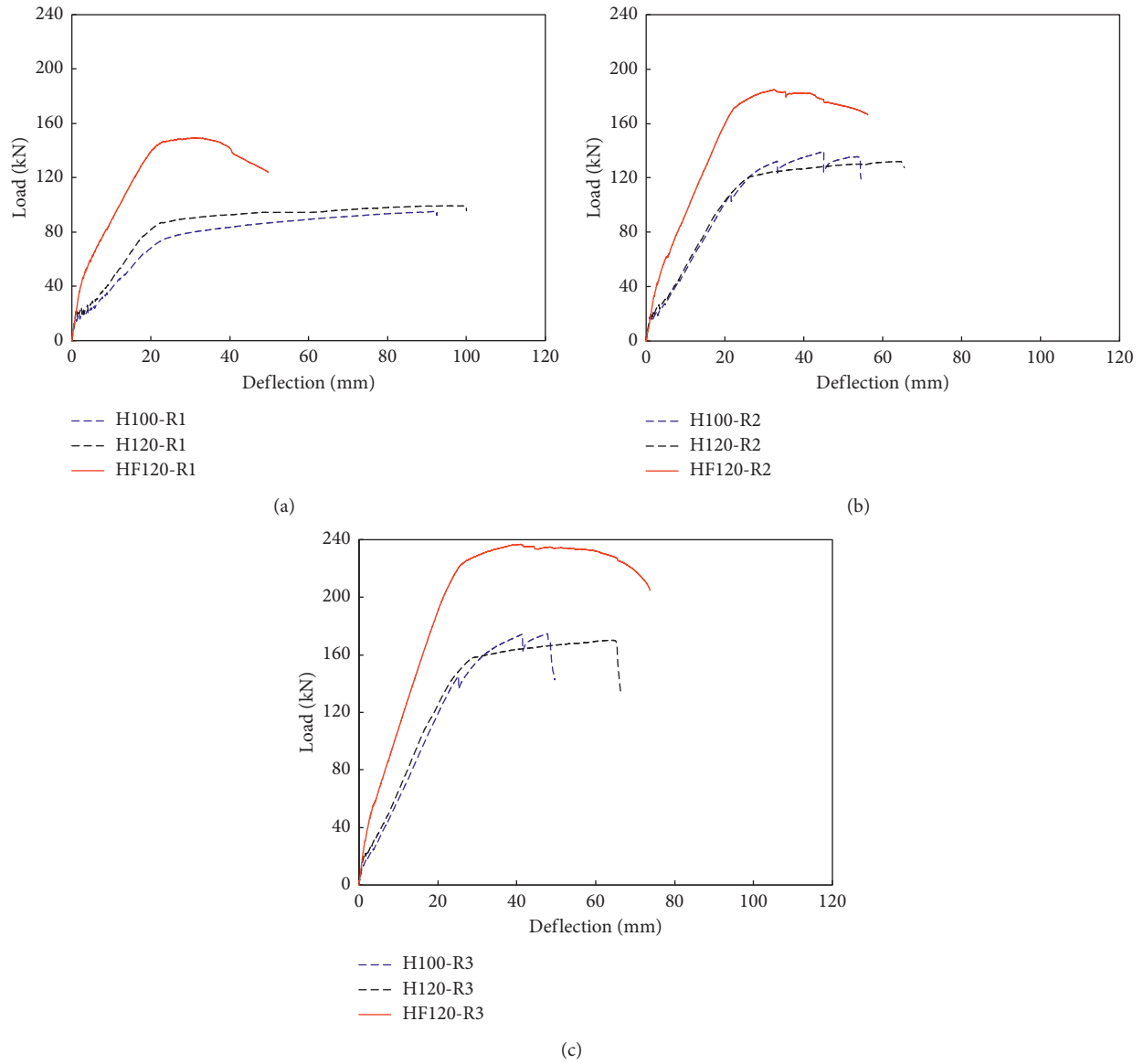
FIGURE 9: Load-deflection curves for different types of concrete. (a) Rebar ratio of 0.98%. (b) Rebar ratio of 1.47%. (c) Rebar ratio of 1.97%.

TABLE 3: Experimental results of the beam specimens.

Beam specimens	Initial cracking state			Yielding state			Peak state			Crack stiffness K_{cr} (kN/mm)	Ductility index	Flexural toughness (kN·mm)	Normalized flexural toughness (kN·mm)
	P_{cr} (kN)	M_{cr} (kN)	Δ_{cr} (mm)	P_y (kN)	M_y (kN)	Δ_y (mm)	P_p (kN)	M_p (kN)	Δ_p (mm)				
H100-R1	16.1	9.6	0.9	78.0	46.8	27.3	95.3	57.2	92.1	2.35	3.38	6,980	6,980
H100-R2	16.4	9.8	1.0	129.0	30.5	30.5	139.6	83.8	45.0	3.82	1.47	5,224	5,224
H100-R3	12.7	7.6	0.9	162.0	32.6	32.6	174.6	104.8	47.8	4.71	1.47	5,641	5,641
H120-R1	23.3	14.0	1.2	86.4	51.8	22.2	99.4	59.6	96.1	3.00	4.34	8,065	8,229
H120-R2	17.4	10.4	0.9	120.4	72.2	26.0	131.6	79.0	60.9	4.11	2.35	6,482	6,614
H120-R3	17.4	10.4	1.0	157.2	94.3	28.5	170.2	102.1	64.5	5.09	2.26	8,230	8,397
HF120-R1	46.4	27.8	2.9	145.1	87.1	22.3	149.3	89.6	30.5	5.09	1.37	5,456	4,950
HF120-R2	62.2	37.3	5.1	172.4	103.4	22.8	185.0	111.0	32.5	6.23	1.43	8,087	7,337
HF120-R3	58.8	35.3	4.2	222.0	133.2	25.7	236.8	142.1	41.0	7.59	1.60	13,971	12,676
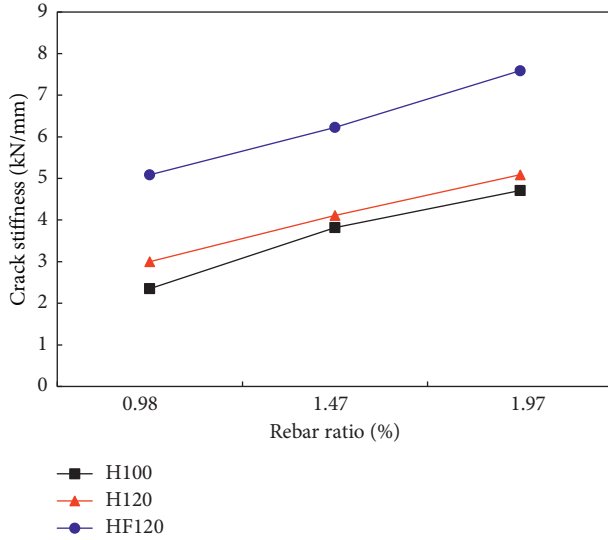
FIGURE 10: Crack stiffness of the HSFRC and HSC beams.

FIGURE 11: Ductility index of the HSC and HSFRC beams.

the H100-R2 and H120-R2 beams, respectively. Therefore, the test results show that the use of HSFRC significantly improved the crack stiffness of the concrete beams.

3.4. Ductility. The deflection at the midspan of each test beam was measured during the bending tests and used to calculate the ductility index. The ductility of the beam was calculated by Equation (2), which was suggested by Singh et al. [27].

$$\mu = \frac{\Delta_p}{\Delta_y}, \tag{2}$$

where μ is the ductility index, Δ_p is the deflection of the beam at the maximum (peak) load, and Δ_y is the deflection of the beam at the yield load.

The ductility indices are shown in Table 3 and Figure 11. This figure shows the ductility indices of the HSC series beams significantly decreased as the rebar ratio increased from 0.98 to 1.47% and decreased slightly or approximately remained the same as the rebar ratio increased from 1.47 to 1.97%. The ductility indices of the H100-R1, H100-R2, and H100-R3 beams were 3.38, 1.47, and 1.47, respectively. Additionally, the ductility indices of the H120-R1, H120-R2, and H120-R3 beams were 4.34, 2.35, and 2.26, respectively.

In contrast, the ductility of the HSFRC beams slightly improved in value and consistency with the rebar ratio. The ductility indices of the HF120-R1, HF120-R2, and HF120-R3 beams were 1.37, 1.43, and 1.60, respectively. The ductility indices of the HSFRC in this study ranged from 1.37 to 1.60, and those of ultra-high-performance concrete beams in a previous study [28] ranged from 1.31 to 1.99. This indicates that the ductility indices range of the HSFRC in this study was similar to that of the ultra-high-performance concrete. Additionally, the test results show that the ductility indices of the HSFRC beams were lower than those of the HSC beams, especially at low rebar ratios.

3.5. Flexural Toughness. The addition of steel fiber to concrete can improve the postcracking response of the concrete beam. Flexural toughness, which is a measure of the energy absorption capacity of the concrete beam, was calculated for each beam in this study. The flexural toughness was measured from the area under the load-deflection curve obtained from the bending test. The load-deflection curves shown in Figure 8 were used to estimate the flexural toughness of each beam.

Flexural toughness is affected by the strengths of concrete and rebar. The yield strengths of the rebar used in each series beam were different from each other. The flexural toughness of the H120 and HF120 series beams was normalized against that of the H100 series beams, which reflected the different yield strengths of the adopted rebar. The normalized flexural toughness was calculated by the following equation:

$$FT_{normalized} = FT \times \frac{f_{y,H100}}{f_y}, \tag{3}$$

where $FT_{normalized}$ is the normalized flexural toughness, $f_{y,H100}$ is the yield strength of rebar used in the H100 series beams, and f_y is the yield strength of rebar used in test beams.

The flexural toughness values of the HSC and HSFRC beams are shown in Table 3 and Figure 12. At the low rebar ratio of 0.98%, the normalized flexural toughness of the HSC beam was greater than that of the HSFRC beam. The normalized flexural toughness of the HF100-R1 and HF120-R1 beams was greater than that of HF120-R1 beam, by 41.0% and 66.2%, respectively.

The normalized flexural toughness of the HSFRC beams increased rapidly with the rebar ratio. However, the normalized flexural toughness of the HSC beams decreased with the increase in the rebar ratio from 0.98 to 1.47% and increased slightly with the rebar ratio from 1.47% to 1.97%.
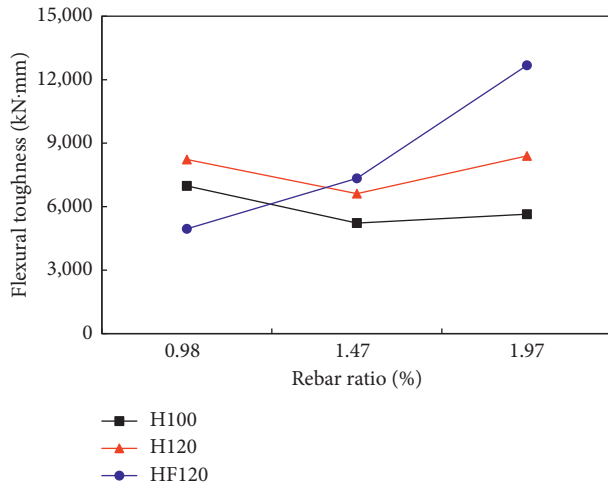
Figure 12: Normalized flexural toughness of the HSC and HSFRC beams.

Figure 13: Comparison of the experimental results of flexural toughness for the HSFRC beams of this study and of previous studies.

The test results show that the flexural toughness of the HSC beams, compared with that of the HSFRC beams, was not affected significantly by rebar ratios between 0.98% and 1.97%.

The normalized flexural toughness of the HSFRC beams was greater than that of the HSC beams at the higher rebar ratios of 1.47% and 1.97%. In particular, the normalized flexural toughness of the HF120-R3 beam was 2.24 and 1.51 times greater than that of the HF100-R3 and HF120-R3 beams, respectively. These results indicate that the energy absorption in the HSFRC beams was greater than that of the HSC beams and that the application of HSFRC at higher rebar ratios would be effective to improve the flexural toughness of concrete structures.

In addition, the experimental results of flexural toughness for the HSFRC beams of this study and those for the similar HSFRC beams of previous studies [21, 24, 29, 30] are compared in Figure 13. It appears that the normalized flexural toughness of the HSFRC beams increased with the rebar ratio, and that, similarly to other studies, the normalized flexural toughness increased with the rebar ratio in this study.

4. Sectional Analysis of the Bending Moment-Curvature Relationship

Finite element analysis can be used to predict the structural performance of the concrete beams. The finite element method allows detailed visualization of the stresses and displacements and gives insight into the design parameters. However, it takes a lot of effort and time to get finite element solutions for structural analysis. Sectional analysis was applied to predict the moment-curvature relationship in this study. The moment-curvature relationship was calculated for the experimental beams. The analysis approach was based on the bending beam theory and modification of the commonly used sectional model by considering constitutive law of materials.
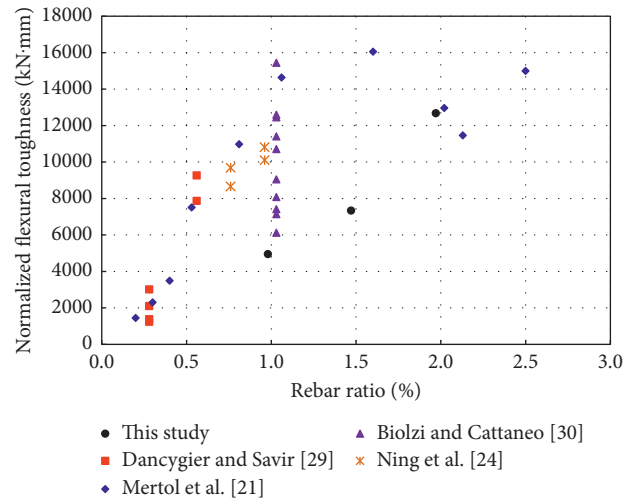
To predict the bending strengths of the H100, H120, and HF120 beams, moment-curvature curve analysis was performed. Sectional analysis was applied to predict the moment-curvature relationship. The strain and stress distributions along the beam depth is shown for a section in Figure 14. The cross section is divided into several layers by applying the multilayer method. The compression and tensile strains are assumed to be linear throughout the cross section. The compression and tensile strain of the section can be calculated by using the assumed curvature and neutral axis depth for each analytical step.

The strain distribution at the cross section is dependent on the neutral axis position for the assumed curvature. After determining the strain distribution, the stress distribution at the section can be obtained. The stress in each layer is calculated by using the stress-strain relationship of the concrete. The compressive stress-strain relationship of both the HSC and HSFRC was obtained from the compression tests for each type of concrete, as shown in Figure 2. The compressive stress-strain relationships of both the HSC and HSFRC were measured to be approximately linear. In addition, the compressive stress-strain relationship of both the HSC and HSFRC was modeled as a linear relationship, while the compressive stress-strain relationship for normal-strength concrete was modeled as a parabolic relationship. The compressive stress-strain relationship model of concrete for the HSC and the HSFRC is shown in Figure 15. The tensile stress-strain relationship of the HSFRC was obtained from the CMOD test results and inverse analysis, incorporating the load-CMOD curve. The tensile stress-strain relationship of the HSFRC was modeled with a linear elastic relationship and a softening relationship, as suggested by the Association Française de Génie Civil (AFGC) design recommendations [31]. The tensile stress-strain relationship of rebar was obtained from the tension test. The bilinear model shown in Figure 16 was used for rebar.
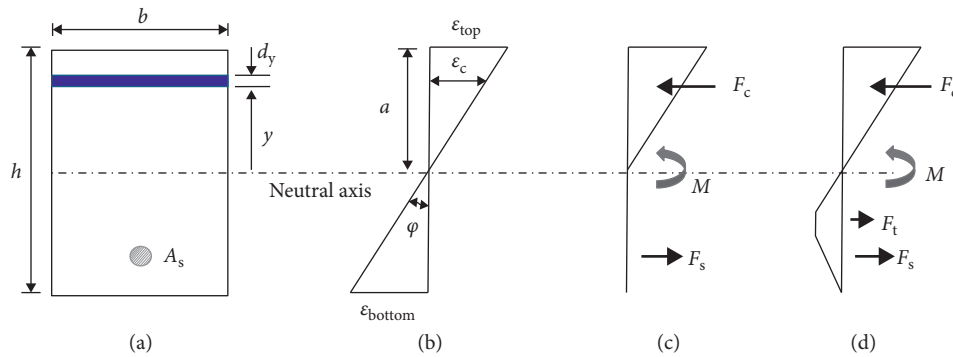
FIGURE 14: Strain and stress distributions in the section: (a) cross section; (b) strain distribution; (c) stress distribution of HSC; (d) stress distribution of HSFRC.
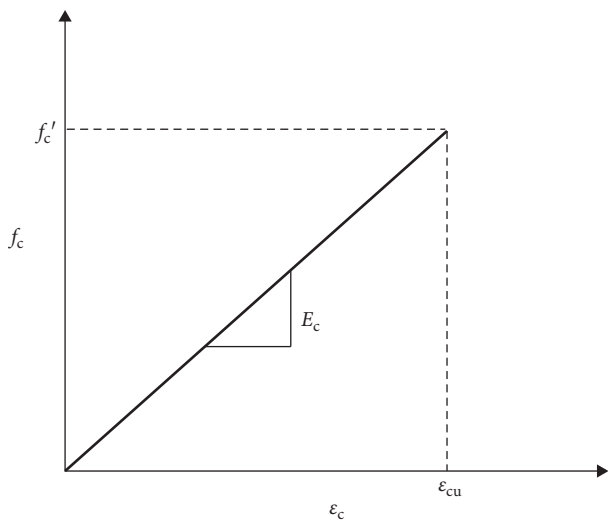
FIGURE 15: Compressive stress-strain relationship model of concrete for HSC and HSFRC.
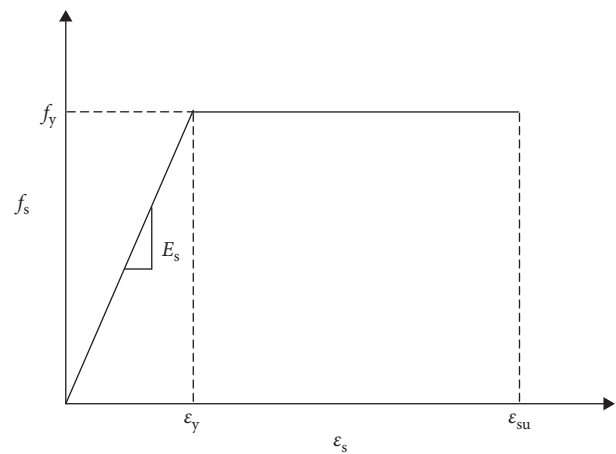
FIGURE 16: Tensile stress-strain relationship model of rebar.

The sectional force can be calculated with the calculation of stress for each layer. For the H100 and H120 series beams, tensile stresses were ignored in the calculation of the sectional force, but for the HF120 series beams, tensile stresses were considered in this calculation. The sum of the sectional forces in the whole layer must satisfy the equilibrium condition of the forces. The bending moment can be calculated based on the stress distribution along the cross section, satisfying the equilibrium condition of the forces.

The maximum bending moment from the test results and section analysis for each member is listed in Table 4. The ratio of the analyzed value to the measured value for the entire member was between 0.99 and 1.19, and the mean value of the ratios was 1.09. A simplified material law was adopted for the rebar by assuming horizontal linear behavior after the yielding point, as shown in Figure 16. In reality, the postyielding behavior of the rebar should be represented by a slightly ascending line resulting from the strain hardening of rebar. Both concrete and rebar contributed to the bending moment resistance. The compressive strength of the HSFRC was greater than that of the HSC, and the tensile strength of the HSFRC was also considered in integrating the stresses

TABLE 4: Test and analytical results.

| Member | Bending strength | | Ratio (1)/(2) |
	Test result (1) kN·m	Analytical result (2) kN·m	
H100-R1	57.2	50.6	1.13
H100-R2	83.8	72.6	1.15
H100-R3	104.8	94.2	1.11
H120-R1	59.6	50.0	1.19
H120-R2	79.3	71.6	1.11
H120-R3	102.1	94.1	1.08
HF120-R1	89.6	87.1	1.03
HF120-R2	111.0	111.6	0.99
HF120-R3	142.1	135.1	1.05
Mean			1.09

over the depth. This implies that, compared to concrete, the relative contribution of the rebar to bending moment capacity was lower in the HSFRC beams than in the HSC beams. Therefore, the consideration of strain hardening might lead to a greater difference between the prediction and test result of the bending moment for the HSC beams than for the HSFRC beams and to the underestimation of the

predicted bending moment for the HSC beams. The maximum bending moment of the HSFRC beams was more accurately estimated than those of the other series beams. Therefore, using this method to predict the bending strength was suitable for the HSFRC beams.

5. Conclusions

A comparative experimental study on the flexural behavior of HSFRC and HSC beams was carried out in this study. The following conclusions are drawn from the experimental results:

(1) The cracks propagated more deeply into the compressive zone in the HSC beam than in the HSFRC beam because the steel fibers arrested the crack propagation in the HSFRC beams. In addition, the crack width in the HSFRC beams was much smaller than that in the HSC beams.

(2) The failure of the HSC beams occurred by the sudden crushing of concrete in the compressive zone after the rebar yielded. On the other hand, the failure of the HSFRC beams typically resulted from the steel fiber pulling out of the concrete matrix along the major cracks.

(3) At the same rebar ratio, the crack stiffness of the HF120 series beams (HSFRC) was much greater than those of the H100 and H120 series beams (HSC). Therefore, the test results showed that the use of HSFRC significantly improved the crack stiffness of the concrete beams.

(4) The ductility index of the HSC beams decreased sharply with the increase in the rebar ratio. However, the ductility of the HSFRC beams slightly increased with the rebar ratio. In addition, HSFRC developed better and more consistent ductility with the increase of rebar ratio.

(5) The flexural toughness of the HSC beam was greater than that of the HSFRC beam at the low rebar ratio. However, the flexural toughness of the HSFRC beams was greater than that of the HSC beams at the higher rebar ratios. Therefore, the application of higher rebar ratios would be effective to improve the energy absorption capacity of HSFRC structures.

Data Availability

The data used to support the findings of this study are available from the corresponding author upon request.

Conflicts of Interest

The authors declare that they have no conflicts of interest.

Acknowledgments

References

[1] L. S. Hsu and C.-T. T. Hsu, "Complete stress-strain behavior of high strength concrete under compression," *Magazine of Concrete Research*, vol. 46, no. 169, pp. 301–312, 1994.

[2] T. H. Wee, M. S. Chin, and M. A. Mansur, "Stress-strain relationship of high-strength concrete in compression," *ASCE Journal of Materials in Civil Engineering*, vol. 8, no. 2, pp. 70–76, 1996.

[3] S. Sarkar, O. Adwan, and J. G. L. Munday, "High strength concrete: an investigation of the flexural behavior of high strength RC beams," *Structural Engineer*, vol. 75, no. 7, pp. 115–121, 1997.

[4] K. H. Min, H. C. Jung, J. M. Yang, and Y. S. Yoon, "Shrinkage characteristics of high-strength concrete for large underground space structures," *Tunneling and Underground Space Technology*, vol. 25, pp. 108–113, 2010.

[5] J. C. M. Ho, J. Y. K. Lam, and A. K. H. Kwan, "Effectiveness of adding confinement for ductility improvement of high-strength concrete columns," *Engineering Structures*, vol. 32, pp. 714–725, 2010.

[6] S. W. Shin, S. K. Ghosh, and J. Moreno, "Flexural ductility of ultra-high-strength concrete members," *ACI Structural Journal*, vol. 86, no. 4, pp. 394–400, 1989.

[7] M. A. Mansur, M. S. Chin, and T. H. Wee, "Flexural behavior of high-strength concrete beams," *ACI Structural Journal*, vol. 94, no. 6, pp. 663–674, 1997.

[8] S. A. Ashour, "Effect of compressive strength and tensile reinforcement ratio on flexural behavior of high-strength concrete beams," *Engineering Structure*, vol. 22, no. 5, pp. 413–423, 2000.

[9] M. A. Rashid and M. A. Mansur, "Reinforced high-strength concrete beams in flexure," *ACI Structural Journal*, vol. 102, no. 3, pp. 462–471, 2005.

[10] M. Mohammadhassani, S. Akib, M. Shariati, M. Suhatril, and M. M. A. Khanouki, "An experimental study on the failure modes of high strength concrete beams with particular references to variation of the tensile reinforcement ratio," *Engineering Failure Analysis*, vol. 41, pp. 73–80, 2014.

[11] P. Richard and M. Cheyrezy, "Composition of reactive powder concrete," *Cement and Concrete Research*, vol. 25, no. 7, pp. 1501–1511, 1995.

[12] B. A. Graybeal, "Material property characterization of ultra-high performance concrete," Tech. Rep. FHWA-HRT-06-103, FHWA, U.S. Department of Transportation, McLean, VA, p. 186, 2006.

[13] A. Abrishambaf, M. Pimentek, and S. Nunes, "Influence of fibre orientation on the tensile behaviour of ultra-high performance fibre reinforced cementitious composites," *Cement and Concrete Research*, vol. 97, pp. 28–40, 2017.

[14] S. T. Kang and J. K. Kim, "Investigation on the flexural behavior of HSFRCC considering the effect of fiber orientation distribution," *Construction and Building Materials*, vol. 28, pp. 57–65, 2012.

[15] H. Al-Mattarneh, "Electromagnetic quality control of steel fiber concrete," *Construction and Building Materials*, vol. 73, no. 30, pp. 350–356, 2014.

[16] B. Akcay and M. A. Tasdemir, "Mechanical behavior and fiber dispersion of hybrid steel fiber reinforced self-compacting concrete," *Construction and Building Materials*, vol. 28, no. 1, pp. 287–293, 2012.

[17] I. H. Yang, C. B. Joh, and B. S. Kim, "Flexural response predictions for ultra-high-performance fiber-reinforced concrete beams," *Magazine of Concrete Research*, vol. 64, no. 2, pp. 113–127, 2012.

[18] Q. Chunxiang and I. Patnaikuni, "Properties of high-strength steel fiber-reinforced concrete beams in bending," *Cement and Concrete Composites*, vol. 21, no. 1, pp. 73–81, 1999.

[19] J. Z. Su, B. C. Chen, and Q. W. Huang, "Experimental studies on the flexural behavior of HSFRC beams," in *Proceedings of AFGC-ACI-fib-RILEM International Symposium on Ultra-High Performance Fibre-Reinforced Concrete, UHPFRC*, Montpellier, France, October 2017.

[20] Q. Guan, P. Zhang, and X. Xie, "Flexural behavior of steel fiber reinforced high-strength concrete beams," *Research Journal of Applied Sciences, Engineering and Technology*, vol. 6, no. 1, pp. 1–6, 2013.

[21] H. C. Mertol, E. Baran, and H. J. Bello, "Flexural behavior of lightly and heavily reinforced steel fiber concrete beams," *Construction and Building Materials*, vol. 98, pp. 185–193, 2015.

[22] L. Chen and B. A. Graybeal, "Modeling structural performance of ultrahigh performance concrete I-girders," *Journal of Bridge Engineering*, vol. 17, no. 5, pp. 754–764, 2012.

[23] B. I. Bae, H. K. Choi, and C. S. Choi, "Flexural strength evaluation of reinforced concrete members with ultra high performance concrete," *Advances in Materials Science and Engineering*, vol. 2016, Article ID 2815247, 10 pages, 2016.

[24] X. Ning, Y. Ding, F. Zhang, and Y. Zhang, "Experiment study and prediction for flexural behavior of reinforced SCC beam containing steel fibers," *Construction and Building Materials*, vol. 93, pp. 644–653, 2015.

[25] RILEM TC 162-TDF, "Test and design methods for steel fiber reinforced concrete; bending test-final recommendation," *Material and Structures*, vol. 35, no. 253, pp. 579–582, 2002.

[26] T. H. K. Kang, W. Kim, Y. K. Kwak, and S. G. Hong, "Flexural testing of reinforced concrete beams with recycled concrete aggregates," *ACI Structural Journal*, vol. 111, no. 3, pp. 607–616, 2014.

[27] M. Singh, A. H. Sheikh, M. S. Mohamed Ali, P. Visintin, and M. C. Griffith, "Experimental and numerical study of the flexural behaviour of ultra-high performance fibre reinforced concrete beams," *Construction and Building Materials*, vol. 138, pp. 12–25, 2017.

[28] I. H. Yang, C. Joh, and B. S. Kim, "Structural behavior of ultra high performance concrete beams subjected to bending," *Engineering Structures*, vol. 32, pp. 3478–3487, 2010.

[29] A. N. Dancygier and Z. Savir, "Flexural behavior of HSFRC with low reinforcement ratios," *Engineering Structures*, vol. 28, pp. 1503–1512, 2006.

[30] L. Biolzi and S. Cattaneo, "Response of steel fiber reinforced high strength concrete beams: experiments and code predictions," *Cement and Concrete Composites*, vol. 77, pp. 1–13, 2017.

[31] AFGC, *Ultra High Performance Fibre-Reinforced Concretes*, Association Française de Génie Civil (AFGC), Paris, France, 2013.

Research Article

Design and Climate-Responsiveness Performance Evaluation of an Integrated Envelope for Modular Prefabricated Buildings

Junjie Li [iD],[1] **Shuai Lu** [iD],[2] **Wanlin Wang,**[1] **Jie Huang,**[1] **Xinxing Chen,**[1] **and Jiayi Wang**[1]

[1]*School of Architecture and Design, Beijing Jiaotong University, Beijing 100044, China*
[2]*School of Architecture and Urban Planning, Shenzhen University, Shenzhen 518060, China*

Correspondence should be addressed to Shuai Lu; lyushuai@szu.edu.cn

Modular prefabricated buildings effectively improve the efficiency and quality of building design and construction and represent an important trend in the development of building industrialization. However, there are still many deficiencies in the design and technology of existing systems, especially in terms of the integration of architectural performance defects that cannot respond to occupants' comfort, flexibility, and energy-saving requirements throughout the building's life cycle. This research takes modular prefabricated steel structural systems as its research object and sets the detailed design of an integrated modular envelope system as the core content. First, the researcher chose two types of thermal insulation materials, high insulation panels and aerogel blankets, in order to study the construction details of integrated building envelopes for modular prefabricated buildings. Focusing on the weakest heat point, the thermal bridge at the modular connection point, this work used construction design and research to build an experimental building and full-scale model; the goal was to explore and verify the feasibility of the climate-responsive construction technique called "reverse install." Second, as a response to climate change, building facades were dynamically adjusted by employing different modular building envelope units such as sunshades, preheaters, ventilation, air filtration, pest control, and other functional requirements in order to improve the building's climate adaptability. Finally, based on the above structural design and research, this study verified the actual measurements and simulation, as well as the sustainability performance of the structure during the operational phase, and provided feedback on the design. The results highlight the environmental performance of each construction detail and optimized possibilities for an integrated envelope design for modular prefabricated buildings during both the design and renovation phases.

1. Introduction

1.1. Research Background. The energy and environmental crisis of the 1970s gave birth to a global awareness of and widespread attention to the issue of sustainable development [1]. In this context, the field of architecture has also expanded, and sustainable architecture has become an important and rapidly developing research proposition [2]. Owing to the environment's potential for sustainability, society's needs, and certain economic aspects (such as saving construction time, improving building quality, reducing material waste, alleviating environmental loads, and reducing cost) [3–5], prefabricated buildings have become an important research

topic in sustainable architecture, now playing an essential role in Western urban construction [6, 7].

Modularization is one means of operation in the manufacture of industrial products. Its production efficiency and delicacy are well established in production [8, 9]. If we look at the problem of building industrialization with an eye towards product manufacture, modular design, and the overall construction methodology, most components are prefabricated at the factory and assembled on-site. In such cases, building space is integrated, construction time is minimized, and on-site construction errors are reduced (as shown in Figure 1) [10, 11]. Modular design also embodies the concept of sustainable development and "green" construction. However,
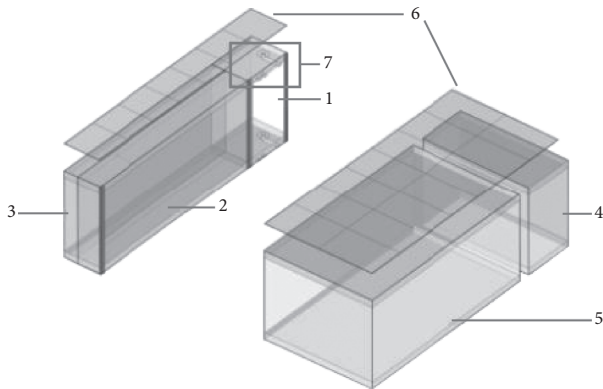
FIGURE 1: Modular prefabricated building prototype (source: authors' own data).

FIGURE 2: Hoisting and installation of a modular prefabricated building prototype (source: authors' own data).

there are currently many deficiencies in both the design and certain technical aspects of the existing system [12], especially with regard to defects in architectural performance and integrated design (as shown in Figure 2). Currently, they cannot respond to occupants' requirements for comfort, flexibility, and energy-saving throughout the building's life cycle [13].

The form of the building envelope has a decisive influence on building performance during the operating phase; it is also one of the most important elements of modular prefabricated buildings [14]. Therefore, this research focused on the sustainability-related performance of modular prefabricated buildings, mainly exploring the construction details of integrated building envelopes and their climate responsiveness.

A master of modernist architecture Le Corbusier first proposed the idea of a "drawer-type residence" in 1947. This served to introduce the topic of modularization and standardization in building design (as shown in Figure 3) [15]. In the 1960s, a Dutch scholar named Habraken proposed the notion of open architecture, creating the SI housing system for residential architecture [16]. The effective separation of S (the skeleton) and I (the infill) led to houses that offered structural durability, flexibility in the indoor space, and quality filling [17]. The German and American architects, Konard Wachsmann and Walter Gropius, respectively, jointly developed the assembly-type General Panel System in 1945. According to the modules, these buildings were decomposed into composite panels, thermal insulation, inside and outside walls, floors, ceiling, roofs, and so on. These architects also developed
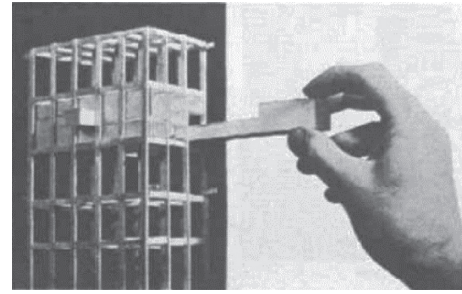
FIGURE 3: Le Corbusier: drawer-type residence (source: [15]).

a connection node system between the plates to meet the requirements of rapid development and system expansion [18, 19]. Ochs invented a prefabricated timber structural envelope module to integrate active equipment such as microheat pumps and full heat exchangers into single building components [20]. The design not only saved time and labor during the construction phase but also satisfied the energy-saving and thermal comfort aspects of building performance [21].

1.2. Objective of This Study. This research focused on the construction details, design, and effective evaluation of integrated building envelopes for modular prefabricated buildings. Three goals were pursued: (1) to use a rational integrated building envelope design to improve the physical environment and energy-saving performance during a modular prefabricated building's operational phase, (2) to resolve weaknesses related to thermal bridges at the connection points of modular prefabricated buildings and advance their sustainable performance during the operational phase, and (3) to improve the climate adaptability capacity of the overall building environment by optimizing the design of integrated building envelopes.

2. Methodology

This research examined modular prefabricated buildings with steel structural systems and set the details of an integrated module design for an envelope system as the core content. Buildings with steel structures offer advantages during prefabrication, transportation, modular hoisting, and installation and thus are the preferred structural system in prefabricated architecture [22]. However, compared with PC and wooden structural systems, the heat transferability of steel structures is stronger and faster, obvious disadvantages in terms of thermal insulation performance [23]. Therefore, this research chose two types of thermal insulation materials, high insulation panels (HIPs) and aerogel blankets (ABs), to study the construction details of integrated building envelopes for modular prefabricated buildings. Focusing on the weakest heat points, the thermal bridges at modular connection points, this study employed construction detail design and research to build an experimental building and full-scale building model. The goal was to explore and verify the feasibility of the climate-responsive construction detail technique called "reverse install." Moreover, the envelope's structural component system featured modularization,
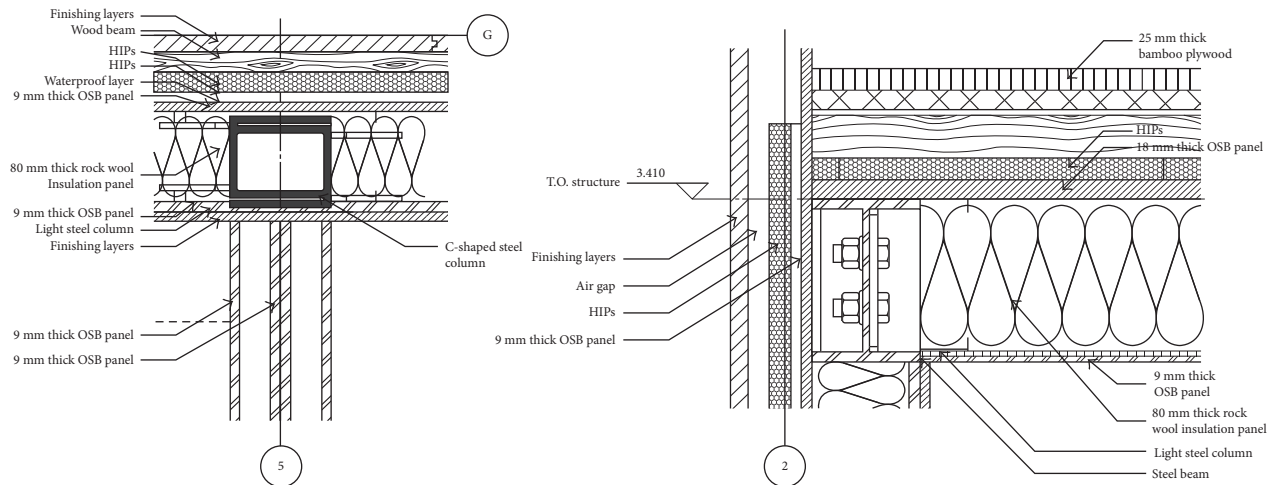
Figure 4: Exterior wall construction detail using the HIP's insulation layer (source: authors' own data).

standardization, and prefabrication [24], characteristics that can be optimized for climate responsiveness. To accommodate new needs stemming from climate change, building facades were dynamically adjusted by using different modular building envelope units, including sunshades, preheaters, ventilation, air filtration, pest control, and other functional requirements. The goal was to improve the building's performance related to climate adaptability. Based on the above structural design and research, this study verified the actual measurements and simulation, as well as the sustainability performance of the construction during the operational phase, and provided design feedback.

2.1. The Reverse Install Integrated Building Insulation Envelope Technique

2.1.1. Using HIPs to Improve Heat Preservation and Solve the Thermal Bridge Problem. Research on ultra-thin vacuum insulation panels began in Europe in 1972. At first, this type of insulation was primarily used for heat preservation in transportation equipment, sophisticated cold storage machinery, and so on. As the research developed, the panels were increasingly applied in the field of architecture, to floors, doors and windows, roofs, interior walls, and building exteriors [25]. HIPs are composed of two parts: a high barrier composite film and the core material. The high barrier composite membrane comprised inorganic fiber cloth, a multilayer aluminum foil, and a multilayer compact material that protects and affixes the HIPs. The high-quality barrier diaphragm guarantees the service life. The core material is made up of porous inorganic substances such as nanometer-superfine silica. The porous structure of the vacuum is beneficial in facilitating low thermal conductivity [26].

The wall construction details for the building used in this research, from inside to outside, were as follows: the interior panel was a 9 mm thick OSB panel that served as a structural layer. There was also a light steel structural infill with an 80 mm thick rock wool insulation panel.

Figure 5: Building's exterior wall with HIPs employed during the building process (source: authors' own data).

There was another 18 mm thick OSB panel that also served as a structural layer, and a waterproof layer composed of a 15 mm thick double-layer HIP with a wood keel and an air gap exterior panel [27], as shown in Figure 4. The building used a 300 mm module, which included the axis, size of the openable doors and windows, and vertical dimensions of the building. Therefore, the HIP dimensions were also controlled according to the following four types: 300 mm × 300 mm, 300 mm × 600 mm, 300 mm × 400 mm, and 400 mm × 600 mm (as shown in Figure 5).

Different from the other ordinary aspects of envelope construction, modular connections must be installed after the module is transported to the site. Installation relies on an integrated envelope panel to improve construction efficiency. Therefore, an integrated envelope unit must first be constructed in a factory, according to the following steps: the OSB panel is used as the basement material, and the HIP's insulation layer is attached to the OSB, with the keel frame in between. It is then covered with a layer of finishing material, while the other side of the OSB is covered with a waterproof layer. Then, the integrated envelope units (including the structural, insulation, moistureproofing, and finishing layers) are installed entirely as a hanging board at the module's connection point (as shown in Figure 6).
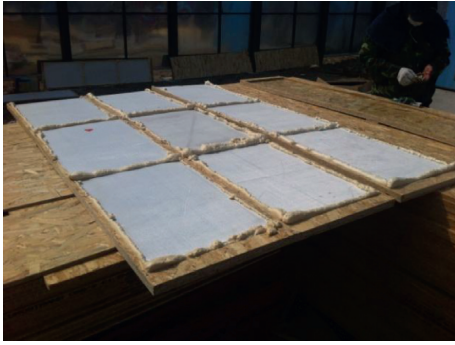
Figure 6: Reverse install integrated building insulation envelope technique (source: authors' own data).

2.1.2. Using ABs to Improve Heat Preservation and Solve the Thermal Bridge Problem

(1) Integrated Building Envelope Using ABs. In 1931, the American researcher S. Kistler developed silica aerogels via an ethanol-based supercritical drying technique. In the 1970s and 1980s, aerogel was used in Cherenkov detectors and to store rocket fuel. In the 1990s, the material was employed as heat insulation for the space shuttle and in US jet propulsion laboratories [28]. In architecture, aerogel is of interest because of the microvoid nanometer-restrained heat transfer of air molecules. Also, the refractive index of silica aerogel is close to 1, and the ratio of the extinction coefficient to infrared and visible light is more than 100; the result is the effective pass-through of sunlight, preventing infrared radiation and related increases in ambient temperature. Therefore, aerogels have become an ideal transparent insulation material, applied in both solar energy utilization and building energy conservation [29]. By means of synthetic methods, aerogel can be combined with glass fiber cotton or preoxidized fiber felt. AB's thermal conductivity can be as low as 0.015 W/(m·K) at a normal temperature and atmospheric pressure. Compared with traditional materials, the thermal conductivity of AB is three to five times better than rock wool of the same thickness [30]. In addition, AB offers certain advantages such as A1 fire protection; it is also easy to cut, lightweight, and has a high hydrophobicity and thus is the insulation material most suitable for prefabricated buildings (as shown in Figure 7).

The construction details of the building envelope using AB as insulation were as follows: a 15 mm thick OSB panel was used as the basement material, and a 10 mm thick AB was attached to the OSB structural layer. The other side of the OSB was attached with a waterproof layer, an upper layer covered with keel, and an exterior finishing layer (as shown in Figures 8 and 9). Since the AB layer had no size constraints, the size of the thermal insulation material could be adjusted according to the modular building's modules.

(2) Design for Thermal Bridge Prevention at Module Connection Points. When the four corners of a module are supported by steel columns and double-steel columns are used at the connection points of a building module, the two modules must be spliced. In the absence of a well-designed

thermal insulation, the steel columns may be directly exposed to the outside on the integrated external wall. This can lead to weaknesses in the thermal bridge to the building environment. A detailed construction plan designed to avoid this weakness must be based on the basic modules of the building and an integrated building envelope unit; after the two building modules are assembled on-site, these modules will hang on the construction. In this case study, the integrated building envelope unit was 600 mm at the two building modules' connection points, as determined by the experimental building's module size. The specific process used a reverse install technique to attach the AB, waterproof layer, keel, and exterior finishing layer to the OSB structural layer. After the integrated envelope unit was constructed, it was installed with the reserved connecting piece of the main steel beam structure and fastened with self-tapping nails. This method integrated the structural, thermal insulation, moisture-proofing, and exterior finishing layers into a single unit, which will be beneficial in the multiple assemblies and disassemblies that often accompany prefabricated buildings (as shown in Figures 10 and 11).

2.2. Replaceable Modules Based on Climate Adaptation.

There are two kinds of climate regulation characteristics related to building envelopes and the spaces they form: climate defense and climate utilization. Climate defense reflects the "buffer" strategy of auxiliary functional space, while climate utilization refers to the dynamic regulation of the joint actions of the building's envelope and space. Thomas Herzog believed that architecture's form can be conceptualized as similar to human skin, and the internal function can be understood like bones. The clothing people wear, its different styles and materials, expresses human diversity and societal individuality. Clothing and building envelopes are similar in that they are both public and private "interfaces" [32]. A building's envelope contains a variety of mass flows and therefore requires multiple functions [33]. According to the time, climate, status of use, and other factors, a building skin incorporates a combination of functions, some complementary and some in competition with one another, including sight penetration, sight view, natural lighting, shading, heat preservation, heating, ventilation, air filtration, natural risk barriers, sound insulation, and climatic buffers.

The southern-facing outer layer of a building's double-skin facade (DSF) was designed and studied in this research. Various replaceable modular designs based on climate adaptation and occupants' requirements were imparted to the outer interface [34, 35]. In the southern facade's vertical direction, the outer interface of the DSF was divided into three segments from bottom to top (according to the human scale and occupant requirements); these included the protected, sight, and shading zones (as shown in Figure 12). The aluminum material panel provided the possibility of numerically controlling the machined processing of the outer layer. Through a computer parameterization algorithm, the bottom of the facade's outer layer (called the protected zone) was designed to be the smallest aperture; this was to guarantee the sturdiness and compactness of the

(a)   (b)   (c)   (d)
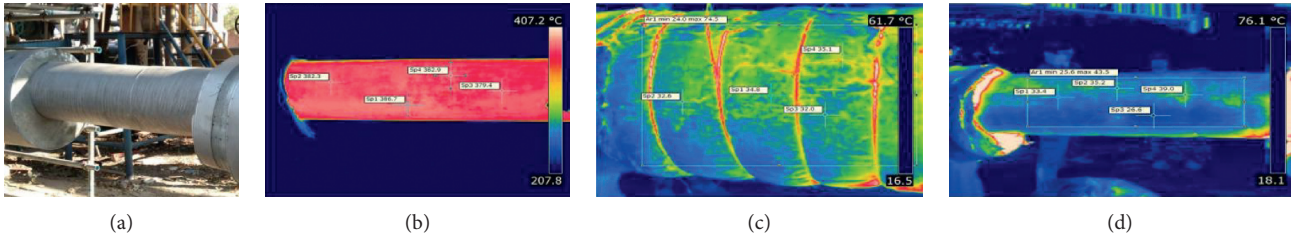
FIGURE 7: Contrast of infrared imaging with the rock wool panel and AB as insulation materials (source: [31]). (a) Pipe photo, (b) infrared thermal imaging of the pipe, (c) rock wool panel as the insulation layer, and (d) AB as the insulation layer.

Bamboo veneer (16 mm)

Wood joist (20*20 mm)

Water-resistive weather barriers

OSB board (15 m)

Thermal insulation aerogel (10 mm)

Thermal insulation (80 mm)

Thermal insulation aerogel (10 mm)

OSB board (15 mm)

Wallpaper
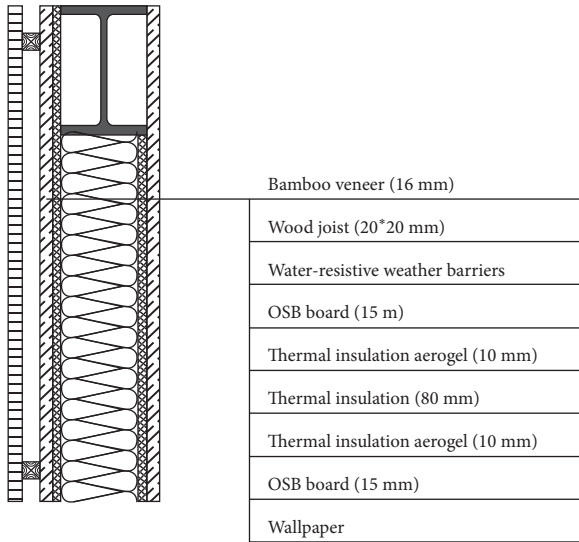
FIGURE 8: Construction design detail of an exterior wall using AB as the insulation material (source: authors' own data).

FIGURE 9: Full-scale model (source: authors' own data).

building's envelope and also to prevent natural creatures near the ground from entering into the building through the hole. The middle of the outer layer, 60 degrees up and down to a height of 1.7 m, was considered the sight zone, with larger holes to ensure users have an adequate view. The southern facade also needed to consider shading during the

summer. Therefore, the hole size was reduced at the upper part of the interface, which prevented excessive solar radiation from entering.

The climate adaptation design is also embodied in the opening mode of the DSF interface. The outer interface could turn from 0 to 90 degrees by using an intermediate axis (as shown in Figure 13). In addition, in order to maximize the flexibility of the usage mode, the detailed design combined a middle axis rotating shaft together with a horizontal push-and-pull rail. Thus, the standard-sized outer interface could be completely retracted at both the western and eastern ends of the building in order to provide an unshielded view or multiple interface forms (as shown in Figure 14).

Important aspects of prefabricated buildings are the standardization and modularization of their design [36]. Besides the outer layer of the DSF, this design tested in this research was also based on the building components' standardization with multiple functions in order to realize various approaches to climate responsibility and adaptability. To achieve goals such as sight penetration and occlusion, natural lighting, shading, thermal insulation, preheating, ventilation, air filtration, the provision of natural risk barriers, sound insulation, and climate buffering, five basic facade treatments were designed: perforated aluminum plates, glass panels, air filter membranes, mosquito net panels, and AB insulation panels. The five interfaces formed a dynamic building interface with different functions that replaced more climate-orientated arrangements (as shown in Table 1). Each interface module was designed to fit the same component size, could be prefabricated as standardized in the factory, and was installed on the metal frame. There were also three trough-cable rails that could be inserted into the metal frame. With a single-slice, double-layer, or three-layer combination arrangement, users could set up these prefabricated interface modules according to their requirements, ultimately achieving a higher building environment performance (as shown in Figure 15).

3. Results and Discussion

3.1. Thermal Environment Performance Evaluation of the Integrated Building Envelope

3.1.1. Comprehensive Thermal Performance of the Integrated Building Envelope. The heat transfer coefficient of a material characterizes its heat transfer capacity, and the comprehensive heat transfer coefficient of a wall indicates the

| | | | | |
| (a) | (b) | (c) | (d) | (e) |
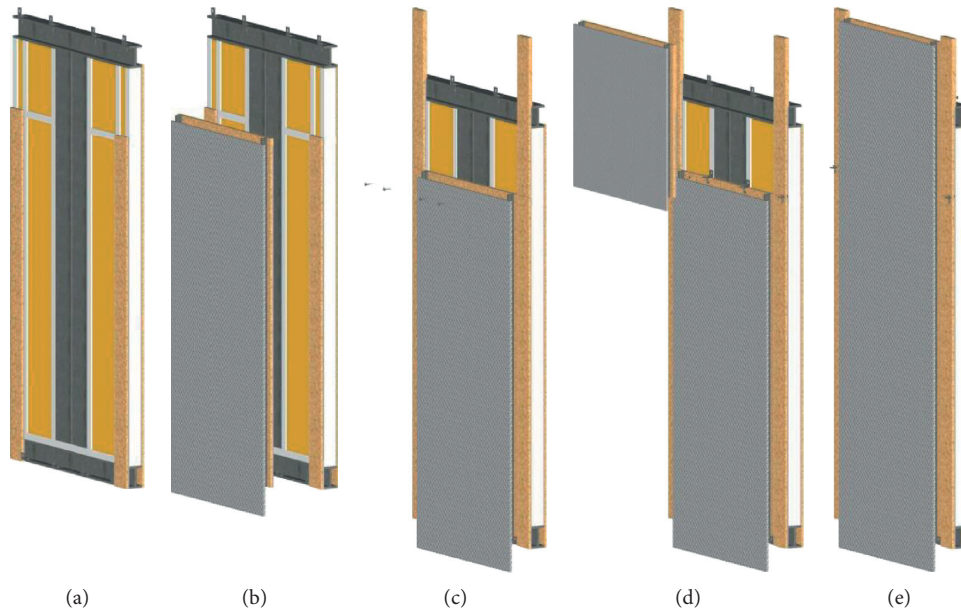
FIGURE 10: Installation instructions for an integrated building envelope using AB (source: authors' own data). (a) The foundation wall at the junction of two modules; (b) integrated wall including exterior decoration, heat preservation, and structural plates; (c) fix integrated wallboard by self-tapping pin; (d) install the upper (parapet) wall; (e) finish.

FIGURE 11: Full-scale model and connection details (source: authors' own data).
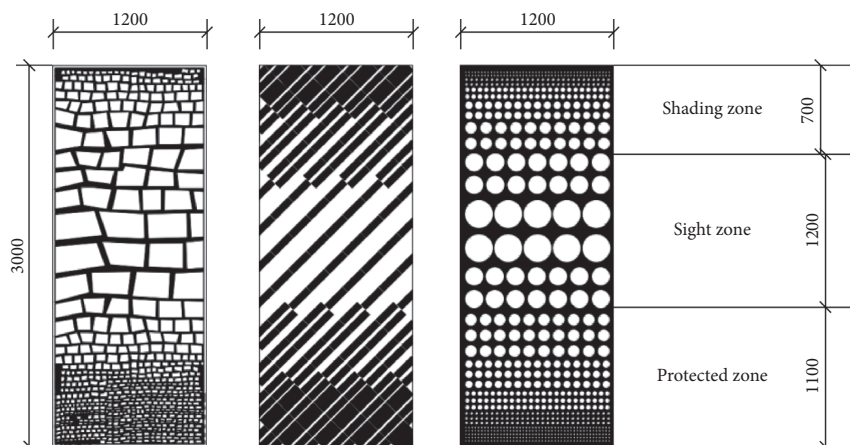
FIGURE 12: Vertical division of the sample outer layer (source: authors' own data).
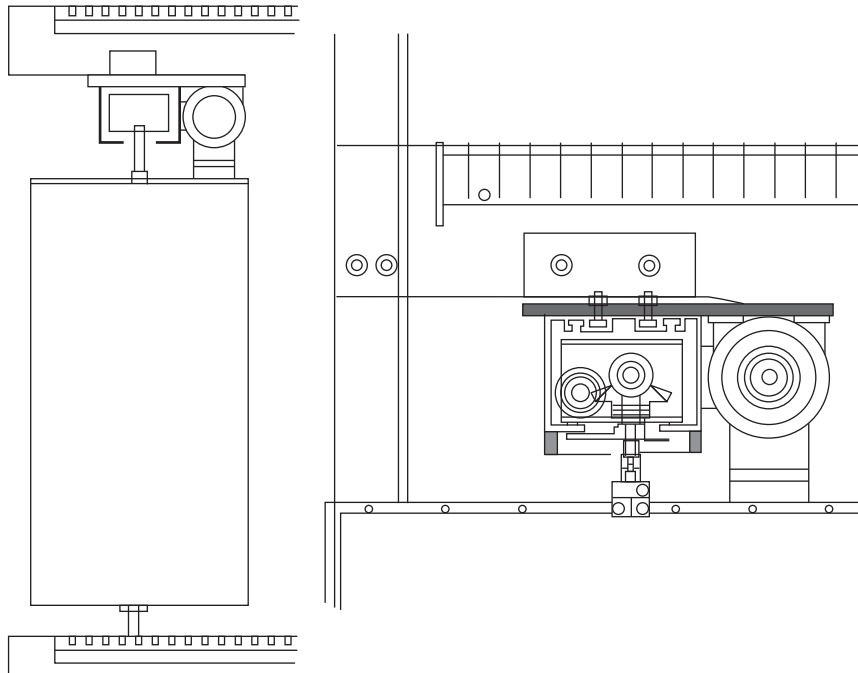
FIGURE 13: Detailed design of a combined middle axis rotating shaft and horizontal push-and-pull rail (source: authors' own data).
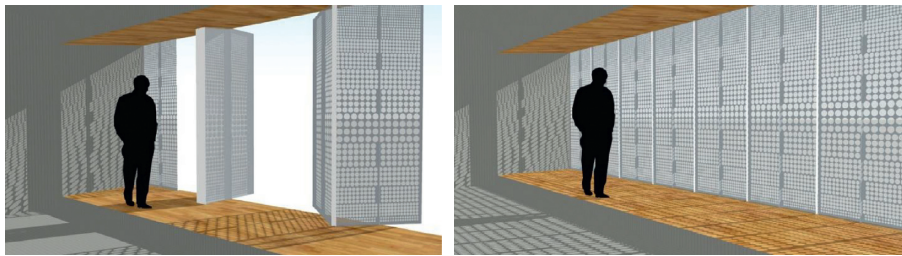
FIGURE 14: A combined middle axis rotating shaft and horizontal push-and-pull rail to realize multiple interface forms (source: authors' own data).

thermal insulation performance of a building. According to the official Chinese standard in the *Design Standard for Energy Efficiency of Public Buildings*, if a building's shape coefficient is less than 0.30, the heat transfer coefficient of the exterior wall should be no higher than $0.50\,W/(m^2 \cdot K)$. If a building's shape coefficient is between 0.30 and 0.50, the heat transfer coefficient of the exterior wall should be no higher than $0.45\,W/(m^2 \cdot K)$ in cold climate zones [37]. If a building's shape coefficient is less than 0.30, the heat transfer coefficient of the building's roof should be no higher than $0.45\,W/(m^2 \cdot K)$. If the building's shape coefficient is between 0.30 and 0.50, the heat transfer coefficient of the building's roof should be no higher than $0.40\,W/(m^2 \cdot K)$ in cold climate zones [37]. The comprehensive heat transfer coefficient achieved by using two kinds of thermal insulation is shown in Table 2. As compared to the national standard, the heat transfer coefficient achieved when using HIPs as the insulation material was calculated as saving 73%~76%. The heat transfer coefficient achieved by using ABs as the thermal insulation material was 43%~49%, as compared to the national standard.

The equation for calculating the comprehensive heat transfer coefficient of a building's exterior (nontranslucent) envelope is shown here as (1). Therefore, the comprehensive heat transfer coefficient, K_0, of the external walls and roofs, based on the two kinds of thermal insulation materials, can be calculated as shown in Table 2:

$$K_0 = \frac{1}{\sum R_0} = \frac{1}{R_i + R_n + R_e}$$

$$= \frac{1}{R_i + (\delta_1/\lambda_1) + (\delta_2/\lambda_2) + (\delta_3/\lambda_3) + \cdots + (\delta_n/\lambda_n) + R_e},$$
(1)

where R_i is the heat transfer resistance value of the inner surface. According to the shape relation of the building and climate conditions, the value can be obtained as $0.11\,m^2 \cdot K/W$. The variable R_n represents the comprehensive heat transfer resistance of the wall, and R_e is the heat transfer resistance value of the outer surface. According to the surface features of the building and the climatic conditions, the value can be obtained as $0.05\,m^2 \cdot K/W$. The variable

TABLE 1: Dynamic combinations of replaceable interface modules.

Layer	Number	Component	Function
Single slice	1	Perforated aluminum plate	Building facade, sun shading, natural risk barrier, sight penetration, and sight occlusion
	2	Glass panel	Buffer layer forming a double curtain wall to preheat the indoor space during winter
	3	Mosquito net panel	Insect barrier and ventilation
Double layer	4	Perforated aluminum plate + mosquito net panel	Building facade, sun shading, insect barrier, sight penetration, sight occlusion, and ventilation
	5	Perforated aluminum plate + air filter membrane	Building facade, sun shading, natural risk barrier, sight penetration, sight occlusion, and air purification
	6	Glass panel + mosquito net panel	Moderate ventilation and heat preservation during transition seasons
	7	Perforated aluminum plate + perforated aluminum plate	Composite interface to adjust building illumination
Triple layer	8	Perforated aluminum plate + AB insulation panel + perforated aluminum plate	A buffer layer to improve thermal insulation during winter nights
	9	Glass panel + mosquito net panel + air filter membrane	Sight penetration, moderate heat preservation, air filtration, and an insect barrier for transition seasons
	10	Perforated aluminum plate + AB insulation panel + glass panel	Integrated design of the building facade, sun shading, heat preservation, and preheating buffer zone
	11	Perforated aluminum plate + AB insulation panel + air filter membrane	Building facade, sun shading, heat preservation, and air filtration
	12	Glass panel + AB insulation panel + glass panel	Buffer layer, preheating, and heat preservation, suitable for winter and nighttime in cold climate zones

Source: authors' own data.
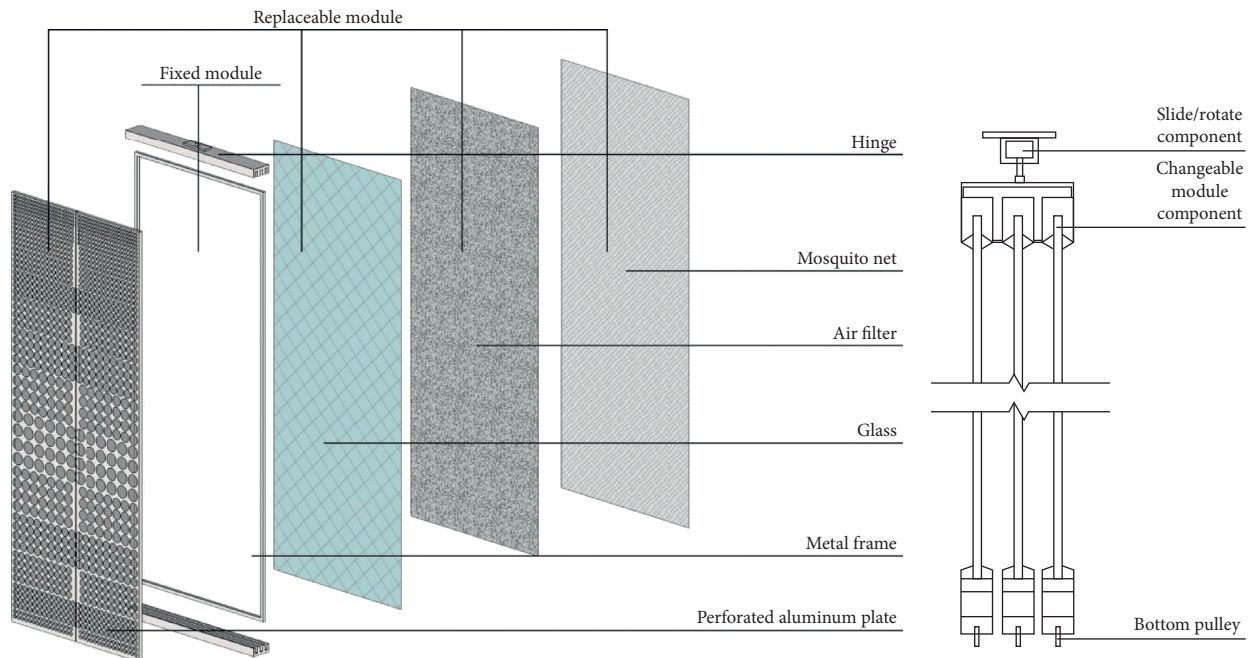
FIGURE 15: Replaceable modules based on climate adaptability (source: authors' own data).

δ represents the thickness of the material (in mm), and λ is the material's thermal conductivity (in W/(m·K))

3.2. Evaluation of the Indoor thermal Environment

3.2.1. Experimental Setup and Measurement Conditions. The building used in this experiment was located in a cold climate zone in Beijing, China. It was a net-zero independent house that had adopted a modular prefabricated building system. The shape coefficient was 0.44, and the building construction footprint was 82 m^2 (as shown in Figure 5); HIPs were used as the insulation material (as shown in Table 2) [38]. To test the effectiveness of the insulation construction detail in different climate conditions over the course of an entire year, the test period was divided into four separate phases. Together, the four phases lasted more than

TABLE 2: Heat transfer performance of the integrated envelope.

Construction details of the integrated prefabricated building envelope	Position	Construction details (from interior to exterior)	Comprehensive heat transfer coefficient of the building's exterior (nontranslucent) envelope
Using HIPs as a thermal insulation material	Exterior wall	6 mm bamboo exterior finished surface; two 15 mm layers of HIP insulation; waterproof layer; 18 mm OSB structural board; light steel structural infill with 80 mm thick rock wool insulation panel; 9 mm interior finished surface	0.124 W/(m²·K)
	Building roof	20 mm bamboo plywood surface layer; waterproofing membrane; 20 mm bamboo plywood surface layer; two 15 mm layers of HIP insulation; 18 mm OSB structural board; light steel structural infill with 140 mm thick rock wool insulation panel; 9 mm interior finished surface	0.105 W/(m²·K)
Using ABs as a thermal insulation material	Exterior wall	12 mm aluminum plastic panel with air gap; 10 mm AB insulation; waterproof layer; 18 mm OSB structural board; light steel structural infill with 80 mm thick rock wool insulation panel; 6 mm AB insulation; 9 mm OSB interior finishing board	0.257 W/(m²·K)
	Building roof	20 mm bamboo plywood surface layer; waterproofing membrane; 20 mm bamboo plywood surface layer; 10 mm AB insulation; 18 mm OSB structural board; light steel structural infill with 140 mm thick rock wool insulation panel; 6 mm AB insulation; 9 mm OSB interior finishing board	0.194 W/(m²·K)

Source: authors' own data.

TABLE 3: Building information.

Climate zone	Cold climate zone in China
Build time	2013
Surrounding environment	In sculpture park, surrounded by green space
Building area	82 m²
Building size	12.1 m (L) × 7.2 m (W) × 3 m (H)
Building storey	1 F
Building structure	Steel frame
Glazing size	South: 40 m²; north: 7.8 m²
Details and parameters	(i) Four layers of low-e insulating glass with a thickness of 5 mm/42 mm and a U-value of 0.48 W/(m²·K), a shading coefficient of 0.443 for the south glazing wall (ii) Wall material: 80 mm mineral wool + HIP, a U-value of 0.2 W/(m²·K) (iii) Roof material: 130 mm mineral wool and HIP, a U-value of 0.1 W/(m²·K) (iv) PV system: 70 m² PV panels with a capacity of 11.5 kW, thin film photovoltaic panels
Other strategies	(v) Solar thermal: solar vacuum tube collectors (vi) HVAC: WSHP (cop = 6) and ASHP (vii) Water system: membrane bioreactor water treatment technology

Source: authors' own data.

one year, beginning in the December of 2013 and ending in the January of 2015. This research selected two physical quantities, temperature and heat flux, which were determined to reflect the thermal environment quality of the building. The goal was to test the actual thermal performance of the structure during the operating phase (Table 3) [39].

3.2.2. Results and Discussion. Figure 16 shows a comparison of the building's indoor and outdoor temperatures during winter, transition seasons, and summer. Through the temperature curve, it can be seen that the outdoor temperature fluctuated conspicuously in winter. During the test period,

the highest temperature was 16°C and the lowest was −3.2°C. While the amplitude of the indoor temperature's fluctuation was very small, its actual fluctuation ranged ±3 degrees above or below 5°C. The indoor temperature was influenced very little by the external temperature, indicating the good insulation ability of the building (as shown in Figure 16(a)). During the transition season (spring), the highest outdoor temperature was 33.8°C and the lowest temperature was 6.7°C; the indoor temperature fluctuated within a range of ±6 degrees above or below 18°C (as shown in Figure 16(b)). In summer, the highest outdoor temperature was 50.3°C, while the lowest temperature was 14.1°C; this meant that the maximum temperature difference in the outdoors reached

(a)

(b)

(c)

(d)

(e)
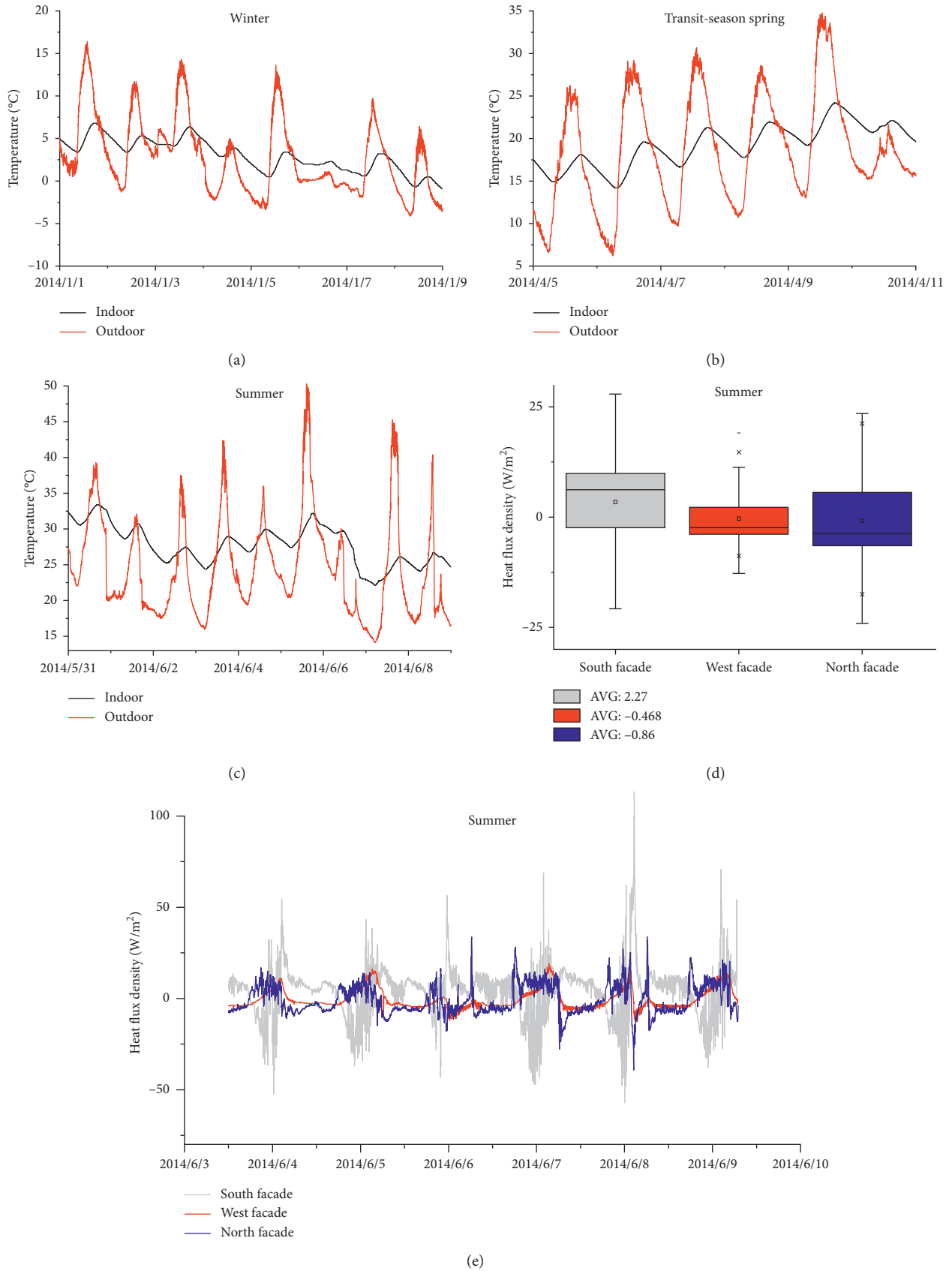
FIGURE 16: Thermal environment test of a modular prefabricated building using HIPs as the insulation material (source: authors' own data). (a) Winter temperatures; (b) transitional season temperatures; (c) summer temperatures; (d) floating box line diagram of summer heat flux density; (e) hourly curve diagram of summer heat flux density.

(a)

(b)

(c)

(d)
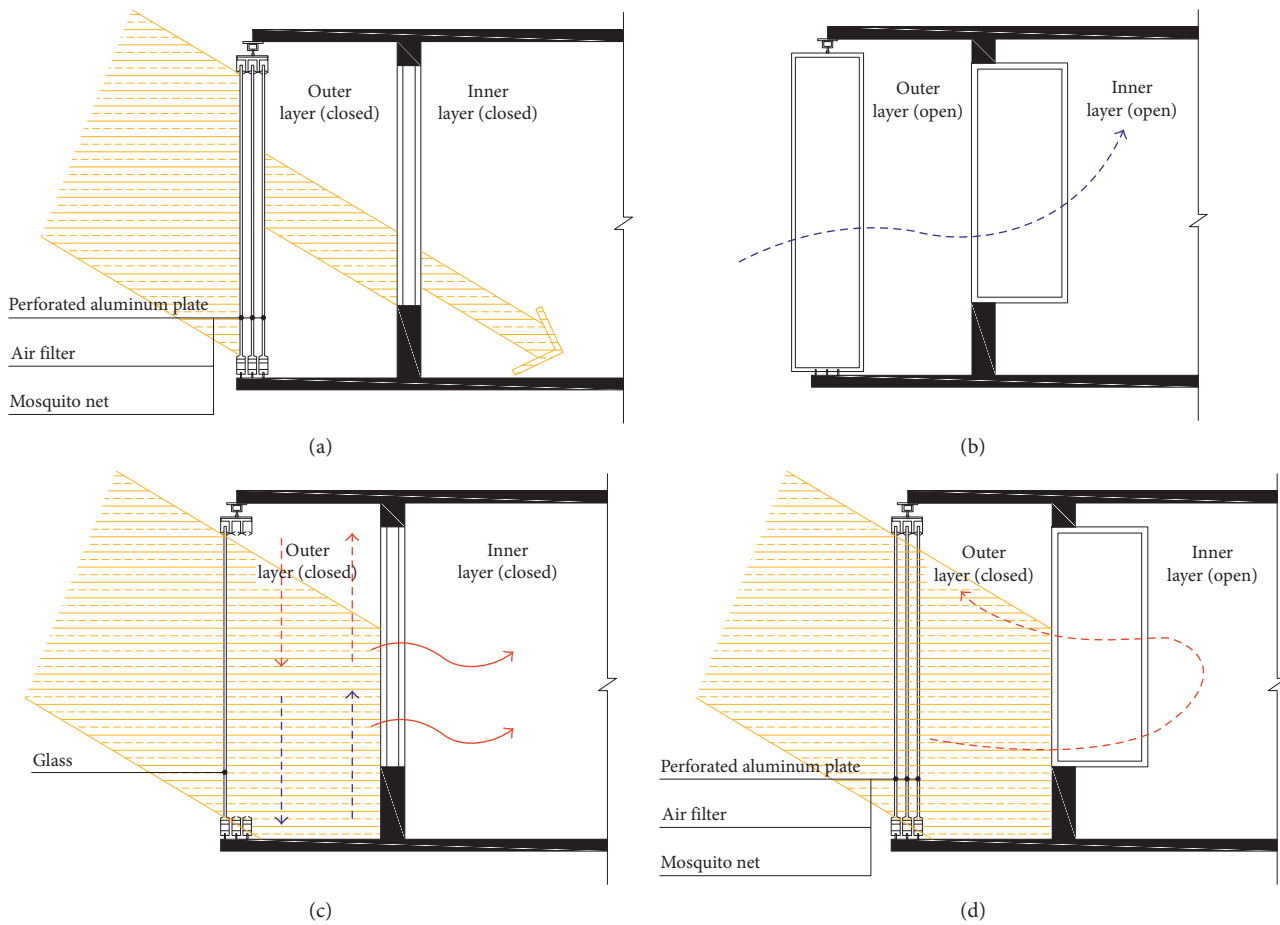
FIGURE 17: The climate adaptation mode of the integrated changeable modules throughout the building's entire life cycle (source: authors' own data). (a) Shading/air filter mode (summer day); (b) natural ventilation mode (summer night); (c) sunspace mode (winter day); (d) sunspace/air filter mode (spring and autumn days).

36.2°C, while the indoor temperature difference was only 8.5°C. This indicates the building's excellent thermal insulation performance (as shown in Figure 16(c)).

The curves in Figures 16(d) and 16(e) illustrate the heat flow densities for the test building's southern, western, and northern walls during summer weather conditions. As can be seen in Figure 16(d), although the southern facade absorbed a considerable amount of solar radiation, the difference among the average heat flux densities for the three facades was very little: southern facade $(2.27 \, \text{W/m}^2)$ > northern facade > $(0.86 \, \text{W/m}^2)$ > western facade $(0.48 \, \text{W/m}^2)$. Therefore, the overall heat gain was relatively small. Figure 16(e) illustrates the changes in the hourly heat flux density curve and thus the differences among the three facades. The fluctuation was more obvious in the southern facade than in the northern and western facades, due to the influence of summer solar radiation.

3.3. The Climate Adaptability of an Integrated Structure throughout an Entire Life Cycle.

Section 2.2 addressed an integrated changeable module facade based on a DSF. Combining the different open and closed status modes of the inner and outer layers simulated the usage pattern of the building throughout an entire year's climatic conditions. Figure 17 illustrates the four modes and all statuses, including the shading/air filter mode in the summer during the day, natural ventilation mode in the summer at night, sunspace mode in winter during the day, and sunspace/air filter mode during the transition season. The simulation of thermal conditions focused on the typical climatic week of an entire summer day and an entire winter day. The comparisons of indoor and outdoor temperatures and cooling and heating loads before and after changes in the variable interface are discussed below.

During summer days, the interface was used to block excess sunlight. The result was that the outer interface of the changeable DSF facade had three layers of modules, including (from outside to inside) a perforated aluminum plate, an air filter, and a mosquito net, all of which played a role in shading and air filtration. Figure 18 shows the thermal environment data for the perforated aluminum plate shading in the experimental building (the building used in this experiment is shown in Figure 5. The shape of the building was rectangular. The size ratio was 12 m (L) × 5.7 m (W) × 3 m (H). The DSF facade was located on the
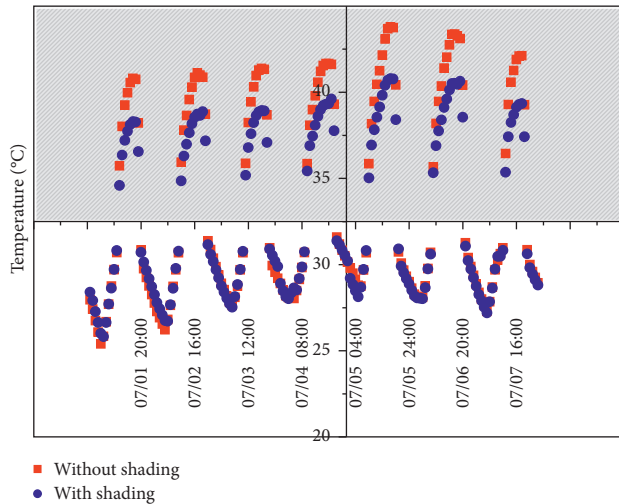
FIGURE 18: Temperature comparison with and without shading/air filtration mode (source: authors' own data).

FIGURE 19: Cooling load comparison with and without shading/air filtration mode (source: authors' own data).

southern facade of the building) in the hot summer and warm winter zones of Shenzhen, during a typical work week (from July 1 to July 7). The red curve indicates the interior temperature environment without shading, and the blue curve illustrates the interior temperature when the sun shading board was in use. This clearly illustrates that the sun-shaded plate inhibited heat transfer, especially during high-temperature times (over 35°C). The maximum temperature difference with and without sun shading was 3°C. Figure 19 shows the corresponding cooling load histogram, which shows that the cooling energy load saving was 10.5%~14.2% from 7 am to 6 pm.

During winter days, the greenhouse effect in the sun-space will preheat the indoor space, improving the indoor temperature and reducing the energy consumption demand. Therefore, a single layer of glass or ETFE film was inserted into the outer interface of the DSF; its effect is shown in Figure 20. This research simulated the combined glass interface and corridor of the experimental building, which were used as a sunspace. The building was located in a cold area, Beijing, during a typical work week (from January 1 to January 7). The red curve illustrates the interior temperature environment without the glass interface, and the blue curve indicates the interior temperature with the combined glass interface and corridor. Under the DSF preheating function, the indoor temperature improved throughout the day and had a positive effect on the indoor thermal environment. Especially during the daytime when there was ample solar radiation, the DSF mode was able to raise the indoor temperature by 2°C, and the highest temperature difference between the interior and exterior reached 5.7°C. Figure 21 shows the corresponding heating load in winter. Depending on the daily solar radiation, there was a marked difference in solar gain in the sunspace. Under typical conditions, this design mode saved heating energy consumption, on average, by approximately 24.6%; at its highest point, these savings reached 38.3% during the daytime, from 7 am to 6 pm, which obviously underscores the usefulness of preheating.
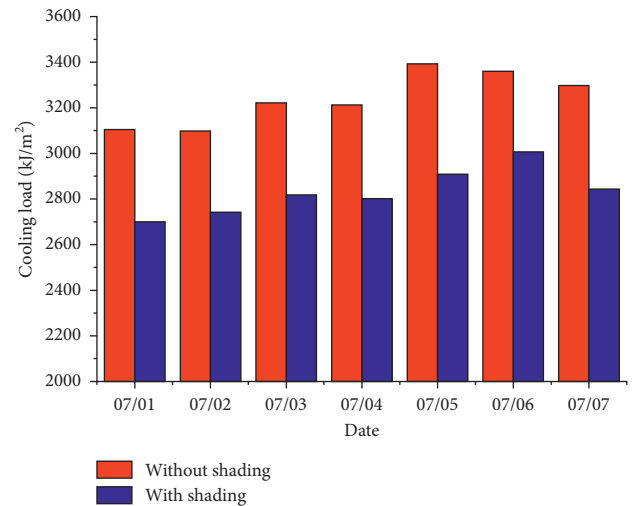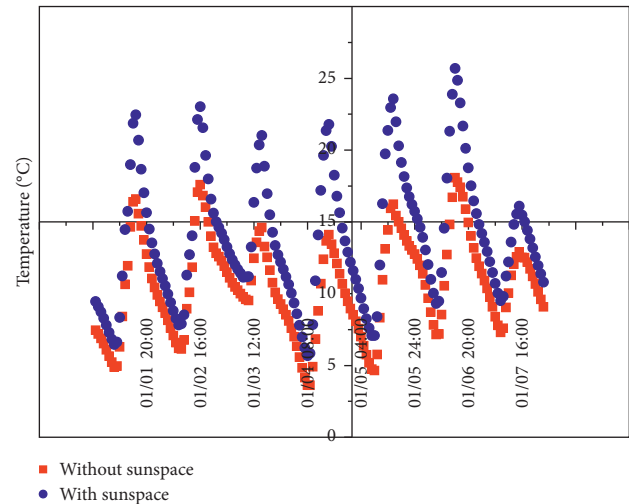
FIGURE 20: Temperature comparison with and without sunspace mode (source: authors' own data).

4. Conclusions

This research designed and evaluated a modular prefabricated building in an effort to improve its performance in terms of sustainability. Certain prefabricated construction details of the modular building envelope were studied, beginning with the steel frame of the modular structural system. In order to improve construction efficiency in this type of modular prefabricated building, as well as to enhance the physical environment and reduce energy consumption during the operational phase via integrated thermal insulation, two basic prefabricated envelope units were developed. The first employed high-performance thermal insulation materials to produce an integrated building envelope and modular connection points, the goal of which was to improve the building's performance in terms of sustainability. The second used the DSF principle to study how changeable module envelope units respond in terms of

Figure 21: Heating load comparison with and without sunspace mode (source: authors' own data).

climate adaptability. By constructing an experimental building, full-scale model, and computer simulation, this research verified the feasibility and effectiveness of several integrated building envelope units. This research has contributed to the literature in three key ways:

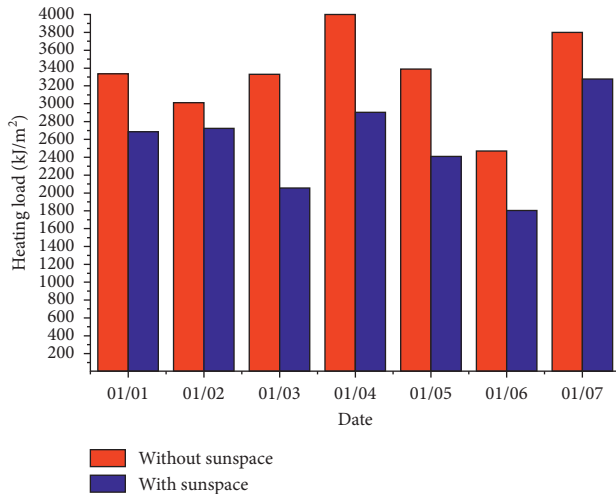(1) This study selected two types of thermal insulation materials, high insulation panels and aerogel blankets, in order to study certain construction details of integrated building envelopes in modular prefabricated buildings. The comprehensive heat transfer coefficients for the two integrated envelopes were $0.124\,\text{W/(m}^2\cdot\text{K)}$ and $0.257\,\text{W/(m}^2\cdot\text{K)}$. With energy savings of 75% and 45%, respectively, both offered insulation capacities significantly better than the current national standard.

(2) Focusing on the weakest heat point, the thermal bridge that occurs at modular connection points, this study attempted to use construction detail design and research to build an experimental building and full-scale building model. The goal was to explore and verify the feasibility of the climate-responsive construction technique called "reverse install." Long-term monitoring of the physical environment proved the effect of the integrated envelope on the connection points of two modules comprising a prefabricated building. When the outdoor temperature difference reached $36.2°C$ during summer days, the interior temperature difference was only $8.5°C$. This illustrates the excellent thermal insulation performance of the building envelope's design.

(3) To address issues related to climate change, building facade units were dynamically adjusted via different modular building envelope units; these included sunshades, preheaters, ventilation, air filtration, pest control, and other functional elements designed to improve the building's climate adaptability performance. The effects of the changeable building envelope units were verified by the computer simulation.

Sun shading in Shenzhen was shown to save cooling energy load consumption by 10.5%~14.2% during the daytime; similarly, in Beijing, sunspace was shown to save the average daily heating load consumption by approximately 24.6%.

Data Availability

The data used to support the findings of this study are available from the corresponding author upon request.

Conflicts of Interest

The authors declare that they have no conflicts of interest.

Acknowledgments

References

[1] H. Lin, "The design and analysis of sustainable architecture system," *Architecture Journal*, vol. 12, pp. 15–17, 2003.

[2] O. Oduyemi and M. Okoroh, "Building performance modelling for sustainable building design," *International Journal of Sustainable Built Environment*, vol. 5, no. 2, pp. 461–469, 2016.

[3] L. Caneparo, *Digital Fabrication in Architecture, Engineering and Construction*, Springer, Dordrecht, Netherlands, 2014.

[4] Y. Wang, L. Wang, E. Long, and S. Deng, "An experimental study on the indoor thermal environment in prefabricated houses in the subtropics," *Energy and Buildings*, vol. 127, pp. 529–539, 2016.

[5] G. Tumminia, F. Guarino, S. Longo et al., "Life cycle energy performances of a Net Zero energy prefabricated building in Sicily," *Energy Procedia*, vol. 140, pp. 486–494, 2017.

[6] Y. Teng, K. Li, W. Pan, and T. Ng, "Reducing building life cycle carbon emissions through prefabrication: evidence from and gaps in empirical studies," *Building and Environment*, vol. 132, pp. 125–136, 2018.

[7] E. Bonamente, M. C. Merico, S. Rinaldi et al., "Environmental impact of industrial prefabricated buildings: carbon and energy footprint analysis based on an LCA approach," *Energy Procedia*, vol. 61, pp. 2841–2844, 2014.

[8] M. Sonego, M. E. S. Echeveste, and H. G. Debarba, "The role of modularity in sustainable design: a systematic review," *Journal of Cleaner Production*, vol. 176, pp. 196–209, 2018.

[9] K. Salonitis, "Modular design for increasing assembly automation," *CIRP Annals*, vol. 63, no. 1, pp. 189–192, 2014.

[10] H. Zhang, J. Li, L. Dong, and H. Chen, "Integration of sustainability in Net-zero House: experiences in Solar Decathlon China," *Energy Procedia*, vol. 57, pp. 1931–1940, 2013.

[11] Z. Chen, J. Liu, Y. Yu, C. Zhou, and R. Yan, "Experimental study of an innovative modular steel building connection," *Journal of Constructional Steel Research*, vol. 139, pp. 69–82, 2017.

[12] G. Juanli, *Research on the Integration Performance of Industrialized Building Envelop Components of Affordable Housing in the Severe Cold Zone of China*, Tianjin University, Tianjin, China, 2013.

[13] N. Soares, P. Santos, H. Gervásio, J. J. Costa, and L. Simões da Silva, "Energy efficiency and thermal performance of lightweight steel-framed (LSF) construction: a review," *Renewable and Sustainable Energy Reviews*, vol. 78, pp. 194–209, 2017.

[14] H. Sozer, "Improving energy efficiency through the design of the building envelope," *Building and Environment*, vol. 45, no. 12, pp. 2581–2593, 2010.

[15] W. Boesiger and H. Girsberger, *Le Corbusier-euvre Complete*, Vol. 5, Birkhäuser, Basel, Switzerland, 1998.

[16] J. N. Habraken, *Conversations with Form: A Workbook for Students of Architecture*, Routledge, London, UK, 2014.

[17] Y. Yinjun, L. Dong Wei, and X. Lei, "The development and application of integration technology and industrial interior design in SI residential," *Architecture Journal*, vol. 4, pp. 55–59, 2012.

[18] Z. H. Jingxiang, "System or individuality–the wooden houses of Konrad Wachsmann and Frank Lloyd Wright in the 1930s," *Architecture Journal*, vol. 7, pp. 22–27, 2015.

[19] L. Caneparo, *Digital Fabrication in Architecture, Engineering and Construction*, Springer, Dordrecht, Netherlands, 2014.

[20] F. Ochs, D. Siegele, G. Dermentzis, and W. Feist, "Prefabricated timber frame façade with integrated active components for minimal invasive renovations," *Energy Procedia*, vol. 78, pp. 61–66, 2015.

[21] T. Konstantinou and U. Knaack, "An approach to integrate energy efficiency upgrade into refurbishment design process, applied in two case-study buildings in Northern European climate," *Energy and Buildings*, vol. 59, no. 4, pp. 301–309, 2013.

[22] Z. Li, M. He, X. Wang, and M. Li, "Seismic performance assessment of steel frame infilled with prefabricated wood shear walls," *Journal of Constructional Steel Research*, vol. 140, pp. 62–73, 2018.

[23] J.-H. Song, J.-H. Lim, and S.-Y. Song, "Evaluation of alternatives for reducing thermal bridges in metal panel curtain wall systems," *Energy and Buildings*, vol. 127, pp. 138–158, 2016.

[24] L. Zhenghao, S. Yehao, S. Jingfen et al., "Climate responsive modular building skin design strategy:a case study of the-studio," *Eco-City and Green Building*, vol. 2, pp. 54–61, 2015.

[25] R. Baetensa, B. P. Jellea, J. V. Thueb et al., "Vacuum insulation panels for building applications: a review and beyond," *Energy and Buildings*, vol. 42, no. 2, pp. 147–172, 2010.

[26] http://jxjc88.cn.china.cn/.

[27] L. Junjie, Z. H. Hong, Z. H. Yuting, and M. Jiajian, "Building envelop technology strategies in green building practices and its problems," *Eco-City and Green Building*, vol. 1, pp. 19–24, 2014.

[28] I. Smirnova and P. Gurikov, "Aerogel production: current status, research directions, and future opportunities," *Journal of Supercritical Fluids*, vol. 134, pp. 228–233.

[29] U. Berardi, "Aerogel-enhanced systems for building energy retrofits: insights from a case study," *Energy and Buildings*, vol. 159, pp. 370–381, 2018.

[30] K.-J. Lee, Y.-J. Choe, Y. H. Kim, J. K. Lee, and H.-J. Hwang, "Fabrication of silica aerogel composite blankets from an aqueous silica aerogel slurry," *Ceramics International*, vol. 44, no. 2, pp. 2204–2208, 2018.

[31] *The Brochure of Tianjin Langhua Science and Technology Development Co., Ltd.*, 2017, http://www.tjhykj.com/.

[32] Master Series, *The Works and Ideas of Herzog and Meuron–The Editing Department of the Master Series Books*, China Electric Power Press, China, 2004.

[33] S. Yehao, W. Jialiang, L. Caldas et al., "Indoor comfort and energy saving building performance created by envelop materials," *Time and Architecture*, vol. 3, pp. 77–81, 2014.

[34] Z. Su, X. Li, and F. Xue, "Double-skin façade optimization design for different climate zones in China," *Solar Energy*, vol. 155, pp. 281–290, 2017.

[35] S. B. Sadineni, S. Madala, and R. F. Boehm, "Passive building energy savings: a review of building envelope components," *Renewable and Sustainable Energy Reviews*, vol. 15, no. 8, pp. 3617–3631, 2011.

[36] P. Pihelo, T. Kalamees, and K. Kuusk, "nZEB renovation with prefabricated modular panels," *Energy Procedia*, vol. 132, pp. 1006–1011, 2017.

[37] Chinese National Standard, *Design Standard for Energy Efficiency of Public Buildings, GB50189*, Chinese National Standard, Taiwan, China, 2015.

[38] J. Li, Y. Song, and Q. Wang, "Experimental verification and pair-group analysis study of passive space design strategies," in *Proceeding of the 4th International Conference on Civil, Architecture and Hydrauic Engineering (ICCAHE'2015)*, Guangzhou, China, December 2015.

[39] S. Yehao, L. Junjie, W. Jialiang et al., "Multi-criteria approach to passive space design in buildings: impact of courtyard spaces on public buildings in cold climates," *Building and Environment*, vol. 89, pp. 295–307, 2015.

Research Article

Dynamical Analysis Applied to Passive Control of Vibrations in a Structural Model Incorporating SMA-SE Coil Springs

Yuri J. O. Moraes [ID],[1] Antonio A. Silva,[2] Marcelo C. Rodrigues,[1] Antonio G. B. de Lima [ID],[2] Rômulo P. B. dos Reis [ID],[3] and Paulo C. S. da Silva[2]

[1]*Department of Mechanical Engineering, Federal University of Paraiba, SN/58.051-085 João Pessoa, PB, Brazil*
[2]*Department of Mechanical Engineering, Federal University of Campina Grande, Avenue Aprígio Veloso, 882/58.429-900 Campina Grande, PB, Brazil*
[3]*Department of Technology and Engineering, Federal University Rural of Semi-Árido, Avenue Francisco Mota, Costa e Silva, 572/59.625-900 Mossoró, RN, Brazil*

Correspondence should be addressed to Yuri J. O. Moraes; yurijmoraes@gmail.com

Mechanical vibrations are severe phenomena of the physical world. These oscillations may become undesirable and may cause temporary and even irreversible damage to the system. There are several techniques to minimizing these vibration effects ranging from passive methods to the use of controllers with smart materials. In this sense, this study aims to analyze a passive vibration control system installed in a structure that simulates two-floor buildings. This system based on the incorporation of one SMA-SE (*Superelastic Shape Memory Alloys*) coil springs configuration for energy dissipation and the addition of damping. Modal analysis was performed using analytical, numerical, and experimental methods. In an experimental basis, response amplitudes were analyzed for free and forced vibrations in different configurations. As compared with the structure configuration with steel spring, the forced vibrations FRF (*Frequency Response Function*) analysis showed a reduction in displacement transmissibility of up to 51% for the first modal shape and 73% for the second mode in the SMA-SE coil spring configuration. As for damping, there was a considerable increase in the order of 59% in the first mode and 119% in the second, for the SMA-SE springs configuration.

1. Introduction

A periodic oscillation or mechanical vibration is a phenomenon defined as any movement that comes repeated after some time. Thus, the theory of vibration studies the oscillatory movements of the bodies and the forces associated with them. In general, a vibratory system alternates the transfer of its potential energy to kinetic energy. This system generally contains a means for storing potential energy, for example, a spring, another for storing kinetic energy, as a mass, and finally, one for gradually dissipating energy, called as damper [1, 2].

Under the viewpoints of mechanics, can be verified these effects easily in our everyday life, whether in the use of domestic appliances or the mining industry, among other forms [3]. However, some physical phenomenon may become undesirable and may cause temporary or irreversible damage in a specific system, due to the malfunction, the progressive increase of noise, shortened life of its components, increased maintenance costs, and in the more severe cases with the own collapse or structural failure. Thus, in the case of an architectural project, taking into account not only the load exerted by the weight of the system is crucial. Also, the loads are derived from the conditions of the own use, such as the movement of people, automobiles, loads, among others. However, it is of equal importance to consider the effects provoked by natural phenomena, like winds, and waves of the sea [4–6].

Another type of excitation in structures is earthquakes, usually associated with a kind of action imposed by a base
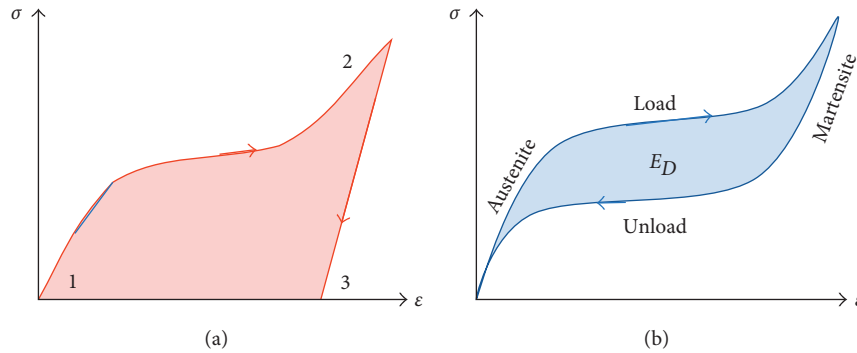
FIGURE 1: Representation of the two effects of an SMA. (a) SME and (b) SMA-SE.

excitation. Earthquake is related to the movements of the surface layers of the Earth, causing a deformation in the broad masses of rocks, which when broken, generate traveling waves in the Earth, provoking the earthquake [7, 8]. The seismic action depends on the mass of the structure, damping, and stiffness of its components. The behavior of a structure under earthquake conditions is a dynamic problem because the seismic movement causes forced vibration in it. Thus, several studies focus on the amplitudes and duration times of the vibration [9–11].

As a result, it is observed that many countries in Europe and Asia suffered the effects of natural disasters, with earthquakes contributing to more significant damage [12, 13]. In Brazil, the risks of a natural cause's shock are of remote chances, since there are no geological faults with sufficient dimensions to generate such an effect; however, specific human activities can also cause earthquakes, the so-called induced earthquakes. These vibrations are due to the construction of significant works, the actions of massive explosions, and the traffic of vehicles, which are associated with the human activity. The collapses and structural failures related to these earthquakes can arise because of the physical phenomenon well known as resonance, defined as the propensity of a system to oscillate at maximum amplitude under specific natural frequencies of the system. At these frequencies, even small forces can produce large-amplitude vibrations because the system stores sizeable vibration energy [14].

Techniques and models have been used to minimize the implications of these vibrations. The first studies with passive viscoelastic absorbers with a structural damping function date back to the 1950s [15–18]. In structural engineering, one of the first applications is related to the design of viscoelastic dampers used in the former WTC (*World Trade Center*) building, located in New York, USA [19], where 10,000 dissipators were used in each of the towers with the specific function of absorbing vibrations originated from dynamic actions of wind.

Currently, the materials most used for the needs imposed by the structural systems are the type with SME (*Shape Memory Effect*), where the main ones are the metallic alloys and polymers. In the metallic materials, the SME characteristic is the reaction to change in temperature, so-called SMA, and in some cases, to change under mechanical stress

known SMA-SE. These reactions are solid-state martensitic transformations [20–22]. Figure 1 shows a typical curve of these two-distinct phenomena. In Figure 1(a) is presented the SMA thermally active, in which the segments 1 and 2 establish that the material is submitted to an external load and modify its shape in the martensitic phase. After removing this external load, one small recovery segment occurred (2-3). To complete recovery, a change in temperature is necessary to transform the martensitic phase in the austenite phase. In the other hand, in SMA-SE the external load (Figure 1(b)) provokes a full-phase transformation from the austenite to the martensitic phase. Upon unloading, a reverse phase transformation is achieved. A complete load-unload cycle gives as result a hysteresis curve. The difference between the curves represents the dissipated mechanical energy.

In this way, the SMA used as an active actuator (requires an external source of energy) is inefficient because it is thermoactive: this means it has a low-frequency response up to 10 Hz. Further, the SMA-SE active per stress field can act as passive damping (without the need of external power source) capable of operating from low frequencies to frequencies above 10 Hz. In fact, the SMA-SE responds as fast as the change in strain submitted to stress field [23].

The use of these materials has greatly increased in the last decades, where many researchers have intensively carried out activities that aim to explore devices and applications that make use of them. In fact, the number of commercial applications is growing each year, with the largest market segment represented by actuators and motors. The global smart materials market in 2010 was approximately $19.6 billion, estimated at $22 billion in 2011, and more than $40 billion by 2016, with an annual growth rate of 12.8% between 2011 and 2016 [24–26].

A selection of SMA is available in the market, but only a few have developed on a commercial scale. From the discovery of Nitinol in 1963, many SMA's were investigated and adapted to specific requirements, such as modulus of elasticity and electrical resistivity, as for the use of sensors and actuators, for example. Nowadays, over 90% of all applications are based on NiTi, NiTiCu alloys, or NiTiNb alloys [27–30].

Then, based on the information related to SMA, this study aimed to perform a comparative analysis between the
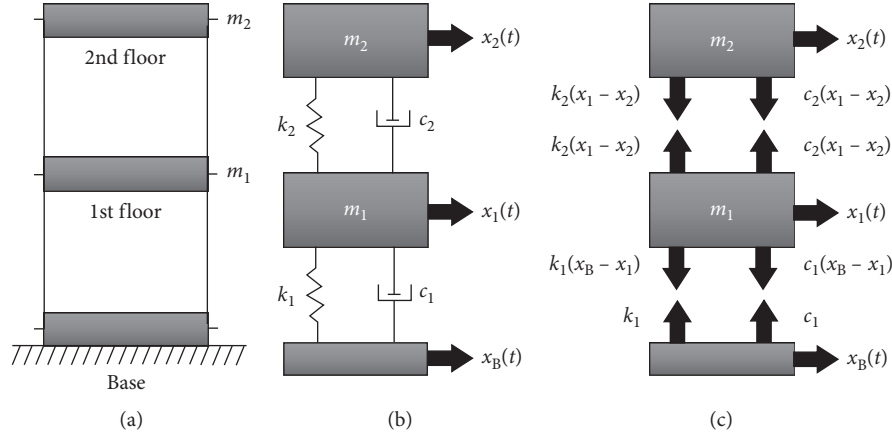
FIGURE 2: Representation of a 2DOF system with base excitation. (a) A simple model that simulates a two-floor building, (b) diagram of concentrated masses, and (c) free-body diagram of the structure.

use of elastic structural elements (steel springs) and elements of Nitinol alloy (SMA-SE springs) for the passive control of vibrations in structural systems. While the steel springs modify the structural parameters of stiffness and mass without incorporating any damping in the system and do not decrease the response amplitudes, the smart material increases the damping with only a small variation of these parameters and reduces the amplitudes in significant percentages, showing its superior efficiency and reliability.

This direct comparison is the main contribution of the research about previous works, showing the high possibility of the use of SMA-SE in dynamic systems with the aim of mitigates mechanical vibrations.

2. Methodology

This section describes a structural model that simulates two-floor buildings. The mathematical formulation is applied in an underdamped system with 2DOF (*Two Degrees of Freedom*) excited by the base. Thus, a numerical modal analysis of the system was performed without the SMA-SE absorbers, followed by the experimental stage, as a way of studying the structure with the elements of dissipation. Finally, a static characterization of the SMA-SE coil springs was performed.

2.1. Analytical Procedure. A free-body diagram illustrating the spring forces acting on each mass (Figure 2(a)) is illustrated in the Figures 2(b) and 2(c). The system will be analyzed when subjected to a forced excitation acting in the base. The constants c1 and c2 indicate the structural damping imposed on the system. More details can found in the literature [31].

Summing the forces applied in each mass (in the horizontal direction) and applying Newton's law of equilibrium to the system yields (1).

$$m_1 \cdot \ddot{x}_1 - c_1 \left(\dot{x}_B - \dot{x}_1 \right) + c_2 \left(\dot{x}_1 - \dot{x}_2 \right)$$
$$- k_1 \left(x_B - x_1 \right) + k_2 \left(x_1 - x_2 \right) = 0, \tag{1}$$

$$m_2 \cdot \ddot{x}_2 - c_2 \left(\dot{x}_1 - \dot{x}_2 \right) - k_2 \left(x_1 - x_2 \right) = 0. \tag{2}$$

After a rearrangement of terms of (1) and (2), (3) is obtained. In this equation, "$f_1(t)$" is the input harmonic force imposed on basis of the structure, which is a function of the stiffness and damping of the first floor. The displacement, velocity, and "$f_2(t)$" are null.

$$\left[m_1 \cdot \ddot{x}_1 + (c_1 + c_2) \cdot \dot{x}_1 + (k_1 + k_2) \cdot x_1 \right]$$
$$+ \left[-c_2 \cdot \dot{x}_2 - k_2 x_2 \right] = \left[k_1 \cdot x_B + c_1 \cdot \dot{x}_B \right] = f_1(t),$$
$$\left[m_2 \cdot \ddot{x}_2 + c_2 \cdot \dot{x}_2 + k_2 \cdot x_2 \right]$$
$$+ \left[-c_2 \cdot \dot{x}_1 - k_2 \cdot x_1 \right] = 0 = f_2(t). \tag{3}$$

Modifying (3) into the domain of Laplace transforms, we assume that the initial conditions of the system are zero and that "$F_1(s) = \{k_1 \cdot [X_B(s)] + c_1 \cdot [s \cdot X_B(s) - x_B(0)]\}$." Now, taking the displacement values in evidence, that is, "$[A] \cdot [X(s)] = [F(s)]$," we can write

$$\begin{bmatrix} s^2 \cdot m_1 + s \cdot (c_1 + c_2) + (k_1 + k_2) & -s \cdot c_2 - k_2 \\ -s \cdot c_2 - k_2 & s^2 \cdot m_2 + s \cdot c_2 + k_2 \end{bmatrix}$$
$$\cdot \begin{bmatrix} X_1(s) \\ X_2(s) \end{bmatrix} = \begin{bmatrix} F_1(s) \\ 0 \end{bmatrix}. \tag{4}$$

For (4), four transfer functions were obtained in the Laplace domain "$[X_1(s)/F_1(s), \ X_1(s)/F_2(s), \ X_2(s)/F_1(s)$ and $X_2(s)/F_2(s)]$." For this case, $F_2(s)$ is always 0 since there is no other force acting in the system, other than the base excitation. Using Cramer's rule, one can solve the matrix equation for the displacements. The results are

$$X_1(s) = \left[\frac{s^2 \cdot m_2 + s \cdot c_2 + k_2}{\det(A)}\right] \cdot F_1(s) + \left[\frac{-s \cdot c_2 - k_2}{\det(A)}\right] \cdot F_2(s),$$

$$X_2(s) = \left[\frac{-s \cdot c_2 - k_2}{\det(A)}\right] \cdot F_1(s)$$

$$+ \left[\frac{s^2 \cdot m_1 + s \cdot (c_1 + c_2) + (k_1 + k_2)}{\det(A)}\right] \cdot F_2(s),$$

$$(5)$$

in which the "$\det(A)$" is given as follows:

$$\det(A) = \left[s^2 \cdot m_1 + s \cdot (c_1 + c_2) + (k_1 + k_2)\right]$$
$$\cdot \left[s^2 \cdot m_2 + s \cdot c_2 + k_2\right] - (-s \cdot c_2 - k_2)^2.$$

$$(6)$$

Since that, "$F_2(s) = 0$," we have only two transfer functions that govern our system "$[X_1(s)/F_1(s) e X_2(s)/F_1(s)]$." So, by multiplying these equations by the modal rigidities "k_1" and "k_2" respectively, we obtain the measured responses in the masses "m_1" and "m_2" simultaneously, as follows:

$$H_{11}(s) = \frac{X_1(s) \cdot k_1}{F_1(s)} = \left[\frac{s^2 \cdot m_2 \cdot k_1 + s \cdot c_2 \cdot \cdot k_1 + k_2 \cdot k_1}{\det(A)}\right],$$

$$(7)$$

$$H_{21}(s) = \frac{X_2(s) \cdot k_2}{F_1(s)} = \left[\frac{-s \cdot c_2 \cdot k_2 - k_2 \cdot k_2}{\det(A)}\right].$$

$$(8)$$

We admit that a system with two independent coordinates subjected to a primary harmonic excitation can be defined by two transfer functions by using the Laplace Transform method, as in (7) and (8).

To obtain the analytical response in the frequency domain, a simulation code in the *Matlab*® software was developed and can be seen in the literature [31].

2.2. Numerical Procedure. For the numerical analysis of the system was developed a virtual structural model. With this model were determined the natural frequencies of the system with their respective modal shapes. In this analysis, the maximum and minimum displacements of amplitudes at each point of the structure can be visualized. For the development of the model, the design and modeling commercial software *AutodeskInventor*® version 2015 was used. For the modal analysis, was used the software *Ansys*® version 15.0 applying the FEM (*Finite Elements Method*).

The structural design in a computational environment was carried out with the objective of determining the geometric dimensions of the system. The idea is verifying the structural stability of the system via modal analysis.

The simulation is an essential stage of design since it has as objective to verify the dynamic behavior of the system, preventing failure in this process, which can compromise the physical integrity of the structure in operation.

In this process, the model was defined from the selection of the materials for each element that constitutes the structure, finishing with the choice of the control block for modal analysis. A mixed mesh with a predominance of hexahedral elements, containing 31,074 nodes and approximately 4,047 elements, was used, along with the selection of the "Base" floor as a fixed component of the system. In Figure 3 is illustrated the mesh generated before the simulation with the use of FEM.

2.3. Experimental Procedure

2.3.1. Structural Model and Absorber Elements. In this study, a structural model was designed and built in the LVI (*Vibration and Instrumentation Laboratory*) of the UFCG (*Federal University of Campina Grande, Brazil*). The prototype model consists of carbon steel beam for the composition of floors, rectangular stainless steel plates (AISI 304) for column composition, and as connecting elements Allen bolts of steel. Table 1 and Figure 4 summarize the number of elements, physical parameters, and dimensions of the prototype used in the fabrication of the structure.

Two structural configurations were used. The first one uses elastic elements of the type steel coil springs and the second with coil springs of superelastic effect (SMA-SE NiTi) at room temperature. In the second case, damping in the structure was due to the thermomechanical property of pseudoelasticity present in SMA-SE.

The SMA-SE coil springs were mechanically characterized by Instron 5582 at room temperature, using quasistatic load, with displacement control at 3 mm/min up to 445% strain. The thermal characterization was done by DSC (*Differential Scanning Calorimeter*) with 5°C/min from 100°C to −60°C, in order to verify the temperatures of the phase transformation.

The SMA-SE coil springs initially have orthodontic function and are commercialized by the Dental Morelli Company. Figure 5 shows the springs used in the study. In their original state, the SMA-SE coil springs are commercialized with different lengths between the eyelets (7.0, 9.0, 12.0, and 15.0 mm). However, the lengths "M7 = 7.0 mm" and "M12 = 12.0 mm" were selected due to better adaptation to the displacement amplitudes of the structure in the second and first floor, respectively. Thus, it is possible to obtain a higher efficiency of energy dissipation.

For other types and configurations of the elements incorporated, the useful length and the length between eyelets (L_u: useful length, L_o: length between eyelets, N_e: number of active turns, and V_m: volume of the useful material) were checked. These values are reported in Table 2.

For SMA-SE spring (M7), the number of active turns is seven, while in SMA-SE spring (M12), that number is twenty-six. Both have an initial turn angle equal to zero, initially closed. For the calculation of the linear deformation of the springs, the useful length of 2.5 mm was considered for M7 and 7.5 mm for M12 according to the point of crimping of the eyelets.

As for system tests incorporating SMA-SE elements, a spring type was attached for each floor, and calculated the total volume of useful material incorporated into the

(a)

(b)
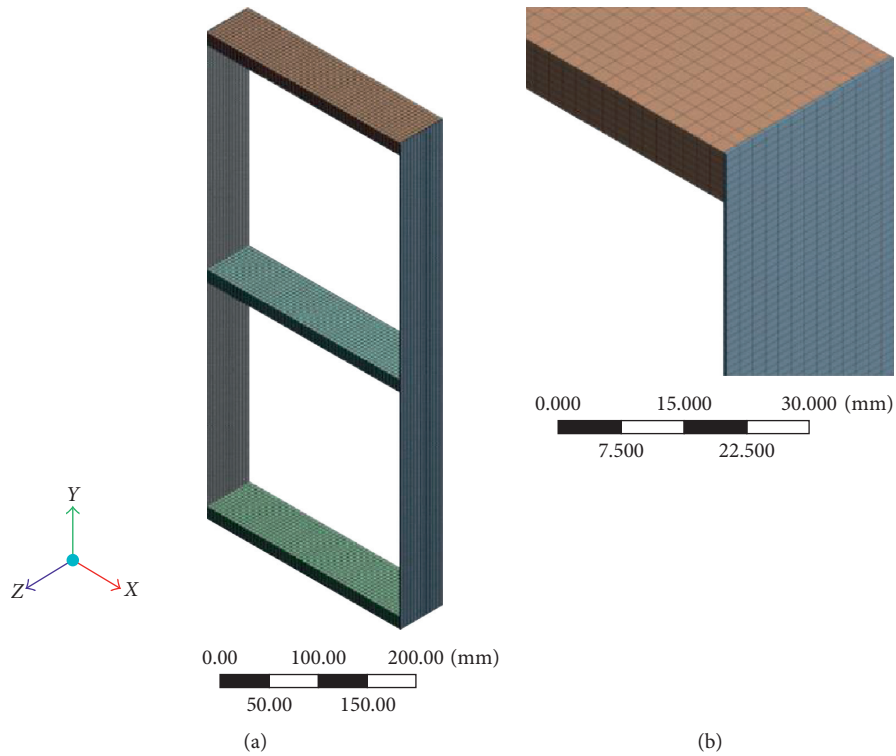
FIGURE 3: (a) The mesh of the physical model and (b) detail of the mesh in the columns.

TABLE 1: Description of the components used in the structural construction.

Description	Dimensions (mm)	E (GPa)	Mass (kg)	Amount (unit)
Steel beam 1020	228.0 × 50 × 12.80	200	1.110	3
Stainless plate 304	501.6 × 50 × 0.97	193	0.190	2
Allen bolt (3/4″)	9.5 × 15.50	200	0.004	24
Total	—	—	3.806	29

(a)   (b)   (c)   (d)
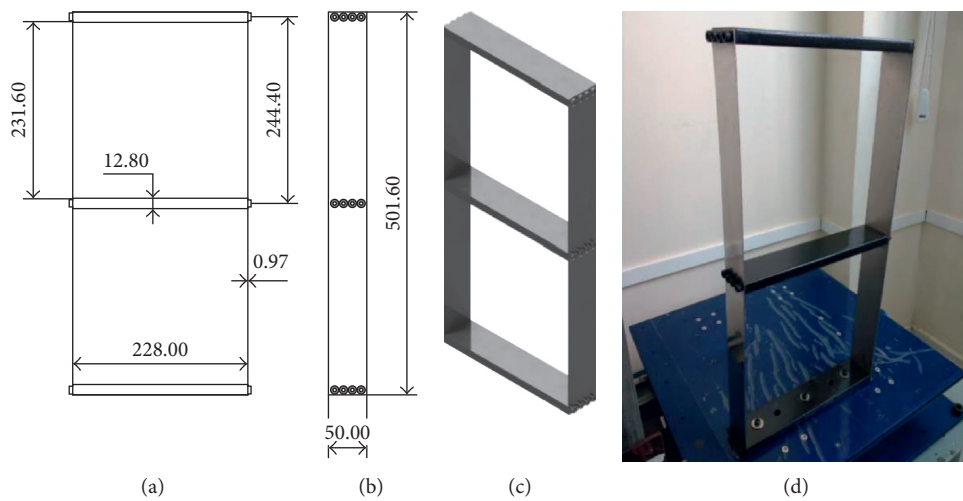
FIGURE 4: Technical drawing of the prototype. (a) Front view, (b) lateral view, (c) exploded view of the structure, and (d) real model on the shake table.

(a)   (b)
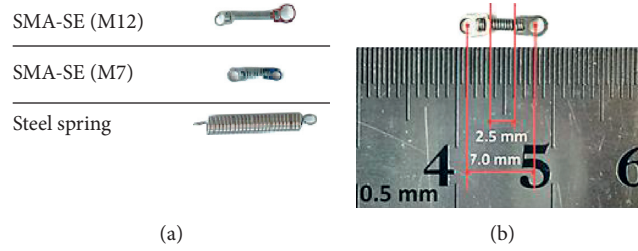
FIGURE 5: Absorber elements. (a) Springs used in the study and (b) length between eyelets and useful of the SMA-SE coil spring (M7).

TABLE 2: Dimensional parameters of the absorber elements.

Absorber elements	L_u (mm)	L_o (mm)	N_e (unit)	V_m (mm^3)
Steel spring	15.0	21.0	47	41.470
SMA-SE coil spring (M7)	2.5	7.0	7	2.494
SMA-SE coil spring (M12)	7.5	12.0	26	7.481

(a)   (b)   (c)
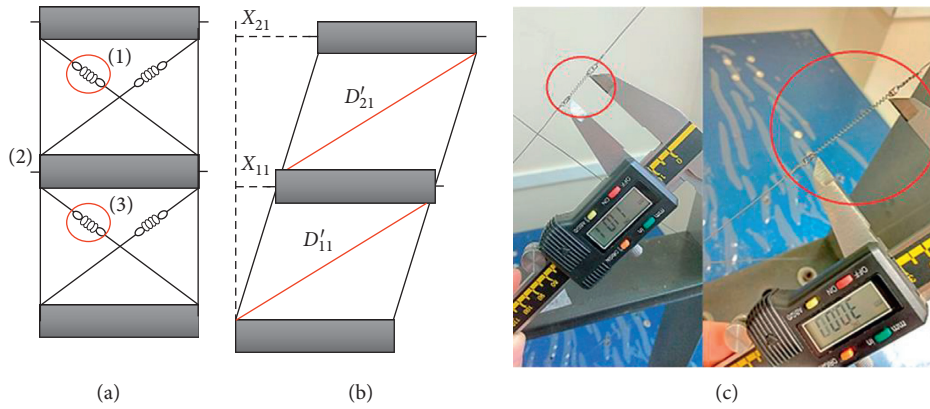
FIGURE 6: Coupling of the springs in the structure. (a) Illustrative representation of the arrangement of the elements, (b) procedure for measuring the deformation of the SMA-SE coil springs, and (c) calibration procedure for the springs.

structure. For the system configuration with SMA-SE springs, the entire material volume was about 88% less than in the case of steel springs, thus verifying that on a real scale, an optimization due to reduction in the material and space of the absorbers will be obtained.

The steel wires were received with an initial pretensioning to deform the SMA-SE springs at a certain level, allowing them to be in the superelastic region before performing dynamic tests. Following this recommendation was obtained this offset through measurements realized with an instrument used to measure displacements.

Assuming the springs have a much lower stiffness than steel wires, we can consider that the increase in damping imposed on the system must be associated with absorbers SMA-SE only. Figure 6(a) shows the connection of the steel wires in the system (1) and (3), which is fixed by anchor bolts (2). One can also observe the calibration procedure for the offset of the springs in Figure 6(c).

In this setup, when requesting the structure, it will move by expanding the vibration absorber element, occurring to the direct/martensitic phase transformation of the SMA-SE, and achieve the reverse/austenitic transformation when

discharging the element, passing through the central point and forming the hysteretic energy dissipation loop.

To obtain the initial deformation, the forced vibration test of the model without the presence of absorbers was carried out, to determine the maximum deflection in each floor of the structure and the deformation in each diagonal.

Figure 6(b) shows the scheme for determining the parameters "D'_{11}" and "D'_{21}" of the first and second floor when it is subjected to the excitation relating to the first modal shape. After analysis of the FRF experimental curves, the displacement values "X_{1i}" and "X_{2i}" can be obtained for the maximum deflection at each floor, with "$i = 1, 2$" corresponding to the first and second modal shapes. These values can be obtained using (9) and (10):

$$X_{1i} = T_{d1i} \cdot A_{1i}, \tag{9}$$

$$X_{2i} = T_{d2i} \cdot A_{2i}, \tag{10}$$

where "T_{d1i}" and "T_{d2i}" represent the transmissibility of displacement with respect to the base and analogously "A_{1i}" and "A_{2i}" the input amplitude at the base for the excitation function. Assuming that "X_{1i}" has the same value for the

(a)

(b)

FIGURE 7: (a) Experimental setup of the structure tests in free vibration and (b) schematic representation of the experimental procedure in the free vibration tests.

entire thickness of the bar, the values of deformation in each diagonal are obtained in the condition of the first modal shape, using (11) and (12) as follows:

$$D'_{11} = \sqrt{(l_1)^2 + (X_{11} + P_1)^2}, \tag{11}$$

$$D'_{21} = \sqrt{(l_2)^2 + [(X_{21} - X_{11}) + P_2]^2}, \tag{12}$$

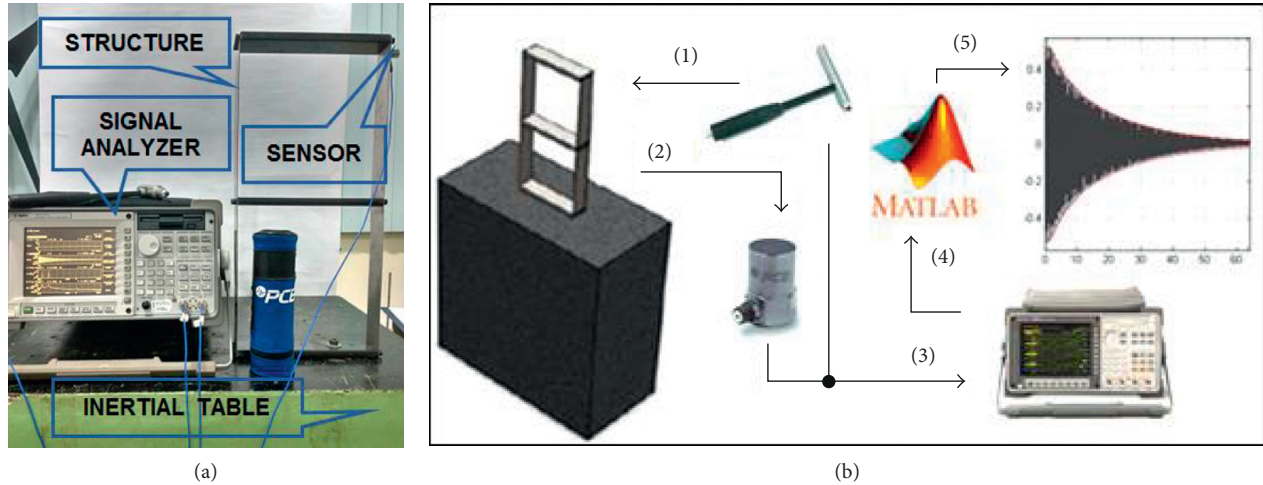where, from the data of the technical drawing of the structure (Figure 4), $l_1 = l_2 = 231.60$ mm and $P_1 = P_2 = 228.00$ mm. Analogously, the values of these same parameters related to the second modal shape of the system can be found using (11) and (12), using ($i = 2$). In this way, the strategy of using a minimum initial elongation must be adopted, ensuring that the maximum deformation does not exceed the elastic or final regime of the hysteresis loop.

2.3.2. Free Vibration Setup.

For the experimental tests in free vibration, was fixed the structure on the inertial table supported by vibra stops. The inertial table has a natural frequency lower than the primary frequencies of the system tested.

This experiment aims to determine the time response graph in which the amplitudes, regarding acceleration, and the period of vibration attenuation in the system are determined. The frequency spectrum was obtained in the cases where it is possible to visualize the natural frequency peaks and values of the structure to validate the analytical results. Figure 7(a) shows the actual assembly and the instrumentation used.

The setup of instrumentation is composed by an impact hammer (*PCB® 086D05*) which was used to generate a transient input signal and an accelerometer type sensor (*PCB 353B01*) to pick up the output signal. The data were collected by the signal analyzer, the (*Agilent® Model 37670A*). Following, they were manipulated in the *Matlab* software.

The tests were divided in three stages: no absorbers elements, with the steel springs, and with the SMA-SE coil

TABLE 3: Characteristics of the *Shake Table II Quanser*.

Dimensions	$61.0 \times 46.0 \times 13.0$ cm
Maximum displacement	± 7.6 cm
Maximum load	7.5 kg
Maximum mass	27.2 kg
Maximum acceleration	24.5 m/s^2
Maximum frequency	15.0 Hz

springs. In all situations was used the same instrumentation. The external force (impact hammer) focused on the second floor of the structure, along with the capture of the output signal (accelerometer) because they present less interference in the signals generated. Figure 7(b) shows the sequence of the experimental procedure.

2.3.3. Forced Vibration Setup.

For the experimental tests of forced vibration, an electromechanical machine *Quanser® Shake Table II* was used. Table 3 shows the main characteristics.

The shake table is managed by a computer and its *QUARC®* control software or the *Matlab* interface from *Simulink®*. The input and output signals of the structure were captured by the LVDT (*Linear Variable Differential Transformer*) type (WI/10 mm T) and (WA/20 mm L), both from the *HBM®* manufacturer and registered by the *QuantumX®* data acquisition system. The signal acquisition software is the *CatmanEasy®*, and data were processed on the *Matlab* software. Figure 8 shows the setup and instrumentation used in the experiments.

For the dynamic tests of the structure under forced vibration, behavior of the structure when subjected to harmonic excitation forces (sinusoidal function), using a peak input amplitude of 0.6 mm was studied.

Based on the choice of motion imposed on the system, it is possible to determine the FRF from the displacement measurements for each floor, extracting from these curves essential values in the analysis, such as the natural

FIGURE 8: Experimental setup of the system under forced vibration.
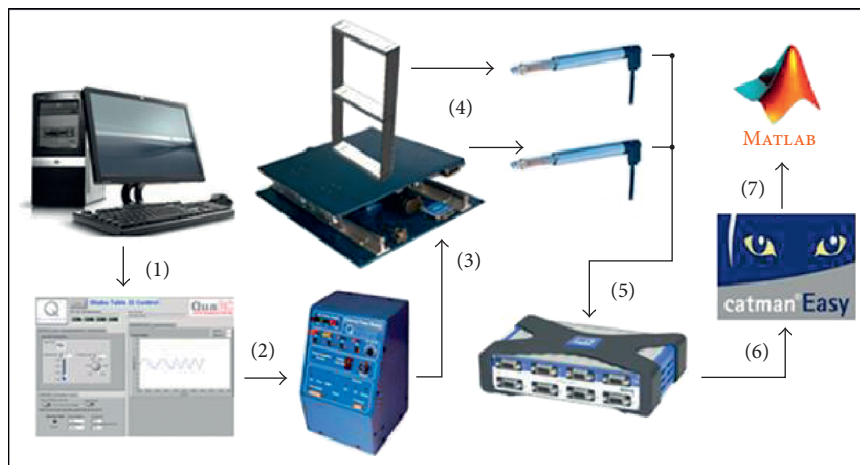
FIGURE 9: Representation of the experimental procedure under forced vibration.

frequencies, the transmissibility of the displacement, and the damping factors. Figure 9 shows the experimental sequence.

There are three stages for the dynamic test of the forced vibration structure: no absorber elements, with the steel springs, and with the SMA-SE coil springs, each subdivided in two measurements concerning the two floors of the structure. The measurements were carried out separately to avoid interference with the reading sensors, due to the small increase in the damping imposed by the friction between the moving parts of the sensor, perceived in previous tests.

All tests followed the same measurement setup and frequency range (1.0 to 11 Hz), by increments of the 0.05 Hz. For signal pickup, at each frequency was applied a hold time of 10 seconds for the system to stabilize. The signal pickup was performed at a rate of 50 Hz and a time period of 10 s, totaling 500 resolution points at each measurement. Therefore, each curve was generated with 201 pts, obtaining a good accuracy in the resonance peaks and increasing the precision of the damping values.

Initially, we cut off the offset value and calculated the FFT (*Fast Fourier Transformer*) for each of these signals and then obtained maximum peak-value. From these maximum peak data points, the FRF was constructed by dividing the output by the input values $[X(w)/Y(w)]$, with a resolution of 201 points, as previously described.

3. Results and Discussion

3.1. SMA-SE Coil Springs Characterization. Figure 10(a) shows the result from DSC of the M7 SMA-SE coil spring and the results from the Instron equipment for both M7 and M12 SMA-SE coil springs. The final temperature of austenite transformation (15.7°C) to the M7 coil spring is below room temperature, to confirm the superelastic behavior. This behavior was not verified to the M12 coil spring. Figure 10(b) illustrates the force versus displacement curves up to 445% of strain. For the M7 coil spring, the energy dissipated was 0.015 J and 0.026 J for M12 coil spring.

3.2. Predicted Results. For determination of the natural frequencies and modal shapes of the structure subjected to forced vibration, we used (7) and (8) and the experimental data of mass, damping, and stiffness. Figure 11 shows the analytical FRF curves of the system without the incorporation of absorbers, for the first and second floors, obtained from the transfer functions modeled by the Laplace transform theory described in Section 2.1. Table 4 displays the natural frequencies of the structure without absorbers.

Figure 12 shows the results of the numerical simulation (FEM) for the modal shapes of the structure without the incorporation of the absorber elements. It was verified that
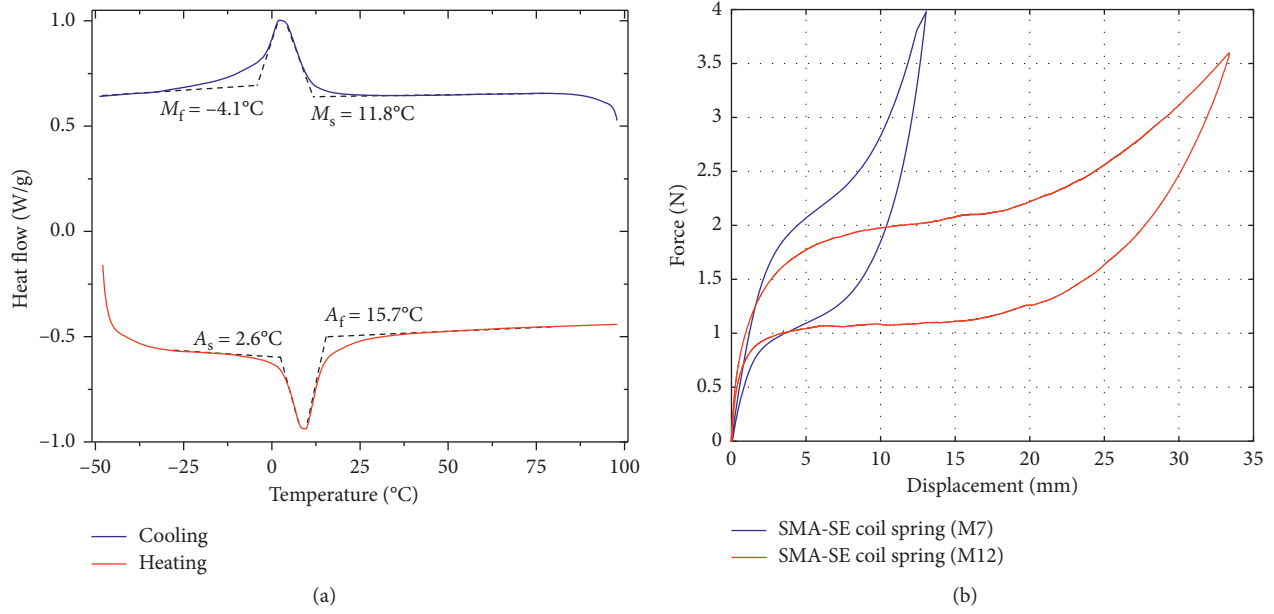
FIGURE 10: Characterization of SMA-SE absorbers elements. (a) DSC and (b) dynamical test at room temperature and quasistatic load.
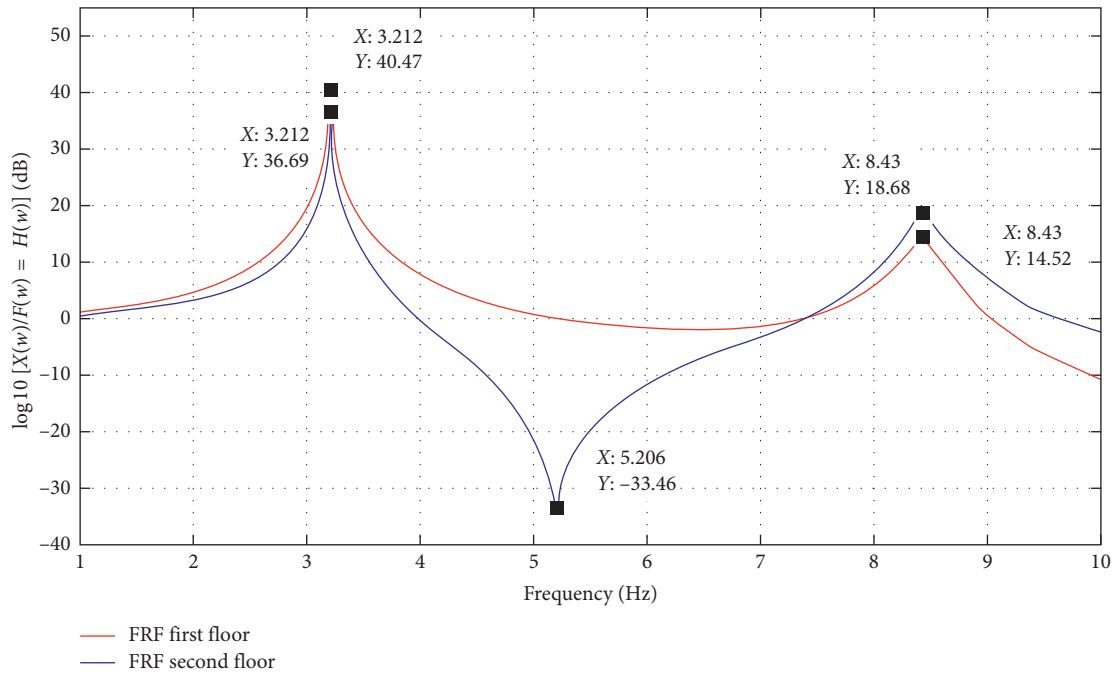
FIGURE 11: FRF analytical obtained by the system transfer functions.

TABLE 4: Natural frequencies of the structure without absorbers (free vibration).

Natural frequencies	A: analytical method (Hz)	B: numerical method (Hz)	C: experimental free vibration (Hz)	Relative error (%) $[(A-C)/A] \times 100$
1st	3.21	3.32	3.08	4.0
2nd	8.43	8.73	8.25	2.1

(a)

(b)
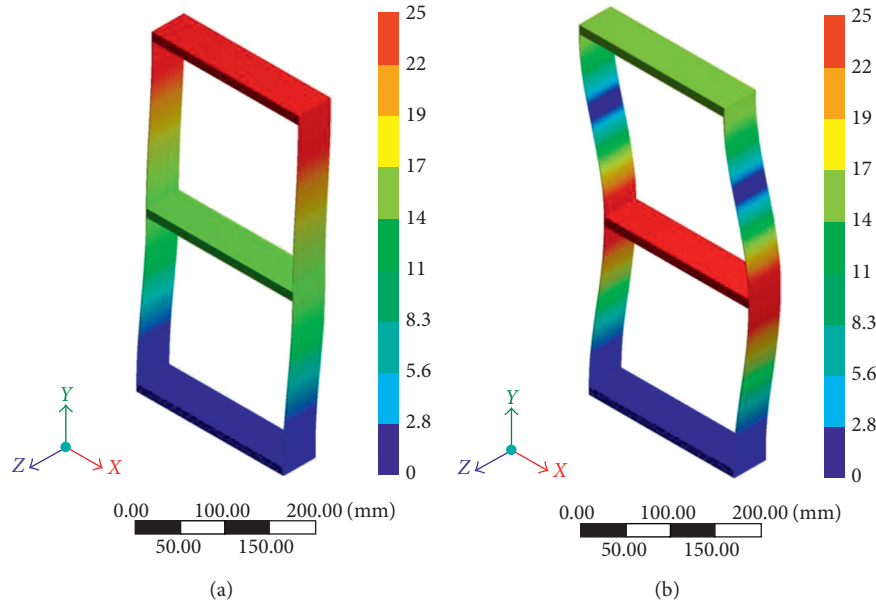
Figure 12: Modal shape obtained by numerical simulation. (a) First mode and (b) second mode.

the convergence analysis for the mesh size adopted validates the simulation. The modal shapes related to the two main frequencies in side view and their respective minimum and maximum displacement amplitudes are shown in the color bar. It is possible to notice the displacement imposed to the system, observing the position variations of the structure at rest when compared to the same one deformed, in its modal shapes of vibration.

According to the predicted results (Figure 11), we notice that they are in agreement with the numerical results (Figure 12) regarding natural frequencies, with errors from up the 3%. For the modal shapes, in the analytical response curve (Figure 11), it was observed that the highest transmissibility of displacements occurs on the second floor and the first mode. This fact was also observed in the numerical simulation (Figure 12(a)).

In the second modal shape, the analytical response curve (Figure 11) shows the greatest amplitude of displacement in the first floor of the structure; the same behavior was also obtained for the numerical simulation (Figure 12(b)), in which the largest displacements also occur on the first floor.

3.3. Experimental Results

3.3.1. Free Vibration. For validation of the predicted results, the transient responses of the structure in the free vibration tests (system acceleration responses) and their respective frequency spectrum FFT were obtained. Figure 13 presents the experimental results for the structure without absorbers and with the incorporation of two configurations, steel springs, and SMA-SE coil springs.

Note that a spring element made of steel stores elastic potential energy and returns a portion to the system in the form of kinetic energy. The difference between the stored energy and the energy recovered is due to the structural damping of the spring itself. However, the damping factor for the steel alloys is tiny and varying between 0.001 and 0.008 [32], so that the mechanical energy dissipation of these elements becomes insufficient to reduce the amplitudes of response. On the other hand, SMA-SE materials have a damping factor about 100 times higher than the steel, on the order of 0.1 to 0.2, and are known as Hidamets (*High Dampers Materials*). Therefore, when applying springs manufactured in SMA-SE, the system response suffers a reduction in amplitude [33].

From Figure 13, we can see that the mean peak amplitude achieved for all studied cases was approximately 0.45 g where "g" represents the gravity acceleration. The response in the time domain for the system without absorbers is very close to that obtained with the incorporation of steel springs (with stiffness similar to that for SMA-SE springs). This behavior confirms that elements of this type of material do not dissipate mechanical energy enough. In opposite, for the SMA-SE spring setup, greater energy dissipation is observed when compared to the previous cases.

Figure 14 illustrates the curves FRF of the system. This function was achieved by dividing the acceleration output signal and the force input signal from a predefined function in the dynamic signal analyzer. The response amplitude peaks are denoted by the behavior described in Figure 13. In this figure, we can see larger amplitudes for the system without the presence of actuators or with the incorporation of steel springs, and a considerable and significant reduction thereof in the SMA-SE coil springs configuration.

Table 4 shows the natural frequency values of the three methods of analysis adopted in this work. When the experimental results of the system in free vibration are compared with the analytical method, for the structure without absorbers, a variation of 4.0% is observed for the
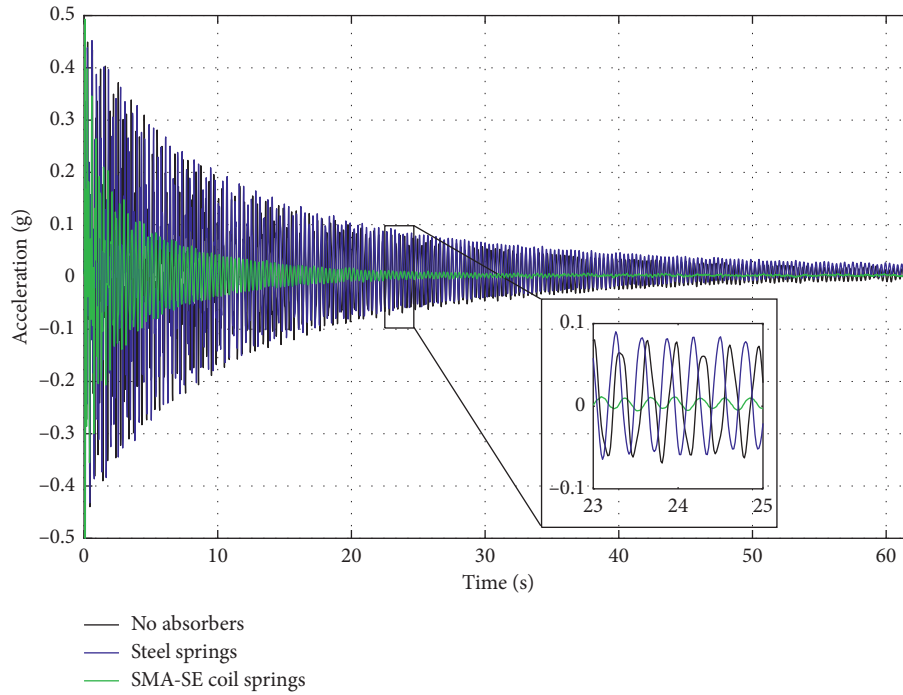
FIGURE 13: Time response for structure subjected to an impact in all configurations.
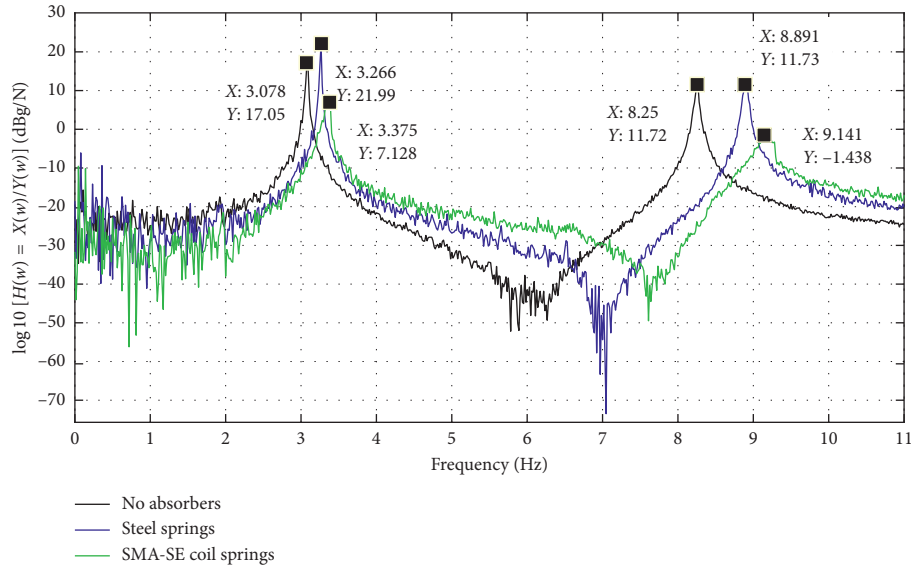
FIGURE 14: Experimental FRF of the system for the configurations adopted in this study.

TABLE 5: Natural frequencies and percentage reduction of amplitudes in free vibration tests.

Configurations	ω_{n1} (Hz)	$H(w)$ (g/N)	%R $[(B-C)/B] \times 100$	ω_{n2} (Hz)	$H(w)$ (g/N)	%R $[(B-C)/B] \times 100$
A: no absorbers	3.08	7.12	—	8.25	3.85	—
B: steel springs	3.26	12.58	—	8.89	3.86	—
C: SMA-SE coil springs	3.37	2.27	82	9.15	0.83	78

first natural frequency and of 2.1% for the second natural frequency.

The reason for this variation can be motivated by the consideration of perfect crimping adopted in the method, a fact that not is verified in the real experimental tests. The bolts make the connection between the floors and the columns, which decreases the stiffness of the model. This fact provokes a decrease in the natural frequencies of the system.
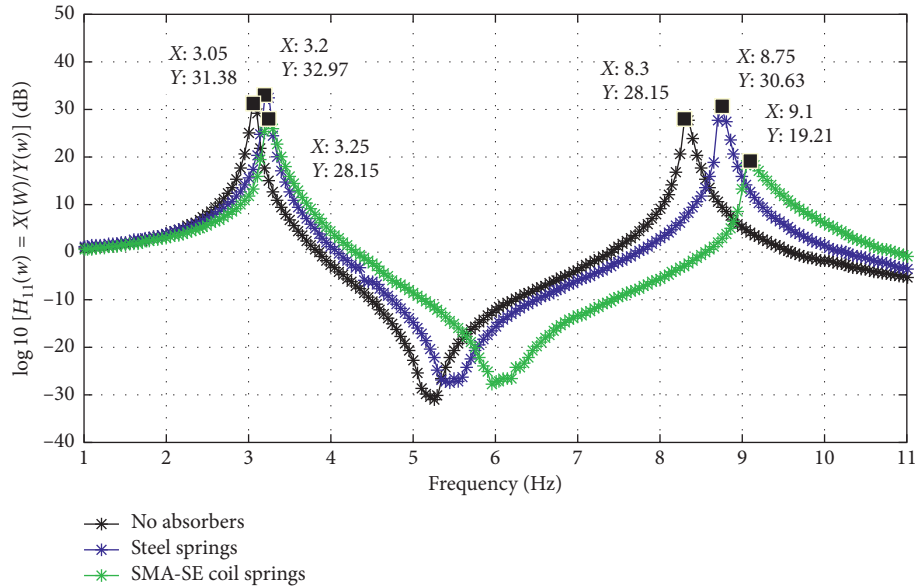
FIGURE 15: Experimental FRF of the first floor of the system.

Table 5 shows the values of the linear acceleration amplitudes. The small variation of natural frequencies of the system in comparison with the structure with steel springs and SMA-SE coil springs is observed. As already expected, an increase in global stiffness causes an increase in the natural frequency. The results of percentage reduction (%R) of acceleration amplitudes confirm the efficiency of the superelastic coil springs in the control of vibrations. In this configuration, reductions of 82% for the first natural frequency and 78% for the second when compared with the structure of steel springs were verified.

If we compare structural damping of the system without absorbers ($\xi = 0.0026$), with the system with steel springs ($\xi = 0.0022$), in both cases, damping factors of the same order of magnitude are observed, which are typical of conventional steel structures.

Concerning the values of attenuation of the of the acceleration signal in time, was verified that when the amplitudes reached a value of 0.03 g, a significant reduction of 72% for the case of the structure with SMA-SE springs compared to the system with steel springs.

The result of adding a steel spring in parallel is one increase in global stiffness. Just see (7) and (8); if "k" increases, the response amplitude increases too. So, add a steel spring without structural damping, and the response amplitude will increase. Also, the inclusion of a steel spring in a structure may characterize the addition of a secondary system with coupling by mass, and the possibility of a resonance phenomenon occurring and consequently the growth of the response amplitude.

3.3.2. Forced Vibration. For the experimental tests of the system subjected to forced vibration, the method established previously in the experimental methodology was followed, obtaining the curves of frequency response functions, in all configurations. Figure 15 illustrates the FRF obtained for the first floor.

Analyzing the curves in Figure 15, one can observe the same behavior already evidenced in the free vibration tests. For the case of the structure with steel springs, the displacement transmissibility peaks presented higher values for the two modal shapes. This fact indicates that elastic steel elements do not control or minimize vibrations in structures subjected to permanent excitations.

As expected, the FRF of the system with the SMA-SE coil springs presented a significant reduction in the transmissibility peaks, evidencing the high levels of mechanical energy dissipation. The behavior described here can also be visualized in an analogous way for the second floor of the structure, as evidenced in Figure 16.

Table 6 presents the values of natural frequencies and displacement transmissibility relation of the system, obtained from linear FRF. For the system with the SMA-SE coil springs, reductions in the transmissibility peaks "T_d" up to 51% in the first modal shape and up to 73% for the second shape were obtained.

Regarding the damping factor (ξ), the behavior of the system follows the same pattern perceived in previous analyzes. Table 7 highlights these rates for all modal shapes and their two floors. It seen that the system incorporated with steel springs does not add damping to the structure, presenting mostly values even lower than the structure without absorber. In the case of the system with the SMA-SE coil springs, there is a significant increase in the damping. There is an increase of up to 59% or approximately 1.6 times in the first modal shape and up to 119% or 2.2 times for the second mode.

4. Conclusions

This paper focuses on the passive control of vibrations using different configurations on the structural system: steel
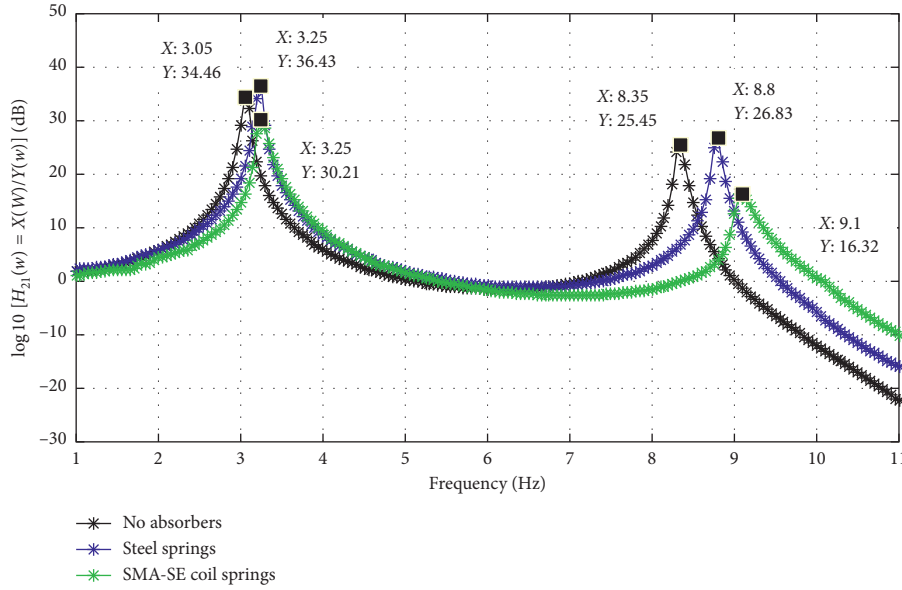
Figure 16: Experimental FRF of the second floor of the system.

Table 6: Natural frequencies and displacement transmissibility in forced vibration, linear scale.

| Configurations | First floor | | | | | | Second floor | | | | | |
| | ω_{n1} Hz | $H(w)_1$ | | ω_{n2} Hz | $H(w)_2$ | | ω_{n1} Hz | $H(w)_1$ | | ω_{n2} Hz | $H(w)_2$ | |
		T_d	%R^*		T_d	%R^*		T_d	%R^*		T_d	%R^*
A: no absorbers	3.0	37.1	—	8.3	26	—	3.0	52.8	—	8.3	19	—
B: steel springs	3.2	44.5	—	8.7	34	—	3.2	66.3	—	8.7	22	—
C: SMA-SE coil springs	3.2	25.5	43	9.1	9.1	73	3.2	32.4	51	9.1	6.5	70

%$R^* = [(B - C)/B] \times 100$.

Table 7: Structural damping of the system in forced vibration, linear scale.

| Configurations | First floor | | | | Second floor | | | |
| | ω_{n1} (Hz) | | ω_{n2} (Hz) | | ω_{n1} (Hz) | | ω_{n2} (Hz) | |
	ξ_1	%$\widehat{A}^*$	ξ_2	%$\widehat{A}^*$	ξ_1	%$\widehat{A}^*$	ξ_2	%$\widehat{A}^*$
A: no absorbers	0.0133	—	0.0067	—	0.0144	—	0.0065	—
B: steel springs	0.0142	—	0.0053	—	0.0123	—	0.0055	—
C: SMA-SE coil springs	0.0172	21	0.0116	119	0.0195	59	0.0115	109

%$\widehat{A}^* = [(C - B)/B] \times 100$.

springs and SMA-SE coil springs (NiTi Alloys). The results obtained by different methods (analytical, numerical, and experimental) were representative to compare the modal shapes. The proposed models were obtained in a simplified form and without absorber elements: however, the result confirms that the formulations represent the system as well. In the numerical analysis, good results were obtained using the Ansys in comparison with the analytical results, despite the limitation by the nonconsideration of the friction and the contact between the parts of the structure. A small relative variation up to 3.5% was obtained for the modal shapes, validating the modeling.

In an experimental modal analysis for the system in free vibration was verified the efficiency of the configurations that adopted the superelastic springs as a vibration absorber element, obtaining significant reductions in the acceleration amplitudes, up to 82% for the SMA-SE coil springs configuration. Regarding the signal attenuation time, it observed that, for the structure subjected to a lateral impulse (impact hammer), the reductions were considerable. There was a reduction up to 72% in the SMA-SE coil spring configuration compared to the steel springs.

When analyzed, the system in forced vibration was verified that there was no significant variation in the natural frequencies for the configuration of steel springs when compared with the SMA-SE coil springs. It is perceived a variation of up to 4.6% for modal shapes. Thus, it is correct to say that amplitude reductions occur due to the increase in structural damping and energy dissipation. Regarding the displacement transmissibility, by analyzing the FRF, it can be

seen that in comparison with the system with steel springs, the SMA-SE coil springs configuration showed a reduction up to 51% in the first modal shape and up to 73% for the second mode.

The damping factors ranging from (0.001 to 0.08) are within the range of expected values for structural damping. If we compare these factors for the SMA-SE spring configuration, there is an increase of up to 59% in the first modal shape and up to 119% in the second mode, in comparison with the worst case, the configuration of springs of steel. Thus, we stated that the objectives of the work were satisfactorily achieved, validating the use of SMA-SE in the passive control of vibrations in structures subjected to dynamic excitations.

Data Availability

The (analytical, numerical, and experimental) data used to support the findings of this study are available from the corresponding author upon request.

Conflicts of Interest

The authors declare that there are no conflicts of interest regarding the publication of this paper.

Acknowledgments

References

[1] S. S. Rao, *Mechanical Vibrations*, vol. 4, Pearson Prentice Hall, São Paulo, SP, Brazil, 2008, ISBN 978-85-7605-200-5.

[2] A. K. Chopra, Dynamics of Structures, Vol. 2, Pearson Prentice Hall, Upper Saddle River, NJ, USA, 1995.

[3] L. N. F. France and J. Sotelo Jr., *Introduction to Mechanical Vibrations*, vol. 1, Edgard Blücher, São Paulo, SP, Brazil, 2006, ISBN 978-85-2120-338-4, in Portuguese.

[4] A. A. Correia, "System vibrations with 1DOF," in *Dynamics*, Higher Technical Institute, Nicosia, Cyprus, 2007.

[5] M. J. Brennan, "Some recent developments in adaptive tuned vibration absorbers/neutralizers," *Shock and Vibration*, vol. 13, no. 4-5, pp. 531–543.

[6] J. Liu and K. Liu, "A tunable electromagnetic vibration absorber: characterization and application," *Journal of Sound and Vibration*, vol. 295, no. 3–5, pp. 708–724, 2006.

[7] P. A. L. Yánez, "Seismic analysis of buildings by continuous environment technique," Ph.D. thesis, Structural Engineering, School of Engineering of São Carlos, Federal University of São Paulo (USP), São Carlos, SP, USA, 1992, in Portuguese.

[8] J. A. V. Veloso, "Man-induced earthquakes," We off the axis, Brasilia, Brazil, July 2016, in Portuguese, http://www.nosrevista.com.br/2012/09/18/terremotos-induzidos-pelo-homem/.

[9] F. L. B. Saavedra, "Comparative study in seismic analysis of building structures," M.S. dissertation, Civil Engineering Sciences, Federal University of Rio de Janeiro (UFRJ), Rio de Janeiro, RJ, Brazil, 1991, in Portuguese.

[10] M. Dolce and D. Cardone, "Mechanical behavior of shape memory alloys for seismic applications: austenite Ni-Ti wires subjected to tension," *International Journal of Mechanical Sciences*, vol. 43, no. 11, pp. 2657–2677, 2001.

[11] M. Dolce, D. Cardone, and R. Marnetto, "SMA re-centering devices for seismic isolation of civil structures," in *Proceedings of the SPIE*, vol. 4330, pp. 238–249, Chiba, Japan, July 2001.

[12] A. E. V. Lopes, "Seismic risk in Brazil and its impact on great works," *Journal of the Institute of Engineering*, no. 58, 2010, in Portuguese, https://www.institutodeengenharia.org.br/site/2010/05/02/edicao-58/.

[13] A. E. V. Lopes, *Seismic Intensities of Earthquakes: Formulation of Seismic Scenarios in Brazil*, vol. 91, pp. 90–102, USP Magazine, São Paulo, SP, Brazil, 2011, in Portuguese, 2011.

[14] D. Halliday and R. Resnick, *Fundamentals of Physics: Mechanics*, vol. 4, LTC, Rio de Janeiro, RJ, USA, 2008, ISBN 978-85-216-1605-4, in Portuguese.

[15] E. M. Kervin Jr., "Damping of flexural waves by a constrained viscoelastic layer," *Journal of Acoustical Society of America*, vol. 31, no. 7, pp. 952–962, 1959.

[16] D. Ross, E. E. Ungar, and E. M. Kervin Jr., "Damping of plate flexural vibrations by means of viscoelastic layer," in *Structural Damping*, ASME, New York, NY, USA, 1959.

[17] K. Williams, G. Chiu, and R. Bernhard, "Adaptative-passive absorbers using shape memory alloys," *Journal of Sound and Vibration*, vol. 249, no. 5, pp. 835–848, 2002.

[18] S. B. Choi and J. H. Hwang, "Structural vibrations control using shape memory actuators," *Journal of Sound and Vibration*, vol. 231, no. 4, pp. 1168–1174, 2000.

[19] P. Mahmoodi, "Structural dampers," *Journal of Structural Division*, vol. 95, no. 8, pp. 1661–1672, 1969.

[20] L. A. P. Semão, "Use of shape memory alloys in the control of vibrations in intelligent civil engineering structures," M.S. dissertation, Civil Engineering-Structures and Geotechnics, Faculty of Sciences and Technology, Nova de Lisboa University, Lisbon, Portugal, 2010, in Portuguese.

[21] M. Alam, M. Youssef, and M. Nehdi, "Utilizing shape memory alloys to enhance the performance and safety of civil infrastructure: a review," *Canadian Journal of Civil Engineering*, vol. 34, no. 9, pp. 1075–1086, 2007.

[22] T. W. Duerig, K. N. Melton, D. Stöckel, and C. M. Wayman, *Engineering Aspects of Shape Memory Alloys*, Butterworth-Heinemann Ltd, London, UK, 1990, ISBN 0-750-61009-3.

[23] D. C. Lagoudas, *Shape Memory Alloys: Modelling and Engineering Application*, D. C. Lagoudas, Ed., Springer, Houston, TX, USA, 2008.

[24] C. Menna, F. Auricchio, and D. Asprone, "Applications of SMA in structural engineering," in *Shape Memory Alloy Engineering*, Butterworth-einemann Limited, Oxford, UK, 2015, ISBN 978-0-08-099920-3.

[25] F. Auricchio, R. L. Taylor, and J. Lubliner, "Shape-memory alloy: macro modelling and numerical simulations of the superelastic behavior," *Computer Methods Applied Mechanics Engineering*, vol. 146, no. 3-4, pp. 281–312, 1997.

[26] J. Wilson and M. Wesolowsky, "Shape memory alloys for seismic response modification: a state-of-the-art review," *Earthquake Spectra*, vol. 21, no. 2, pp. 569–601, 2005.

[27] L. Lecce and A. Concilio, *Shape Memory Alloy Engineering: For Aerospace, Structural and Biomedical Applications*, Butterworth-Heinemann, Oxford, UK, 2015, ISBN: 978-0-08-099920-3.

[28] L. Delaey, R. V. Krishnan, and H. Tas, "Thermoelasticity, pseudoelasticity, and the memory effects associated with martensitie transforations: structural and microestructural changes associated with the transformations," *Journal of Materials Science*, vol. 9, no. 9, pp. 1521–1535, 1974.

[29] L. Delaey, R. V. Krishnan, and H. Tas, "Thermoelasticity, pseudoelasticity, and the memory effects associated with martensitie transforations: the macroscopic mechanical behavior," *Journal of Materials Science*, vol. 9, no. 9, pp. 1536–1544, 1974.

[30] K. Tanaka, S. Kobayashi, and Y. Sato, "Thermo-mechanics of transformation pseudo-elasticity and shape memory effect in alloys," *International Journal of Plasticity*, vol. 2, no. 1, pp. 59–72, 1986.

[31] Y. J. O. Moraes, "Dynamical analysis applied to control passive of vibrations in a structural device incorporating superelastic NiTi mini coils springs," M.S. thesis, Mechanical Engineering, Federal University of Campina Grande, Campina Grande, PB, Brazil, 2017, in Portuguese.

[32] C. E. Beards, *Structural Vibration: Analysis and Damping*, Halsted Press, New York, NY, USA, 1996.

[33] S.-H. Chang and S.-K. Wu, "Damping characteristics of SMA on their inherent and intrinsic internal friction," in *Handbook of Mechanics of Materials*, C.-H. Hsueh, S. Schmauder, C.-S. Chen et al., Eds., Springer Nature Singapore Pvt. Ltd., Singapore, 2018.

Research Article

Numerical Analysis to Enhance Delamination Strength around Bolt Holes of Unidirectional Pultruded Large Smart Composite Platform

Sheedev Antony, Monssef Drissi-Habti [iD], and Venkadesh Raman

PRES LUNAM IFSTTAR, CS4 Route de Bouaye, 44344 Bouguenais, France

Correspondence should be addressed to Monssef Drissi-Habti; monssef.drissi-habti@ifsttar.fr

As a part of the DECID2 French National Project (2008–2012), construction of a large platform entirely made of smart composites was carried out and two demonstrators were installed. During a previous study, an ABAQUS model of smart composite platform was set up to perform numerical simulations that predict the mechanical behaviour of bolt-fastened platform under static three-point bending load, and a stress concentration is observed around the bolt holes. Unidirectional composites are subjected to delamination at very low stress, and this cannot be tolerated because most of the applications of pultruded structures are in civil engineering, which involves human safety. Therefore, it is essential to study the correlation of delamination onset and find a technology to enhance delamination strength. In this study, a numerical analysis was carried out to enhance the delamination strength around the bolt holes. Bidirectional fiberglass cloths were wrapped around unidirectional pultruded beams to reinforce the structure and to prevent delamination. Due to the high cost of these cloths, a study was also carried out to select an appropriate cloth material by taking into account two aspects: density and number of layers of cloths. The selected cloth was compared with conventional continuous fibreglass mat, and it was found that bidirectional fibreglass cloth material performs well in preventing delamination, even though it is expensive.

1. Introduction

Fiber-reinforced polymer composites are materials that are composed of polymer-based resin and fibres as reinforcement. Composite material properties are mainly determined based on fibres and resin properties, fibre volume fraction, and geometry and orientation of fibres. Utilization of polymer matrix composites is increasing day by day in many industries due to their better mechanical properties, corrosion resistance, and strength-to-weight ratio, but their durability remains an issue. The introduction of smart composite material structures with structural health monitoring (SHM) techniques is one solution to these problems. In SHM, sensors will detect strain at different locations of composite structures and monitor the health of the structure. The detailed studies of smart composite materials are discussed in the previous work [1].

The main goal of DECID2 project (2008–2012) was the construction of mechanically oriented platforms made of pultruded composite materials (Figure 1). Two demonstrators of dimensions $20 \, m \times 3.5 \, m$ were installed in IFSTTAR Nantes and Technocampus EMC2. The parts were attached using single and double lap-bolted joints. Different studies were carried out to reduce delamination and to study the behaviour of bolted joints in composite structures [2, 3]. It was found that high-speed drilling and low feed rates may reduce the intensity of delamination [2], but DECID2 project has been started prior to the publishing of these studies, and conventional drilling methods were used during construction. Strain sensors and ultrasonic sensors were embedded in pultruded composite structures. This technique is called structural heath monitoring where strain will be continuously monitored and warned when it reaches the strain limit. Several possible sensors for monitoring large smart composite
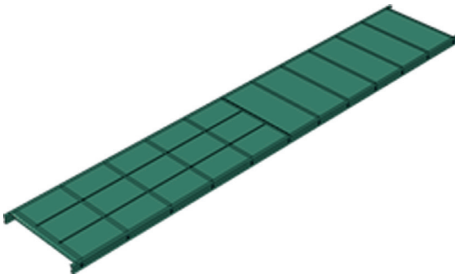
Figure 1: DECID2 platform.

Figure 2: Smart composite platform CAD model [7].

structure have been studied previously [4, 5], and further works were extended to the study of UV radiation defect on mechanical behaviour of the DECID2 smart composite platform [6]. For further studies, a CAD model of large smart composite platform was set up, and a numerical simulation to predict the mechanical behaviour of the structure under static load has been performed (Figure 2). As a result of this work, it was observed that there was a stress concentration around bolt holes (Figure 3) [7].

Pultrusion is a continuous manufacturing process of composite materials with constant cross sections. In this technology, parts are made by the matrix extrusion process and by pulling the unidirectional fibres. This process will allow the fibres to align well before polymerization of the matrix. It is a highly automated, cost-effective process and produces finished parts with high volume fraction. Pultrusion is used to make products like beams, pipes, and tubes, which are used in civil structures like bridges, light poles, and towers (Figure 4) [8].

But in many cases, unidirectional composites are subjected to delamination at very low stress, and these issues cannot be tolerated in some demanding applications. In [11], it is mentioned that debonding (Figure 5) occurs prior to other local defects, and this will lead to delamination (Figure 6). As mentioned earlier, most of the applications of pultruded materials are in civil engineering industries, which involve human safety. Therefore, it is essential to study the correlation of delamination onset and find a technology to enhance delamination strength as high as possible. In this technology, unidirectional composite will be wrapped with bidirectional fiberglass cloth with appropriate density and number of layers, which can enhance the delamination strength and decrease the risk of catastrophic failure of the structure. In order to validate the use of bidirectional fiberglass cloth over the cheap continuous fiberglass mat, a comparative study will be also carried out.

The aim of this work is to suggest a technique to enhancing delamination strength around bolt holes of unidirectional pultruded composite. All the experimental validation tests of the platform have been carried out, except those relating to the local analysis of stainless steel-bolted joints. Indeed, we were forced to complete the project in the allotted time, and there remain some scientific and technological points to complete numerically. Experimental validation is unfortunately no longer possible because the composite material platform is already manufactured and cannot be dismantled for testing. In this paper, we have performed a numerical analysis of the assembly areas, and we have demonstrated numerically how these areas could be reinforced by fiberglass fabrics. On the one hand, the innovation lies more in the proposal of the concept of local extra thickness to be applied to the zones of assemblies, and on the other hand, the calculations made it possible to optimize the type and the density of fibreglass fabrics Our assumptions are strongly below the critical threshold of matrix cracking. We have therefore taken into account this mechanism which is even the source of this work. Firstly, a composite micromechanical model will be set up in ABAQUS. The bidirectional fibreglass cloth wrapping method (Figure 7) will be used to reduce delamination around bolt holes, and this method will be validated. Due to the high cost of bidirectional fibreglass cloths, a study will also be carried out to select an appropriate cloth material by taking into account two aspects: density and number of layers of cloths. The selected bidirectional fibreglass cloths will be compared with conventional continuous fiberglass mat to evaluate the difference in damage reduction performance.

2. Technology Proposed and Numerical Modelling

2.1. Wrapping Technology. In the wrapping technique, unidirectional pultruded beams will be wrapped using bidirectional fiberglass cloths or continuous fiberglass mats. In this study, thin bidirectional fiberglass cloths with E-glass vinylester material was used due to their better mechanical properties (Tables 1 and 2). The orientation of bidirectional fiberglass cloths will be set to 0° and 90°, and thicknesses will be scaled down for the following simulations.

Bolted joint fasteners and drilling method are the most commonly used techniques in composite structure to join parts. While drilling a unidirectional pultruded composite structure (Figure 8), the fibres will start to separate near the bolt holes and this will lead to a huge defect in the whole structure. The separation will start from the interface between fibre and matrix, which is called debonding. This debonding in microscale will lead to delamination, and it is very essential to avoid or decrease the intensity of this defect. This fibre separation can be reduced to an extent by wrapping these unidirectional pultruded fibres using bidirectional fiberglass cloths. This will reinforce composite structure and protect them from delamination by holding unidirectional fibres together. Bidirectional fiberglass cloth will also allow the structure to be reinforced in both directions while it was before reinforced in unidirectional only.

2.2. Micromechanical Model. To study delamination, a composite micromechanical model of pultruded unidirectional
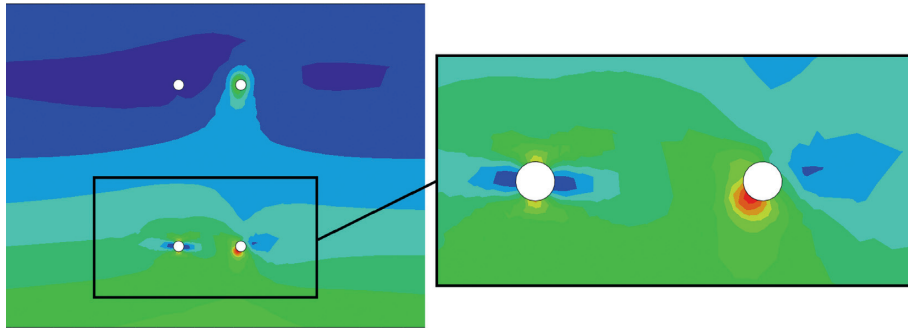
FIGURE 3: Stress concentration around the bolt holes (red contour indicating high stress) [7].

(a)

(b)

FIGURE 4: Pultruded retaining wall in Azerbaijan (a) and pultruded railway bridge barriers in England (b) [9, 10].
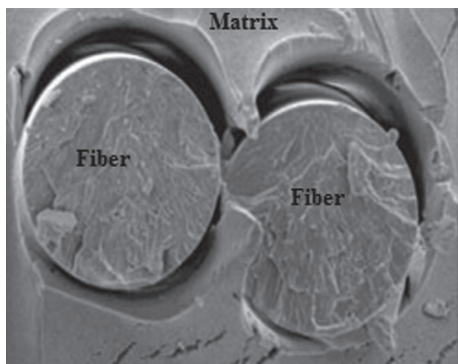
FIGURE 5: Fiber-matrix debonding [12].
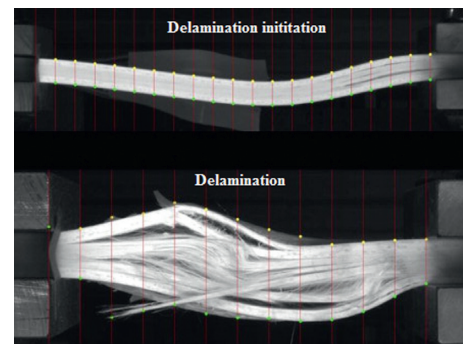
FIGURE 6: Delamination [13].

material with a hole was set up (Figure 9). This model is just a representation of composite structure with a hole that was cut through the fibres. The material properties assigned were E-glass and vinylester (Tables 3 and 4). The diameter of the fibres were 0.014 mm, and size of the micromechanical model was 0.06 mm × 0.06 mm × 0.06 mm. Fibre volume fraction is considered as around 66% (pultrusion). Fibres and matrix were created separately and assembled together. Cohesive surface contact (interface) properties were assigned between fibres and matrix.

2.3. Theoretical Considerations of Interaction Properties.
Surface-based cohesive behaviour allows the specification of generalized traction-separation behaviour for surfaces. This behaviour was offering capabilities that are very similar to the cohesive elements, which were defined using traction-separation law, and it requires only less computational time compared with cohesive element in ABAQUS. Surface-based cohesive behaviour was very easy to define, and it allows the simulation of a wider range of cohesive interactions. This method was very useful in this analysis because the surfaces
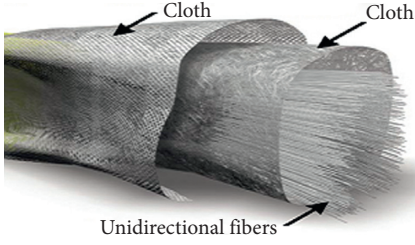
FIGURE 7: Bidirectional E-glass cloth and unidirectional E-fiberglass [14].

TABLE 1: Properties of E-glass vinylester bidirectional fiberglass composite [15].

Parameter (unit)	E-glass vinylester bidirectional
Density (kg/m^3)	1988
E_1 (MPa)	20,769
E_2 (MPa)	20,769
ϑ_{12}	0.09
G_{12} (MPa)	4133
Thickness (mm)	0.1

TABLE 2: Parameters for damage analysis of E-glass vinylester bidirectional fiberglass composite [15].

Parameter (unit)	Notation	Value
Longitudinal tensile strength (MPa)	X_T	395
Longitudinal compressive strength (MPa)	X_C	260
Transverse tensile strength (MPa)	Y_T	395
Transverse compressive strength (MPa)	Y_C	260
Longitudinal shear strength (MPa)	S_L	75
Transverse shear strength (MPa)	S_T	75
Cross product term coefficient		−0.5
Stress limit		0

were in contact (fibre and matrix), and there were no interface thicknesses.

Nominal traction stress vector t is a combination of three components: t_n, t_s, and t_t which represent the normal and two shear tractions, respectively. The corresponding separations are denoted by δ_n, δ_s, and δ_t. And cohesive element thickness is defined as T_0. Nominal strain can be written as

$$\epsilon_n = \frac{\delta_n}{T_0} \quad \epsilon_s = \frac{\delta_s}{T_0} \quad \epsilon_t = \frac{\delta_t}{T_0}. \tag{1}$$

Elastic behaviour can be represented by

$$t = \left\{ \begin{matrix} t_n \\ t_s \\ t_t \end{matrix} \right\} = \left[\begin{matrix} k_{nn} & k_{ns} & k_{nt} \\ k_{sn} & k_{ss} & k_{st} \\ k_{tn} & k_{ts} & k_{tt} \end{matrix} \right] \left\{ \begin{matrix} \delta_n \\ \delta_s \\ \delta_t \end{matrix} \right\}. \tag{2}$$

Damage modelling was helpful to simulate degradation and eventual failure of the bond between two cohesive surfaces. The failure mechanism in surface-based cohesive behaviour consists of two parameters:

(i) Damage initialization criterion

(ii) Damage evolution law

Damage will evolve according to the damage evolution law after damage initiation criterion is met. A quadratic stress damage initiation criterion and an energy damage evolution law are defined. The graph (Figure 10) shows the typical traction-separation response with a failure mechanism. The damage was assumed to initiate when a quadratic interaction function involving the separation ratios reaches a value of one. This criterion can be represented as

$$\left\{ \frac{\langle t_n \rangle}{t_n^0} \right\}^2 + \left\{ \frac{\langle t_s \rangle}{t_s^0} \right\}^2 + \left\{ \frac{\langle t_t \rangle}{t_t^0} \right\}^2 = 1, \tag{3}$$

where t_n, t_s, and t_t are the contact stress normal to the interface along first and second shear directions, respectively; t_n^0, t_s^0, and t_t^0 are the peak values of contact stress when separation is either purely normal to interface or purely in the first or second shear direction, respectively; and $\langle \rangle$ is the Macaulay bracket indicating that a purely compressive stress state does not initiate damage.

Damage evolution was assigned based on the energy. Simplest way to define the fracture energy was to specify it directly as a function of the mixed mode in tabular form. Fracture energy G_c is equal to the area under the traction-separation curve. The tie contact interaction was used to attach bidirectional fiberglass cloths to micromechanical model of unidirectional pultruded composite [16].

The cohesive elements are modelled as undergoing progressive damage leading to failure and the progressive damage modelling involves softening in the material response, which can lead to convergence difficulties in an implicit solution procedure: ABAQUS/Standard. In order to avoid these convergence issues, ABAQUS/Standard provides a viscous regularization capability that helps in improving the convergence. The use of viscous regularization of the constitutive equations causes the tangent stiffness matrix of the softening material to be positive for sufficiently small time increments [17].

In this study, traction-separation laws are regularized in ABAQUS/Standard using viscosity by permitting stresses to be outside the limits set by the traction-separation law, and this regularization process involves the use of viscous stiffness degradation variable, D_v, which is defined by the following evolution equation:

$$\dot{D}_v = \frac{1}{\mu} (D - D_v), \tag{4}$$

where μ is the viscosity parameter and D is the current damage.

For viscous material, the damage response is

$$t = (1 - D_v)\bar{t}. \tag{5}$$

Using viscous regularization with a small value of the viscosity parameter (small compared to the characteristic time increment) usually helps in improving the rate of convergence of the model in the softening regime, without compromising results. The basic idea is that the solution of the viscous system relaxes into that of the in viscid case as $t/\mu \to \infty$ where t represents time. The use of viscous regularization is a powerful and often necessary tool that enables accurate prediction of delamination, and this approach

(a)

(b)
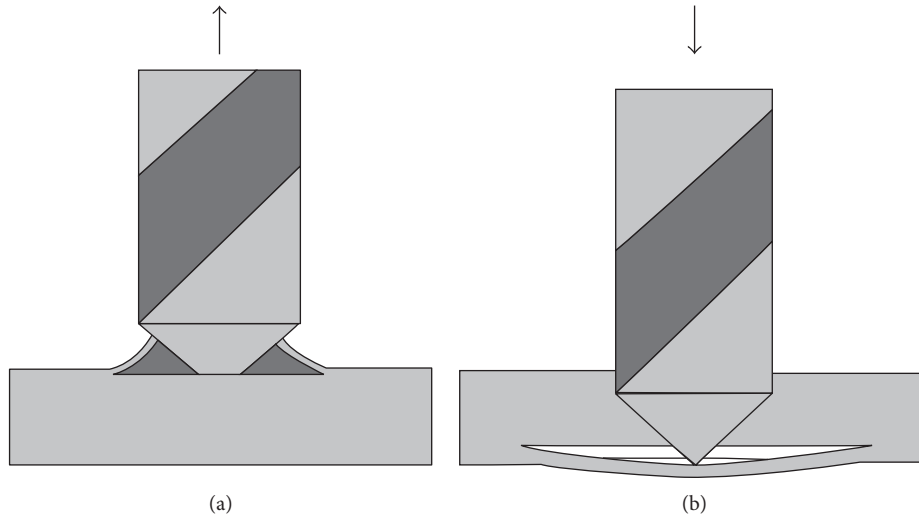
FIGURE 8: Schematic of delamination push-out at exit (a) and peel-up at the entry (b).
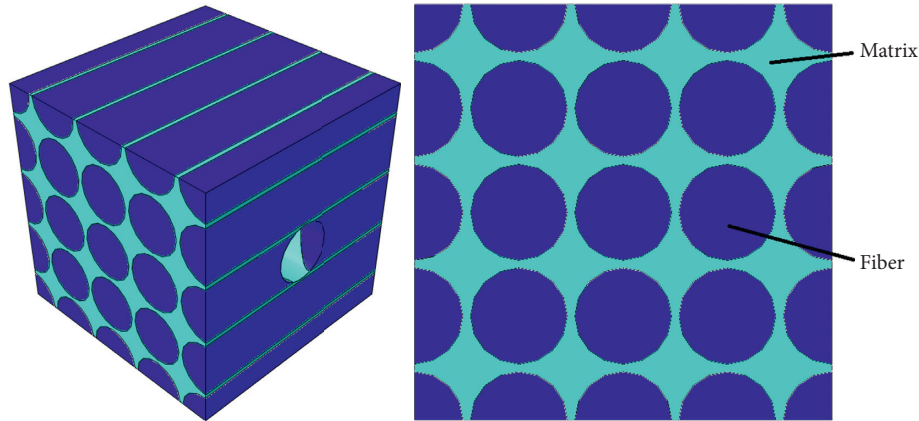
FIGURE 9: Composite micromechanical model.

TABLE 3: Properties of vinylester resin [11].

Parameter (unit)	Vinylester
Density (g/cm^3)	1.05
Poisson coefficient, ϑ	0.35
Shear modulus (GPa)	1.24
Tension	
Modulus, E (GPa)	3.2
Tensile strength, σ_{ult} (MPa)	86
Compression	
Modulus, E (GPa)	3.35
Yield strength, σ_{y} (MPa)	103

TABLE 4: Properties of E-fiberglass [15].

Parameter (unit)	E-glass
Density (g/cm^3)	2.54
Young's modulus in tension (GPa)	73
Tensile strength (MPa)	2400
Compressive strength (MPa)	1450
Shear modulus (GPa)	33.3
Poisson coefficient, ϑ	0.22
Diameter (μm)	14

is used here in order to improve the rate of convergence of the model [17, 18].

In this analysis, a global stabilization factor (dissipated energy fraction) of 2×10^{-4} was used to perform numerical analysis [19]. By adopting a weakening factor of f_w 0.3, the interfacial strength properties were reduced from the matrix material [20–22] which indicate a relatively weak interface in pultruded glass fibre-reinforced material. The elastic stiffness (per unit area) of the interface was assumed to be equal to 10^6 N/mm^3 [23]. The critical normal interface tractions

of the cohesive zone elements were equal to the normal tensile strength of the unidirectional layers in the direction normal to the fibres (Table 5), that is, 13.5 N/mm^2, and the critical shear interface tractions were equal to the unidirectional shear strength (Table 5), that is, 13.5 N/mm^2. For the pultruded material mode I, mode II, and mode III critical energy release rates G_{Ic} and $G_{\text{IIc}} = G_{\text{IIIc}}$ were taken as 0.2 N/mm and 0.5 N/mm, respectively [24]. The bidirectional fibreglass cloth was attached to the unidirectional micromechanical model using tie contact constraint in the four surfaces.
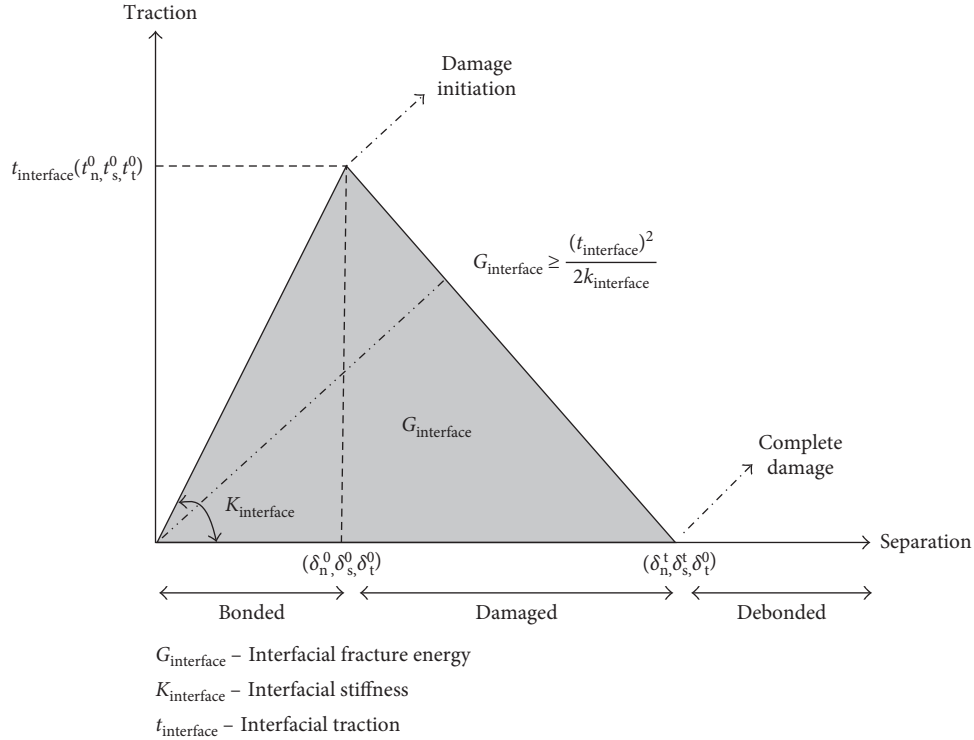
FIGURE 10: Typical traction-separation response [18].
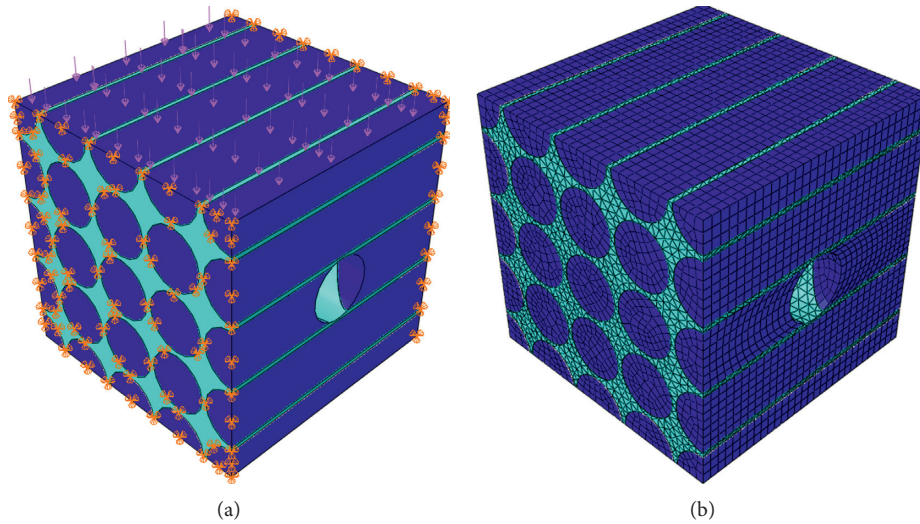
FIGURE 11: Load and boundary conditions (a) and mesh (b) on the composite micromechanical model.

2.4. Load and Boundary Conditions and Mesh. The micromechanical model was subjected to pressure force from the top. As the interest was to study delamination, left and right surfaces are constrained using the pinned join boundary condition that was allowing the material to delaminate easier and was comparatively easy for simulation convergence (Figure 11). This method of load and boundary conditions and mesh was maintained similar in all simulations that were carried out.

The parts of the model were meshed separately. Fibre was meshed using 26,664 C3D8R elements and matrix using 65,290 C3D10 elements. Cloth layer 1 was meshed using

TABLE 5: Parameters for damage analysis of E-glass vinylester unidirectional composite [16].

Parameter (unit)	Notation	Value
Longitudinal tensile strength (MPa)	X_T	1200
Longitudinal compressive strength (MPa)	X_C	620
Transverse tensile strength (MPa)	Y_T	45
Transverse compressive strength (MPa)	Y_C	100
Longitudinal shear strength (MPa)	S_L	45
Transverse shear strength (MPa)	S_T	45
Cross product term coefficient		−0.5
Stress limit		0
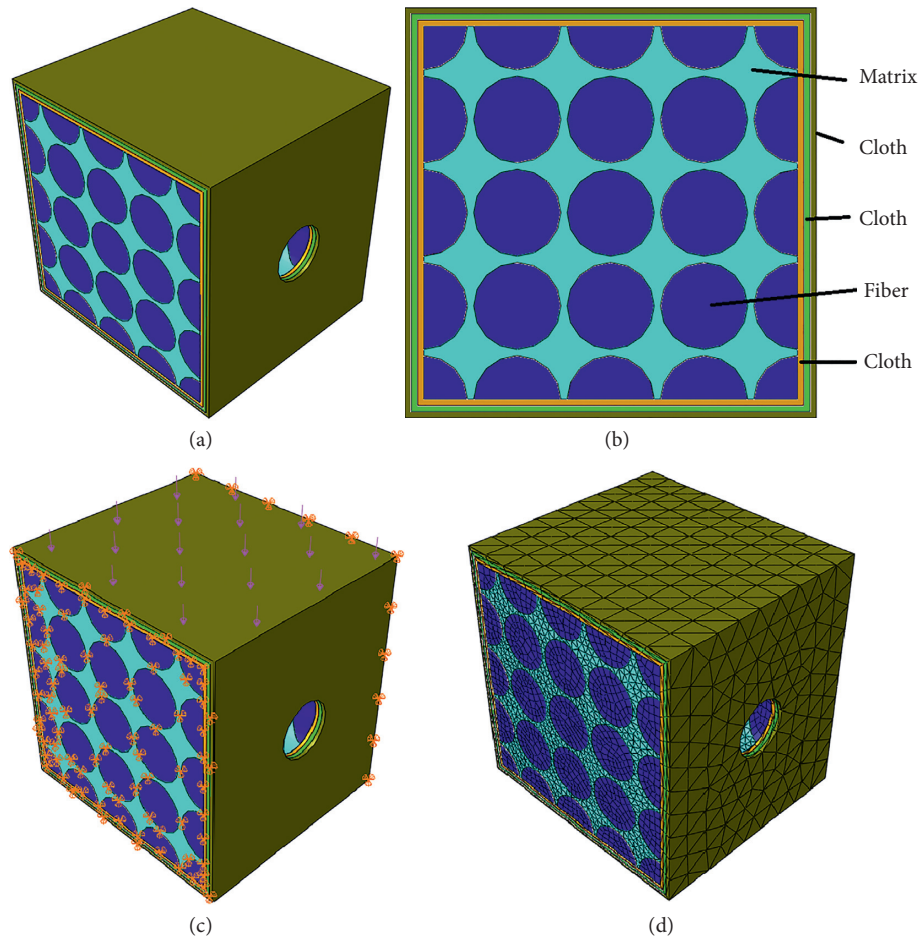
FIGURE 12: Composite micromechanical model: (a) isometric view; (b) front view; (c) load and boundary conditions; (d) mesh of composite micromechanical model with 3-layer cloth.

C3D10 2643 elements, cloth layer 2 was meshed using C3D10 2423 elements, and cloth layer 3 was meshed using 2494 C3D10 elements (Figure 12). Different simulations were performed using these composite micromechanical models to study the damage. (C3D8R: continuum 3-D, 8-node, reduced integration; C3D10: continuum 3-D, 10-node).

The bidirectional fiberglass cloths with different number of layers and densities were wrapped on the composite micromechanical model, and different simulations were performed. These simulations were carried out to select a better bidirectional fiberglass cloth, which can decrease stress concentration and damage. Due to the cost-effectiveness considerations and small thicknesses of beams, the appropriate number of layers of wraps and the better material selection were evident. Weight and thickness of the bidirectional fiberglass cloth chosen are shown in Table 6.

3. Results and Discussion

For comparison, numerical simulations were carried out without wrapping fibreglass cloths and with wrapping different layers of bidirectional fiberglass cloths. Damage initiation stress and interface damage occurring between fibre and matrix of each model were used for comparison.

TABLE 6: Weight and thickness of the bidirectional fiberglass cloth [25].

Weight (g/m^2)	Thickness (mm)
186	0.14
295	0.23
318	0.28

3.1. Micromechanical Model. Stress contour plots obtained from different numerical simulations were plotted to visualize the performance of the model before and after wrapping different layers of bidirectional fibreglass cloths. Micromechanical models were subjected to high loads in order to study damage. Figure 13(a) shows stress contour plot of the micromechanical model before wrapping bidirectional fibreglass cloths. A maximum stress of 5344 MPa and fibre-matrix separation are observed in this model. Debonding is decreased in Figure 13(b) after addition of 1 layer of bidirectional fibreglass cloth. Bidirectional fibreglass cloth wrapping reinforced the model and decreased maximum stress to 3674 MPa. Similarly, maximum stress is decreased for 2 layer and 3 layer as shown in Figure 13(c), and maximum stress is also decreased to 3175 MPa and 2433 MPa, respectively, as shown in Figure 13(d). Maximum
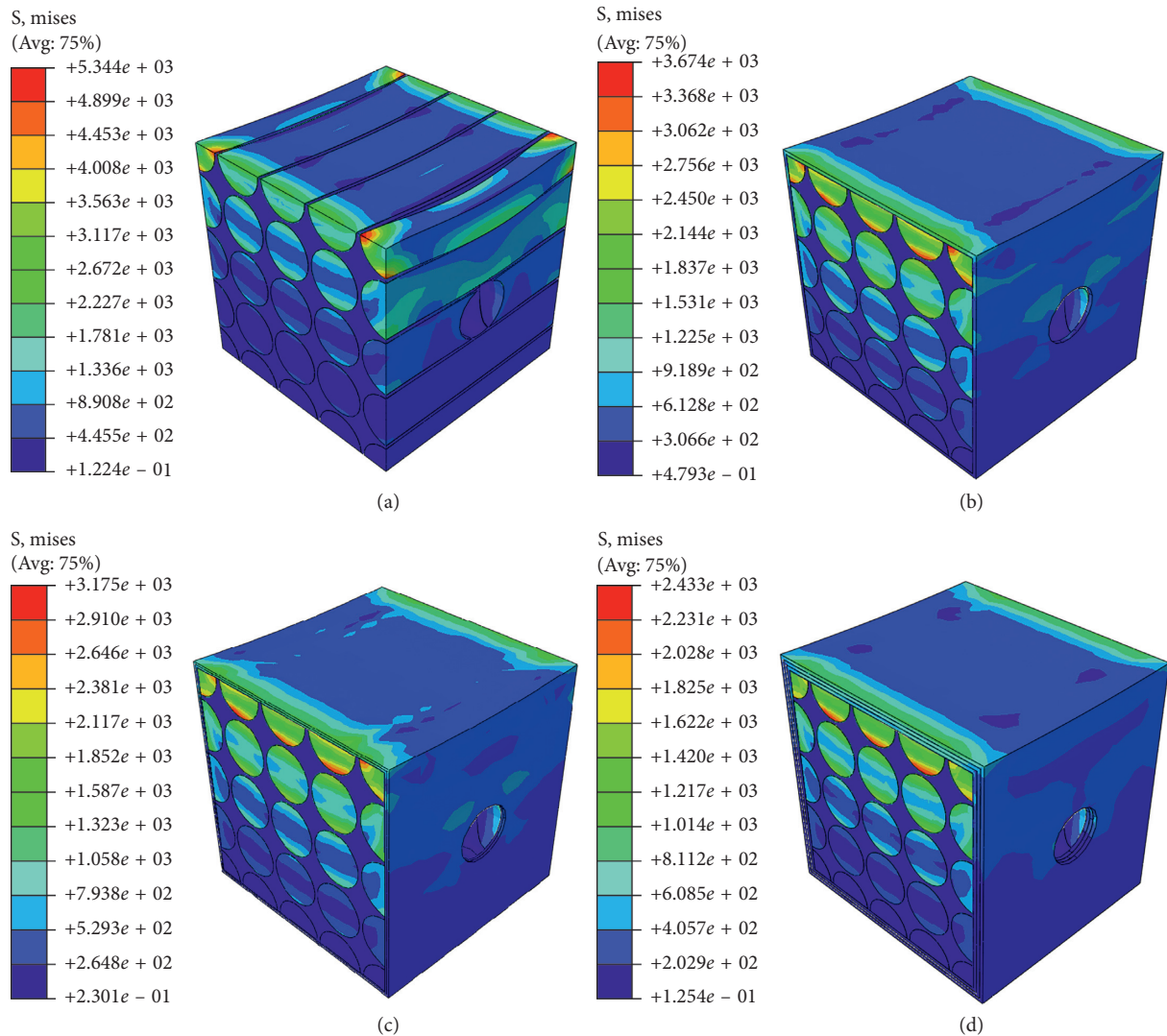
FIGURE 13: Stress on the composite micromechanical model: (a) without cloth; (b) with 1 layer cloth; (c) with 2 layer cloth; (d) with 3 layer cloth.

stresses were found near the fibre-matrix interface in all models, and addition of bidirectional fiberglass cloths results in decreasing of these stresses.

The result of stress versus damage obtained from different models was plotted together, and Figure 14 shows the behaviour of stress versus damage for each model. In the micromechanical model without cloth, damage initiation stress was estimated as 18 MPa. High interface damage and fibre-matrix debonding are observed in this model. In order to increase damage initiation stress, the micromechanical model is wrapped with one layer of bidirectional fiberglass cloth. After wrapping, fibre-matrix debonding is restricted and interface damage is decreased. As a result, damage initiation stress is increased to 23 MPa. Bidirectional fiberglass cloth wrapping has reduced fibre-matrix debonding by holding them together. Similarly, more bidirectional fiberglass cloths were wrapped, and damage initiation stress is increased to 28 MPa and 36 MPa for 2 layer and 3 layer of bidirectional fibre cloth wraps, respectively. It was observed that bidirectional fiberglass cloth wrapping assists fibre-matrix bonding to be stronger and reduces delamination,

which occurs around the bolt hole of the unidirectional pultruded model.

Considering Figure 14 into 2 areas, in Area 1, damage is initiated and stress is incrementing steadily from 16 MPa to 22 MPa for the model without cloth, 23 MPa to 51 MPa for 1-layer cloth, 28 MPa to 60 MPa for 2-layer cloth, and 34 MPa to 83 MPa for 3-layer cloth in the damage coefficient limit 0 to 0.8. The increase in the stress value near to damage coefficient 0.8 is due to starting of complete damage. In Area 2, huge variation in stress can be observed due to the complete damage to the models, and the difference in variation of the stress value for each model shows their restriction to damage. A model without cloth is fully damaged in less stress limit comparatively, and after adding bidirectional fibreglass cloths, damage is restricted and stress required for complete damage is extended for each layer.

3.2. Effect of Bidirectional Fiberglass on Platform Model.

The micromechanical analysis provided an evident result of the impact of wrapping bidirectional fiberglass cloths on
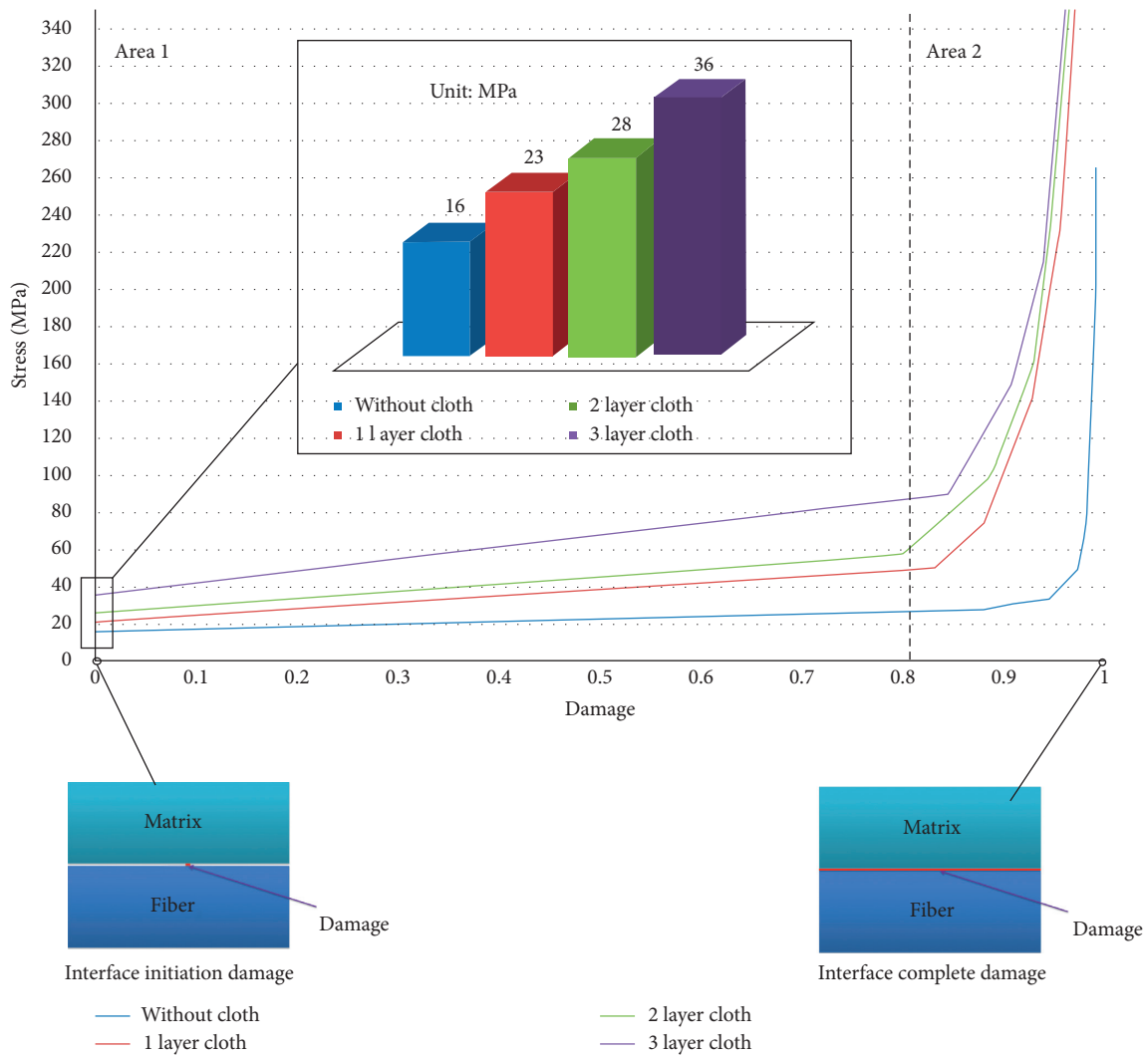
FIGURE 14: Comparison of stress versus damage.

unidirectional pultruded structure, and this method is implemented on the large smart composite platform. From the previous study [4–7], maximum stress near the bolt hole was around 75 MPa which was on ply-1 (Figure 15). After adding bidirectional fiberglass cloths to the large platform shell model, it is observed that the effect of stress concentration near the bolt hole had decreased to around 67 MPa in ply-1 (Figure 16). In this model, a maximum stress of 82 MPa was on bidirectional fiberglass cloth ply. Here, cloths act as a protective layer to the unidirectional fibreglass material from damage and decreased the stress from 75 MPa to 67 MPa. This result shows that there is an improvement in reduction of stress concentration effect on large smart composite platform, and this can enhance delamination strength.

3.3. Comparison of Different Bidirectional Fibreglass Cloths.
To select an appropriate bidirectional fibreglass cloth material which can enhance delamination strength, numerical simulations were performed with three different densities

and results were plotted (Figure 17). They were selected considering the beam thickness of smart composite platform and industrial availability. The bidirectional fiberglass cloth with a weight of $186 \, g/m^2$ and thickness of $0.14 \, mm$ has damage initiation stress around 41 MPa; the bidirectional fiberglass cloth with a weight of $295 \, g/m^2$ and thickness of $0.23 \, mm$ has damage initiation stress around 49 MPa; and the bidirectional fiberglass cloth with a weight $318 \, g/m^2$ and thickness $0.28 \, mm$ has damage initiation stress around 59 MPa. The bidirectional fiberglass cloth with a weight of $318 \, g/m^2$ and thickness of $0.28 \, mm$ which showed better performance in reducing damage has been selected for large smart composite platform.

In order to study the effect of number of wraps, different layers of bidirectional fiberglass cloths were wrapped on the micromechanical model and numerical simulations were performed. The results were plotted (Figure 18), and the damage initiation stress value after adding each layer was estimated. It was observed that after 3 layers of wrapping, damage initiation stress was saturating. Simulations were carried out up to 7 layers in order to estimate the variation in

S, mises
PLY-1 (bottom)
(Avg: 75%)

74.637
68.418
62.198
55.978
49.759
43.539
37.319
31.099
24.880
18.660
12.440
6.221
0.001

Max: 74.637
Elem: long beam-1.2306
Node: 69
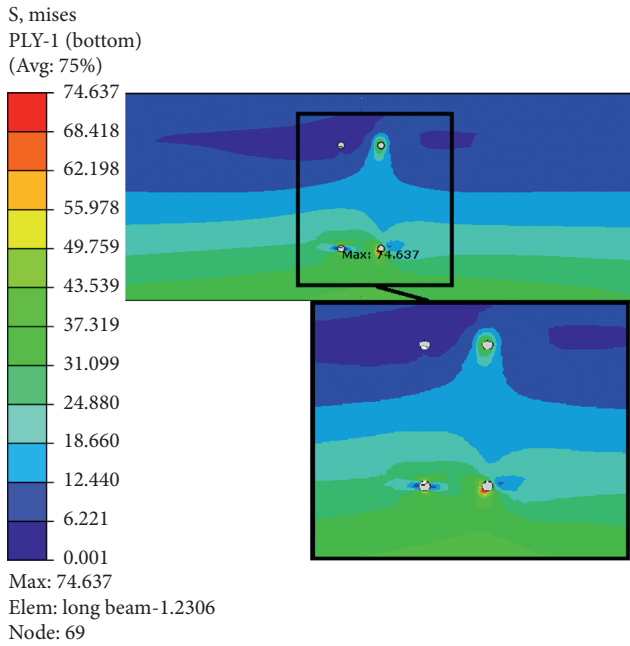
FIGURE 15: Stress contour plot around bolt for unidirectional pultruded composite platform before adding cloth.

S, mises
PLY-1 (bottom)
(Avg: 75%)

82.021
75.186
68.351
61.516
54.681
47.846
41.011
34.176
27.341
20.506
13.671
6.836
0.001

Max: 67.769
Elem: long beam-1.2303
Node: 1562
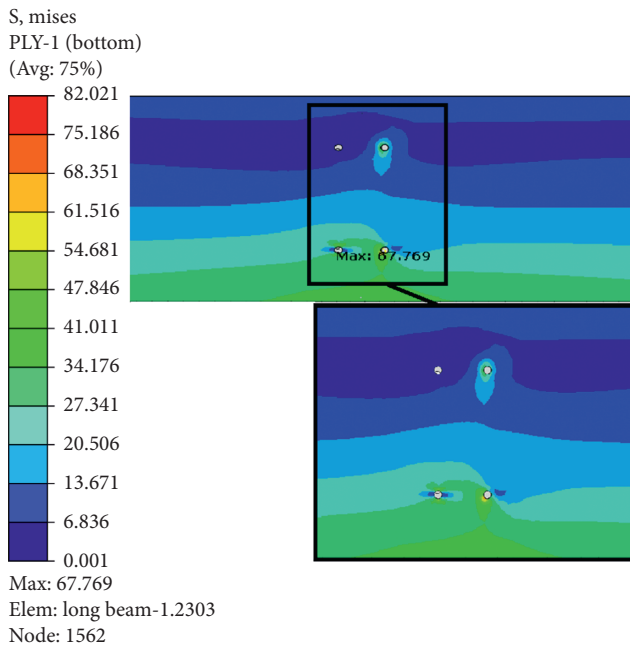
FIGURE 16: Stress contour plot around bolt for unidirectional pultruded composite platform after adding cloth.

Unit: MPa

- Without cloth
- Weight 186 g/m^2, thickness 0.14 mm
- Weight 295 g/m^2, thickness 0.23 mm
- Weight 318 g/m^2, thickness 0.28 mm

FIGURE 17: Comparison of damage initiation stress for different bidirectional fiberglass cloths with 3 layers.

Unit: MPa

- Without cloth
- 1 layer
- 2 layer
- 3 layer
- 4 layer
- 5 layer
- 6 layer
- 7 layer
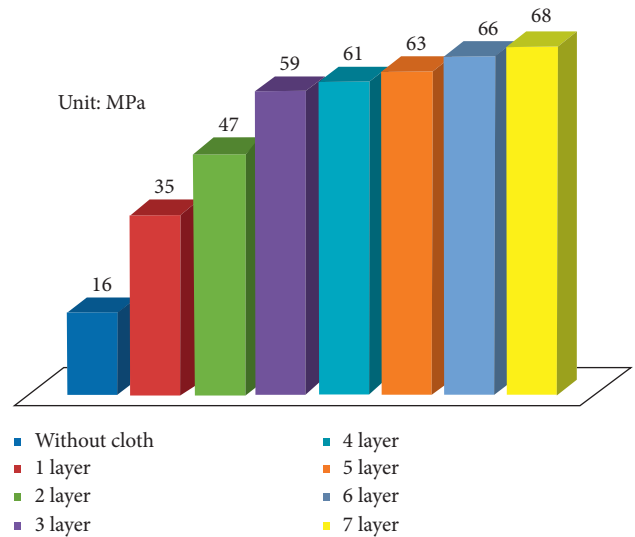
FIGURE 18: Comparison of damage initiation stress for 7 layers.

exceed interlaminar shear strength (ILSS) [26]. In Handbook of Adhesion [27], interlaminar shear strength (ILSS) for E-glass/vinylester was estimated as 51 MPa. As mentioned above, damage initiation stress for layer 3 is 59 MPa; that is, damage initiation stress for layer 3 is above interlaminar shear strength (ILSS) limit, and it can restrict delamination. So, the number of layers is selected as three.

3.4. Comparison of Bidirectional Fiberglass Cloths and Conventional Continuous Fiberglass Mats. Bidirectional fiberglass cloths have better mechanical properties compared to the conventional continuous fibreglass mat due to the proper orientation of fibres in both directions, whereas fibres are oriented randomly in mats (Figure 20). As the aim of this study is to decrease damage and increase delamination strength, a better material that can reinforce the structure

stress values. Damage initiation stress was 35 MPa, 47 MPa, 59 MPa, 61 MPa, 63 MPa, 66 MPa, and 68 MPa from layer 1 to layer 7, respectively. From Figure 19, it is evident that layer 4, layer 5, layer 6, and layer 7 have very less improvement in damage initiation stress. The addition of more layers without obtaining better performance will increase the budget and the weight of the structure. Delamination failure will occur when the transverse shear load experienced will

FIGURE 19: Damage initiation stress versus layer.

(Unit: MPa)	1	2	3	4	5	6	7
	35	47	59	61	63	66	68

(a)
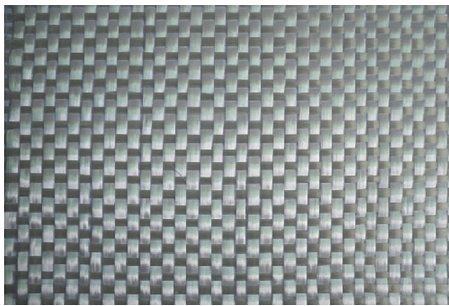
(b)

FIGURE 20: (a) Continuous fiberglass mat and (b) bidirectional fiberglass cloth.

will be a better choice. The quality of each mat from different industries is dissimilar, and as mentioned earlier, the applications of pultruded structures are mainly in civil engineering. So, selection of good quality material c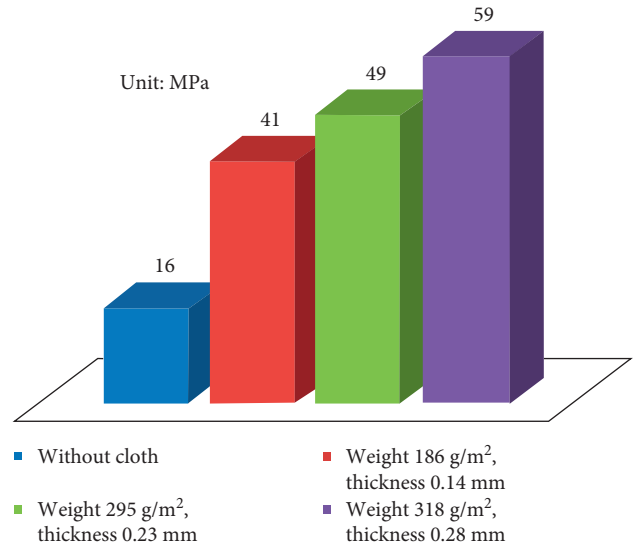loth is better compared to that of lower quality mat in order to avoid the risk of human life and increase safety. Moreover, from Figure 21, damage initiation stress for bidirectional fiberglass and continuous fiberglass mat are 59 MPa and 44 MPa, respectively. This difference shows that bidirectional fiberglass cloths have better properties in restricting delamination. Considering all these facts, bidirectional fiberglass cloths have better performance despite their cost compared to continuous fibreglass mats.
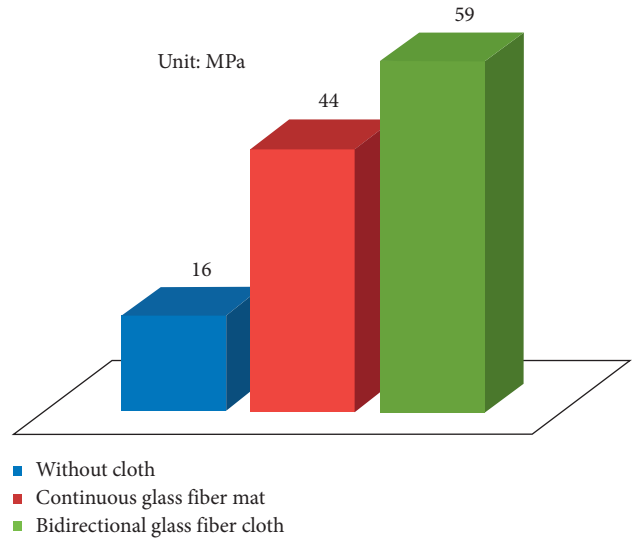
FIGURE 21: Comparison of the damage initiation stress for bidirectional fiberglass cloths and continuous fiberglass mats.

4. Conclusion

Unidirectional composites are subjected to delamination at very low stress, and these issues cannot be tolerated in some demanding applications. Most of the applications of pultruded structures are in civil engineering, which involves human safety. Therefore, it is essential to study the correlation of delamination onset and find a technology to enhance delamination strength as high as possible. The aim of this work was to enhance delamination strength of unidirectional pultruded large smart composite platforms. The micromechanical model of unidirectional pultruded composite was created, and different simulations were carried out in order to investigate defects. From the bibliography, it was found that debonding between fibre and matrix will occur before other defects, and this will lead to delamination. Bidirectional fiberglass cloth wrappings were used to prevent delamination, and different simulations were performed without wrapping cloths and with different layers of cloth wrapping. From a numerical simulation results, it was estimated that the bidirectional fiberglass cloth wrapping method was effective in preventing delamination. Due to the high cost of bidirectional fiberglass cloths, a study was also performed considering the number of layers and density to select an appropriate bidirectional fiberglass cloth material that can be considered as cost effective. After these studies, bidirectional fiberglass cloth with a weight of 318 g/m², thickness of 0.28 mm, and 3 layers of wrap were selected. The result of a comparison study shows that bidirectional fiberglass cloths have better ability to restrict delamination compared to continuous fiberglass mats.

Data Availability

The data used to support the findings of this study are available from the corresponding author upon request.

Conflicts of Interest

The authors declare that there are no conflicts of interest regarding the publication of this paper.

References

[1] M. Drissi-Habti, "Smart composite materials project DECID2 for structural applications," *JEC Composites*, vol. 42, pp. 28-29, 2008.

[2] L. M. P. Durão, J. M. R. Tavares, V. H. C. De Albuquerque, J. F. S. Marques, and O. N. Andrade, "Drilling damage in composite material," *Materials*, vol. 7, no. 5, pp. 3802–3819, 2014.

[3] L. M. P. Durão, D. J. S. Gonçalves, J. M. R. S. Tavares, V. H. C. de Albuquerque, and A. T. Marques, "Comparative analysis of drills for composite laminates," *Journal of Composite Materials*, vol. 46, no. 14, pp. 1649–1659, 2012.

[4] X. Chapeleau, M. Drissi-Habti, and T. Tomiyama, "Embedded optical fiber sensors for in situ and continuous health monitoring of civil engineering structures in composite materials," *Materials Evaluation*, vol. 68, no. 4, pp. 409–415, 2010.

[5] X. Chapeleau, M. Drissi-Habti, and T. Tomiyama, "Embedded optical fiber sensors for in situ and continuous health monitoring of composite materials in civil engineering structures," *Japan Society for Composite Materials*, vol. 36, no. 1, pp. 227–235, 2010.

[6] A. Cordelle and M. Drissi-Habti, "Nanoindentation characterization of vinylester glass-fiber composites submitted to dense ultraviolet radiation exposure," *Materials Evaluation*, vol. 71, no. 4, 2013.

[7] I. D. Madukauwa-David and M. Drissi-Habti, "Numerical simulation of the mechanical behavior of a large smart composite platform under static loads," *Composites Part B: Engineering*, vol. 88, pp. 19–25, 2016.

[8] P. Carlone, G. Salvatore Palazzo, and R. Pasquino, "Pultrusion manufacturing process development by computational modelling and methods," *Mathematical and Computer Modelling*, vol. 44, no. 7, pp. 701–709, 2006.

[9] Creative Pultrusions, *Composite Sheet Pile Wall System*, Creative Pultrusions, Pleasantville, PA, USA, 2016, http://www.creativepultrusions.com/index.cfm/fiberglass-pultruded-systems/composite-sheet-pile-system.

[10] G. Ginger, *Rail Line Landmark Restoration via Pultrusion*, CompositesWorld, Scottsdale, AZ, USA, 2016, http://www.compositesworld.com/articles/rail-line-landmark-restoration-via-pultrusion-.

[11] M. U. Farooq, L. A. Carlsson, and B. A. Acha, "Determination of fiber/matrix adhesion using the Outwater–Murphy single fiber specimen," *Engineering Fracture Mechanics*, vol. 76, no. 18, pp. 2758–2765, 2009.

[12] M. S. Kumar, K. Raghavendra, M. A. Venkataswamy, and H. V. Ramachandra, "Fractographic analysis of tensile failures of aerospace grade composites," *Materials Research*, vol. 15, no. 6, pp. 990–997, 2012.

[13] Y. Bai, T. Vallée, and T. Keller, "Delamination of pultruded glass fiber-reinforced polymer composites subjected to axial compression," *Composite Structures*, vol. 91, no. 1, pp. 66–73, 2009.

[14] DuraGrid, *DURAGRID® Benefits*, 2016, http://www.prmetals.com/Product/Grating/Fiberglass-Grating/Pultruded-Fiberglass-Grating/DURADEK/DURADEK-I6000-Pultruded-Grating–112-Depth.

[15] R. Karakuzu, T. Gülem, and B. M. İçten, "Failure analysis of woven laminated glass–vinylester composites with pin-loaded hole," *Composite Structures*, vol. 72, no. 1, pp. 27–32, 2006.

[16] A. Shukla, Y. D. Rajapakse, and M. E. Hynes, *Blast Mitigation: Experimental and Numerical Studies*, Springer Science & Business Media, Berlin, Germany, 2013.

[17] ABAQUS, *Abaqus 6.10 Analysis User's Manual, Volume V: Prescribed Conditions, Constraints & Interactions. 33.1.10 Surface-Based Cohesive Behavior*, 2016, http://abaqusdoc.ucalgary.ca/pdf_books/ANALYSIS_5.pdf.

[18] W. G. Jiang, R. Z. Zhong, Q. H. Qin, and Y. G. Tong, "Homogenized finite element analysis on effective elastoplastic mechanical behaviors of composite with imperfect interfaces," *International Journal of Molecular Sciences*, vol. 15, no. 12, pp. 23389–23407, 2014.

[19] A. M. G. Coelho, J. T. Mottram, and N. Matharu, "Virtual characterization of delamination failures in pultruded GFRP angles," *Composites Part B: Engineering*, vol. 90, pp. 212–222, 2016.

[20] M. Knops, *Analysis of Failure in Fiber Polymer Laminates: The Theory of Alfred Puck*, Springer Science & Business Media, Berlin, Germany, 2008.

[21] A. Puck and H. Schürmann, "Failure analysis of FRP laminates by means of physically based phenomenological models," *Composites Science and Technology*, vol. 62, no. 12-13, pp. 1633–1662, 2002.

[22] J. Qureshi, J. T. Mottram, and B. Zafari, "Robustness of simple joints in pultruded FRP frames," *Structures*, vol. 3, pp. 120–129, 2015.

[23] P. P. Camanho, C. G. Davila, and M. F. De Moura, "Numerical simulation of mixed-mode progressive delamination in composite materials," *Journal of Composite Materials*, vol. 37, no. 16, pp. 1415–1438, 2003.

[24] A. M. G. Coelho, "Finite element guidelines for simulation of delamination dominated failures in composite materials validated by case studies," *Archives of Computational Methods in Engineering*, vol. 23, no. 2, pp. 363–388, 2016.

[25] HexForce, *Hexcel Technical Fabrics Handbook*, HexForce, Stamford, CT, USA, 2016, http://www.hexcel.com/Resources/DataSheets/Brochure-Data-Sheets/HexForce_Technical_Fabrics_Handbook.pdf.

[26] Z. Fan, M. H. Santare, and S. G. Advani, "Interlaminar shear strength of glass fiber reinforced epoxy composites enhanced with multi-walled carbon nanotubes," *Composites Part A: Applied Science and Manufacturing*, vol. 39, no. 3, pp. 540–554, 2008.

[27] D. E. Packham, *Handbook of Adhesion*, John Wiley & Sons, Hoboken, NJ, USA, 2006.

Research Article

Bioimmobilized Limestone Powder for Autonomous Healing of Cementitious Systems: A Feasibility Study

Nafeesa Shaheen,[1] Rao Arsalan Khushnood [ORCID],[2] and Siraj Ud din[1]

[1]*NUST Institute of Civil Engineering (NICE), School of Civil and Environmental Engineering (SCEE), National University of Sciences and Technology (NUST), Sector H-12, Islamabad 44000, Pakistan*
[2]*Department of Structural, Geotechnical and Building Engineering (DISEG), Politecnico di Torino, Corso Duca degli Abruzzi 24, Torino 10129, Italy*

Correspondence should be addressed to Rao Arsalan Khushnood; rao_nust@yahoo.com

For preserving concrete structures and hindering ingress of chemicals through cracks and fissures, repair is inevitable. Microbial calcite precipitation is an intrinsic approach for crack rectification and emulating way of sustainability for reducing anthropogenic greenhouse gases (GHGs) along with conserving the natural resources. In this study, *Bacillus subtilis* strain is applied for intrinsic repair of concrete's cracks because of its high pH endurance and capability of sporulation. For prolonged survival of microorganisms, immobilization technique was employed. *B. subtilis* was immobilized through limestone powder (LSP) before adding into cement matrix. Self-healing proficiency of *B. subtilis* was deliberated in terms of mechanical strength regain after cracking at 3, 7, 14, and 28 days. To examine the microstructure and characterization of healing precipitate, micrographical (field emission scanning electron microscopy), chemical (energy dispersive X-ray), and thermal (thermogravimetric analysis) analyses were performed after the healing period of 28 days. The results revealed evident signs of calcite precipitation in nano-/microcracks subsequent to microbial activity. Furthermore, immobilized LSP improved the compressive strength of the analyzed formulations.

1. Introduction

Concrete, an extensively used construction material, is a source of anthropogenic greenhouse gas (GHG) emissions, depleting the raw materials, consuming the fossil fuels, and intensifying the environmental concern [1]. Additionally, it is susceptible to crack under tensile stresses, ensuing in the dramatic increase in its porosity, consequences in declined strength, and durability [2]. Numerous advanced cementitious systems have been investigated and practiced for limiting the ingress of deleterious chemicals through pores for enhancing the durability of cementitious systems [3]. But they involved external interventions which are labor dependent and cost extensive [4]. Researchers are probing for sustainable solutions to reduce cost as well as the environmental impacts. One of the potential solutions is self-healing concrete, which can repair its cracks itself [5].

Self-healing mechanisms in concrete are categorized as autogenous and autonomous healing [6]. Autogenous self-healing can be achieved by adding anhydrous cement particles or some pozzolanic material. When cracks appear in humid environments, anhydrous particles endure secondary hydration that seals the internal microcracks and fissures. But it is a limited process with minimal recurring rate having ability of 0.1-0.2 mm trivial crack-healing widths [7, 8]. For accomplishing distinct crack-healing widths by persistent process of repairs, autonomous healing is recommended [9]. Concrete, autonomously, can be healed through addition of engineered cementitious crystalline admixtures, polymers, shape-memory alloys, and microbes [10]. Microbial calcite precipitation attained imperative position among all of them since calcite formation is a way of emulating sustainability in cementitious systems [11]. Microbes secrete calcite under favorable surroundings; the

secreting process consumes CO_2 from the environment and acts as sink for CO_2 dumping [12]. But problems associated with such healing systems are survival of bacteria for relatively longer periods and reduction in mechanical properties of concrete [13]. Moreover, the healing rate depends upon the type of microbial strain, its endurance in high alkalinity, food source, and immobilization techniques [14]. Microbes having ability of sporulation can stay relatively long in dormant stage and are therefore preferred in the bio-influenced cementitious systems [15]. Microbes are either directly induced through mixing water or immobilized using different techniques [16]. These immobilization techniques include encapsulation, entrapment, and adsorption of microbes [17]. These immobilization techniques are reported efficient for enhancing the microbes' survival but deficient in attaining intended mechanical properties [18, 19].

Numerous researchers are probing for optimization of immobilization techniques and struggling for appropriate immobilizers. Wiktor and Jonker embedded microbe's *B. alkalinitrilicus* and calcium lactate into porous expanded clay (EC) particles for formulating healable cementitious mortar. Both components are adsorbed on the surface and entrapped into pores of EC. EC particles released microbes on ingress of water and achieved maximum of 0.46 mm crack-healing width [20]. In another study, *B. sphaericus* were adsorbed in diatomite earth (DE) and offered 0.15 to 0.17 mm crack-healing widths. When *B. sphaericus* immobilized through polyurethane sheet or silica gel, they contributed in lowering the permeability of the system [18, 21]. Then, microencapsulation technique was used for immobilization of microbes into melamine capsules using the condensation process. Maximum crack-healing width of 0.97 mm was attained, which was 40% to 80% higher as compared to purely melamine capsules, but it reduced the compressive strength by 15–34% [22]. Hydrogels were also employed for microbial immobilization, and microbes were attached to hydrogels through the cross-linking process. Hydrogels repaired cracks up to 0.5 mm in mortar [19]. Natural diatomite has been investigated for bacterial adsorption and entrapment into the pores with final insertion made in the form of pellets. Addition of pellets enhanced compressive strength but lowered the permeability of the resultant matrix [23]. Ceramsite (sand) was also used as a carrier, but microbes and nutrients were immobilized separately in that case, eventually providing an accomplished repair rate of 87.5% [24]. Expanded perlite (EP) was also tried for enhancing microbial survival, and the results were compared to direct induction and EC [25]. Furthermore, zeolite powder, graphite nanotubes (GNPs), and light weight aggregate (LWA) have also been explored for immobilization of microbes [15, 16]. The state of the art highlighted that each bioimmobilizer has some related pros and cons. Researchers are still struggling to explore viable alternatives to successfully immobilize microbes in cementitious systems for relatively longer periods.

This work is basically a contributing effort to explore potential usage of LSP as an immobilizer in self-healing cementitious systems. LSP has been employed in the construction industry since eras, and it is still divulging

contemporary applications owing to its versatility. It is a by-product of aggregate formation from rocks and a prime source of calcium oxide (CaO) provision in the cement manufacturing industry [26]. Moreover, it has been investigated as secondary raw material (SRM) in the cementitious systems for dense microstructure and imparting durability as a cement and sand replacement for fabricating a sustainable concrete to shrink CO_2 footprints [26–28]. Furthermore, LSP is an inert media and acts as a filler, but it reacts with aluminates phases to form carboaluminates and influence the hydration rates of cementitious systems [29]. Initially, hemicarboaluminate component was formed, and then, it converted into monocarboaluminate (Al_2O_3-Fe_2O_3-mono) AFm group [30]. The newly formed AFm improved the microstructure of cementitious systems and enhanced its durability. In a recent study, LSP was used as a cement replacement to enhance calcite precipitation rate via CO_2 curing. Supplementary content replacement of LSP helped in more calcite formation owing to pore structure and nucleation site provision by LSP [31]. The promising results of that study motivated the researchers to investigate the feasibility of LSP as a microbial immobilizer in self-healing cementitious systems as calcite production is a key for microbial activity. Moreover, researchers supported the argument that LSP addition influenced the mechanical properties of cementitious systems positively such as melamine microencapsulation that reduced the compressive strength [22]. Furthermore, its chemical nature resembles instigated calcite that makes it compatible to provide sufficient sites for precipitation as GNPs serving as microbial immobilizers killed the microbes [16]. Additionally, LSP retains its shape and position by filling the empty voids that ensure its homogeneous distribution inside the host matrix for uniform healing.

2. Experimental Program

2.1. Materials

2.1.1. Cement and Sand. Ordinary Portland cement CEM-I (grade 53), conforming to ASTM C-150, was used for all mortar formulations. The average particle size of cement grains is 16.4 μm with density of 3.17 g/cm^3. The oxide composition as determined via X-ray fluorescence (XRF) test is presented in Table 1.

Locally available sand from Lawrencepur, Pakistan, was used in the study. The fineness modulus of sand was determined according to the ASTM C-136, and the calculated value was 2.018 with specific gravity of 2.65 having $D_{50} = 0.215$ mm. Absorption capacity of sand was 2.4% as determined according to ASTM C-128.

2.1.2. Microorganisms. Cementitious composite's environment is highly alkaline in nature having pH around 11–13 [32]. So, bacterial strains must be capable of enduring high pH and have ability of sporulation for ensuring survival within the harsh environment of cementitious composites [33]. Moreover, bacterial strains must be proficient in production of copious amount of calcite, which is

TABLE 1: Chemical composition of OPC and LSP (%).

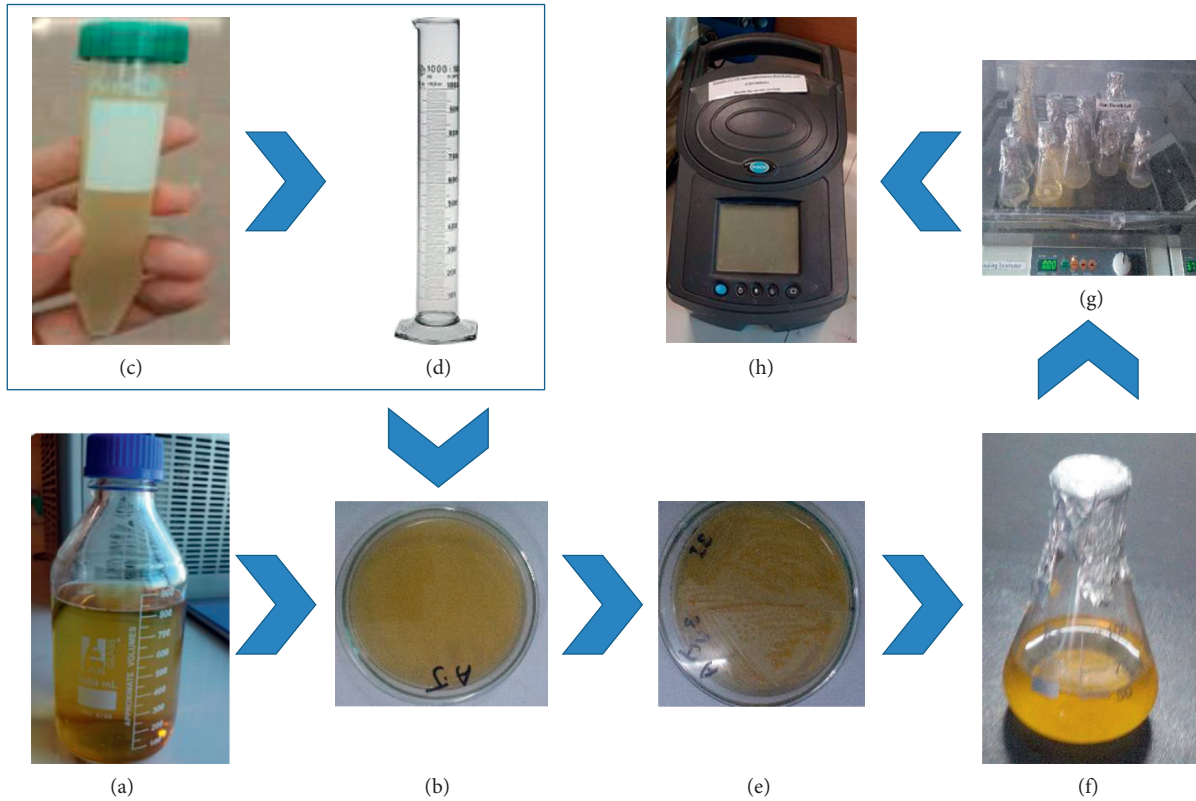| Parameters	CaO	SiO_2	MgO	Al_2O_3	Fe_2O_3	TiO_2	Na_2O	K_2O	P_2O_5	MnO	LOI
OPC	65.00	19.19	2.23	4.97	3.27	0.29	0.58	0.51	0.08	0.04	3.84
LSP	52.67	3.00	0.67	0.69	0.27	0.04	0.30	0.10	—	0.01	42.24

FIGURE 1: Microbial solution preparation. (a) LB media. (b) Agar plating for growth of microbial colonies. (c) *B. subtilis* spores. (d) Distilled saline. (e) Microbial colonies. (f) Inoculum in LB. (g) Incubation in shaker. (h) OD measurements.

responsible for crack healings [34]. *Bacillus subtilis*, soil-based bacteria, was selected for the purpose. *B. subtilis* is a gram-positive alkaliphilic bacterium having characteristics of sporulation and can survive for prolonged durations [35].

B. subtilis was revived from glycerol stock. 1 ml of frozen glycerol was mixed with 5 ml of 0.9% autoclaved saline solution. Then, this solution was spread on agar media by cotton swab and incubated for 24 hours. Nutrition broth used for *B. subtilis* was standard Luria broth (LB) consisting of 5 g tryptone, 5 g NaCl, and 2 g of LG broth in 1000 ml of distilled water. Incubation was done for 6 to 8 hours at 37°C while shaking at 200 rpm; after that, 15 ml of LB was inoculated on satirized colony of *B. subtilis*.

For sporulation, Difco sporulation medium (DSM) was used. DSM consisted of 2.5 g of peptone, 0.1 g of KCl, 1.5 g of meat extract, 0.5 ml of $MgSO_4$ (1 M), and 0.25 g of $MnSO_4$ in 500 ml of water and sterilized by autoclave. 0.25 ml of $CaCl_2$, 0.5 ml of $FeSO_4$, and 2.5 ml of LB was added into DSM shown in Figure 1(a). The entire solution was incubated for 4 days with shaking at 200 rpm at 37°C. Bacterial cells were pelletized at 9000 rpm for 20 minutes then washed 8 to 10 times. Spores were identified by light microscope. Bacterial solution is shown in Figure 1(c). Calcium lactate was used as food source for microbes.

The concentration of bacteria in the solution was calculated by HACH DR 2400 portable spectrophotometer shown in Figure 1(h). Spectrophotometer was calibrated by using 0.5 ml blank solution at 600 nm wavelength. Bacteria concentration in the solution was measured using the expression $Y = 8.59 \times 10^7 X^{1.3627}$ [36], where Y is bacterial concentration and X is wavelength value at OD_{600}. The cell concentration during the mixing of the mortar samples was kept constant at 6×10^6 cells/cm^3.

2.1.3. Limestone Powder.

LSP used in the study was taken from local source and produced by milling of limestone rock. Average particle size of LSP was 22.3 μm with a specific surface area of 3048 m^2/kg and absorption capacity of 26% having density of 2.72 g/cm^2. Particle size distribution of LSP is given in Figure 2 and XRF analysis results are presented in Table 1.

The field emission scanning electron microscope (FESEM) image of LSP is shown in Figure 3. It is evident from SEM that the LSP particles are rhombohedral in nature with sharp indents having rough superficial textures and apparently seem porous. These characteristics contribute in
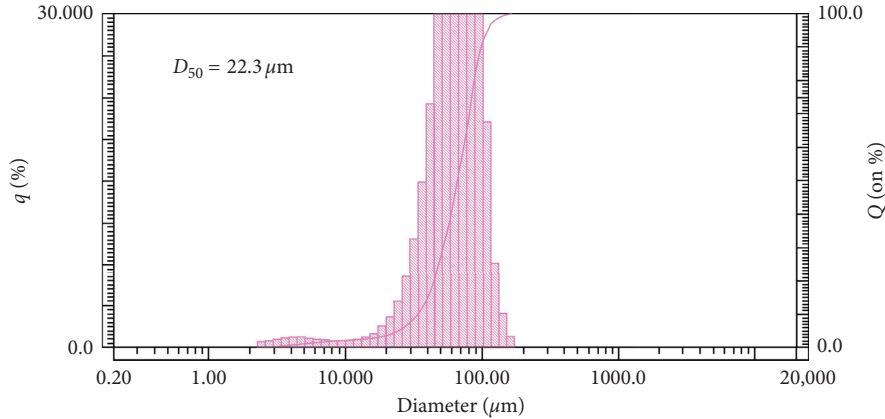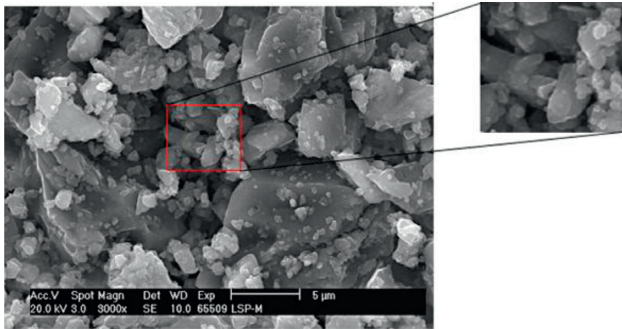
FIGURE 2: Particle size distribution of LSP.

FIGURE 3: FESEM micrograph of LSP.

developing good bond among grains of cementitious matrix [37, 38].

2.2. Mixing and Testing Regimes. Two types of formulations were investigated with their mix proportions mentioned in Table 2. Standard consistency was ensured in accordance with ASTM standard C191-11. Initial and final setting times of mortar formulations were monitored as per the standard set forth in ASTM C187-11. The analyzed formulations were designated as CM and LSP-B. CM corresponds to the controlled formulation without any addition of LSP, whereas LSP-B contains *B. subtilis* immobilized via 10% LSP in replacement to cement. Mix proportion of cement to sand was set as (1 : 1.4) with constant water to cement ratio (w/c) of 0.4. Quantities of cement and sand were 930 kg/m³ and 1400 kg/m³ with water 372 l/m³. Calcium lactate of 18.7 kg/m³ was used, which was 2% of the cement in both formulations, whereas bacterial solution of 7.6 Liter/m³ was only added in LSP-B formulation. Limestone powder particles were soaked in bacterial solution for 24 hours to ensure maximum adsorption and entrapment.

All ingredients were mixed in Hobart mixer of 5 L capacity in accordance with ASTM C-305. Mortar cube specimens of $50 \times 50 \times 50$ mm³ dimensions were prepared for both the formulations. Specimens were demolded after 24 hours and moist cured till the age of testing in controlled conditions (25°C temperature, 100% relative humidity).

Compressive resistance of specimens was gauged at the age of 3, 7, 14, and 28 days in accordance with ASTM C-109.

For healing inspection, specimens were precracked at 3, 7, 14, and 28 up to 80% of their maximum compressive strength $(0.8 \times \text{fc})$ of respective days to induce internal microcracks. The precracked specimens were immersion cured for the healing period of 28 days. After that, the specimens were again subjected to compressive strength analysis, and healing was estimated in terms of percentage regain in compressive strength using the following relation:

$$\text{RCS}\% = \left[1 - \frac{\text{Cu}_{28} - \text{Cr}}{\text{Cu}_{28}} \times 100 \right] \quad (1)$$

where Cu_{28} = ultimate compressive strength at 28 days and Cr = regained compressive strength after 28 days of curing.

In total, 48 samples were casted, and reported values are the average of three specimens. Field emission scanning electron microscope (FESEM), energy dispersive X-ray analysis (EDX), and thermogravimetric analysis (TGA) were employed to evidence the precipitation of $CaCO_3$.

3. Results and Discussions

For assessment of self-healing efficiency, two types of testing were conducted, and their results are discussed here. One was based on compressive strength analysis while the other was related to the affirmation of calcite precipitates in the induced cracks, through FESEM, EDX, and TGA.

3.1. Compressive Strength Analysis. Compressive strength of mortar specimens was measured using MCC8 compression-testing machine at a controlled loading rate of 0.2 MPa/sec conforming to standard ASTM C-109. The attained compressive resistance of the investigated formulations is given in Figure 4 at the age of 3, 7, 14, and 28 days. It can be seen that the addition of *B. subtilis* immobilized by LSP improved the strength of mortar specimens in compression during the entire hydration tenure.

The calcite precipitated by microbes within the cementitious matrix actually plugs the pores, and hence, contributes in improvement of compressive strength.

TABLE 2: Mix proportions of mortar formulations having mixing ratio of (1 : 1.4) with w/c of 0.4.

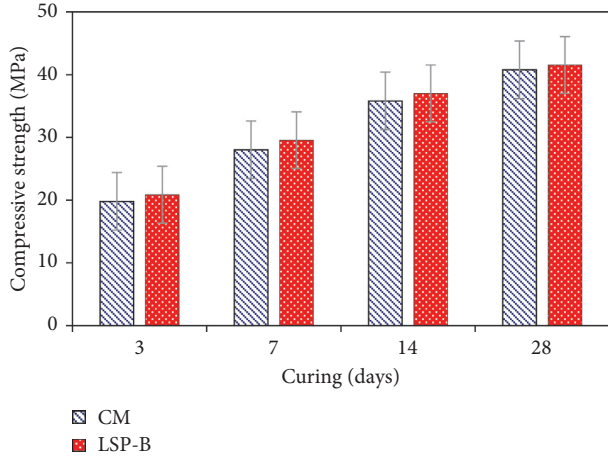| Specimens Units	Cement kg/m³	Fine aggregates kg/m³	Water cement ratio	Calcium lactate kg/m³	Bacterial solution Liter/m³	Immobilization media
CM	930	1400	0.4	18.7	—	None
LSP-B	840	1400	0.4	18.7	7.6	LSP (10% of C)

FIGURE 4: Compressive strength of mortar formulations with and without immobilized microbes at different curing ages.
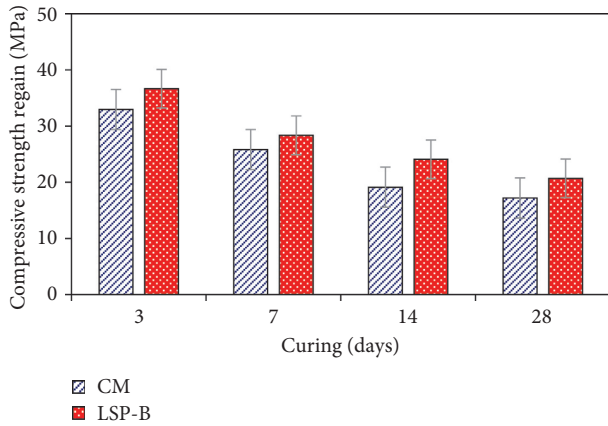

FIGURE 5: Compressive strength regain in mortar formulations with and without immobilized microbes at different precracking periods.

The reaction kinetics in the presence of microbes also endorses the formation of additional CSH gel as a result of CO_2 consumption as revealed by Li et al., which further adds in compressive strength [39]. The involved chemical reaction is as follows:

$$C_3S/C_2S + CO_2 + H_2O \longrightarrow C\text{-}S\text{-}H + CaCO_3 \qquad (2)$$
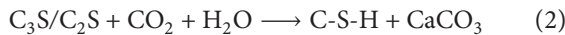
Generally, the addition of microorganisms through an immobilizer reduces the compressive strength of the cementitious matrix [19, 21, 22]. But on the contrary, immobilization via LSP increased the compressive strength of mortar formulations due to its filling ability that plugs the inner pores and homogenized distribution [40, 41]. At the age of 3 days, CM and LSP-B indicated 19.81 MPa and
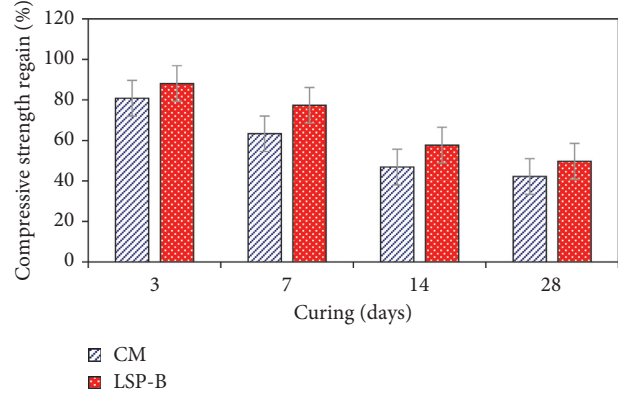
FIGURE 6: Percentage regain in compressive strength of mortar formulations with and without immobilized microbes at different precracked ages.

20.87 MPa values of compressive strength. LSP-B showed 5% more strength than CM formulation. Similar trend was observed at 7-day strength of both the formulations. At 14 days, CM and LSP-B showed 35.81 MPa and 37 MPa values of compressive strength, respectively, and LSP-B possessed 3.5% more strength than CM. At 28 days, both formulations attained maximum compressive strength showing values of 40.77 MPa and 41.98 MPa. The reported increase further enhanced to a maximum of 11.5% (instead of 5%) while focusing the isolated behavior of microbes with reference to 10% LSP diluted cement formulation. This reveals LSP as quite promising media that adds to the compressive strength of mortar specimens.

3.2. Compressive Strength Regain. Self-healing efficiency was evaluated via regain in compressive strength after pre-cracking in mechanical mode. The compressive strength regain values are plotted in Figure 5 while Figure 6 shows the percentage regain in compressive strength using (1).

Both formulations showed regain in compressive strength. In CM formulation, compressive strength regain is attributed to autogenous healing due to secondary hydration of unhydrated cement grains and carbonation of calcium hydroxide into calcite crystals [42, 43]. While in LSP-B, microbial activity is responsible for regain in compressive strength of specimens. LSP-B exhibited more compressive strength regain than CM at each stage of curing as a result of calcite precipitation induced by microbial actions. The analyzed formulations showed maximum strength regain at 3 days which was around 81% for CM and 88% for LSP-B specimens. At 7 days of curing, compressive strength regain was reduced to 63% and 77% for CM and LSP-B, respectively. Then at 14 and 28 days of curing, similar trend was observed in regained strength with a noticeable

FIGURE 7: EDX spectrum of extracted powder out of healed crack in LSP-B formulation.

reduction to 42% and 50% in CM and LSP-B formulations, respectively.

The decrease in compressive strength regain with increase in the testing age of specimens may be attributed with reduction in microbial activity at later ages. Microbes' survival depends on food and carrier media. The involved phenomena that can 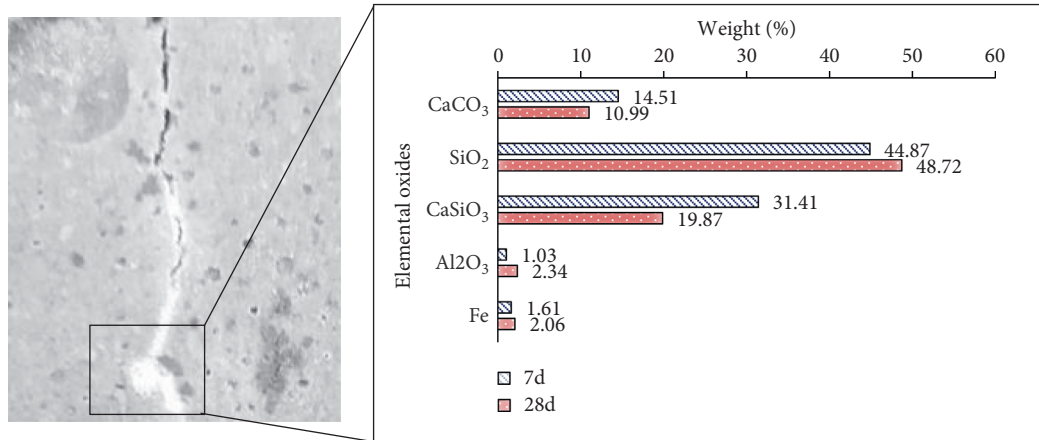justify the reduction in compressive strength regain are as follows: first, the production of microbial calcite ceased due to lack of food, and second, LSP did not sustain pressure at later stages subsequent to densified microstructure of mortar matrix in later ages ensuing in microbial crushing. However, the comparison of results of microbial formulation to referenced CM gives an isolated effect of bio-influenced self-healing process in the regain of mechanical strength. LSP showed higher preservation efficiency in the earlier phase of hydration that reduces in the later part.

3.3. Energy Dispersive X-Ray Analysis.

Energy dispersive X-ray (EDX) spectroscopy is a chemical mode of microstructural analysis. Precracked LSP-B specimens at 7 and 28 days were subjected to EDX spectroscopy after 28 days of healing period to inspect the instigation of possible calcite. The EDX spectrograph of LSP-B samples are given in Figure 7.

The results made the manifestion of calcite precipitation in both the formulations at the age of 7 and 28 days. But, at 7 days, calcite content was more as compared with 28 days. It is further concluded that microbial activity slowed down with the passage of time. However, it remained active till the age of 28 days that renders the investigated media efficient enough to effectively shield *B. subtilis* for relatively longer durations.

3.4. Field Emission Scanning Electron Microscopy.

To further explore the instigated calcite, field emission scanning electron microscopy (FESEM) was used. The FESEM micrograph was carefully sketched along the healed crack to observe any possible signs of calcite precipitation. FESEM micrograph of LSP-B formulations is shown in Figure 8 at the precracking age of 7 and 28 days.

In the presence of *B. subtilis*, calcium lactate converted into calcite, by consuming oxygen, and produced rhombohedra crystals. The reaction activity is shown in (3) [44].

$$CaC_6H_{10}O_6 + 6O_2 \longrightarrow CaCO_3 + 5CO_2 + 5H_2O \qquad (3)$$

Fabrication of calcite crystals can be clearly seen in both the micrographs of cryofractured cementitious formulations at 7 and 28 days of precracking consequent to microbial healing that ensures the persistence of microbes till the age of 28 days.

3.5. Thermogravimetric Analysis.

The thermogravimetric analysis (TGA) is a mode of thermal analysis which is performed in an instrument named as the thermogravimetric analyzer. Mass, time, and temperature are considered basic measurements of TGA. The analyzer continuously measures the mass of the substance while temperature of the sample changes continuously at a constant rate [45]. This change in mass of the substance assists in recognition of different chemical compounds categorized by their decomposition temperature.

TGA was conducted on the white powder scratched from the surface of healed specimens for confirmation of precipitated calcite after 28 days of healing. The decomposition temperature of $CaCO_3$ crystals ranges from 600 to 850°C [46]. The decomposition reaction of $CaCO_3$ is as given in (4), and the TGA result of healed powder is plotted in Figure 9.

$$CaCO_3(s) \longrightarrow CaO(s) + CO_2(g) \qquad (4)$$
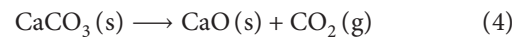
It is clearly evident from the curve that major mass loss of 6.2% occurred in the predefined range of 600–850°C that endorses the presence of calcite ensuing in strong microbial action. Hence, it can be inferred that LSP effectively preserved the microbes "*B. subtilis*" up till the formation of cracks in the mortar formulations.

4. Concluding Remarks

LSP is locally available, cost-efficient alternative to immobilize *B. subtilis* in highly alkaline cementitious environment. The addition of microbes immobilized on LSP

(a)

(b)

FIGURE 8: (a) FESEM micrograph of LSP-B specimen. (b) FESEM micrograph of LSP-B specimen precracked at 7 and 28 days.

FIGURE 9: TGA curve of extracted powder out of healed crack in LSP-B formulation.

contributed in the enhancement of compressive strength at 3, 7, 14, and 28 days of curing with maximum increment of 5.75% at 14 days comparative to CM formulation. The regained compressi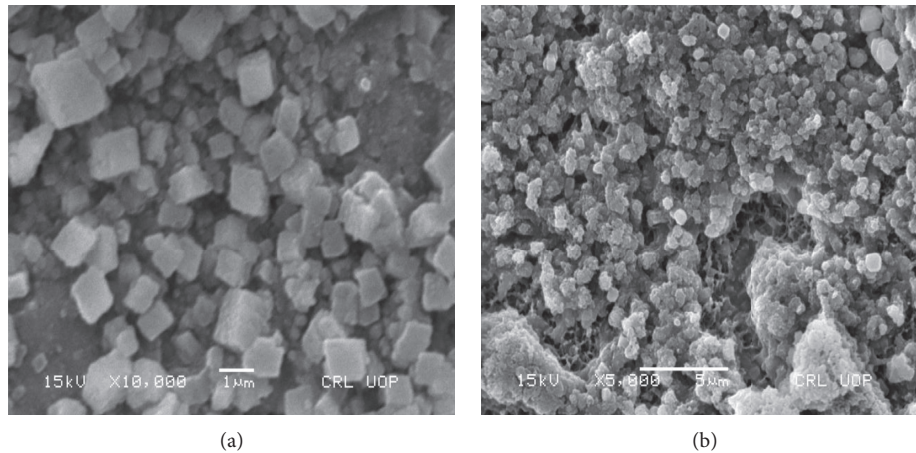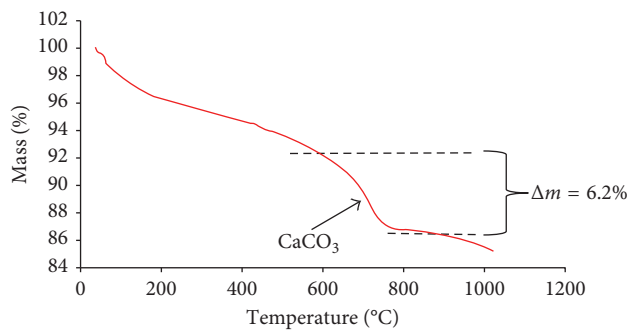ve strength gauging the healing efficiency in mechanical mode endorsed the maximum regain at 3 days of precracking age, which declined later on with increased age of specimens. LSP-B formulation exhibited more regained compressive strength at each testing age. Moreover, micrographical analysis through FESEM, chemical analysis by EDX, and thermal analysis via TGA on the powdered specimens from the near vicinity of healed cracks further evidenced visible signs of calcite precipitation consequent to microbial activity. Hence, LSP can be claimed as a promising carrier media for *B. subtilis* ensuring its preservation for relatively longer durations in highly alkaline cementitious environment.

Abbreviations

FESEM: Field emission scanning electron microscopy
EDX: Energy dispersive X-ray
TGA: Thermogravimetry analysis
LSP: Limestone powder
XRF: X-ray florescence
CSH: Calcium-silicate-hydrate.

Data Availability

The data used to support the findings of this study are available from the corresponding author upon request.

Conflicts of Interest

The authors declared no potential conflicts of interest with respect to the research, authorship, and/or publication of this article.

Acknowledgments

References

[1] V. Achal and A. Mukherjee, "A review of microbial precipitation for sustainable construction," *Construction and Building Materials*, vol. 93, pp. 1224–1235, 2015.

[2] H. Schlangen, H. Jonkers, S. Qian, and A. Garcia, "Recent advances on self healing of concrete," in *FraMCos-7: Proceedings of the 7th International Conference on Fracture Mechanics of Concrete and Concrete Structures*, pp. 23–28, Jeju Island, Replic of Korea, May 2010.

[3] K. Arbi, M. Nedeljković, Y. Zuo, and G. Ye, "A review on the durability of alkali-activated fly ash/slag systems: advances, issues, and perspectives," *Industrial & Engineering Chemistry Research*, vol. 55, no. 19, pp. 5439–5453, 2016.

[4] A. Vaysburd and P. Emmons, "How to make today's repairs durable for tomorrow—corrosion protection in concrete repair," *Construction and Building Materials*, vol. 14, no. 4, pp. 189–197, 2000.

[5] H. M. Jonkers, A. Thijssen, G. Muyzer, O. Copuroglu, and E. Schlangen, "Application of bacteria as self-healing agent for the development of sustainable concrete," *Ecological Engineering*, vol. 36, no. 2, pp. 230–235, 2010.

[6] W. Tang, O. Kardani, and H. Cui, "Robust evaluation of self-healing efficiency in cementitious materials–a review," *Construction and Building Materials*, vol. 81, pp. 233–247, 2015.

[7] D. Snoeck, P.-A. Smetryns, and N. De Belie, "Improved multiple cracking and autogenous healing in cementitious materials by means of chemically-treated natural fibres," *Biosystems Engineering*, vol. 139, pp. 87–99, 2015.

[8] M. G. Meharie, J. W. Kaluli, Z. Abiero-Gariy, and N. D. Kumar, "Factors affecting the self-healing efficiency of cracked concrete structures," *American Journal of Applied Scientific Research*, vol. 3, no. 6, p. 80, 2017.

[9] K. Van Tittelboom and N. De Belie, "Self-healing in cementitious materials—A review," *Materials*, vol. 6, no. 6, pp. 2182–2217, 2013.

[10] P. Minnebo, G. Thierens, G. De Valck et al., "A novel design of autonomously healed concrete: towards a vascular healing network," *Materials*, vol. 10, no. 1, p. 49, 2017.

[11] S. Sangadji, "Can self-healing mechanism helps concrete structures sustainable?," *Procedia Engineering*, vol. 171, pp. 238–249, 2017.

[12] R. Chang, S. Kim, S. Lee, S. Choi, M. Kim, and Y. Park, "Calcium carbonate precipitation for CO_2 storage and utilization: a review of the carbonate crystallization and polymorphism," *Frontiers in Energy Research*, vol. 5, p. 17, 2017.

[13] N. De Belie and W. De Muynck, "Crack repair in concrete using biodeposition," in *Proceedings of the International Conference on Concrete Repair, Rehabilitation and Retrofitting (ICCRRR)*, pp. 291-292, Cape Town, South Africa, 2008.

[14] M. Araujo, S. Van Vlierberghe, J. Feiteira et al., "Cross-linkable polyethers as healing/sealing agents for self-healing of cementitious materials," *Materials and Design*, vol. 98, pp. 215–222, 2016.

[15] S. Bhaskar, K. M. A. Hossain, M. Lachemi, G. Wolfaardt, and M. O. Kroukamp, "Effect of self-healing on strength and durability of zeolite-immobilized bacterial cementitious mortar composites," *Cement and Concrete Composites*, vol. 82, pp. 23–33, 2017.

[16] W. Khaliq and M. B. Ehsan, "Crack healing in concrete using various bio influenced self-healing techniques," *Construction and Building Materials*, vol. 102, pp. 349–357, 2016.

[17] M. Elakkiya, D. Prabhakaran, and M. Thirumarimurugan, "Methods of cell immobilization and its applications," *Methods*, vol. 5, no. 4, 2016.

[18] J. Wang, N. De Belie, and W. Verstraete, "Diatomaceous earth as a protective vehicle for bacteria applied for self-healing concrete," *Journal of Industrial Microbiology and Biotechnology*, vol. 39, no. 4, pp. 567–577, 2012.

[19] J. Wang, D. Snoeck, S. Van Vlierberghe, W. Verstraete, and N. De Belie, "Application of hydrogel encapsulated carbonate precipitating bacteria for approaching a realistic self-healing in concrete," *Construction and building materials*, vol. 68, pp. 110–119, 2014.

[20] V. Wiktor and H. M. Jonkers, "Quantification of crack-healing in novel bacteria-based self-healing concrete," *Cement and Concrete Composites*, vol. 33, no. 7, pp. 763–770, 2011.

[21] J. Wang, K. Van Tittelboom, N. De Belie, and W. Verstraete, "Use of silica gel or polyurethane immobilized bacteria for self-healing concrete," *Construction and building materials*, vol. 26, no. 1, pp. 532–540, 2012.

[22] J. Y. Wang, H. Soens, W. Verstraete, and N. De Belie, "Self-healing concrete by use of microencapsulated bacterial spores," *Cement and Concrete Research*, vol. 56, pp. 139–152, 2014.

[23] N. N. T. Huynh, N. M. Phuong, N. P. A. Toan, and N. K. Son, "*Bacillus subtilis* HU58 Immobilized in micropores of diatomite for using in self-healing concrete," *Procedia Engineering*, vol. 171, pp. 598–605, 2017.

[24] H. Chen, C. Qian, and H. Huang, "Self-healing cementitious materials based on bacteria and nutrients immobilized respectively," *Construction and Building Materials*, vol. 126, pp. 297–303, 2016.

[25] J. Zhang, Y. Liu, T. Feng et al., "Immobilizing bacteria in expanded perlite for the crack self-healing in concrete," *Construction and Building Materials*, vol. 148, pp. 610–617, 2017.

[26] O. M. Omar, G. D. A. Elhameed, M. A. Sherif, and H. A. Mohamadien, "Influence of limestone waste as partial replacement material for sand and marble powder in concrete properties," *HBRC Journal*, vol. 8, no. 3, pp. 193–203, 2012.

[27] D. P. Bentz, C. F. Ferraris, S. Z. Jones, D. Lootens, and F. Zunino, "Limestone and silica powder replacements for cement: early-age performance," *Cement and Concrete Composites*, vol. 78, pp. 43–56, 2017.

[28] S. A. Rizwan and T. A. Bier, "Blends of limestone powder and fly-ash enhance the response of self-compacting mortars," *Construction and Building Materials*, vol. 27, no. 1, pp. 398–403, 2012.

[29] M. Zajac, A. Rossberg, G. Le Saout, and B. Lothenbach, "Influence of limestone and anhydrite on the hydration of Portland cements," *Cement and Concrete Composites*, vol. 46, pp. 99–108, 2014.

[30] A. Ipavec, R. Gabrovšek, T. Vuk, V. Kaučič, J. Maček, and A. Meden, "Carboaluminate phases formation during the hydration of calcite-containing Portland cement," *Journal of the American Ceramic Society*, vol. 94, no. 4, pp. 1238–1242, 2011.

[31] Z. Tu, M.-Z. Guo, C. S. Poon, and C. Shi, "Effects of limestone powder on $CaCO_3$ precipitation in CO_2 cured cement pastes," *Cement and Concrete Composites*, vol. 72, pp. 9–16, 2016.

[32] O. Aviam, G. Bar-Nes, Y. Zeiri, and A. Sivan, "Accelerated biodegradation of cement by sulfur-oxidizing bacteria as a bioassay for evaluating immobilization of low-level radioactive waste," *Applied and environmental microbiology*, vol. 70, no. 10, pp. 6031–6036, 2004.

[33] H. Huang, G. Ye, C. Qian, and E. Schlangen, "Self-healing in cementitious materials: materials, methods and service conditions," *Materials and Design*, vol. 92, pp. 499–511, 2016.

[34] P. Anbu, C.-H. Kang, Y.-J. Shin, and J.-S. So, "Formations of calcium carbonate minerals by bacteria and its multiple applications," *SpringerPlus*, vol. 5, no. 1, p. 250, 2016.

[35] E. J. Hayhurst, L. Kailas, J. K. Hobbs, and S. J. Foster, "Cell wall peptidoglycan architecture in Bacillus subtilis," *Proceedings of the National Academy of Sciences*, vol. 105, no. 38, pp. 14603–14608, 2008.

[36] S. K. Ramachandran, V. Ramakrishnan, and S. S. Bang, "Remediation of concrete using micro-organisms," *ACI Materials Journal*, vol. 98, no. 1, pp. 3–9, 2001.

[37] B. Barra, L. Momm, Y. Guerrero, and L. Bernucci, "Characterization of granite and limestone powders for use as fillers in bituminous mastics dosage," *Anais da Academia Brasileira de Ciências*, vol. 86, no. 2, pp. 995–1002, 2014.

[38] S. A. Rizwan, *High-Performance Mortars and Concrete Using Secondary Raw Materials*, Ph.D. thesis, American Concrete Institute (ACI), Farmington Hills, MI, USA, 2006.

[39] M. Li, X. Zhu, A. Mukherjee, M. Huang, and V. Achal, "Biomineralization in metakaolin modified cement mortar to

improve its strength with lowered cement content," *Journal of Hazardous Materials*, vol. 329, pp. 178–184, 2017.

[40] Z. Tan, G. De Schutter, G. Ye, and Y. Gao, "The effect of limestone powder addition on strength of slag blended cement," in *Proceedings of Concrete under Severe Conditions: Environment and Loading (CONSEC-2013)*, pp. 1888–1898, RILEM Publications, Vancouver, BC, Canada, 2013.

[41] S. Türkel and Y. Altuntaş, "The effect of limestone powder, fly ash and silica fume on the properties of self-compacting repair mortars," *Sadhana*, vol. 34, no. 2, pp. 331–343, 2009.

[42] J. Reis, D. Moreira, L. Nunes, and L. Sphaier, "Evaluation of the fracture properties of polymer mortars reinforced with nanoparticles," *Composite Structures*, vol. 93, no. 11, pp. 3002–3005, 2011.

[43] H. M. Jonkers and E. Schlangen, "A two component bacteria-based self-healing concrete," in *Concrete Repair, Rehabilitation and Retrofitting II: 2nd International Conference on Concrete Repair, Rehabilitation and Retrofitting, ICCRRR-2*, pp. 24–26, CRC Press, Cape Town, South Africa, November 2008.

[44] O. Regnault, V. Lagneau, and H. Schneider, "Experimental measurement of portlandite carbonation kinetics with supercritical CO_2," *Chemical Geology*, vol. 265, no. 1-2, pp. 113–121, 2009.

[45] V. Kodur and M. Sultan, "Effect of temperature on thermal properties of high-strength concrete," *Journal of Materials in Civil Engineering*, vol. 15, no. 2, pp. 101–107, 2003.

[46] I. Halikia, L. Zoumpoulakis, E. Christodoulou, and D. Prattis, "Kinetic study of the thermal decomposition of calcium carbonate by isothermal methods of analysis," *European Journal of Mineral Processing and Environmental Protection*, vol. 1, no. 2, pp. 89–102, 2001.

Research Article

Evaluation of Self-Healing Performance of PE and PVA Concrete Using Flexural Test

Choonghyun Kang,[1] Jungwon Huh [ID],[1] Quang Huy Tran [ID],[1] and Kiseok Kwak[2]

[1]*Chonnam National University, Yeosu, Republic of Korea*
[2]*Geotechnical Engineering Research Institute, KICT, Goyang, Republic of Korea*

Correspondence should be addressed to Jungwon Huh; jwonhuh@chonnam.ac.kr

The self-healing performance of PE and PVA concrete was evaluated, by using the three-point bending test with a notch. Four different crack inducement days were applied (7, 28, 49, and 91 days), and the same 21 days of healing period were applied to each case. The self-healing environments were in 20°C water, and in the curing room with 20°C temperature and 60% humidity. The flexural strength and the initial flexural stiffness of before and after healing were compared. As a result, both the strength recovery effect and the stiffness recovery effect decreased with the delay of crack inducement, and specimens in the water environment showed higher healing effect than those in the air environment. PVA fiber showed a relatively greater recovery effect than PE fiber.

1. Introduction

Self-healing of concrete is focused on a good solution to not only decrease the lifecycle cost but also to ease an environmental problem. Previous studies have mainly focused on improving the strength and durability of concrete. As a result, ultrahigh-performance concrete of over 150 MPa was developed, and concrete of 30 MPa is applied in the field [1–4]. The use of additives (such as fly ash) is also applied, to increase the durability of concrete [5–7]. The main focus of these studies is to reduce the construction cost, by reducing the cross section of the structure members. Meanwhile, other studies reported that the total cost maintenance of concrete structure for 30 years is similar to that of the construction cost [8–10]. The self-healing method is attracting attention in relation to maintenance cost reduction. The self-healing method causes the concrete structure to recover by detecting a deterioration itself and making possible an appropriate response before serious damage is developed. An appropriate response means timely correct repair or reinforcement, resulting in reduced maintenance cost [11, 12]. In addition, the increase in the overall service life of concrete structures will reduce the generation of carbon dioxide from cement production, positively affecting the environment in the long run.

Self-healing of concrete has been studied from various aspects over the past decade. The most well-known research is on a capsule containing an adhesive agent [13, 14]. The capsule is located at the crack propagation break, and the adhesive agent flows and recovers the crack automatically. A bacterium, which is an organic material, was investigated [15, 16]. It helps or maximizes the production of substances favorable for self-healing. These techniques can be categorized as an active method because they actively prepare cracks during the design and construction sequence, and the JCI self-healing committee defines this as Activated Repairing. On the other hand, passive self-healing is classified into Natural Healing, which is the recoverability of the concrete itself, and Autonomic Healing, which improves the self-healing performance of additional materials. Natural Healing and Autonomic Healing are classified as Autogenous Healing. However, Autonomic Healing can be classified as an active method because of the use of additional materials. Autonomic Healing and Activated Repairing are

TABLE 1: Mix proportion of fiber concrete.

Fiber	W/C (%)	s/a (%)	Volume fractions of fiber (%)	Unit content (kg/m^3)						Additive (cc/m^3)
				Water	Cement	Sand	Gravel	Fly ash	Fiber	SP
PE	45	47	0.25	175	389	618	879	137	2.43	0.97
PVA			0.19							

SP, superplasticizer.

TABLE 2: Properties of cement and aggregates.

Component	Density (g/cm^3)	Absorption (%)
Portland cement	3.15	—
Gravel	2.58	0.2
Sand	2.51	3.2

TABLE 3: Properties of fly ash.

SiO$_2$	53.98%
Moisture	0.01%
Loss on ignition	1.00%
Density	2.27 g/cm^3
Specific surface area	3,460 cm^2/g
Activity index	85% (28 days) 100% (91 days)

classified as Engineered Healing/Repairing. In a large category, all of them are designated as self-healing/repairing [17]. In recent years, self-healing has been studied not only in ordinary concrete but also in modified composites such as ECC [18].

The purpose of this study was to investigate the self-healing performance of concrete containing fly ash and fiber for improving healing performance. One important aspect of self-healing research is how to measure it, and various techniques have been tried in the past studies. This study selected the bending test in which the direct measurement of self-healing using the same specimen is possible. The self-healing performance was evaluated by comparing the flexural load and the flexural stiffness before and after the crack, using the notched specimen.

2. Experiment

2.1. Materials and Mixes. Table 1 shows the mix proportion of the two kinds of concrete prepared in this study. Depending on the fiber type, two proportions were determined, and the type and amount of the other materials were the same. Ordinary Portland cement, river gravel, and standard sand were used. Table 2 shows the properties of cement and aggregates estimated at preliminary experiments. Fly ash, which is reported to improve the durability of concrete, is also reported to help recovery by the precipitation of calcium carbonate (CaCO$_3$) and pozzolanic reaction [19, 20]. This study used fly ash with silicon dioxide (SiO$_2$) content of over 50%, and Table 3 shows the detailed physical properties. Fly ash was added of 50% of the cement volume. The water-cement ratio (w/c) was 45%, and the water-binder ratio (w/b) was 33.3%. Sand-to-aggregate (s/a) ratio was 47%. The air-entraining (AE) water-reducing agent was added to improve the workability. It has been reported that the polypropylene fiber embedded in concrete acts as a bridge between the crack surfaces and affects precipitation during the healing period. This study prepared polyethylene (PE) fiber and polyvinyl alcohol (PVA) fiber. Figure 1 shows the samples of each fiber, and Table 4 shows the properties of the fibers. As far as possible, different properties were applied equally in order to compare only differences according to fiber types. However, it is difficult to perfectly match the two fiber concretes since the thickness and density of the fibers are different, so the same weight was applied for the convenience of an experiment.

(a)

(b)

FIGURE 1: Sample of fibers: (a) polyethylene fiber; (b) polyvinyl alcohol fiber.

2.2. Specimen. Prismatic specimens of L400 mm × W100 mm × D100 mm with a notch were prepared in this study. Figure 2 shows the dimension and the experimental view. Since concrete is a brittle material, cracks develop rapidly. Since concrete

TABLE 4: Properties of fibers.

Content	PE	PVA
Length	4 mm	4 mm
Diameter	0.012 mm	0.040 mm
Density	0.97 g/cm^3	1.30 g/cm^3
Elastic modulus	88 GPa	41 GPa
Tensile strength	2,700 MPa	1,560 MPa

(a)

(b)

FIGURE 2: Flexural test: (a) specimen size; (b) test view.

TABLE 5: Cases and test program.

| Case | Days after casting | | Healing | |
	1st and 2nd loading	3rd loading	Condition	Period
PE-7–28-A PVA-7–28-A PE-7–28-W PVA-7–28-W	7	28	Air Water	21 days
PE-28–49-A PVA-28–49-A PE-28–49-W PVA-28–49-W	28	49	Air Water	21 days
PE-49–70-A PVA-49–70-A PE-49–70-W PVA-49–70-W	49	70	Air Water	21 days
PE-91–112-A PVA-91–112-A PE-91–112-W PVA-91–112-W	91	112	Air Water	21 days

a postintroduction method, in which a cutter is used. The latter has some problems, in that it can introduce some damage to the specimen during cutting, but it is easier than the former. No significant difference was found in the posthealing behavior of the mutual comparisons through preliminary experiments. The posthealing behavior depends on the crack depth that could be healed by self-healing, and this is formed almost constant during the loading sequence. The notch introduction was conducted at 7 days after casting, which is the fastest loading day of all cases, and a diamond wet cutter was used.

Each specimen was cast in a steel prismatic mold after mixing. Then, 24 hours later, specimens were demolded and cured in fresh water with a temperature of $(20 \pm 3)°C$. Crack inducements (1st loading) were conducted at 7, 28, 49, and 91 days from the casting. The 2nd loading was conducted just after crack inducement, and it was the control value before the self-healing. The same 21 days of the healing period were applied to specimens after the 2nd loading. The self-healing environment was different for each case, such as in water and air. The water environment means healing in fresh water with a temperature of $(20 \pm 3)°C$, which is the same condition as the curing after casting. The air environment means healing in the curing room with a temperature of $(20 \pm 3)°C$ and relative humidity of 60%. The 3rd loading was conducted after the healing period, and it was the evaluation value of the self-healing performance. Table 5 shows the test program.

The case was named considering the fiber name, the crack induction (1st loading) and 2nd loading, the 3rd loading, and the self-healing environment. For example, PE-7–28-W means that the specimen is PE fiber concrete, the crack induction and 2nd loading were conducted at 7 days after casting, the 3rd loading was conducted at 28 days after casting, and specimens were cured in the water condition after crack inducement. All cases had four specimens.

2.3. Flexural Test. The most important process in the evaluation of the self-healing of concrete is to generate an adequate crack. Van Breugel reported that a crack with only

is a nonhomogeneous material, it is difficult to specify the location of the cracks. This is why the notch was applied in this study. The depth of the notch determines the maximum flexural load, and RILEM recommends a notch of 20–25% of the specimen thickness [21]. However, it has been confirmed through preliminary experiments that it is difficult to control crack propagation, because the propagation speed of the cracks is too fast, due to the high maximum flexural load. In the case of a notch being too deep, it was judged that the crack generation region where self-healing will be performed is too narrow to allow evaluation of the self-healing performance. We concluded that the application of 33 mm, which is 1/3 of the specimen thickness, is effective for both crack control and evaluating the self-healing performance. The introduction of the notch can be classified into a preintroduction method, in which an acrylic bar or the like is installed and removed, and

less than 0.2 mm width could be expected to recover by self-healing [22]. This study used a crack mouth opening displacement (CMOD) by measuring a clip gauge set at the notch opening, and CMOD controlled the crack width during loading. Meng et al. reported that the effects of the notch-to-depth ratio are associated with the loading rate, and it is less than 10% at a deflection rate up to 1.25 mm/min [23]. But the loading speed of this study was 0.5–1.0 mm/min; therefore, the effect is insignificant.

The self-healing performance was evaluated by three-times loading. The crack inducement (1st loading) was the process to make an adequate crack. The exact crack width could not be measured, but CMOD makes an almost constant crack width because the crack width and CMOD are linearly proportional [24]. The unloading point was set as CMOD 0.05 mm, which is a point after the peak load. After finishing the unloading of the crack inducement (1st loading), the 2nd loading was conducted. To prevent further crack propagation, the unloading point of the 2nd loading was the same as CMOD 0.05 mm. The next process was the healing. Specimens were healed in water and air, respectively, by case. Lastly, the 3rd loading was conducted. The 3rd loading was to evaluate the self-healing performance, and loading was performed, until the specimen was completely separated.

Figure 3 shows a typical load-CMOD curve. The peak load appeared between 0.02 and 0.03 mm CMOD, and the unloading point was the load-drop region. Both load and CMOD decrease during the unloading sequence, and a right downward convex curve was drawn. The 2nd loading curve was similar to the 1st loading curve, as a left upward convex curve, and the maximum load of the 2nd loading was lower than the peak load of the 1st loading. The unloading curve after the 2nd loading was also a right downward convex curve, and the unloading completion points after both the 1st loading and the 2nd loading were almost the same. The 3rd loading curves were different by case. According to the degree of self-healing, the curves were drawn near the curve of the 2nd loading, and the maximum load point also appeared at a different point, not CMOD 0.05 mm.

2.4. Evaluation of Self-Healing Performance

2.4.1. Flexural Strength. Firstly, the flexural strength of cases was compared. Granger et al. also used the flexural strength comparison for evaluation of the self-healing performance [25]. However, the flexural strength of the healed specimen was compared with the flexural strength of the unhealed specimen. Relative flexural strength recovery could be compared, but it is not a direct comparison because it is not a comparison of values from the same specimen. This study compared two values before and after self-healing from the same specimen. The reference point was CMOD 0.05 mm, and the comparison target was the maximum load value of the 3rd loading. The flexural behavior after deterioration generally decreases, compared to that before deterioration. This is the reason why the maximum load of the 2nd loading is lower than the load of the unloading point of the 1st loading, even though the CMOD was the same at 0.05 mm. If the maximum load of the 3rd loading is greater than the load of the
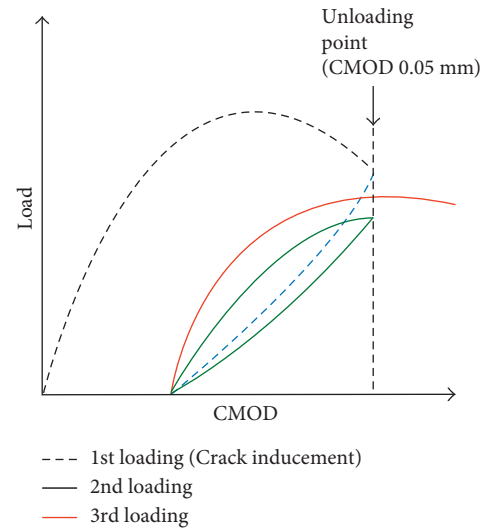

Figure 3: Typical load-CMOD curve.

unloading point of the 1st loading, the self-healing contributed to the strength recovery. In this study, the ratio between the maximum load of the 3rd loading and the load of the unloading point of the 1st loading is called the strength recovery effect. If the strength recovery effect is higher than 1.0, this means that the self-healing restored the flexural strength.

2.4.2. Flexural Stiffness. Self-healing evaluation by flexural strength implies the aging effect of an uncracked part. After casting, concrete has a constant hydration reaction. The flexural strength means the maximum load carrying capacity of the whole section, such as cracked and uncracked parts. In other words, the aging effect of the uncracked part cannot be avoided. In order to accurately evaluate the self-healing performance, it is necessary to distinguish the recovery effect from the aging effect. However, it is not easy to separate the self-healing effect from the aging effect in the flexural strength comparison.

This study focused on the different initial behaviors of the load-CMOD curve of the 2nd and the 3rd loading. It is known that the load-CMOD gradient in the three-point bending test is proportional to the modulus of elasticity of the specimen [26, 27]. The initial behavior of the load-CMOD curve is related to the crack opening, so the change of the crack circumstance will be represented most sensitively. Figure 4 shows the initial behavior of the load-CMOD curve of the 2nd and the 3rd loading of PE-7–28-W and shows the different initial slopes by the loading. This study estimated the initial slope of the load-CMOD, which used data from the start point CMOD to (0.003–0.005) mm. The ratio between the initial slope of the 3rd loading and that of the 2nd loading is known as the stiffness recovery effect. If the stiffness recovery effect is higher than 1.0, this means that the self-healing restored the flexural stiffness.

3. Results and Discussion

3.1. Load-CMOD Curve. The load-CMOD curves of the 1st loading (crack inducement) and the 2nd loading were
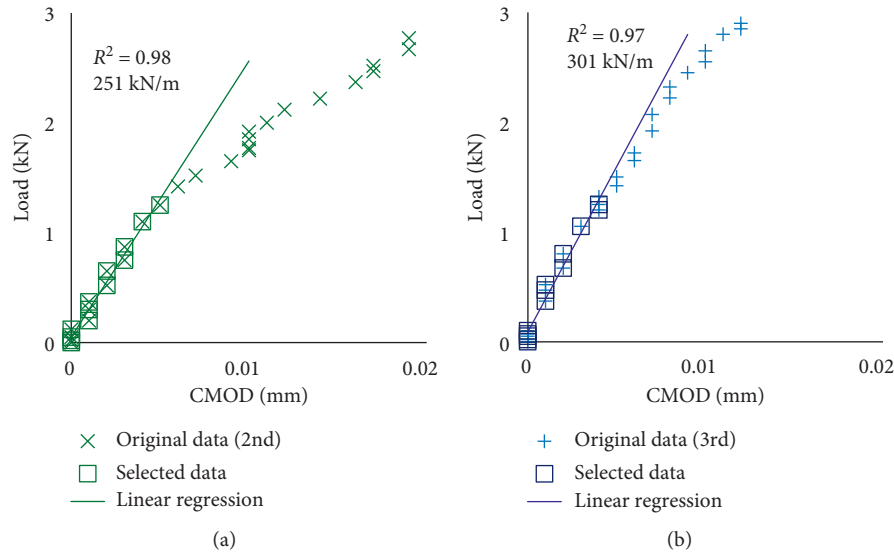
FIGURE 4: Example of the initial slope of the load-CMOD curve of (a) the 2nd loading and (b) the 3rd loading (PE-7–28-W).

similar, regardless of the variables. Figure 5 shows typical load-CMOD curves of PE concrete with different 1st loading days and different self-healing environments, respectively. Figure 6 shows typical load-CMOD curves of PVA concrete with different 1st loading days and different self-healing environments, respectively. The peak load appeared between CMOD 0.02 and 0.03 mm. The maximum loads of the 2nd loading were measured at CMOD 0.05 mm, and the peak load of the 3rd loading was measured. Tables 6 and 7 show the detailed load value of PE and PVA concrete, respectively. The peak load increased with a delay of the 1st loading days, and the average peak load increased as in Figure 7. The average peak loads of PVA concrete were higher than those of PE concrete (except the case of 49 days), but the difference was not significant, considering the deviation. A load of the unloading point increased with increase in the peak load and was about 87%. The CMODs of the unloading completion after the 1st loading were 0.016 ± 0.002 mm, and it was confirmed that there was no correlation between the type of fiber and the 1st loading days. This indicates that the degree of crack propagation was almost constant, regardless of the variables. The slopes of the load-CMOD curve of the 2nd loading were lower than those of the 3rd loading, but a certain pattern due to the specimen did not appear. The maximum load of the 2nd loading was (95 ± 3)% of the load of the unloading point, regardless of the variables. The CMOD of the unloading completion after the 2nd loading was almost the same as that of the 1st loading.

The behavior of the load-CMOD curve of the 3rd loading after healing showed different patterns, depending on the 1st loading day and the self-healing environment. If the initial slope of the load-CMOD curve of the 3rd loading was greater than that of the 2nd loading, the maximum load of the 3rd loading was also greater than that of the 2nd loading. The CMOD at the maximum load also increased and was over 0.05 mm. In contrast, if the initial slope of the load-CMOD curve of the 3rd loading was smaller than that of the 2nd

loading, the maximum load of the 3rd loading was also smaller than that of the 2nd loading. Except for the 7–28 and 28–49 cases, which have relatively fast 1st loading days, the maximum load was smaller than that of the 2nd loading.

3.2. Flexural Strength Recovery Effect. Figure 8 shows the flexural strength recovery effect with different 1st loading days and different self-healing environment of PE concrete and PVA concrete, respectively. Firstly, both the PE-7–28 case and PVA-7–28 case had the strength recovery effect of over 1.0, regardless of the self-healing environment. This means that the maximum load of the 3rd loading is greater than the load of the unloading point of the 1st loading. In other words, the flexural strength of the section was recovered during the healing period. At only 7 days after casting, the ratio of unhydrated cement in the specimen may be quite high, and it means that an aging can happen not only in the uncracked part but also in the cracked part. The strength recovery effect of over 1.0 in 7–28 cases could be explained as being due to this significant aging effect. However, the strength recovery effect decreased with the delay of the 1st loading day; in particular, the values of the PE concrete with air environment showed less than 0.5. This means that the specimen did not recover at all. The deterioration during the 2nd loading could be the reason for the decrease in flexural strength. The strength recovery effect with water environment decreased continuously with the delay of the 1st loading day, but it converged for the 91–112 cases.

In air environment, there was a prominent difference between the PE and PVA concrete. The strength recovery effect of the PE-28–49-A case shows a sharp fall, and after that, it is almost constant. On the other hand, the strength recovery effect of PVA concrete with air environment shows a gradual decrease pattern, and the PVA-7–28-A and PVA-28–49-A cases show similar values to the PVA-7–28-W and PVA-28–49-W cases. It is presumed that the hydrophilicity of PVA fiber has affected the strength recovery effect.
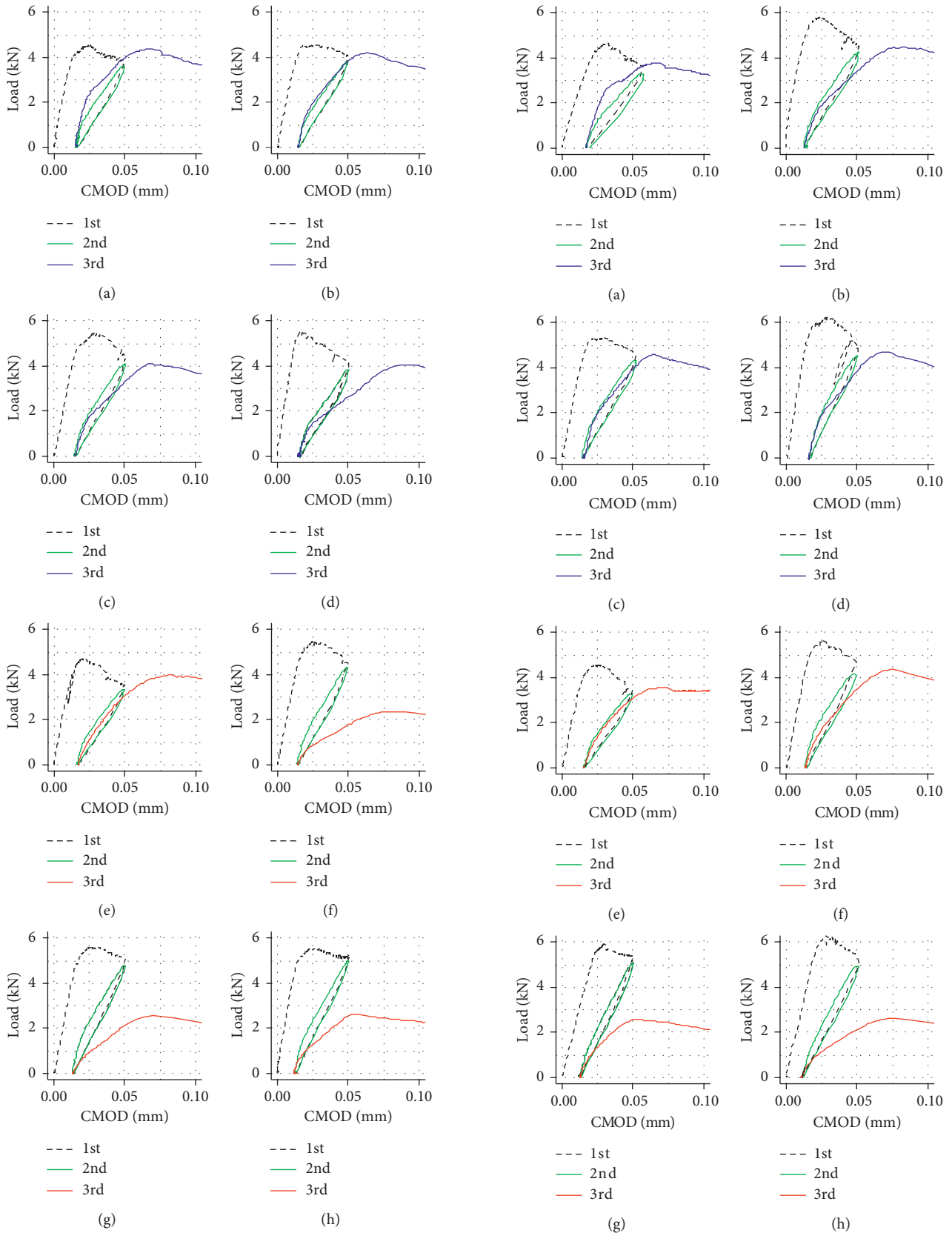
Figure 5: Typical load-CMOD curves of PE concrete: (a) PE-7–28W, (b) PE-28–49-W, (c) PE-49–70-W, (d) PE-91–112-W, (e) PE-7–28-A, (f) PE-28–49-A, (g) PE-49–70-A, and (h) PE-91–112-A.
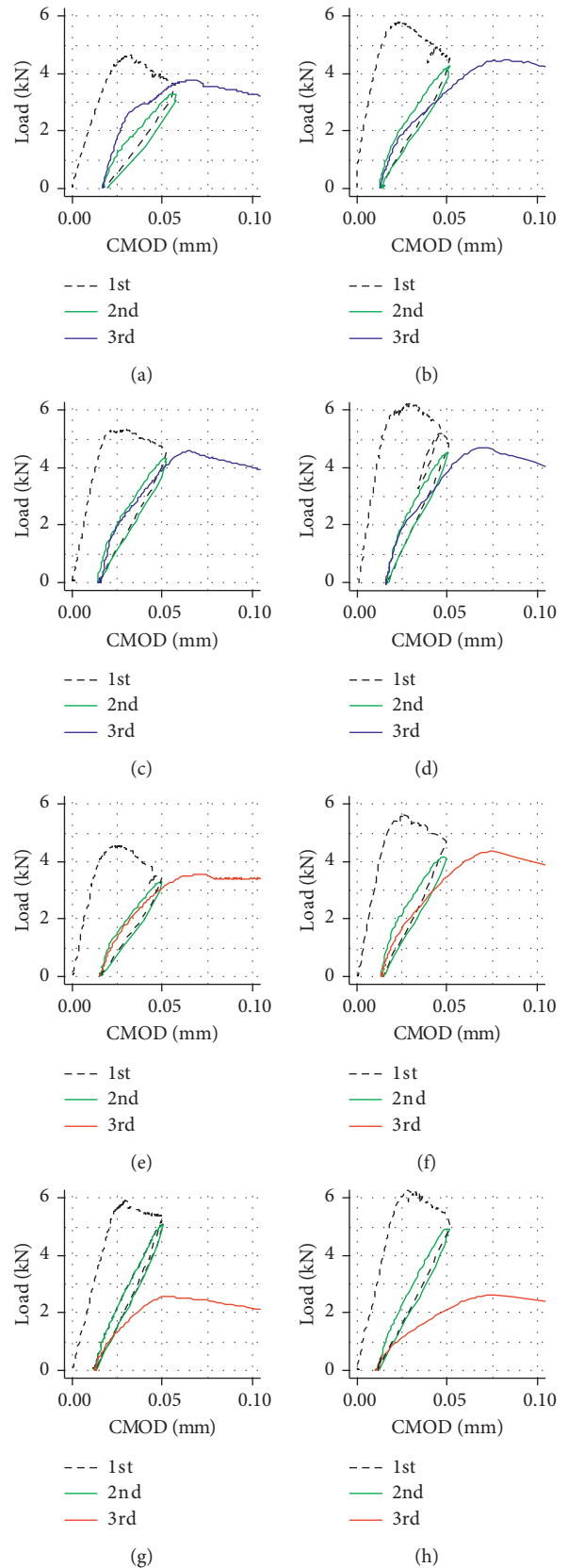
Figure 6: Typical load-CMOD curves of PVA concrete: (a) PVA-7–28W, (b) PVA-28–49-W, (c) PVA-49–70-W, (d) PVA-91–112-W, (e) PVA-7–28-A, (f) PVA-28–49-A, (g) PVA-49–70-A, and (h) PVA-91–112-A.

Table 6: Peak and maximum load of PE concrete.

Case	Peak/maximum load		
	1st loading	2nd loading (CMOD 0.05 mm)	3rd loading
PE-7–28-W	4.48	3.40	3.90
	4.53	3.83	4.38
	4.43	3.88	4.55
	4.60	3.75	4.30
PE-28–49-W	5.93	5.43	5.10
	4.58	3.95	4.20
	4.83	4.25	4.30
	5.30	4.43	4.55
PE-49–70-W	5.25	4.75	4.58
	5.98	5.20	4.95
	5.45	4.30	4.10
	6.15	5.48	5.13
PE-91–112-W	6.13	4.53	4.33
	6.48	4.70	4.58
	5.53	4.00	4.05
	5.48	4.85	4.88
PE-7–28-A	4.70	3.50	4.00
	4.78	3.45	4.08
	4.03	2.80	3.15
	4.50	3.55	4.63
PE-28–49-A	5.38	5.03	2.61
	5.65	4.85	2.45
	5.23	5.00	2.69
	5.45	4.53	2.36
PE-49–70-A	5.60	5.08	2.55
	5.60	5.10	2.59
	5.50	5.18	2.56
	6.30	5.30	2.46
PE-91–112-A	5.53	5.23	2.64
	5.73	3.95	2.04
	5.88	3.95	2.18
	4.95	4.50	2.04

Table 7: Peak and maximum load of PVA concrete.

Case	Peak/maximum load		
	1st loading	2nd loading (CMOD 0.05 mm)	3rd loading
PVA-7–28-W	4.40	3.23	3.60
	4.85	3.88	4.05
	4.63	3.63	3.78
	4.55	3.68	4.10
PVA-28–49-W	5.73	4.70	4.40
	5.55	5.55	5.53
	5.78	4.53	4.50
	6.15	5.38	5.03
PVA-49–70-W	5.35	4.65	4.28
	5.63	4.53	2.85
	5.35	5.00	5.08
	5.23	5.18	4.10
PVA-91–112-W	6.25	4.88	4.70
	6.10	5.60	4.50
	6.38	5.78	5.55
	6.83	6.63	4.90
PVA-7–28-A	4.55	3.45	3.55
	5.03	4.88	5.00
	4.50	4.20	4.53
	4.40	4.05	4.63
PVA-28–49-A	5.75	5.00	4.98
	5.65	4.68	4.35
	5.58	4.18	4.00
	5.38	4.50	4.12
PVA-49–70-A	5.20	4.90	3.96
	5.38	2.98	3.15
	5.93	5.38	2.71
	5.75	4.78	2.26
PVA-91–112-A	6.30	5.43	2.63
	5.45	5.08	2.63
	6.93	5.35	2.66
	—	—	—

The decrease in the strength recovery effect in inverse proportion to the delay of the 1st loading day is similar to the decrease in the strength increase ratio according to the aging effect. The strength increase capacity of the uncracked part may be high in 7–28 cases, but it must be lower than before in the 49–70 and 91–112 cases. In other words, the high strength recovery effect of the early 1st loading was dominant in the aging effect of the uncracked part, and it almost disappeared after 49 days. However the self-healing prevented further decrease.

3.3. Flexural Stiffness Recovery Effect. Figure 9 shows the flexural stiffness recovery effect with different 1st loading days and different self-healing environment of PE concrete and PVA concrete, respectively. The flexural stiffness recovery effect was inversely proportional to the delay of the 1st loading, regardless of the fiber type. The flexural stiffness recovery effect was over or around 1.0 with the water environment. This means that the initial slope of the load-CMOD curve of the 3rd loading was greater than that of the 2nd loading, and the recovery at the crack tip could be

expected. Otherwise, the flexural stiffness recovery effects with air environment were less than 1.0, regardless of the fiber type.

The average stiffness recovery effect of PVA concrete was 13% higher than that of PE concrete, 13% higher in the water environment, and 51% higher in the air environment. In particular, the average stiffness recovery effect of the PVA-7–28-W case shows over 1.4, and in the PVA-91–112-W case, over 1.0 was confirmed. These results are also attributed to the hydrophilicity of PVA fiber.

As a distinct difference between the air and the water environment of the stiffness recovery effect, the stiffness recovery effect more efficiently represents the self-healing performance. The reason is that the stiffness recovery effect was evaluated using the limited crack tip part where the healing effect was concentrated. It cannot be concluded that the stiffness recovery effect is the result of completely excluding the aging effect because it is also involved in not only the recovered crack tip part but also the enhanced uncracked part by the aging effect. Nevertheless, it can be deduced that the initial slope of the load-CMOD curve is influenced by the restoration of the flexural stiffness of the part where cracks are reopened, rather
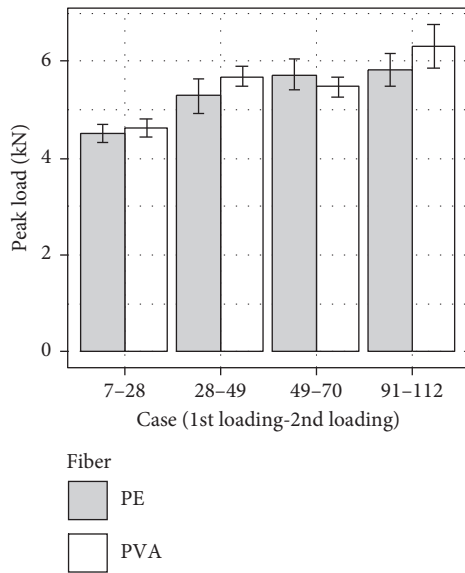
Figure 7: Peak load according to the 1st loading days.

than the aging effect. Therefore, it is considered to be an index that can more effectively evaluate the self-healing performance.

3.4. Crack Observation. Figure 10 shows the microscopic images of the 7–28 cases of PE and PVA concrete. It can be seen that debris-like substances are deposited all over the crack surface in the PE-W case, and the visual crack width appears to be relatively narrow. However, no precipitated material was observed around the fibers seen between the cracks. The PE-A case also showed deposited substances at the crack surface, but the amount was relatively small. The seen fiber between the cracks was also relatively clean. On the other hand, it was confirmed that not only the crack surfaces but also the bridged fiber had been covered by deposited substances in the PVA-W case. As mentioned above, it is considered as an additional evidence of why the PVA specimens showed a relatively high recovery in both strength and stiffness. The PVA-A case also showed deposited substances. However, the amount was relatively small, and the fibers appeared relatively clean.

This result does not represent the entire crack surface circumstance because the optical microscope can observe only a shallow depth from the surface. It was judged as a qualitative basis to supplement the quantitative comparison of the flexural strength and stiffness because almost similar patterns were observed in all the specimens tested in this study.

4. Conclusion

This study evaluates the self-healing performance with different crack inducement days and different self-healing environment. The PE concrete and PVA concrete were compared, and the flexural test using the notched three-point bending specimen was conducted. The results are summarized as follows:

(1) Regardless of the type of fiber, the degree of recovery of flexural strength and the flexural stiffness decreased
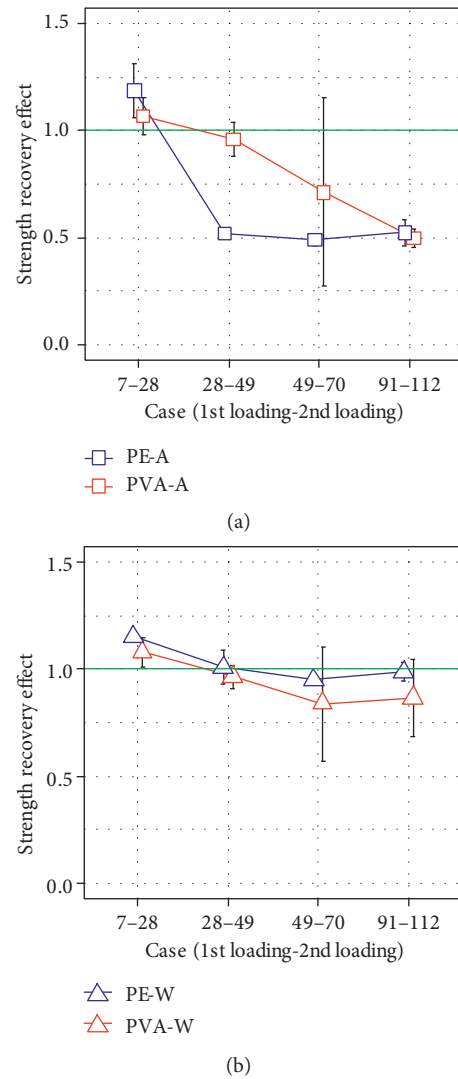

(a)

(b)

Figure 8: Strength recovery effect: (a) air environment; (b) water environment.

in inverse proportion to the delay of the crack inducement day (1st loading). Moreover, the water environment always showed high recovery effect than the air environment in all cases. These results confirm that the fast crack inducement has an advantage for self-healing, and the water environment is more suitable for self-healing.

(2) The evaluated self-healing performance exhibits similar characteristics to the aging effect. The recovery effect decreases in inverse proportion to the crack inducement time, and it shows more recovery in the water environment. The self-healing performance is closely related to the aging effect, and this means that the self-healing performance contains a considerable aging effect.

(3) Comparison of the flexural strength before and after healing cannot completely exclude the aging effect because not only the cracked part, but also the

(a)

(b)
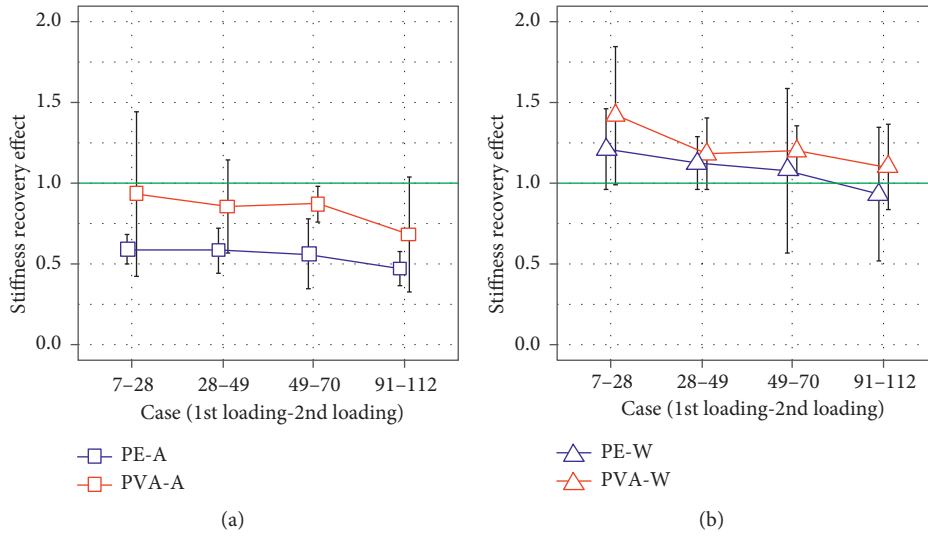
FIGURE 9: Stiffness recovery effect: (a) air environment; (b) water environment.

(a)

(b)

(c)

(d)
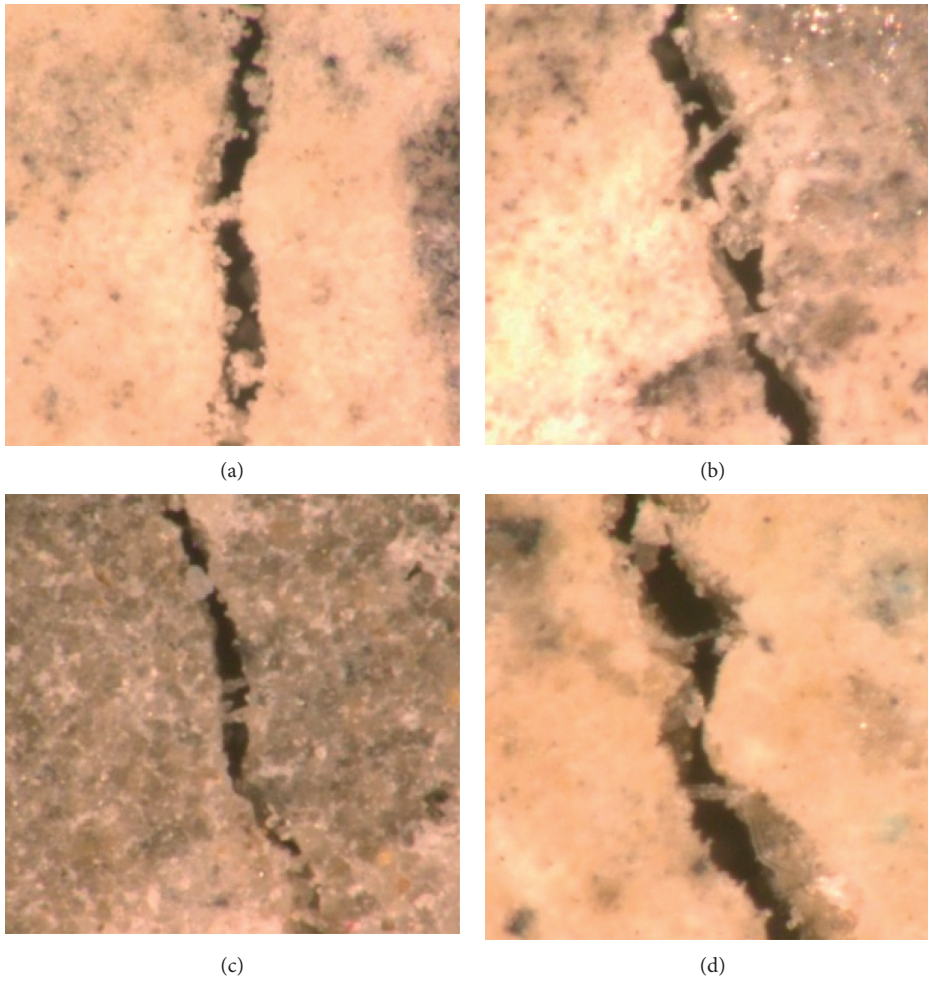
FIGURE 10: Optical microscopic images observed the crack surface: (a) PE-W, (b) PE-A, (c) PVA-W, and (d) PVA-A.

uncracked part participated in the strength. On the other hand, comparison of flexural stiffness is dominant at the crack tip, where the recovery due to

self-healing is concentrated, and the aging effect is relatively small. It is considered that comparing the flexural stiffness, rather than the flexural strength, is

more appropriate for more accurate evaluation of the self-healing performance.

(4) PVA concrete has a relatively greater self-healing performance than PE concrete in both the air and water environment. It is considered that the hydrophilicity of PVA fiber has an effect.

Data Availability

The data used to support the findings of this study are available from the corresponding author upon request.

Conflicts of Interest

The authors declare that they have no conflicts of interest.

Acknowledgments

References

[1] G. A. Barbos and M. Pastrav, "State-of-the-art report on ultra-high performance concrete (UHPC)," *Constructii*, vol. 15, no. 1, pp. 63–69, 2014.

[2] A. Alsalman, C. N. Dang, G. S. Prinz, and W. Micah Hale, "Evaluation of modulus of elasticity of ultra-high performance concrete," *Construction and Building Materials*, vol. 153, pp. 918–928, 2017.

[3] W. Meng and K. Khayat, "Effects of saturated lightweight sand content on key characteristics of ultra-high-performance concrete," *Cement and Concrete Research*, vol. 101, pp. 46–54, 2017.

[4] Y. Bao, M. Valipour, W. Meng, K. H. Khayat, and G. Chen, "Distributed fiber optic sensor-enhanced detection and prediction of shrinkage-induced delamination of ultra-high-performance concrete overlay," *Smart Materials and Structures*, vol. 26, no. 8, p. 085009, 2017.

[5] A. Bilodeau and V. M. Malhotra, "High-volume fly ash system: concrete solution for sustainable development," *ACI Materials Journal*, vol. 97, no. 1, pp. 41–48, 2000.

[6] S. Cheng, Z. Shui, T. Sun, R. Yu, G. Zhang, and S. Ding, "Effects of fly ash, blast furnace slag and metakaolin on mechanical properties and durability of coral sand concrete," *Applied Clay Science*, vol. 141, pp. 111–117, 2017.

[7] H. Liu, Q. Zhang, V. Li, H. Su, and C. Gu, "Durability study on engineered cementitious composites (ECC) under sulfate and chloride environment," *Construction and Building Materials*, vol. 133, pp. 171–181, 2017.

[8] D. M. Frangopol, K. Y. Lin, and A. C. Estes, "Life-cycle cost design of deteriorating structures," *Journal of Structural Engineering*, vol. 123, no. 10, pp. 1390–1401, 1997.

[9] D. M. Frangopol and M. Liu, "Maintenance and management of civil infrastructure based on condition, safety, optimization, and life-cycle cost," *Structure and Infrastructure Engineering*, vol. 3, no. 1, pp. 29–41, 2007.

[10] V. W. Tam, S. Senaratne, K. N. Le, L. Y. Shen, J. Perica, and I. C. S. Illankoon, "Life-cycle cost analysis of green-building implementation using timber applications," *Journal of Cleaner Production*, vol. 147, pp. 458–469, 2017.

[11] S. J. Park and S. Y. Ghim, "Applications and prospects of calcium carbonate forming bacteria in construction materials," *Journal of Microbiology and Biotechnology*, vol. 40, no. 3, pp. 169–179, 2012.

[12] E. J. Choi, J. Wang, J. H. Yoon, S. E. Shim, J. H. Yun, and I. Kim, "Self-healing Engineering Materials: I. Organic materials," *Clean Techology*, vol. 17, no. 1, pp. 1–12, 2011.

[13] S. R. White, N. R. Sottos, P. H. Geubelle, and J. S. Moore, "Autonomic healing of polymer composites," *Nature*, vol. 409, no. 6822, pp. 794–797, 2001.

[14] E. N. Brown, S. R. White, and N. R. Sottos, "Microcapsule induced toughening in a self-healing polymer composite," *Journal of Materials Science*, vol. 39, no. 5, pp. 1703–1710, 2004.

[15] W. J. Kim, S. T. Kim, S. J. Park, S. Y. Ghim, and W. Y. Chun, "A study on the development of self-healing smart concrete using microbial biomineralization," *Journal of the Korean Concrete Institute*, vol. 21, no. 4, pp. 501–511, 2009.

[16] S. Qian, J. Zhou, and D. Rooij, "Self-healing behavior of strain hardening cementitious composites incorporating local waste materials," *Cement and Concrete Composites*, vol. 31, no. 9, pp. 613–621, 2009.

[17] S. Igarashi, M. Kunieda, and T. Hishiwaki, "Research activity of JCI technical committee TC-075B: autogenous healing in cementitious materials," in *Proceedings of 4th International Conference on Construction Materials: Performance, Innovations and Structural Implications*, pp. 89–96, Nagoya, Japan, August 2009.

[18] H. Liu, Q. Zhang, C. Gu, H. Su, and V. Li, "Self-healing of microcracks in Engineered Cementitious Composites under sulfate and chloride environment," *Construction and Building Materials*, vol. 153, pp. 948–956, 2017.

[19] P. Termkhajornkit, T. Nawa, and K. Kurumisawa, "Effect of water curing conditions on the hydration degree and compressive strengths of fly ash–cement paste," *Cement and Concrete Composites*, vol. 28, no. 9, pp. 781–789, 2006.

[20] R. H. Haddad and M. A. Bsoul, *Self-Healing of Polypropylene Fiber Reinforced Concrete: Pozzolan Effect*, Ph.D. dissertation, Jordan University of Science and Technology, Irbid, Jordan, 1999.

[21] TC162-TDF RILEM, "Test and design methods for steel fibre reinforced concrete: bending test," *Materials and Structures*, vol. 33, pp. 3–5, 2000.

[22] K. Van Breugel, "Self-healing en vloeistofdichtheid," *Cement*, vol. 7, pp. 85–89, 2003.

[23] W. Meng, Y. Yao, B. Mobasher, and K. H. Khayat, "Effects of loading rate and notch-to-depth ratio of notched beams on flexural performance of ultra-high-performance concrete," *Cement and Concrete Composites*, vol. 83, pp. 349–359, 2017.

[24] P.-E. Petersson, *Crack Growth and Development of Fracture Zones in Plain Concrete and Similar Materials*, Ph.D. dissertation, Lund University, Lund, Sweden, 1981.

[25] S. Granger, A. Loukili, G. Pijaudier-Cabot, and G. Chanvillard, "Mechanical characterization of the self-healing effect of cracks in Ultra High Performance Concrete (UHPC)," in *Proceedings Third International Conference on Construction Materials, Performance, Innovations and Structural Implications, ConMat*, vol. 5, pp. 22–24, Vancouver, Canada, August 2005.

[26] Y. Jenq and S. P. Shah, "Two parameter fracture model for concrete," *Journal of Engineering Mechanics*, vol. 111, no. 10, pp. 1227–1241, 1985.

[27] S. P. Shah, "Determination of fracture parameters (KIcs and CTODc) of plain concrete using three-point bend tests," *Materials and Structures*, vol. 23, no. 6, pp. 457–460, 1990.

Review Article

Cement Types, Composition, Uses and Advantages of Nanocement, Environmental Impact on Cement Production, and Possible Solutions

S. P. Dunuweera [iD] [1,2] **and R. M. G. Rajapakse** [iD] [1,2]

[1]Department of Chemistry, Faculty of Science, University of Peradeniya, Peradeniya, Sri Lanka
[2]Postgraduate Institute of Science (PGIS), University of Peradeniya, Peradeniya, Sri Lanka

Correspondence should be addressed to R. M. G. Rajapakse; rmgr@pdn.ac.lk

We first discuss cement production and special nomenclature used by cement industrialists in expressing the composition of their cement products. We reveal different types of cement products, their compositions, properties, and typical uses. Wherever possible, we tend to give reasons as to why a particular cement type is more suitable for a given purpose than other types. Cement manufacturing processes are associated with emissions of large quantities of greenhouse gases and environmental pollutants. We give below quantitative and qualitative analyses of environmental impact of cement manufacturing. Controlling pollution is a mandatory legal and social requirement pertinent to any industry. As cement industry is one of the biggest CO_2 emitters, it is appropriate to discuss different ways and means of CO_2 capture, which will be done next. Finally, we give an account of production of nanocement and advantages associated with nanocement. Nanofillers such as nanotitania, nanosilica, and nanoalumina can be produced in large industrial scale via top-down approach of reducing size of naturally available bulk raw materials to those in the nanorange of 1 nm–100 nm. We mention the preparation of nanotitania and nanosilica from Sri Lankan mineral sands and quartz deposits, respectively, for the use as additives in cement products to improve performance and reduce the amount and cost of cement production and consequent environmental impacts. As of now, mineral sands and other treasures of minerals are exported without much value addition. Simple chemical modifications or physical treatments would add enormous value to these natural materials. Sri Lanka is gifted with highly pure quartz and graphite from which silica and graphite nanoparticles, respectively, can be prepared by simple size reduction processes. These can be used as additives in cements. Separation of constituents of mineral sands is already an ongoing process.

1. Introduction

This paper is an extended version of the Conference Paper published in the Proceedings of the 28th International Symposium on Transport Phenomena, 22–24 September 2017, Peradeniya, Sri Lanka [1]. As described in it, cement is a powdery substance made with calcined lime and clay as major ingredients. Clay used provides silica, alumina, and iron oxide, while calcined lime basically provides calcium oxide. In cement manufacturing, raw materials of cement are obtained by blasting rock quarries by boring the rock and setting off explosives [2]. These fragmented rocks are then transported to the plant and stored separately in silos. They are then delivered, separately, through chutes to crushes where they are then crushed or pounded to chunks of ~1/2 inch–sized particles [3]. Depending on the type of cement being produced, required proportions of the crushed clay, lime stones, and any other required materials are then mixed by a process known as prehomogenization and milled in a vertical steel mill by grinding the material with the pressure exerted through three conical rollers that roll over a turning milling table. Additionally, horizontal mills inside which the

TABLE 1: Approximate composition of the cement clinker.

Compound	Formula	Notation	wt.%
Celite (tricalcium aluminate)	$Ca_3Al_2O_6$ [$3CaO \cdot Al_2O_3$]	C_3A	10
Brownmillerite (tetracalcium aluminoferrite)	$Ca_4Al_2Fe_2O_{10}$ [$4CaO \cdot Al_2O_3 \cdot Fe_2O_3$]	C_4AF	8
Belite (dicalcium silicate)	Ca_2SiO_4 [$2CaO \cdot SiO_2$]	C_2S	20
Alite (tricalcium silicate)	Ca_3SiO_5 [$3CaO \cdot SiO_2$]	C_3S	55
Sodium oxide	Na_2O	N	≤2
Potassium oxide	K_2O	K	
Gypsum (calcium sulphate dihydrate)	$CaSO_4 \cdot 2H_2O$ [$CaO \cdot SO_3 \cdot 2H_2O$]	CSH_2	5

Adapted from [2]; http://www.engr.psu.edu/ce/courses/ce584/concrete/library/construction/curing/Composition%20of%20cement.htm.

material is pulverized by means of steel balls are also used. It is then homogenized again and calcined, at 1400°C, in rotary kilns for the raw material to be transformed to a clinker, which is a small, dark grey nodule 3-4 cm in diameter. The clinker is discharged from the lower end of the kiln while it is red-hot, cooled by various steps, ground and mixed with small amounts of gypsum and limestone, and very finely ground to produce cement [4].

In the calcination process, in the kiln, at high temperatures, the above oxides react forming more complex compounds [5]. For instance, reaction between $CaCO_3$, $Al_3(SiO_3)_2$, and Fe_2O_3 would give a complex mixture of alite, $(CaO)_3SiO_2$; belite, $(CaO)_2SiO_2$; tricalcium aluminate, $Ca_3(Al_2O_3)$; and ferrite phase tetracalcium aluminoferrite, $Ca_4Al_2O_3Fe_2O_3$ with the evolution of CO_2 gas in the Portland cement clinker [6]. However, there can be many other minor components also since natural clay also contains Na, K, and so on. In the chemical analysis of cement, its elemental composition is analyzed (e.g., Ca, Si, Al, Mg, Fe, Na, K, and S). Then, the composition is calculated in terms of their oxides and is generally expressed as wt.% of oxides. For simplicity, if we assume that the clinker contains the above four main oxides, they can be simply represented by the Bogue formulae where CaO, Al_2O_3, Fe_2O_3, and SiO_2 are denoted as C, A, F, and S, respectively [7]. In this notation, alite (tricalcium silicate) [$(CaO)_3SiO_2$], belite (dicalcium silicate) [$(CaO)_2SiO_2$], celite (tricalcium aluminate) [$Ca_3Al_2O_6 = 3CaO \cdot Al_2O_3$], and brownmillerite (tetracalcium aluminoferrite) [$Ca_4Al_2Fe_2O_{10} = 4CaO \cdot Al_2O_3 \cdot Fe_2O_3$] are represented by C_3S, C_2S, C_3A, and C_3AF, respectively. If we analyze the elemental composition of Ca, Al, Fe, and Si, usually from X-ray fluorescence spectroscopy, then we express them as wt.% of their respective oxides. For example, if the experimentally determined clinker composition is CaO = 65.6%, SiO_2 = 21.5%, Al_2O_3 = 5.2%, and Fe_2O_3 = 2.8%, then Bogue calculations would give C_3S = 64.7%, C_2S = 12.9%, C_3A = 9.0%, and C_4AF = 8.5%, respectively [8]. However, cement contains water (H_2O), sulphate (SO_3), sodium oxide (Na_2O), potassium oxide (K_2O), gypsum ($CaSO_4 \cdot 2H_2O$), which are denoted as H, S, N, K, and CSH_2, respectively. Note that gypsum (calcium sulphate dihydrate) is considered as $CaO \cdot SO_3 \cdot 2H_2O$ and hence its notation is

CSH_2. As such, approximate composition of the cement clinker is different from the above values and is depicted in Table 1.

There are several different types of cements of which Portland cement, Siliceous (ASTM C618 Class F) Fly Ash, Calcareous (ASTM C618 Class C) Fly Ash, slag cement, and silica fume are the major types [9, 10]. They differ from their chemical composition. Table 2 gives the compositions of the above cement types in terms of SiO_2, Al_2O_3, Fe_2O_3, CaO, MgO, and SO_3, and the remaining can be other materials such as Na_2O and K_2O. Note that SO_3 stands for oxide of S, where S is derived from gypsum ($CaSO_4 \cdot 2H_2O$). Given in Table 2 are also important physical properties such as specific surface area (surface area per unit mass, SSA) and specific gravity (SG) of these different types of cements [11, 12].

General use of the Portland cement, Siliceous (ASTM C618 Class F) Fly Ash, Calcareous (ASTM C618 Class C) Fly Ash, slag cement, and silica fume in concrete is as primary binder, cement replacement, cement replacement, cement replacement, and property enhancer, respectively [16].

2. Types of Cements and Their Composition and Uses

There are over ten different types of cements that are used in construction purposes, and they differ by their composition and are manufactured for different uses. These are rapid-hardening cement (RHC), quick-setting cement (QSC), low-heat cement (LHC), sulphate-resisting cement (SRC), blast furnace slag cement (BFSC), high-alumina cement (HAC), white cement (WC), coloured cement (CC), pozzolanic cement (PzC), air-entraining cement (AEC), and hydrophobic cement (HpC). RHC has increased the lime content compared to the Portland cement (PC) [17, 18]. Purpose of having high lime content is to attain high strength in early days. It is used in concrete when formwork is to be removed early. Since hardening of cement is due to the formation of $CaCO_3$ by absorbing atmospheric CO_2 by CaO, increased CaO results in increased $CaCO_3$ formation even at the early stage to result in rapid hardening [19].

TABLE 2: Composition of components as wt.% used to make different types of cements.

Component	Portland cement	Siliceous fly ash	Calcareous cement	Slag cement	Fume silica
SiO_2	21.9	52.0	35.0	35.0	85–97
Al_2O_3	6.9	23.0	18.0	12.0	0
Fe_2O_3	3.9	11.0	6.0	1.0	0
CaO	63.0	5.0	21.0	40.0	<1
MgO	2.5	0	0	0	0
SO_3	1.7	0	0	0	0
SSA $(m^2 \cdot g^{-1})$	0.37 Blaine	0.42 Blaine	0.42 Blaine	0.40 Blaine	15–30 BET
SG	3.15	2.38	2.65	2.94	2.22

SSA = specific surface area; SG = specific gravity. Adapted from [13–15].

QSC is produced by adding a small percentage of aluminium sulphate as an accelerator and reducing the amount of gypsum used with fine grinding. This cement is used when the work is to be completed very quickly as in static and running waters. LHC has reduced the amount of C_3A, which is used to produce massive concrete constructions like gravity dams. LHC has compressive strength to heat of the hydration ratio of at least 7 at the age of 13 weeks. The usual wt. ratio of CaO to SiO_2 is between 0.8 and 1.5, but Al_2O_3 wt.% is less than 10% [20]. This is prepared by grinding the CaO, SiO_2, and Al_2O_3 materials, melting the mixture, quenching the melt, and grinding the quenched matter to have mainly amorphous material of the above composition. Alumina is a hydratable material and reduced alumina gives reduced hydration to produce less heat of hydration. This is important in the construction of large structures to avoid possible thermal cracking during concrete setting [21].

Sulphate attack on concrete is a chemical breakdown mechanism, where sulphate reacts with C3A and/or $Ca(OH)_2$ components of the hardened cement forming ettringite, which is hexacalcium aluminate trisulphate hydrate $[(CaO)_6(Al_2O_3) (SO_3) 32H_2O = C_6ASH_{32}]$. Sulphate ions can react with C_3A and/or $Ca(OH)_2$ in hardened concrete in the presence of water forming gypsum. These newly formed ettringite and gypsum crystals occupy empty spaces of concrete, and as they grow, they tend to damage the paste by cracking. The most important parameters determining the sulphate attack are C_3A, C_3S/C_2A ratio, and C_4AF. It has been reported that the addition of pozzolonic admixtures such as fly ash reduces the C_3A content of cement [22] when sulphate is present in water and soil used; in places like canal linings, culverts, retaining walls, and siphons, it is important to use SRC. SRC is prepared by maintaining C_3A content below 6%.

BFSC is prepared by grinding the clinkers with ~60% slag. BFSC resembles properties of the Portland cement and is used for works in which economic considerations are predominant. HAC is obtained by melting a mixture of bauxite and lime and grinding the mixture with the clinker. Since it contains high alumina content, it is rapid-hardening cement with initial and final setting times of about 3.5 h and 5 h, respectively [22]. HAC is used in works where concrete is subjected to high temperatures, frost, and acidic conditions. WC is prepared from raw materials free from iron oxides and oxides of other transition metals such as Cr, Mn, Cu, V, and Ti. The colouring effect takes the order

$Cr_2O_3 > Mn_2O_3 > Fe_2O_3 > V_2O_3 > CuO > Ti_2O_3$. As such, the amounts of these transition metal ions, particularly Cr^{3+}, Mn^{3+}, and Fe^{3+}, should be minimized to form white cement. Usually, Cr_2O_3, Mn_2O_3, and Fe_2O_3 are kept below 0.003%, 0.03%, and 0.35%, respectively, in the clinker [23]. Cheap quarried raw materials usually contain Cr, Mn, and Fe. For example, lime stones and clays usually contain 0.3–1% and 5–15% Fe_2O_3. Keeping Fe_2O_3 below 0.5% is desirable to make WC, and as such, kaolin and sand are used instead of other clays in making WC. The abrasiveness of sand particles with size <45 μm also ensures less wearing of chrome-steel grinding mill used to grind raw materials, which would otherwise contaminate the mixture with Fe and Cr. Usually, sand is ground separately using ceramic grinding media to avoid chromium contamination. WC is costly and hence used in aesthetic applications such as precast curtain wall and facing panels and terrazzo surface. Contrary to WC, CC is prepared by deliberately adding mineral pigments to cement. CCs are widely used in decorative works on floors. Iron oxides are used to get red, yellow, and black base colours, and several mixed colours such as browns-terracotta-tuscany-sepia-beach. Standard green and blue pigments are chrome oxide and cobalt aluminium oxide, respectively. TiO_2 is the usual white pigment. PzC is prepared by grinding the pozzolanic clinker with the Portland cement [24]. It is used in marine structures, sewage works, and for laying concrete under water such as in bridges, piers, and dams.

AEC is produced by adding air-entraining agents that are surfactants such as alkali salts of wood resins, synthetic detergents of the alkyl-aryl sulphonate type, calcium lignosulphate derived from the sulphite process in paper making, and calcium salts of glues and other proteins obtained in the treatment of animal hides, animal and vegetable fats, oil and their acids, wetting agents, aluminium powder, and hydrogen peroxide, during the grinding of the clinker [25]. They are added in 0.025–0.1% in either solid or liquid form. At the time of mixing, AEC produces tough, tiny, discrete noncoalescing air bubbles of 10–500 μm in diameter in the body of the concrete. These bubbles can compress to some extent, and hence, they can absorb stress created by freezing.

HpC is prepared by adding water-repellent chemicals [26]. They are prepared particularly for use in high-rainfall regions to prevent water absorption during storage. Particles of HpC are coated with nonpolar substances, usually by

Table 3: Masses of emitted pollutants from the European cement kilns per year.

Pollutant	Mass emitted (tonnes per year)
CO_2	1.5456 million
CO	460–11500
SO_2	Up to 11125
NO_x as NO_2	334–4670
Dust	0.62–522
TOC/VOC	2.17–267
HCl	0.046–46
HF	0.21–23.0
PCCD/PCDF	0.0000276–0.627 g per year

Adapted from http://ena.lp.edu.ua:8080/bitstream/ntb/16692/1/55-Stajanca-296-302.pdf.

adsorbing oleic acid, stearic acid, and so on, to cement particles [27, 28]. When adsorbed, these surfactant molecules self-assemble by coordinating with surface cations through their carboxylic acid groups thereby allowing the nonpolar hydrocarbon chain to extend from the particles. When a water drop falls on them, they are stuck on hydrocarbon chains and stay as spherical particles as does by the lotus leaf. The cement particles are then not wetted, and water drops roll off when slightly slanted. These hydrophobic coatings prevent the attacks by chloride and sulphate ions, and hence, they resist to deterioration of concretes by these ions [29].

3. Environmental Effects of Cement Manufacturing

Measured data of the European cement kiln emissions show that cement industry contributes substantially to environmental pollution. Table 3 lists main environmental pollutants emitted by the European cement kilns in tonnes per year.

TOC/VOC, PCCD, and PCDF indicate total organic compounds including volatile organic compounds, polychlorinated dibenzo-p-dioxins, and polychlorinated dibenzofurans, respectively. It has been reported that toxic metals such as Hg, Cd, Tl, As, Sb, Pb, Cr, Co, Cu, Mn, Ni, and V are also emitted in considerable amounts. For example, masses of Hg, $\sum$ (Cd, Tl), and $\sum$ (As, Sb, Pb, Cr, Co, Cu, Mn, Ni, V) emitted in kg per year are 0–1311, 0–1564, and 0–9200, respectively [30]. In addition to material pollutants, noise emission is also associated with almost all the processes involved in cement manufacturing. These environmental impacts contribute to abiotic depletion, global warming, acidification, and marine ecotoxicity [31].

Cement is produced by utilizing an extensive amount of raw materials treated and reacted at extreme conditions such as high temperatures. The high-temperature processes are called pyroprocessing processes where raw materials are heated at high temperatures for solid-state reactions to take place, which utilize fuel sources such as coal, fuel oil, natural gas, tires, hazardous wastes, petroleum coke, and basically anything combustible [32]. Some cement manufacturing plants utilize the organic waste generated in other industries

such as rubber processing industries. As such, cement industry contributes to a significant extent of anthropogenic carbon dioxide emissions, which is in the range of 5–7% of total anthropogenic carbon dioxide emissions [33]. In the clinker burning process, in order to produce 1 tonne of clinkers, 1.52 tonnes of raw materials are used on average. The balance of 0.52 tonne of raw materials is converted mainly to carbon dioxide by the processes such as $CaCO_3 \rightarrow CaO + CO_2$. This is a serious global environmental problem since increase in carbon dioxide in the atmosphere has direct consequences on global warming. In addition to CO_2, other key polluting substances emitted to air by the cement industry include dust, other carbon oxides such as carbon monoxide (CO), nitrogen oxides (NO_xs), sulphur oxides (SO_xs), polychlorinated dibenzo-p-dioxins, dibenzofurans, total organic carbon, metals, hydrogen chloride, and hydrogen fluoride, which are serious health-hazardous substances and some are hilariously odorous [34]. However, the type and amount of air pollution caused by the cement industry depend on various parameters, such as inputs (the raw materials and fuels used) and the type of process used in the industry.

As for water pollution, the contribution from cement industry may be insignificant through the storage and handling of fuels that may contribute to soil and groundwater contaminations [35]. In order to reduce the amount of raw materials, particularly in the manufacturing of specialized cement types as described above, supplementary cementitious materials such as coal fly ash, slag, and natural pozzolans such as rice husk ash and volcanic ashes are used. This will not only reduce the waste materials generated for landfilling but also the cost of cement production [36].

However, cement is an essential material for human survival nowadays. As such, there is no alternative, but the production of cement is mandatory. At the same time, controlling pollution created by cement industry is also very important. In the next section, we discuss ways and means of controlling pollution resulting from cement industries.

4. Pollution Control in Cement Manufacturing

The air pollution occurs in the excavation activities, dumps, tips, conveyer belts, crushing mills, and kilns of cement industry. Minimizing air pollution is a mandatory legislative requirement, which also contributes to minimizing wastage and survival of the industry [37]. Dust particles emitted at sites other than kilns can be captured using a hood or other partial enclosure and transported through a series of ducts to the collectors. The dust collected can be fed to the kiln provided that it is not too alkaline not exceeding 0.6% as per the Na_2O (N) content. However, if the alkalinity is higher than this value, then the dust must be either discarded or pretreated before feeding to the kiln. Flexible pulse jet filters, electrostatic precipitators, wet scrubbers, and baghouse method can be used to collect dust from flue gas [38]. The US Environmental Protection Agency has reviewed the available and emerging technologies for reducing greenhouse gas emissions from Portland cement industry. The primary greenhouse gas emitted in the cement industry is carbon

dioxide, but in lower quantities, NO_xs and SO_xs are also emitted as detailed in Table 3 [39].

4.1. Carbon Capture and Storage.

This involves separation and capture of carbon dioxide from the flue gas, pressurization, and transportation via pipelines, injection, and long-term storage. In regard to this, several processes have been developed as detailed below.

4.1.1. Calera Process.

This involves capture of CO_2 from flue gas and conversion to carbonates. This utilizes a scrubber containing high-pH water with calcium, magnesium, sodium, hydroxide, and chloride as the scrubbing liquid. CO_2 captured by this water is converted to $CaCO_3$ and $MgCO_3$, which are precipitated out of the solution. The precipitates can be filtered, washed, and dried for reuse as feed material for the kiln to make blended cement. Water used may be seawater or reject brine. Capture efficiency of over 90% has been reported in a 10 -MW coal-fired pilot plant. It is interesting to note that when captured carbon is reused, the overall carbon footprint becomes negative since the carbon emissions avoided from the cement manufacturing process could be greater than those of carbon emissions from the power plant [39, 40].

4.1.2. Oxy-Combustion Process.

In the oxy-combustion process, fuel is burnt with pure or nearly pure oxygen instead of air. Since there is no nitrogen gas, the fuel consumption is reduced due to the fact that there is no need to heat and burn nitrogen gas. Since air contains nearly 79% nitrogen gas and any combusted nitrogen comes as NO_x in flue gas, the volume of flue gas and NO_x in it is significantly reduced when pure oxygen is used for combustion [39, 41]. This process should utilize an air separation process to separate out nitrogen gas, which can be used for other processes such as for inflating vehicle tires. Nitrogen-removed air basically contains majority of oxygen, and it can be used for the oxy-combustion process. When oxy-combustion is used, the resulting kiln exhaust contains over 80% CO_2 gas, which can be recovered by the Calera process. There are several technical issues as laid down in [42] that have to be tackled before implementing this process in cement industry.

4.1.3. Monoethanolamine (MEA) Process.

When flue gas is passed through a column containing monoethanolamine, CO_2 gas is selectively absorbed. High-pressure, low-temperature conditions favour the absorption. When CO_2-rich MEA solution is subjected to low-pressure, high-temperature conditions, it releases absorbed CO_2 which can be converted to some other product like $CaCO_3$ or $MgCO_3$ and the solvent recovered can be reused. One of the problems with this method is that acidic gases such as SO_x and NO_x present in the flue gas can react with MEA. Therefore, levels of these gases must be kept below 0.001% prior to absorption by MEA. Instead of regular amines, hindered amines can also be used. Hindered
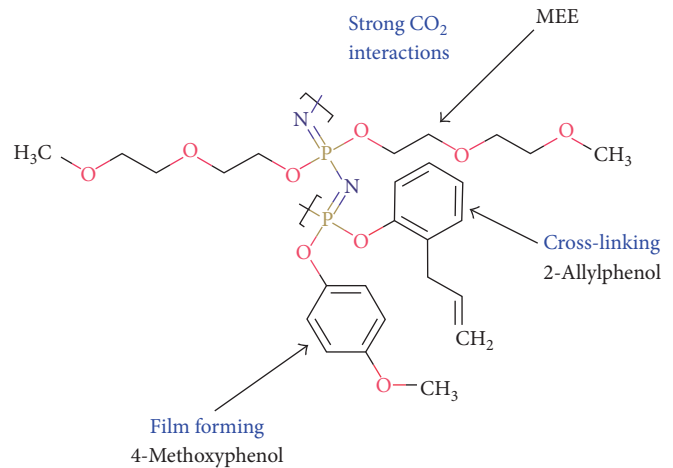

FIGURE 1: General structure of stabilized poly(methoxyethoxy) ethanol phosphazene hollow fibre membrane.

amines have special functional to prevent degradation of the amine [43].

4.1.4. Flue Gas Desulphurized Mixture.

Flue gas contains SO_x, which could be separated using limestone-based compounds. They are then converted to slurries to use as CO_2 absorbents. This way, both SO_x and CO_2 can be removed from flue gas [43].

4.1.5. Cryogenic Distillation.

Cryogenics is the science that addresses the production and effects of very low temperatures. In the cryogenic separation, all other gases except CO_2 and N_2 have to be removed prior to subjecting to low-temperature conditions. The triple point for CO_2 is 256.68°C and 7.4 atm, and when these conditions are maintained, CO_2 will condense while N_2 will remain as a gas. N_2 gas is then escaped through an outlet at the top of the chamber, and the dense liquid is taken from the bottom of the chamber. Refrigeration under pressure is an alternative method to cryogenic distillation but utilizes even harsh conditions such as higher pressures and lower temperatures. Cryogenic methods have distinct advantages over other separation methods. Since CO_2 is separated as a liquid, it can be transported via pipelines for sequestration. Also, the recovery and purity of CO_2 is very high (CO_2 purity after distillation can exceed 99.95%) [43].

4.1.6. Membrane Separation.

Suitable membranes can be used to separate or adsorb CO_2 in the kiln exhaust gas. Poly (methoxyethoxy)ethanol phosphazene (MEEP) hollow fibre membranes are excellent CO_2 separation and storing membranes, where (methoxyethoxy)ethanol groups attached P have strong interactions with CO_2 [44–46]. One such example is given in Figure 1.

Polymer blends with required properties such as strong interaction with CO_2 can be used as CO_2-selective membranes. For example, cross-linked thin-film composite of poly(vinylalcohol) (PVA)/polyvinylpyrrolidone (PVP) blend
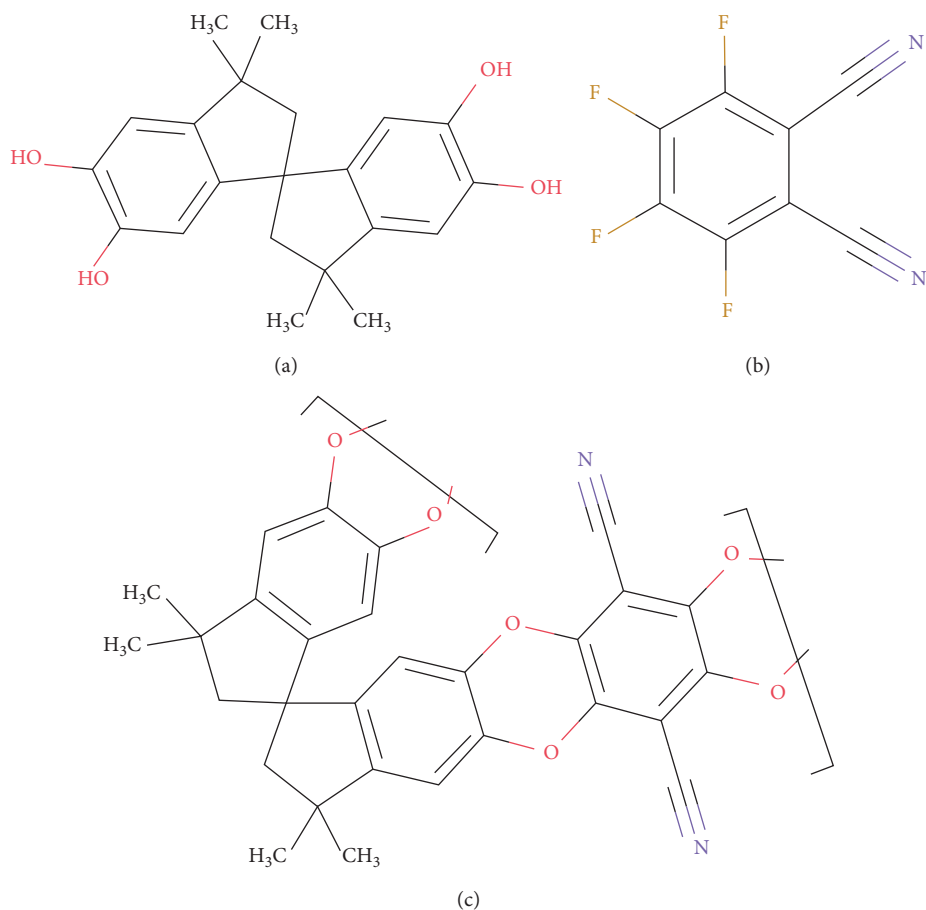
(a)

(b)

(c)

Figure 2: Chemical structures of (a) 5,5,6,6-tetrahydroxy-3,3,3,3-tetramethylspiro-bisindane, (b) tetrafluorophthalonitrile, and (c) polycondensate polymer PIM-1 [49].

membranes doped with suitable amine carriers are excellent CO_2-selective membranes as reported by Mondal and Mandal. The CO_2 permeability of this membrane is 1396 Barrer at 2.8 atm and 100°C [47]. Combination of grafting and cross-linking is an advanced technique capable of suppressing plasticization. In this respect, Achoundong et al. developed cellulose acetate (CA) membranes and grafted vinyl-trimethoxysilane (VTMS) to –OH groups, which due to subsequent condensation of hydrolyzed methoxy groups on the silane form cross-linked polymer networks. The modified membranes have an order of magnitude higher CO_2 permeability than neat cellulose acetate membranes [48].

Polymers of intrinsic microporosity (PIMs), thermally rearranged polymers (TRPs), polyimides, and polyurethanes are advanced polymers with high selectivity for CO_2 and hence are suitable membranes for CO_2 separation. PIMs are ladder polymers with high free volume and high selectivity for CO_2. These ladder polymer backbones can be prepared by polycondensation reaction of tetrahydroxy monomers containing spiro- or contorted centres with tetrafluoromonomers. One such example is the PIM-1 prepared by the polycondensation reaction of commercial monomers such as 5,5,6,6-tetrahydroxy-3,3,3,3-tetramethyl-1,1′-spiro-bisindane with tetrafluorophthalonitrileo. Chemical structures of the monomers are given in Figure 2.

These polymers have high CO_2 solubility and spirocentres, such as thianthrene [50], 9,10-dimethyl-9,10-dihydro-9,10-ethanoanthracene [51], ethanoanthracene [52], and pyrazine [53], and could be incorporated in PIM membranes for adjusting the gas permeation properties.

Thermally rearranging polymers (TRPs) are prepared by a thermal postmembrane conversion process of functionalized polyimides. They have uniform cavities with tailored free-volume elements with well-connected morphology in the amorphous state [54]. For example, thermal rearrangement of poly(hydroxyimide)s is shown in Figure 3.

TRPs have good CO_2/CH_4 separation performance, good resistivity to CO_2-induced plasticization, and high chemical resistivity [55].

4.2. Adsorption of CO_2 into Advanced Sorbents.

Separation of CO_2 from a gas mixture by selective adsorption involves both thermodynamics (adsorption) and kinetics (diffusion selectivity), and designing adsorbents for CO_2 in the presence of gases such as CH_4 and N_2 is challenging since all three gases have similar kinetic diameters of 3.30 Å, 3.76 Å, and 23.64 Å, respectively [55]. In this sense, sorbents such as zeolites and metal-organic frameworks (MOFs) stand out as adsorbents of CO_2.
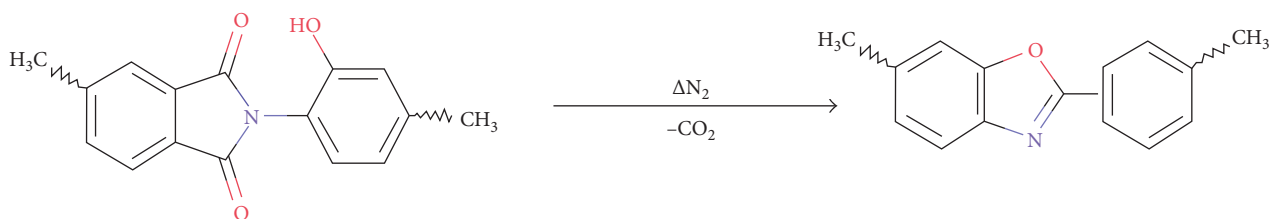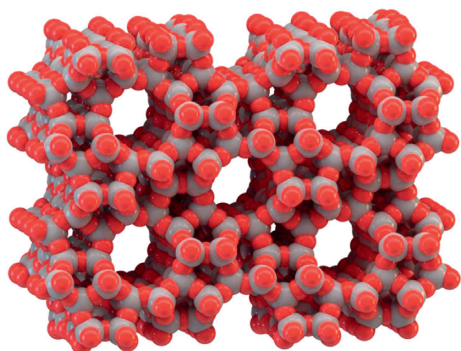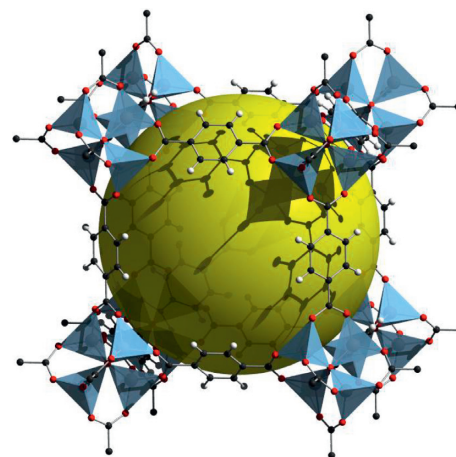
FIGURE 3: Thermal rearrangement of poly(hydroxyimide)s.

FIGURE 4: The microporous molecular structure of zeolite, ZSM-5. (Thomas Splettstoesser (www.scistyle.com), own work, CC BY-SA 4.0, File:Zeolite-ZSM-5-vdW.png (created: 23 June 2015); https://en.wikipedia.org/wiki/Zeolite (accessed: June 11, 2017)).

FIGURE 5: An example for MOF: MOF-5. Large pore is shown with the yellow ball (Tony Boehle, own work: https://en.wikipedia.org/wiki/Metal-organic_framework#/media/File:IRMOF-1_wiki.png).

4.3. Zeolites. Zeolites are microporous aluminosilicate minerals such as analcime, chabazite, clinoptilolite, heulandite, natrolite, phillipsite, and stilbite. Figure 4 shows the microporous molecular structure of zeolite, ZSM-5. Synthetic zeolites are prepared by the slow crystallization of a silica-alumina gel in the presence of alkalis and organic templates.

Zeolites are added to the Portland cement as a pozzolan and water reservoir to reduce chloride permeability and to improve workability. Siriwardane et al. have studied competitive gas adsorption properties of zeolites 13X, 4A, 5A, UOP-WE-G 592, and UOP APG-II with gas mixtures containing CO_2 and found that all of them have good CO_2 adsorption capacities down to ppm levels from a gas mixture containing 15% CO_2, 3% O_2, and 83% N_2 [56]. Zeolites are microporous and aluminosilicate minerals commonly used as commercial adsorbents. Zeolite has been used for trapping CO_2 from ice or air [57]. A zeolite trap was also used as an alternative to a cryogenic trap for collecting CO_2 from oxidation of organic carbon. The selective gas absorption and desorption characteristics of zeolite as a function of temperature will be useful for simplifying the system for trapping CO_2 and transferring the gas to a graphitization reactor [58].

4.4. Metal Organic Frameworks (MOFs). Metal organic frameworks (MOFs) are yet another good sorbents for CO_2. Their structures are composed of metal-containing nodes linked by organic ligand bridges, which are assembled through strong coordination bonds (Figure 5) [59].

Compared to other CO_2 sorbents such as zeolites and activated carbon, MOFs have higher pore volume and surface area and hence have higher CO_2 sorption capacity [60, 61]. Adsorption is the process of entrapping atoms or molecules which are incident on a surface; hence, the adsorption capacity of a material concerned increases with respect to its surface area. In 3D nature, the maximum surface area would be obtained by a structure that is highly porous such that molecules and atoms can access internal surfaces of the materials. It clearly suggests that the highly porous metal organic frameworks (MOFs) should have to have an excellent ability of entrapping CO_2. Generally, the most successful MOFs demonstrate extremely high BET surface areas of $4,000–7,000\,m^2{\cdot}g^{-1}$ with many also possessing coordinatively unsaturated metal sites [62]. In order to gain high efficiency of CO_2 entrapment inside the MOF and for the development of higher performance MOFs, the interior part of MOFs should be designed to have coordinative porosity, hydrophobicity, defects and embedded nanoscale metal catalysts, unsaturated metallic suitable sites, specific heteroatoms, and other building unit interactions [63]. Some examples of MOFs capable of CO_2 sorption are $Ni^{II}_2Ni^{III}(\mu_3\text{-}OH)(pba)_3(2,6\text{-}ndc)_{1.5}$ (MCF-19; pba = 4-(pyridin-4-yl)benzoate, 2,6-ndc = 2,6-naphthalenedicarboxylate), $Zn_4O(bdc)_3$ (MOF-5 or IRMOF-1, bdc = 1,4-benzenedicarboxylate), $Zn_4O(btb)_2$ (MOF-177, btb = benzene-1,3,5-tribenzoate), and $Zn_4O(bte)_{14/9}(bpdc)_{6/9}$ (MOF-210, bte = 4,4,4-(benzene-1,3,5-triyltris(ethyne-2,1-diyl))tribenzoate, bpdc = biphenyl-4,4-dicarboxylate) [64–66].
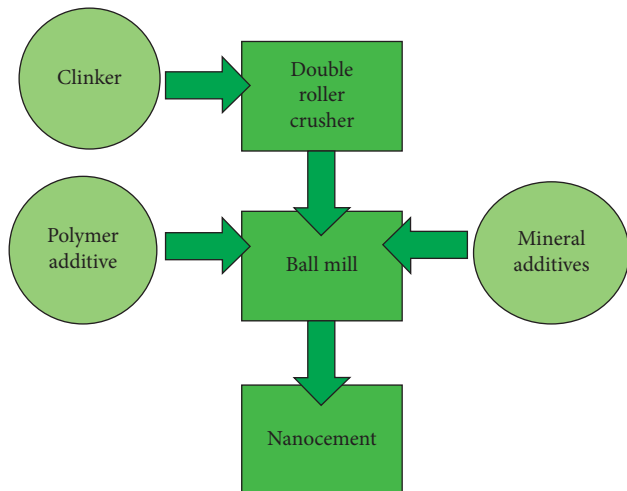
Figure 6: Schematic representation of the nanocement production process.

5. Nanocement

Nanocement is the cement produced by mechanical activation of nuclear cement particles in the size range 2-3 μm by coating with 10 to 100 nm-thick membranes of modifier materials. More than 65% of mineral supplements such as sand, ash, slag, and tuff and polymer additives are used as modifier materials [67]. The development of modern cement and concrete industry seeks for the improvement of the durability of the materials by the addition of required amount of nanoparticles, or nano-based structure of cement-based materials can be improved. Frequently used nanoparticles are nanosilica, nanoclay, and carbon nanotubes [68, 69]. Improvement of durability of the materials is approached through alteration of the physicochemical properties of the binder. In addition, usages of nanoclay and carbon nanotubes can decrease the transport property, optimize microstructure, and decrease the volume instability of cement-based materials. The process of nanocement production is shown schematically in Figure 6. It has been reported that nanocement can be used to produce 500–800 brands of high-strength concretes and 1300–1500 brands of heavy-duty concretes [70]. "US Patent on Method for producing nano-cement, and nano-cement" [71] deals with the procedure developed to produce nanocement, which involves mechanochemical activation of dispersed grains of the Portland cement in the presence of a polymeric modifier. They used at least 60% by wt. of sodium naphthalenesulfonate and mineral siliceous additive containing at least 30 wt.% SiO_2 and gypsum to form nanoshells around cement grins. Capsules of 20–100 nm thickness are formed around Portland cement grains, which are made of sodium naphthalenesulfonate and structured by calcium cations. Subsequent to mechanochemical activation, the resultant material is ground to a specific surface area of 300–900 $m^2 \cdot kg^{-1}$. Nanocement improves the technical quality of the Portland cement, reduces cost of production due to the use of 70 wt.% mineral additives, 1.2–2 times reduction of the fuel cost, and

2-3 times reduction of emission of NO_x, SO_2, and CO_2 per tonne of cement. Nanocement has very high performance; for instance, the deflection strength of nanocement-based concrete and ordinary Portland cement-based concrete at 2-day hardening are around 6.3–7.1 MPa and 2.9 MPa with corresponding compressive strengths of 49.3–54.7 MPa and 21.3 MPa, respectively. At 28-day hardening, deflection strength improves to 8.2–8.7 MPa and 6.4 Mpa, respectively, while compressive strength improves to 77.5–82.7 MPa and 54.4 MPa, respectively [72].

Use of nano-graphite as an additive in cement is also currently under investigation. Use of graphite nanoparticles in cement is expected to not only improve mechanical properties but also improve faster curing time, inhibition of premature failure in concretes, and ability to withstand large external forces produced in earthquakes and explosions [73]. The use of less concrete is also possible which means eventual contribution to the production of less Portland cement and hence reduction of consequent environmental problems associated with Portland cement manufacturing [74]. Other nanofillers used to improve properties of Portland cement include nanotitania (TiO_2), carbon nanotubes, nanosilica (SiO_2) and nanoalumina (Al_2O_3), nanohematite/iron oxide (iii) (Fe_2O_3), nano-magnetite/iron oxide (ii) (Fe_3O_4), nano-ZnO_2, nano-ZrO_2, nano-Cu_2O_3, nano-CuO, nano-$CaCO_3$, as nanotubes or fibres (carbon nanotubes and carbon nanofibers, and nano-clay).

According to the Feldman–Sereda model, the cement paste consists principally of gel pores, capillary pores, and an interlayer of water. In the concrete, there is an interfacial transition zone between the cement paste and the aggregates, which establishes a weak link in the concrete, basically the site at which the first cracks occur. Hence, it is significant to generate crack-free concrete with the possible incorporation of nanosilica to pursue [75]. Chen et al. demonstrated that TiO_2 is an inert and stable compound during the cement hydration process, in which the total porosity of the cement pastes decreased, so that the pore size distribution is also changed. Normally, the acceleration of the hydration rate and the change in the microstructure also affected the physical and mechanical properties of the cement-based materials. The nano-TiO_2 role is to work as a catalyst in the cement hydration reactions. Water absorption and capillary absorption show a significant decrease when TiO_2 nanoparticles are included in the concrete, as the nanoparticles represent as nanofillers and thereby improve the concrete's resistance to water permeability. Moreover, TiO_2 nanoparticles can progress the filler effect, and also the great pozzolanic action of fine particles substantially rises the quantity of strengthening gel formed [76]. Nanomontmorillonite (NM) is the most common member of the smectite clay family, which is sometimes referred to as nanoclay. This kind of clay belongs to a general mineral group of clays, which have particles with a sheet-like structure in which the dimensions in two directions far exceed the thickness.

We have investigated the production of these nanoparticles from both top-down and bottom-up approaches. Top-down approach is more industrially viable since large quantities of bulk materials found naturally can be used to

produce corresponding nanomaterials through particle size reduction. The top-down approach relies on reducing the size of bulk materials to the size of the nanorange of 1–100 nm. This can be done by crushing bulk materials to make powders, sieving to different fractions, further crushing of large size fractions, and finally milling to obtain sizes in the nanorange. Sri Lanka is gifted with very high-purity quartz, which contains almost 100% SiO_2. This quartz can be used to obtain nanosized SiO_2 particles. Our ongoing research in collaboration with the Sri Lanka Industrial Technology Institute (ITI) is very successful, and we are able to produce 50 nm size SiO_2 nanoparticles in large quantities by this top-down approach. We have also attempted converting ilmenite obtained from Sri Lanka Mineral Sand Corporation to produce nanotitania with great success. Birgisson et al. [77] summarized the key breakthroughs in concrete technology most probable to result from the usage of nanotechnology. Basically, it has shown the development of high-performance cement and concrete materials as measured by their mechanical and durability properties, development of sustainable concrete materials and structures through engineering for different adverse environments, reducing energy consumption during cement production and enhancing safety, improvement of intelligent concrete materials through the integration of nanotechnology-based self-sensing and self-powered materials and cyber infrastructure technologies, advancement of novel concrete materials through nanotechnology-based innovative processing of cement and cement paste, and also development of fundamental multiscale model(s) for concrete through advanced characterization and modeling of concrete at the nano-, micro-, meso-, and macroscale [78]. The frost resistance of concrete comprising nano-Al_2O_3 is better than that comprising the same amount of nano-SiO_2. The compressive strength of normal concrete containing nano-SiO_2 is higher than that of the same amount of nano-Al_2O_3. The frost resistance of the concrete mixtures can be improved significantly by adding either nano-Al_2O_3 or nano-SiO_2. These nanomaterials not only promote the pozzolanic reaction, but they also act as fillers, thereby improving the pore structure of the concrete and densifying the microstructure of the cement paste. The frost resistance of the concrete containing nano-Al_2O_3 is better than that containing the same amount of nano-SiO_2.

Nanoparticles have a large surface area to volume ratio than their bulk counterparts, and due to their small size, they can fill in small cavities of the cement matrix, densifying the structure to result in improved strength and faster chemical reactions such as hydration reactions associated with cement setting. Further, the material requirement can be reduced drastically thus saving fast depleting natural resources and energy requirements for cement manufacturing and reducing associated adverse environmental consequences.

6. Conclusion

Basically, different types of cements and their chemical composition and applications in the current engineering and chemical world have been discussed in detail. Different types

of enhancing materials and fillers developed using nanotechnology for the productive and effective cement manufacturing have been mentioned with the chemical background. The mechanical defects when concrete is concerned and possible solutions that can be given through chemistry and nanotechnology have been deliberated in detail. In addition, CO_2-entrapping chemical compounds such as zeolites and metal organic framework and their contribution in making durability of the cement manufacturing have been illustrated with their chemistry. Environment effects of cement manufacturing and how to control the pollution of the environment when manufacturing processes that are being executed have been discussed using several standard processes, including the Calera process, oxy-combustion process, and monoethanolamide (MEA) process. Currently, the applications of nanoscience and nanotechnology have been gaining popularity in different fields of science and technology. The potential of nanotechnology to progress the performance of concrete and to lead to the development of novel, sustainable, advanced cement-based composites, and smart materials with unique mechanical, thermal, and electrical properties is promising, and many novel opportunities are expected to arise in the future. So finally, the newest trend of making nanocement and its development towards current developing and updating world is described in advance.

Conflicts of Interest

The authors declare that there are no conflicts of interest.

References

[1] S. P. Dunuweera and R. M. G. Rajapakse, "Cement types, composition, uses, environmental impact and possible solutions," in *Proceedings of the 28th International Symposium on Transport Phenomena*, Peradeniya, Sri Lanka, September 2017.

[2] T. C. Powers and T. L. Brownyard, "Studies of the physical properties of hardened Portland cement paste," *ACI Journal Proceedings*, vol. 43, no. 9, pp. 101–132, 1946.

[3] F. Lea, *The Chemistry of Cement and Concrete*, February 2018, https://ci.nii.ac.jp/naid/10003996296/.

[4] M. Schneider, M. Romer, M. Tschudin, and H. Bolio, "Sustainable cement production—present and future," *Cement and Concrete Research*, vol. 41, no. 7, pp. 642–650, 2011.

[5] A. Elimbi, H. Tchakoute, and D. Njopwouo, "Effects of calcination temperature of kaolinite clays on the properties of geopolymer cements," *Construction and Building Materials*, vol. 25, no. 6, pp. 2805–2812, 2011.

[6] M. Ali, R. Saidur, and M. Hossain, "A review on emission analysis in cement industries," *Renewable and Sustainable Energy Reviews*, vol. 15, no. 5, pp. 2252–2261, 2011.

[7] M. Thiery, G. Villain, P. Dangla, and G. Platret, "Investigation of the carbonation front shape on cementitious materials: effects of the chemical kinetics," *Cement and Concrete Research*, vol. 37, no. 7, pp. 1047–1058, 2018.

[8] *Portland Cement Clinker: The Bogue Calculation*, July 2017, http://www.understanding-cement.com/bogue.html#.

[9] *Composition of Cement*, July 2017, http://www.engr.psu.edu/ce/courses/ce584/concrete/library/construction/curing/Composition%20of%20cement.htm.

[10] S. Mindess and J. F. Young, *Concrete*, Prentice-Hall, Inc., Englewood Cliffs, NJ, USA, 1981.

[11] S. Kosmatka and W. Panarese, *Design and Control of Concrete Mixtures*, Portland Cement Association, Skokie, IL, USA, 1988.

[12] M. Mamlouk and J. Zaniewski, *Materials for Civil and Construction Engineers*, Addison Wesley Longman, Inc, Menlo Park, CA, USA, 1999.

[13] T. C. Holland, *Silica Fume User's Manual*, Technical Report FHWA-IF-05-016, Silica Fume Association and United States Department of Transportation Federal Highway Administration, Washington, DC, USA, 2005.

[14] S. Kosmatka, B. Kerkhoff, and W. Panerese, *Design and Control of Concrete Mixtures*, Portland Cement Association, Skokie, IL, USA, 14th edition, 2002.

[15] W. Gamble, "Cement, Mortar and Concrete," in *Mark's Handbook for Mechanical Engineers*, T. Baumeister and A. Avallone, Eds., p. 177, McGraw Hill, New York, NY, USA, 8th edition, 1916.

[16] Patents.google.com, "Portland cement manufacture," Patent No. US4081285A, 2018, https://patents.google.com/patent/US4081285A/en.

[17] R. Medeiros-Junior and M. G. Lima, "Electrical resistivity of unsaturated concrete using different types of cement," *Construction and Building Materials*, vol. 107, pp. 11–16, 2016.

[18] M. Korsch and W. Walther, "Peri-implantitis associated with type of cement: a retrospective analysis of different types of cement and their clinical correlation to the peri-implant tissue," *Clinical Implant Dentistry and Related Research*, vol. 17, no. S2, pp. e434–e443, 2015.

[19] T. Matschei, B. Lothenbach, and F. Glasser, "The role of calcium carbonate in cement hydration," *Cement and Concrete Research*, vol. 37, no. 4, pp. 551–558, 2007.

[20] K. Nakatsu, T. Goto, T. Higaki, H. Endo, S. Hirose, and Y. Yamazaki, "Compositions for low heat cements," US Patent No. US5547505, 1996.

[21] R. Novotný, E Bartoníþková, J Švec, and M Monþeková, "Influence of active alumina on the hydration process of Portland cement," *Procedia Engineering*, vol. 151, pp. 80–86, 2016.

[22] *Sulphate Attack on Concrete—Process and Control of Sulphate Attack*, July 2017, https://theconstructor.org/concrete/sulphate-attack-on-concrete-prevention/2162/.

[23] A. Duran, J Fernandez Navarro, P. Mazon, and A. Joglar, "Coloured coatings containing mixed transition metal oxides," *Journal of Non-Crystalline Solids*, vol. 100, no. 1–3, pp. 494–500, 1988.

[24] I. Fernández Olmo, E. Chacon, and A. Irabien, "Influence of lead, zinc, iron (III) and chromium (III) oxides on the setting time and strength development of Portland cement," *Cement and Concrete Research*, vol. 31, no. 8, pp. 1213–1219, 2001.

[25] M. Murat and F. Sorrentino, "Effect of large additions of Cd, Pb, Cr, Zn, to cement raw meal on the composition and the properties of the clinker and the cement," *Cement and Concrete Research*, vol. 26, no. 3, pp. 377–385, 1996.

[26] F. Tittarelli, "Oxygen diffusion through hydrophobic cement-based materials," *Cement and Concrete Research*, vol. 39, no. 10, pp. 924–928, 2009.

[27] I. J. de Vries and R. B. Polder, "Hydrophobic treatment of concrete," *Construction and Building Materials*, vol. 11, no. 4, pp. 259–265, 1997.

[28] A. M. AIshamsi, K. I. Alhosani, and K. M. Yousri, "Hydrophobic materials, superplasticizer and microsilica effects on setting of cement pastes at various temperatures," *Magazine of Concrete Research*, vol. 49, no. 179, pp. 111–115, 2015.

[29] O. S. Misnikov, "A study of the properties of portland cement modified using peat-based hydrophobic admixtures," *Polymer Science Series D*, vol. 7, no. 3, pp. 252–259, 2014.

[30] M. Stajanča and A. Eštoková, *Environmental Impacts of Cement Production*, July 2017, http://ena.lp.edu.ua:8080/bitstream/ntb/16692/1/55-Stajanca-296-302.pdf.

[31] C. Chen, G. Habert, Y. Bouzidi, and A. Jullien, "Environmental impact of cement production: Detail of the different processes and cement plant variability evaluation," *Journal of Cleaner Production*, vol. 18, no. 5, pp. 478–485, 2010.

[32] C. Branquinho, G. G. Oliveira, S. Augusto, P. Pinho, C. Máguas, and O. Correia, "Biomonitoring spatial and temporal impact of atmospheric dust from a cement industry," *Environmental Pollution*, vol. 151, no. 2, pp. 292–299, 2008.

[33] Y. Lei, Q. Zhang, C. Nielsen, and K. He, "An inventory of primary air pollutants and CO_2 emissions from cement production in China, 1990–2020," *Atmospheric Environment*, vol. 45, no. 1, pp. 147–154, 2011.

[34] M. Schuhmacher, J. L. Domingo, and J. Garreta, "Pollutants emitted by a cement plant: health risks for the population living in the neighborhood," *Environmental Research*, vol. 95, no. 2, pp. 198–206, 2004.

[35] O. A. Al-Khashman and R. A. Shawabkeh, "Metals distribution in soils around the cement factory in southern Jordan," *Environmental Pollution*, vol. 140, no. 3, pp. 387–394, 2006.

[36] A. M. Farmer, "The effects of dust on vegetation—a review," *Environmental Pollution*, vol. 79, no. 1, pp. 63–75, 1993.

[37] K. T. Hindy, H. I. A. Shafy, and S. A. Faraga, "The role of the cement industry in the contamination of air, water, soil and plant with vanadium in Cairo," *Environmental Pollution*, vol. 66, no. 3, pp. 195–205, 1990.

[38] D. Zimwara, L. Mugwagwa, and T. R. Chikowore, "Air pollution control techniques for the cement manufacturing industry: a case study for Zimbabwe," in *CIE42 Proceedings*, Cape Town, South Africa, July 2012.

[39] *Available and Emerging Technologies for Reducing Greenhouse Gas Emissions from the Portland Cement Industry (2010) Sector Policies and Programs Division Office of Air Quality Planning and Standards U.S. Environmental Protection Agency Research Triangle Park, North Carolina 27711*, June 2017, https://www.epa.gov/sites/production/files/2015-12/documents/cement.pdf.

[40] Calera Inc., *Notes on Sustainability and Potential Market*, 2009.

[41] D. J. Barker, S. A. Turner, P. A. Napier-Moore, M. Clark, and J. E. Davison, "CO_2 Capture in the Cement Industry," *Energy Procedia*, vol. 1, no. 1, pp. 87–94, 2009.

[42] A. D. Ebner and J. A. Ritter, "Carbon dioxide separations: state-of-the-art adsorption and membrane separation processes for carbon dioxide production from carbon dioxide emitting industries," *Separation Science and Technology*, vol. 44, no. 6, pp. 1273–1421, 2009.

[43] D. Aaron and C. Tsouris, "Separation of CO_2 from flue gas: a review," *Separation Science and Technology*, vol. 40, no. 1–3, pp. 321–348, 2005.

[44] L. M. Robeson, "The upper bound revisited," *Journal of Membrane Science*, vol. 320, no. 1-2, pp. 390–398, 2008.

[45] C. J. Orme, M. K. Harrup, T. A. Luther et al., "Characterization of gas transport in selected rubbery amorphous polyphosphazene membranes," *Journal of Membrane Science*, vol. 186, no. 2, pp. 249–256, 2001.

[46] A. Brunetti, F. Scura, G. Barbieri, and E. Drioli, "Membrane technologies for CO_2 separation," *Journal of Membrane Science*, vol. 359, no. 1-2, pp. 115–125, 2010.

[47] A. Mondal and B. Mandal, "Novel CO_2-selective cross-linked poly(vinyl alcohol)/polyvinylpyrrolidone blend membrane

containing amine carrier for CO_2–N_2 separation: Synthesis, characterization, and gas permeation study," *Industrial & Engineering Chemistry Research*, vol. 53, no. 51, pp. 19736–19746, 2014.

[48] C. S. K. Achoundong, N. Bhuwania, S. K. Burgess, O. Karvan, J. R. Johnson, and W. J. Koros, "Silane modification of cellulose acetate dense films as materials for acid gas removal," *Macromolecules*, vol. 46, no. 14, pp. 5584–5594, 2013.

[49] M. M. Khan, G. Bengtson, S. Neumann, M. M. Rahman, V. Abetza, and V. Filiz, "Synthesis, characterization and gas permeation properties of anthracene maleimide-based polymers of intrinsic microporosity," *RSC Advances*, vol. 4, no. 61, pp. 32148–32160, 2014.

[50] N. Du, G. P. Robertson, I. Pinnau, and M. D. Guiver, "Polymers of intrinsic microporosity with dinaphthyl and thianthrene segments," *Macromolecules*, vol. 43, no. 20, pp. 8580–8587, 2010.

[51] T. Emmler, K. Heinrich, D. Fritsch et al., "Free volume investigation of polymers of intrinsic microporosity (PIMs): PIM-1 and PIM1 copolymers incorporating ethanoanthracene units," *Macromolecules*, vol. 43, no. 14, pp. 6075–6084, 2010.

[52] B. S. Ghanem, N. B. McKeown, P. M. Budd, and D. Fritsch, "Polymers of intrinsic microporosity derived from bis(phenazyl) monomers," *Macromolecules*, vol. 41, no. 5, pp. 1640–1646, 2008.

[53] P. M. Budd, N. B. McKeown, and D. Fritsch, "Polymers of intrinsic microporosity (PIMs): High free volume polymers for membrane applications," *Macromolecular Symposia*, vol. 245-246, pp. 403–405, 2006.

[54] A. E. Amooghin, H. Sanaeepur, M. Z. Pedram, M. Omidkhah, and A. Kargari, "New advances in polymeric membranes for CO_2 separation," in *Polymer Science: Research Advances, Practical Applications and Educational Aspects*, A. Méndez-Vilas and A. Solano, Eds., pp. 354–368, 2016, http://www.formatex.info/polymerscience1/book/354-368.pdf.

[55] D. F. Sanders, Z. P. Smith, R. Guo et al., "Energy-efficient polymeric gas separation membranes for a sustainable future: a review," *Polymer*, vol. 54, no. 18, pp. 4729–4761, 2013.

[56] R. V. Siriwardane, M. S. Shen, and E. P. Fisher, "Adsorption of CO_2 on zeolites at moderate temperatures," *Energy & Fuels*, vol. 19, no. 3, pp. 1153–1159, 2005.

[57] J. E. Bauer, P. M. Williams, and E. R. M. Druffel, "Recovery of submilligram quantities of carbon dioxide from gas streams by molecular sieve for subsequent determination of isotopic (13C and 14C) natural abundances," *Analytical Chemistry*, vol. 64, no. 7, pp. 824–827, 1992.

[58] S. M. L. Hardie, M. H. Garnett, A. E. Fallick, A. P. Rowland, and N. J. Ostle, "Carbon dioxide capture using a zeolite molecular sieve sampling system for isotopic studies (13C and 14C) of respiration," *Radiocarbon*, vol. 47, no. 3, pp. 441–451, 2005.

[59] S. L. Jamesa, "Metal-organic frameworks," *Chemical Society Reviews*, vol. 32, no. 5, p. 276, 2003.

[60] A. R. Millward and O. M. Yaghi, "Metal–organic frameworks with exceptionally high capacity for storage of carbon dioxide at room temperature," *Journal of the American Chemical Society*, vol. 127, no. 51, pp. 17998-17999, 2005.

[61] J. R. Li, Y. Ma, M. C. McCarthy et al., "Carbon dioxide capture-related gas adsorption and separation in metal-organic frameworks," *Coordination Chemistry Reviews*, vol. 255, no. 15-16, pp. 1791–1823, 2011.

[62] K. S. Walton and R. Q. Snurr, "Applicability of the BET method for determining surface areas of microporous metal–organic frameworks," *Journal of the American Chemical Society*, vol. 129, no. 27, pp. 8552–8556, 2007.

[63] B. Arstad, H. Fjellvåg, K. O. Kongshaug, O. Swang, and R. Blom, "Amine functionalised metal organic frameworks (MOFs) as adsorbents for carbon dioxide," *Adsorption*, vol. 14, no. 6, pp. 755–762, 2008.

[64] R. Siriwardane, M. Shen, E. Fisher, and J. Losch, *CO₂ Capture Utilizing Solid Sorbents*, U.S. Department of Energy National Energy Technology Laboratory, Pittsburgh, PA, USA, 2003, https://www.netl.doe.gov/publications/proceedings/04/carbon-seq/039.pdf.

[65] A. U. Czaja, N. Trukhanb, and U. Müllerb, "Industrial applications of metal–organic frameworks," *Chemical Society Reviews*, vol. 38, no. 5, p. 1284, 2009.

[66] U. Mueller, M. Schubert, F. Teich, H. Puetter, K. Schierle-Arndta, and J. Pastréa, "Metal–organic frameworks—prospective industrial applications," *ChemInform*, vol. 37, no. 23, 2006.

[67] F. Merlin, H. Lombois, S. Joly, N. Lequeux, J. L. Halarya, and H. V. Damme, "Cement-polymer and clay-polymer nano- and meso-composites: spotting the difference," *Journal of Materials Chemistry*, vol. 12, no. 11, pp. 3308–3315, 2002.

[68] S. Chuah, Z. Pan, J. G. Sanjayan, C. M. Wang, and W. H. Duan, "Nano reinforced cement and concrete composites and new perspective from graphene oxide," *Construction and Building Materials*, vol. 73, pp. 113–124, 2014.

[69] A. E. Aleem, M. Heikal, and W. M. Morsi, "Hydration characteristic, thermal expansion and microstructure of cement containing nano-silica," *Construction and Building Materials*, vol. 59, pp. 151–160, 2014.

[70] Moscow IMET International, *Nano Cements*, June 2017, https://www.globalimet.com/single-post/2015/05/10/Nano-cements.

[71] Marsel Yanovich Bickbau, "Method for producing nano-cement, and nano-cement," US Patent Publication No. EP 3006415 A1, 2016.

[72] https://nanotekmaterials.squarespace.com/advantages/, June 2017.

[73] M. S. Kirgiz, "Advancements in mechanical and physical properties for marble powder–cement composites strengthened by nanostructured graphite particles," *Mechanics of Materials*, vol. 92, pp. 223–234, 2016.

[74] http://www.nanotechmag.com/zenyatta-receives-funding-develop-nano-graphite-reinforced-cement/, 2017.

[75] R. F. Feldman and P. J. Sereda, "A model for hydrated Portland cement paste as deduced from sorption-length change and mechanical properties," *Matériaux et Constructions*, vol. 1, no. 6, pp. 509–520, 1968.

[76] J. Chen, S.-C. Kou, and C.-S. Poon, "Hydration and properties of nano-TiO₂ blended cement composites," *Cement and Concrete Composites*, vol. 34, no. 5, pp. 642–649, 2012.

[77] B. Birgisson, A. K. Mukhopadhyay, G. Geary, M. Khan, and K. Sobolev, *Nanotechnology in Concrete Materials: A Synopsis. Transportation Research Circular E-C170*, Transportation Research Board, Washington, DC, USA, 2012.

[78] B. Birgisson, P. Taylor, J. Armaghani, and S. P. Shah, "American road map for research for nanotechnology-based concrete materials," *Transportation Research Record: Journal of the Transportation Research Board*, vol. 2142, pp. 130–137, 2010.